PhD thesis

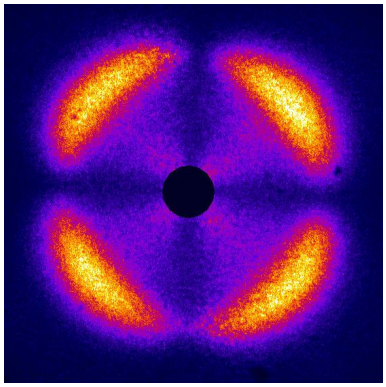

Influence of shear on the transient and steady state properties of lyotropic bilayer systems

submitted in partial fulfillment of the requirements

for the degree of "Doktor rerum naturae" to the

Faculty of Mathematics and Science

Christian-Albrechts University of Kiel

Florian Nettesheim

Kiel 2004

March 18, 2004

Statement of Authenticity

This PhD work was carried out at the Institute of Macromolecular Chemistry at Albert-Ludwigs University of Freiburg from April 2000 until October 2000 and continued at the Institute of Physical Chemistry at Christian-Albrechts University of Kiel from November 2000 until March 2004.

Florian Nettesheim

Referent: Prof. Dr. W. Richtering

Koreferent: Prof. Dr. Dr. h. c. G. Lagaly

Tag der Disputation:

Zum Druck genehmigt, Kiel den

Der Dekan

I certify that this thesis does not incorporate, without acknowledgment, any material previously submitted for a degree or diploma in any university, and that, to the best of my knowledge, it does not contain any material previously published or written by another person except where due reference is made in the text. The work in this thesis is my own, except for the contributions made by others as described in the Acknowledgments.

(Florian Nettesheim)

Acknowledgments

Expressing gratitude to persons who played a role during a PhD-thesis can be an unending task for even minor or seemingly unrelated contributions may affect or influence it substantially. That is why I want to start with my parents, whose contribution was not related directly to the work itself but without knowing of their moral support and assurance as well as without their education, their found conviction in principle question of life and their strong belief, this work would not have been possible. I truly owe everything to them, my gratitude and acknowledging their choices and decisions, which build the basis for a unique family. Therefore I dedicate this work to my parents Martin and Mercedes Nettesheim.
Here, I also wish to express my gratitude to my siblings, Maria, Andreas, Johannes and Stefan, who are essential to my life and whom I don't want to miss.

- First of all I wish to express my gratitude to Prof. Dr. Walter Richtering for offering the opportunity to carry out the PhD-work in his research group, for his way of guiding without predetermining ideas and finally for supporting my research stays in France and Sweden, from which vital scientific collaborations developed.

- Furthermore, I owe my gratitude to Prof. Dr. Ulf Olsson who, as my second supervisor, initiated the idea of a half year stay in Sweden. He played a key role as an initiator of interesting approaches, feeding me with problems, giving me a deeper insight of the formalisms of scattering and thermodynamic problems of general nature, for never imposing concepts but rather guiding in a maieutic manner and for constant motivation. He made my stay in Sweden both successful and enjoyable.

- Prof. Dr. Gerhard Lagaly for being the co-referee of my PhD-thesis.

- I also wish to thank Dr. Peter Lindner, who tutored my internship at the ILL and introduced me to the handling of a small-angle neutron scattering experiment. David Boyer was always a great help with technical matters at D11, regardless if it meant to be there at weekends or after working hours.

- The former members of the research group in Freiburg, in particular Johannes Zipfel, for a good atmosphere, which convinced me to join the group. Johannes Zipfel earns special

thanks for his involvement in the beginning of my PhD-work, especially during the time in Grenoble and for introducing me to French cheese and other delicacies.

- The research group in Kiel also guaranteed a lively atmosphere and I address my thanks to:

  - Markus Stieger and Stacy Pyett (to be mentioned together). Markus for mutual support during the studies and at D11. To Stacy I am deeply indebted for supplying us with Oreos and on top with self made cookies, which played a vital role for surviving long days and late nights from December 2003 through March 2004.
  - Matthias Soddemann for helping me to move from Grenoble to Kiel,
  - Ingo Berndt for hard core and heavy metal at D11,
  - Edda Kettler for making the research group a sociable experience again and for cooking in Blavand and on other occasions,
  - Claus Bernd Müller for the blessings of LaTeX and his enthusiasm in his independent project,
  - Niels Greinert for introducing me by the name "the cheeseman" to Bindu,
  - Sven Koschoreck for excitement,
  - David Löf for Swedish hospitality, and for convincing us of Swedish-Iranian cuisine,
  - Stefanie Mayer for her delicious cakes and for getting us all together for a group-breakfast.
  - Marriam Webster for her prosaic support.

- I wish to thank the members of the Physical Chemistry Department in Lund for the enjoyable time. There I experienced group dynamics on a large scale, with fluctuating cast and a constant flux of incoming and outgoing foreign students to at some degree rule the positive atmosphere.

  - Especially Joakim Balogh for organizing a bike for me, and for being one of the most sociable persons I met.
  - Alan Bream for all the new and truly important English vocabulary (not to be mentioned here in detail).

  - Cecilia Leal and Rita Dias for bringing a bit of a Portuguese air to Lund.
  - Jörgen Jansson, Daniel Topgaard and Jan-Willem Benjamins for being office mates in Lund.
  - Stefanie Schneider, Iseult Lynch, Maria Karlberg, Katarina Flödstrom, Martin Olsson and again Joakim Balogh for sharing the Vasaloppet experience.

- I also thank Isabelle Grillo for collaborating on clay doped lamellar phases and contributing her experience in contrast variation.

- I would like to thank all the people who have contributed to various aspects of the work, in particular, Mr. Will for generously supplying the technical sketches of the Searle shear cell and the personell of the technical workshop for technical support. Mr. Eggers and Mr. Warns for providing their expertise in electronic matters. Dr. Monkenbusch and Dr. Biehl for their great support in doing NSE-experiments and their help with the data evaluation.

- Dr. Falk and Kertin Renth, Jens and Nele Riedel for welcoming me here in northern Germany and being good friends. In particular, Jens and Nele for their legendary summer parties.

Lebenslauf
Florian Nettesheim

Kappelner Str. 5, D-24106 Kiel, Deutschland

Staatsangehörigkeit: deutsch

Familienstand: ledig

Geb.: 27.8.1974 in Bonn

Schulzeit

1980 - 86: Katholische Grundschule St. Ursula in Berlin, Zehlendorf

1986 - 93: Ernst-Moritz-Arndt Gymnasium Berlin, Dahlem.
Humanistisch, altsprachiger Zweig. Leistungskurse: Chemie und Kunst
Wahlpflichfach: Deutsch und Politische Weltkunde

1989 / 90: Schulsprecher, Organisation einwöchiger Projekt Tage

1990/92: Mitglied der Schulkonferenz

28.5.93: Abitur, Note 2,3

Ausbildung

1993 - 2000: Chemie Diplomstudium an der Albert-Ludwigs-Universität, Freiburg
Diplomarbeit: "Einfluss elektrostatischer Aufladung lyotroper lamellarer Phasen auf das Verhalten von Vesikeln unter Scherung" bei P.D. Dr. W. Richtering

8.3.2000: Diplom, Note: sehr gut

1.4.2000 - 04: Promotion bei Prof. Dr. W. Richtering in der Physikalischen Chemie an der Christian-Albrechts-Universität zu Kiel: "Influence of shear on the transient and steady state properties of lyotropic bilayer systems"

Auslandsaufenthalte

Sept. 1996 - Sept. 1997: Studium der Chemie an der University of Massachusetts in Amherst, MA, USA. Austausch im Rahmen des Massachusetts-Badenwürtemberg Programms.

Jul. - Dez. 2000: Praktikum im Rahmen eines DAAD Stipendiums am Institut-Laue-Langevin (ILL) in Grenoble, Frankreich. Betreuer: Dr. Peter Lindner.

Aug. - Oct. 2001 sowie **Feb. - April 2002:** Forschungsaufenthalte im Rahmen eines Marie-Curie-Stipendiums in Lund, Schweden. Betreuer: Prof. Dr. Ulf Olsson.

Praktika

Feb. - März 1994: Praktikum am Institut für angewandte Polymerchemie der Fraunhofer Gesellschaft (IAP FHG) in Teltow.
"Synthese von Polyestern mit Hilfe von Titanorganyl-Komplexen als Katalysator"
Betreuer: Dr. habil. G. Rafler.

Jun. / Jul. 1997: Praktikum in der chemischen Fakultät der University of North Carolina, Chapel Hill, North Carolina, USA
"Synthesis of a Siloxane-Elastomer with a 4.4'-bis-n-hexyldiphenyldiacetylene as mesogen." Betreuer: Prof. Dr. E. Samulski.

Publications

1. **Publications in scientific journals:**

   a) F. Nettesheim, J. Zipfel, P. Lindner, W. Richtering "Influence of sodium dodecyl sulfate on the structure and rheology of aqueous solutions of the nonionic surfactant tetraethyleneglycol-monododeccyl ether ($C_{12}E_4$)", *Colloids and surfaces A* **2001**, *183-185*, 563-574.

   b) J. Zipfel, F. Nettesheim, P. Lindner, T. D. Le, U. Olsson, W. Richtering "Cylindrical intermediates in a shear-induced lamellar-to-vesicle transition", *Europhys. Lett.* **2001**, *53*(3), 335-341.

   c) F. Nettesheim, J. Zipfel, U. Olsson, F. Renth, P. Lindner, W. Richtering "Pathway of the Shear-Induced Transition between Planar Lamellae and Multilamellar Vesicles as Studied by Time-Resolved Scattering Techniques", *Langmuir* **2003**, *19*, 3603-3618.

   d) F. Nettesheim, U. Olsson, P. Lindner, W. Richtering "Effect of flow reversal on the shear induced formation of multilamellar vesicles", *submitted to J. Phys. Chem. B* **2004**.

   e) F. Nettesheim, I. Grillo, P. Lindner, W. Richtering "Effect of clay insertion on a nonionic lamellar phase under shear", *Langmuir* **2004**, *accepted.*

   f) F. Nettesheim, U. Olsson, P. Lindner, W. Richtering "Correction Method for the Asymmetry of the Tangential Beam in a Couette (or Searle) Geometry used in Rheo-Small-Angle Neutron-Scattering", *submitted to J. Appl. Cryst.* **2004**.

2. **Poster contributions at conferences:**

   a) F. Nettesheim, P. Lindner, W. Richtering: "Formrelaxation scherdeformierter multilamellarer Vesikel." Nachwuchstagung der Kolloidgesellschaft **2000**, Heinrich-Heine-Universität Düsseldorf.

   b) F. Nettesheim, I. Grillo, P. Lindner, W. Richtering: "Change of intermembrane spacing as a function of stress in a lamellar phase with clay particles dispersed." 17th European Colloids and Interface Society (ECIS) Conference, **2003** in Florence.

3. **Oral contributions at conferences:**

a) F. Nettesheim, J. Zipfel, U. Olsson, P. Lindner, W. Richtering: "Pathway from planar lamellae to multilamellar vesicles." 73rd annual meeting of the Society of Rheology (SOR), **2001** in Bethesda, Maryland, USA.

b) F. Nettesheim, J. Zipfel, U. Olsson, F. Renth, P. Lindner, W. Richtering: "The shear-induced transition between planar lamellae and multilamellar vesicles as studied by time resolved scattering techniques." 102. Bunsentagung, **2003** an der Christian-Albrechts-Universität zu Kiel.

c) W. Richtering, F. Nettesheim: "Shear induced structures in doped lamellar mesophases of nonionic surfactants." ACS 77th Colloid and Surface Science Symposium, **2003** at the Georgia Institute of Technology, Atlanta, Georgia, USA.

Symbols and Abbreviations

a_s – Area per headgroup of a surfactant molecule

C_nE_m – Nonionic hydrocarbon-ethyleneoxide surfactant with hydrophobic n and hydrophilic chain length m

$\dot{\gamma}$ – Shear rate

$\dot{\gamma}_c$ – Critical shear rate

$\dot{\gamma}_{sat}$ – Saturation shear rate

γ – Strain

d – Lamellar spacing

$\Delta\rho$ – Excess neutron-scattering length density

δ – Dry thickness of a surfactant film (hydrophilic and hydrophobic parts)

δ_t – Hydrophobic thickness of a surfactant film

ϵ – Thickness of a platelet

η – Viscosity

η_{caille} – Caillé-parameter

$\vec{F}$ – Force

G' – Storage modulus

G" – Loss modulus

G_f – Helfrich free energy of a surfactant film

H_0 – Spontaneous curvature of a surfactant film

H – Actual curvature of a surfactant film

$\langle H \rangle$ – Mean bilayer curvature

K – Gaussian splay modulus

$\langle K \rangle$ – Mean Gaussian bilayer curvature

κ_{mono} – Bending modulus

κ_b – Bilayer bending modulus

$\bar{\kappa}_{mono}$ – Gaussian modulus

$\bar{\kappa}_b$ – Bilayer Gaussian modulus

$\vec{k}_i$ – Wave vector of the incident radiation

$\vec{k}_s$ – Wave vector of the scattered radiation

L_s – Length of a surfactant molecule

L_α-phase – Lamellar phase

L_3-phase – Sponge phase

λ_0 – Vacuum wavelength of radiation

MLV – Multilamellar vesicle

MLC – Multilamellar cylinder

n – Refractive index

n_c – Number of connections

n_h – Number of handels

OAM – Optical analysis modul

p – Packing parameter

P(q) – Form factor

Φ – Volume fraction

Φ_s – Surfactant volume fraction

Φ_o – Oil volume fraction

Φ_m – Membrane volume fraction

Φ_p – Particle volume fraction

q – Scattering vector (momentum transfer)

R_0 – Spontaneous radius of a surfactant film

σ – Shear stress

SANS – Small-angle neutron scattering

SALS – Small-angle light scattering

SAXS – Small-angle X-ray scattering

S(q) – Structure factor

θ – Scattering angle

ξ – Correlation length

S/L – Weight of dried solid (clay) per weight stock solution in percent

V_s – Volume of a surfactant molecule

V_p – Volume of particle

Short Summary

The work presented in this thesis comprises in-situ structural determination under shear using time-resolved scattering techniques and flow birefringence. These techniques were used to study transient structures occurring in surfactant bilayer systems under shear on length scales from a few nanometers up to several micrometers. The major concern of this thesis is the lamellar-to-MLV dynamic transition under shear, which is one of the unsolved mysteries in the area of complex fluids.

In particular, details of the structural transition from a state of well aligned lamellae in parallel orientation to multilamellar vesicles (MLV) under the influence of a shear field were studied by a combination of time resolved small-angle neutron (SANS) and small-angle light scattering (SALS) using a nonionic surfactant lamellar phase. The study revealed five distinct transient states of bilayer organization and yielded strong support for a stress rather than a rate control of the transition. Reversible and irreversible parts of the transition, i.e., elastic storage of deformation on one hand and dissipation, which thus contributes to MLV formation, on the other, were determined in flow reversal experiments using the above mentioned time-resolved scattering techniques.

Furthermore, the intriguing problem of particle inclusion in concentrated surfactant systems and its effect of the dynamic properties of such a sample was addressed by studying the incorporation of clay in a nonionic surfactant lamellar phase. Flow-SANS revealed a drastic decrease in lamellar spacing leading to the conclusion, that a micro phase separation takes place in such systems.

The influence of shear on the bilayer organization was furthermore studied in a L_3- (or sponge-) phase using flow-birefringence and transmission measurements. Here, the critical shear rates for the transition from the disordered L_3- to the shear aligned L_α-phase displayed an unexpected scaling with membrane volume fraction and shear quench experiments revealed relaxation times for the structural recovery of the L_3-phase orders of magnitude slower than the inverse critical shear rate.

Finally, a study of instrumental concern was carried out to solve the problem of the asymmetry of the tangential beam for a Couette or Searle-type shear cell used in Rheo-SANS experiments. In addition to considering the geometry of a tangential experiment, a practical method for experimentally accounting for the asymmetry is proposed.

Kurzzusammenfassung

Die hier vorgestellte Doktorarbeit umfasst in-situ Strukturaufklärung unter Scherung. Mit Hilfe zeitaufgelöster Streumethoden sowie Fließdoppelbrechung wurden scherinduzierte transiente Strukturen auf Längenskalen zwischen wenigen Nano- bis zu einigen Mykrometern näher untersucht. Das hauptsächliche Anliegen dieser Arbeit besteht in der Aufklärung der dynamischen Umwandlung planarer Lamellen zu multilamellaren Vesikeln (MLV) unter Scherung. Dieser Übergang ist eines der bisher ungelösten Rätsel im Bereich der Komplexen Fluide.

Insbesondere wurden die Details der Strukturumwandlung ausgehend von einem wohl definierten Zustand parallel orientierter Lamellen zu multilamellaren Vesikeln unter Schereinfluß mittels zeitaufgelöster Kleinwinkelneutronen- und Kleinwinkellichtstreuung an einer nicht-ionischen lamellaren Phase untersucht. Das ermöglichte die Unterscheidung fünf verschiederner transienter Zustände der Lamellenorientierung. Weiterhin lieferten diese Experimente starke Hinweise auf eine Schubspannungs- und nicht eine Scherratenkontrolle des Übergangs. In Fließumkehrexperimenten wurde detailierter Aufluß über die reversiblen und respektive irreversiblen und damit der elasisch gespeicherten bzw. der dissipierten, zur Vesikelbildung beitragenden Anteile der Deformation in einem solchen Übergang erhalten. Diese Untersuchungen wurden ebenfalls mit Hilfe der oben genannten zeitaufgelösten Streumethoden durchgeführt.

Weiterhin beschäftigt sich diese Arbeit mit der faszinierenden Fragestellung, welchen Einfluß die Dotierung einer nicht-ionischen lamellaren Phase mit Tonpartikeln auf ihr Verhalten unter Scherung hat. Rheo-SANS Experimente förderten eine drastische Verringerung des Lamellenabstandes zu tage, die als solche nur durch eine Mikrophasenseparation erklärt werden konnte.

Darüber hinaus wurde der Einfluß von Scherung auf eine L_3- (oder Schwamm-) Phase mit Hilfe von Rheo-Doppelbrechung und Transmissionsmessungen untersucht. Dabei trat zu tage, dass die kritische Scherrate, die den Übergang von der L_3-Phase zu vollständig scherorientierten L_α-Phase beschreibt, in einer unerwarteten Weise vom Membranvolumenbruch abhängt. Relaxationsexperimente lieferten Relaxationszeiten für die sturkturelle Erholung der L_3-Phase, die mehrere Größenordnungen langsamer sind als die theoretisch erwarteten.

Abschießend wurde eine Untersuchung von eher intrumentellem Interesse durchgeführt, um die Problematik der Asymmetrie der tangentialen Streukonfiguration, die in Rheo-SANS Experimenten unter Verwendung einer Couette bzw. Searle-Scherzelle auftritt, zu lösen. Zusätzlich zu der geometrischen Beschreibung wird auch eine praktikable, experimentelle Vorgehensweise für die Korrektur der Asymmetrie in tangentialer Konfiguration aufgenommener Streubilder vorgeschlagen.

Contents

1 Introduction

Surfactant systems are important to the evolution of live as they are fascinating molecules to study. Their capability to self-assemble in a variety of colloidal structures is the reason for their abundance in nature. The most prominent example for a surfactant self-assembled structure in nature is the cell membrane, a closed phospholipid bilayer, serving the purpose of compartmentalization, control of metabolism and information exchange.

The size of colloidal aggregates ranges from a few nanometers to several micrometers, a size range which is intermediate between atomic and macroscopic sizes. It is therefore called the mesoscopic (or colloidal) size range. A balance of guaranteeing the complexity of metabolic reactions, storing and exchanging information and protecting the self-containing unit (the cell) from its environment seemed to have favored this size range for the development of live.[1]

Colloids in general comprise all entities on this size range, whether solid particulate or self assembled systems. The term colloid was initially used for glue like substances for which a classification in liquid or solid (crystalline) was not possible. The word derives from the Greek word $\kappa o \lambda \lambda \acute{\alpha}$ for glue or slime.

In addition to their relevance in nature, surfactants find wide use in industrial and pharmacological applications such as soap, lotions, stabilizers, flow enhancers, dairy products and liposomes for drug targeting just to mention a few. In prospective applications the knowledge about the relation between microscopic structure and macroscopic properties is of essential relevance. In many cases processing involves external fields such as shear and consequently non-equilibrium structures may be formed. These may alter properties such as viscosity, elasticity or texture of a product substantially, which has to be considered during processing. Shear thickening or shear thinning for instance may on one hand impede processing of a material; on the other hand it may as well be used deliberately as in paints, lubricants, personal care products and more.[2,3] Thus, understanding the structural response to external fields will lead to better

means of controlling the desired product qualities.

Bilayer structures as they find use in liposomes have to be well characterized with respect to their membrane properties so that a design in view of their prospective and normally very distinct pharmaceutical, pharmacological and medical applications is possible.[4–6]

Multilamellar vesicles (MLV), closed concentric bilayer structures, which appear in lamellar phases when they are exposed to shear, are promising candidates for a range of the above mentioned applications. Easy controll of their size in a well defined shear field and their longtime stability, under certain circumstances also if diluted, opens perspectives to encapsulate proteins and DNA, a field that received substantial interest recently.[7]

Although steady state structures of the lamellar phase under shear are very well characterized, and despite the large number of studies in this field, the morphological lamellar–to–MLV dynamic transition under shear, is a mystery there to be unraveled. The detailed understanding of the formation mechanism of these interesting entities, the knowledge about possible transition states and the parameters, which govern it, may open possibilities to a carefully directed control of aggregate shapes and sizes tailored for the specific application. The dynamics of this transition may as well be of interest for applications, where the formation kinetics of MLVs needs to be controlled.

Therefore, a variety of studies is solely dedicated to the fascinating topic of MLV-formation under shear.[2,8] The general approach is to combine in-situ structure determination with a rheological experiment. As to the specific design of the rheological experiment there are no limits to the scientists creativity. So far, the most widely studied condition is steady shear,[9–26] but also dynamic experiments have been performed.[27]

Another intriguing possibility is including a third component into the lamellar phase and studying the formation of MLVs under the altered conditions. These may be water soluble polymers,[28,29] block-copolymers which anchor to the membrane,[30–35] proteins,[7] differently charged surfactants[26,36] or colloids.[37,38] All these approaches intend to change the membrane properties or introducing defects into the lamellar phase and thus enabling the investigation of the influence of bending rigidity, coulomb or osmotic interactions or the defect density on the lamellar–to–MLV transition.

The PhD-thesis presented here comprises experiments starting from a well aligned state of lamellae to investigate the details of the transition from reproducible starting conditions on one hand

and incorporating anisotropic clay particles into the lamellar phase on the other. An excursion is made to the shear induced alignment of the L_3-phase. This transition from a liquid like bilayer organization to a shear induced smectic order itself is a fascinating and unsolved puzzle. Since the work involved extensive use of small-angle neutron scattering under shear for structure determination on a nanometer length scale the problem of the asymmetry of the scattering, as it is encountered in tangential beam experiments, was examined closer.

2 Motivation

The general aim of this thesis is to gain a better understanding of the influence of shear on the bilayer organization in nonionic surfactant phases. Two bilayer organizations are known for nonionic surfactants of the C_nE_m-type; on one hand the lamellar phase, where bilayers are organized in periodic stacks and on the other the L_3- (or sponge-) phase with a liquid bilayer organization. In both cases shear leads to interesting changes in the local bilayer organization as a function of deformation and/or shear rate. Since at least for the lamellar phase the steady state structures are well characterized for a variety of surfactant systems, the study of transient structures occurring during the transition from planar lamellae to MLVs will be emphasized.

In particular, the dynamic lamellar–to–MLV transition under shear will be examined in continuous shear experiments using the nonionic surfactant systems $C_{10}E_3$ and $C_{12}E_4$ in D_2O. The intention is to characterize the transient structures occurring during the transition from planar lamellae to MLVs. Using a combination of time-resolved scattering methods small-angle neutron and light scattering and rheometry, a direct correlation between morphology changes on a microscopic and mesoscopic scale and the bulk properties of the sample can be established. There is also an ongoing debate as to whether the transition is controlled by the strain rate or by shear stress, namely whether the coupling of the shear field with fluctuations (bilayer undulations) is responsible for MLV-formation or introducing a certain energy per bilayer to create curvature.[9,10,13,39–42]

With the detailed knowledge about the transition path under varying conditions (shear rate, temperature, surfactant), the symmetry of the intermediates and their stability at rest provide the basis for further experiments, such as following the question as to how the transition occurs within the gap or probing larger length scales.

An intriguing experiment is subjecting the lamellar phase to an alternating shear field, such as oscillatory shear. There are many questions in this respect, which are worth being studied. In

the case of thermotropic smectics large amplitude oscillatory shear is known to iron out defects and thus producing a defect free well oriented smectic.[43] So far, only very few such experiments have been performed on the lyotropic analogues. The amplitudes that lead to a suppression of defects (MLV-formation) can be expected to be lower than in the case of thermotropic smectics. Thus the experiment needs to be designed differently to also allow the simultaneous execution of scattering experiments, either SANS or SALS. With a series of so-called flow reversal experiments with different strain amplitudes such an experiment is available, yielding structural information and thus revealing information about the reversible and irreversible parts of the transition from planar lamellae to MLVs.

Incorporating particles into the lamellar phase introduces conflicts, which at rest are not so apparent. If for instance anisotropic particles are used, the lamellar order will be perturbed and especially the MLV-formation will be affected, since stiff anisotropic particles are in conflict with a curved bilayer. In the presented work, laponite particles (a synthetic hectorite) will be included in a lamellar phase of $C_{12}E_4$ in a H_2O/D_2O mixture.

An excursion to the shear alignment of the L_3-phase is worthwhile. The topology of this peculiar phase is governed by the same principles as the lamellar phase. Shear alignment occurs at a specific shear rate, specific for the bilayer thickness and the membrane volume fraction.[44] There is a general consensus that the transition to the shear aligned state is caused by the suppression of bilayer fluctuations on length scales defined by the applied shear rate and the viscosity of the medium. The multiply connected bicontinuous liquid structure undergoes an disorder-order transition to the shear aligned state. However, there is an ongoing debate about the scaling of this critical shear rate with membrane volume fraction. Theoretical considerations suggest Φ_m^3-scaling of the free energy density from its scale invariance. Based on these arguments a Φ_m^3-scaling of the critical shear rate can be derived. Therefore, a series of experiments using the same nonionic surfactant system as that studied by Le et al. will be performed. In particular the scaling of the critical shear rate and of the relaxation from the shear aligned back to the isotropic state with volume fraction will be studied using flow-birefringence.

A problem, which is often encountered in rheo-SANS studies is the asymmetry of the 2-dimensional intensity distribution in tangential beam experiment. A detailed description is missing so far, although the tangential beam is widely used for a complete characterization of aggregate orientations is not possible without it. As a consequence most of the tangential beam data is not

presented on absolute scale or even without the proper background correction. Unfortunately, this leads to a loss of valuable information that can be extracted from properly normalized data. Therefore an instrumental study was performed to solve the problem, which is primarily of geometric nature. As a result, a rather simple experimental approach to account for the asymmetry will be proposed.

3 Theory

3.1 Surfactant Self-Assembly

Surfactants are molecules with two incompatible moieties, either of them soluble in one of two immiscible liquids, most commonly oil and water, in which the surfactant is composed of a hydrophilic and a hydrophobic part. The first is often termed hydrophilic headgroup, the latter hydrophobic tail. Furthermore, they can be categorized in several ways, relating to the nature of the headgroup or to the number of hydrophobic tails. The first is more common and one distinguishes between ionic (cationic, anionic and zwitterionic or gemini-surfactants) and non-ionic surfactants. Their amphoteric nature is the origin of their rich phase behavior in water.

3.1.1 Hydrophobic Effect

The hydrophobic effect is normally made responsible for the self-aggregation of surfactant molecules. If molecularly dispersed, a surfactant molecule exposes its hydrophobic tail to a hydrophilic environment. Water molecules in the vicinity would have to attain a higher order, which is entropically unfavorable. Consequently, there is a gain in entropy if the larger surfactant molecules self-aggregate and the water molecules can realize more disorder.[45]

3.1.2 Structures

The variety of structures possible in surfactant water mixtures is caused by a subtle interplay of surfactant geometry and attractive forces (such as the hydrophobic effect) and can be strongly temperature dependent, as is the case for nonionic surfactants. The surfactant geometry can be described by the so-called packing parameter,

$$p = \frac{V_s}{L_s a_s} \tag{3.1}$$

introduced by Israelachvili,[46] which defines the spontaneous curvature according to:

$$H_0 = 1/R_0 = \frac{1.5 - \sqrt{3p - 0.75}}{L_s} \tag{3.2}$$

Common micelle structures are shown in figure 3.1. At higher surfactant concentration the mi-

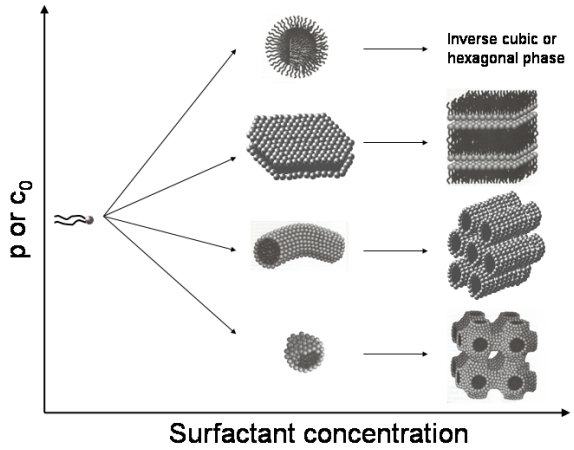

Figure 3.1: Surfactant aggregates as concentration increases. Depending on surfactant geometry spherical (p<1/3), cylindrical (1/3<p<1/2), planar micelles (1/2<p<1) or reverse micelles (1<p) are possible. At high concentration micelles organize in superstructures called mesophases.

celles themselves can organize to build so-called mesoscopic structures, such as cubic, hexagonal, lamellar and bicontinuous phases.

3.1.3 Phase Diagrams

Figure 3.2 shows a phase diagram of the nonionic surfactant pentaethyleneglycol monododecyl ether ($C_{12}E_5$).[47] The main features are identical for all nonionic surfactants of this series, only the phase transition temperatures increase with increasing surfactant length, or more precisely with the length of the hydrophobic tail. All phase diagrams of nonionic C_nE_m-type surfactants (n: number of carbon atoms in the hydrophobic chain, m: number of ethylene oxide units) display a lamellar phase at higher concentrations, which in a certain temperature range can be swollen with water up to 95% or more. At high enough swelling they display irridecence, due to Bragg-diffraction of visible light, i.e., the inter bilayer separation is of the order of the

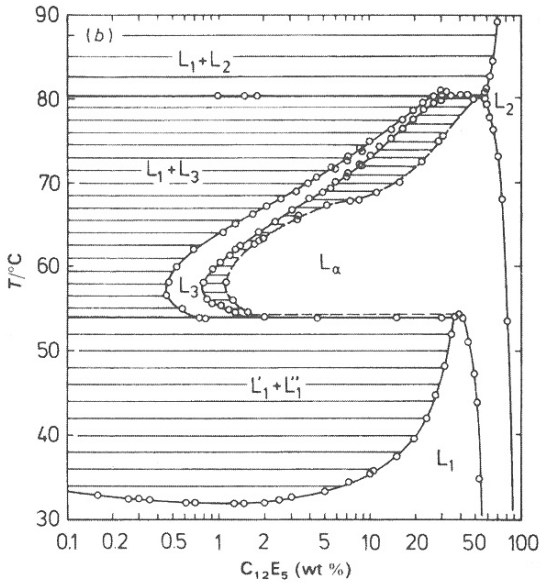

Figure 3.2: Phasediagram of $C_{12}E_5$.[47]

wavelength of visible light. Over a wide concentation range the linear swelling law is applicable, namely the lamellar spacing increases with δ/Φ_m.[48] Here, δ and Φ_m denote bilayer thickness and membrane volume fraction, respectively. At very high dilution corrections have to be made to account for a change of effective bilayer area owing to out of plane undualtions.[49,50]

3.1.4 L_α-Phase under shear

Exposed to an external field, such as a shear field, lamellar phases can undergo a variety of morphological transitions, which have been characterized in terms of an orientation diagram.[9] In the case of shear they can orient with their layer normal along the gradient (parallel orientation) or along the vorticity direction (perpendicular orientation). With increasing shear rate one commonly observes the sequence parallel-perpendicular.[9,51] In some cases the reorientation back to the parallel has been observed at very high shear rates.[25] For most lyotropic lamellar phases there exists a region in the orientation diagram, where multilamellar vesicles are the steady state structure. A typical orientation diagram is shown in figure 3.3, taken from ref.[9] Up to now steady state structures under shear are well studied for a variety of surfactant

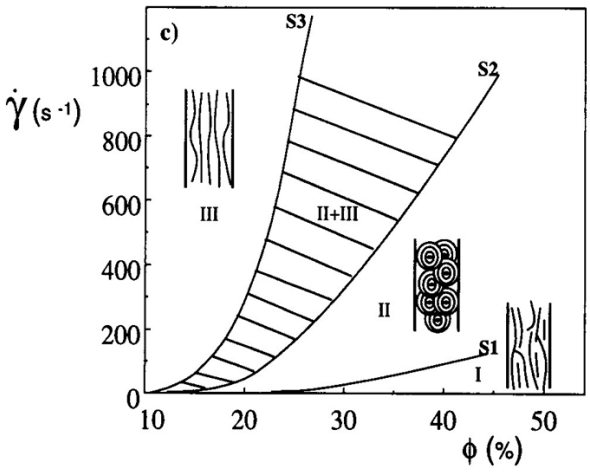

Figure 3.3: Orientation diagram for lyotropic lamellar phases taken from ref.[9]

systems.[2,8] Nevertheless, the transition between different steady state structures, and even from the equilibrium structure at rest, remain elusive. So far, no complete theoretical description exists, which captured all the details of the shear induced transition from planar lamellae to MLVs entirely.[40–42]

3.2 Techniques

3.2.1 Rheology

Rheology (from the Greek word $\rho\epsilon\tilde{\imath}\nu$ - to flow) is the science of the flow behavior of matter. Characteristic material quantities like viscosity (η), elastic (G') and loss moduli (G") can be determined by subjecting the material to different kinds of shear fields. In principle there are two categories of materials, either Newtonian fluids where the viscosity is independent of the applied shear rate ($\dot{\gamma}$) or non-Newtonian fluids where the viscosity is a function of shear rate. The latter can display either shear thinning or shear thickening, i.e., with shear rate decreasing or increasing viscosity and also be viscoelastic (Bingham solid).[52]

A schematic of a shear experiment is shown in figure 3.4, where the liquid is between two parallel plates. One plate is moved with a certain force $\vec{F}$ with respect to the other. The stress σ is defined as the force per area. According to Newtons law, a certain strain rate ($\dot{\gamma}$) results, with the proportionality between shear stress and strain (or shear) rate being the viscosity. Strain

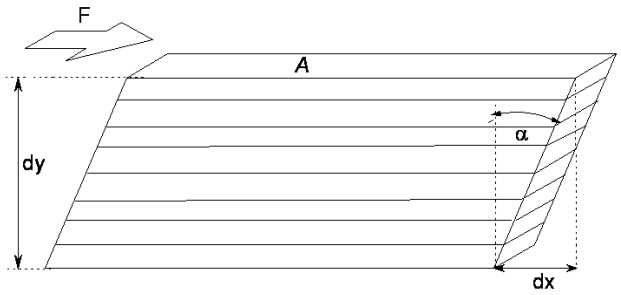

Figure 3.4: Schematic of a shear experiment between parallel plates with area A, applied force F, sample thickness dy, displacement dx and displacement angle α.

itself is the ratio of the displacement dx and the sample thickness dy.

3.2.2 Scattering Techniques

Scattering in general is a powerful non-invasive tool for the determination of particles size and shape in the range of 100nm to a few μm in the case of light scattering and 1 to about 1000nm in small-angle neutron (SANS) and X-ray scattering (SAXS). An important advantage is, that the measured quantities (dynamics, size, shape, molecular weight, specific volume or surface area etc.) are averaged over the whole sample. These quantities can be extracted from the scattering with almost no approximation or model.[53] The mathematical description is generally very similar for the different types of radiation, and therefore a few things can be introduced before talking about scattering with a specific radiation.

In order to compare results from experiments with different wavelength the scattering vector q is introduced. The scattering vector q describes the momentum transfer from the incident to the scattered radiation, i.e.

$$|\vec{q}| = \left|\vec{k}_s - \vec{k}_i\right| = \frac{4\pi n}{\lambda_0} \cdot sin\left(\frac{\theta}{2}\right) \tag{3.3}$$

where $\vec{k}_i$ and $\vec{k}_s$ are the wave vectors of the incident and the scattered beam, respectively, n the optical density (for scattering with light this is the refractive index) and λ_0 the vacuum wavelength of the incident radiation. For elastic scattering $\vec{k}_i = \vec{k}_s = 2\pi n/\lambda_0$. In the case of neutron and X-ray scattering n becomes unity. From equation 3.3 it is obvious, that q is an inverse length and thus the length scales that are studied in a scattering experiment are inversely

proportional to q.

The scattering from inhomogeneities which are much smaller than the wavelength of the incident radiation ($R<\lambda/20$) is angle independent. If the objects, however, are larger one has to assume more than one scattering center per particle and hence an angle dependence of the scattering intensity results. This can be described by a form factor. According to theory[54] the form factor is the Fourier transform of the spatial correlation function $\gamma(r)$ of scattering length density $\rho(r)$. Thus form factors for different particle shapes are available. The simplest case is the form factor of a homogeneous sphere, first derived by Lord Rayleigh,[55] given by:

$$P_s(q) = (F_s(q))^2 = \Delta\rho^2 V_p^2 \left(\frac{3j_1(qR)}{qR}\right)^2 \tag{3.4}$$

Here F_s is the form factor amplitude, $\Delta\rho$ the contrast in scattering length densities of the particle and its environment (solvent), V_p the volume of the particle and $j_1(x) = sin(x)/x^2 - cos(x)/x$ the first-order spherical Bessel function.

Another special case has to be considered here. The form factor of a platelet of thickness ϵ is required in order to model the scattering from clay (equation 3.5).[38,56]

$$P_p(q) = (F_p(q))^2 = \left(\frac{sin(q\epsilon cos\alpha)}{q\epsilon cos\alpha}\frac{2J_1(qRsin\alpha)}{qRsin\alpha}\right)^2 \tag{3.5}$$

The orientation angle α is the angle between q and the normal to the particles surface. J_1 is a first-order Bessel function.

An orientational average has to be performed, since the clay platelets are isotropically distributed:

$$P_p(q) = \int_0^{\pi/2} \left(\frac{sin(q\epsilon cos\alpha)}{q\epsilon cos\alpha}\frac{2J_1(qRsin\alpha)}{qRsin\alpha}\right)^2 sin\alpha d\alpha \tag{3.6}$$

By setting the limits of the integral to a smaller range, one achieves an incomplete orientational averaging and thus gets an idea, how the intensity distribution of partially oriented clay suspensions might look like. The more rigorous approach would be convoluting the form factor with an appropriate orientation distribution function.

In the absence of particle–particle interactions, i.e., at high dilution, the structure factor (containing interparticle correlations) is unity and the scattered intensity is merely the product of the form factor of the platelet and a contrast factor defined by $K = \Delta\rho^2\Phi_p V_p$. Φ_p is the volume fraction of the platelets and V_p the volume of a single particle.

4 Experimental

4.1 Samples

Three systems were used in the presented studies.

1. Two different nonionic surfactants of the C_nE_m-type, where indicies n and m stand for the number of carbons in the aliphatic chain and of ethylene oxide groups in the hydrophilic headgroup of the surfactant, respectively, were used in studies of the pathway of MLV-formation. Binary mixtures of $C_{10}E_3$ and $C_{12}E_4$ in D_2O with a concentration of 40wt% were used. The use of heavy water was necessary in order to obtain contrast for the small-angle neutron scattering experiments. For reasons of comparability D_2O was used in all studies, since changing the solvent from H_2O to D_2O affects the phase transition temperatures by a few degrees. The concentraitions of the two binary surfactant systems are listed in table 4.1 and the relevant physical properties in table 4.4.

2. $C_{12}E_4$ was used for studies of the effect of clay insertion on the properties of a lamellar phase under shear. For this purpose two different surfactant volume fractions, namely Φ_s=0.363 and 0.437 were prepared and Laponite RD, a synthetic hectorite of 1nm thickness and $\approx$ 15nm radius, was inserted into the lamellar phase by S/L=0.39% or 0.5%, respectively. Here S/L is the ratio of the mass of dried clay per mass of stock solution. Both samples were prepared in a H_2O/D_2O mixture of 0.327(w/w) in order to suppress the scattering contributions owing to the clay particles. Additionally, the samples of Φ_s=0.363 were prepared with H_2O/D_2O mixture of 0.9(w/w) to obtain laponite contrast. The respective concentraitions are summarized in table 4.2. The physical properties of the laponite can be found in table 4.4.

3. In order to investigate the influence of shear on a L_3-phase, $C_{12}E_5$ was used as a surfactant and n-decane as an oil. The samples were prepared by diluting a stock solution of $C_{12}E_5$

	Surfactant	Solvent	c / wt%	c / mol%	Φ_s
1.	$C_{10}E_3$	D_2O	40	4.39	0.440
2.	$C_{12}E_4$	D_2O	40	3.55	0.437

Table 4.1: Concentrations of lamellar phases consisting of the nonionic surfactant triethylenglycol mono decyl ether ($C_{10}E_3$) and tetraethyleneglycol mono dodecyl ether ($C_{12}E_4$), both in heavy water (D_2O).

	$C_{12}E_4$ (wt%)	Laponite (S/L in %)	H_2O/D_2O (w/w)	Φ_s
1.	33.00	0.39	0.327	0.363
2.	35.16	0.40	0.90	0.363
3.	40	0.5	0.327	0.437

Table 4.2: Concentrations of the lamellar phases containing laponite particles in water/heavy water mixtures to selectively match the scattering length density of either the surfactant ($C_{12}E_4$) or the laponite.

and n-decane (51.9:48.1 wt%) with water. This way a constant membrane composition was assured. The membrane volume fraction Φ_m was calculated according to $\Phi_m = 0.5 \cdot \Phi_s + \Phi_o$, where Φ_s and Φ_o are the surfactant and the oil volume fractions, respectively. The different membrane volume fractions are summarized in table 4.3. The physical properties of the components can be found in table 4.4.

4.2 Rheology

Flow curves of the respective samples were recorded with a stress controlled Bohlin CVO-120 HR or a Bohlin CVO-R using a cone–plate geometry with a radius of 20mm and opening angle of 1 or 3°, if rheo-small-angle light scattering was performed. For rheo-birefringence measurements a plate-plate geometry was chosen with a radius of 20mm and a sample thickness of 0.2mm. A Searle type shear cell was employed, when small-angle neutron scattering was performed under shear.

	mass H_2O /g	mass Stock solution /g	Φ_m
1.	2.850	0.1280	0.03875
2.	9.250	0.6398	0.05813
3.	2.700	0.2559	0.07750
4.	8.500	1.2795	0.01163
5.	2.400	0.5118	0.15500
6.	2.100	0.7677	0.23250
7.	1.800	1.0236	0.31000

Table 4.3: Composition of the L_3-phase consisting of pentaethyleneglycol monododecylether ($C_{12}E_5$), n-decane and water with the respective membrane volume fractions calculated from $\Phi_m = 0.5 \cdot \Phi_s + \Phi_o$.

Component	M_w g mol^{-1}	density at 20°C g/ml	scattering length density ρ cm^{-2}
H2O	18	1	$-5.7 \cdot 10^9$
D2O	20	1.107	$5.76 \cdot 10^{10}$
$C_{10}E_3$	290.45	0.94	$4.72 \cdot 10^8$
$C_{12}E_4$	362.55	0.95	$7.73 \cdot 10^8$
$C_{12}E_5$	406.55	0.967	$1.29 \cdot 10^9$
Laponite	-	2.65	$3.94 \cdot 10^{10}$
SDS	288.38	-	-

Table 4.4: Selected physical properties of the components of the different samples.

4.3 Rheo-birefringence

In order to record flow birefringence an optical analysis module (OAM) allowing birefringence, dichroism and transmission measurements, purchased from Rheometrics, was employed. A schematic of the optical components of the OAM is shown below (figure 4.1). It is mounted below the Rheometer such, that the laser passes the sample along the gradient direction, yielding information about anisotropies in the velocity-neutral plane.

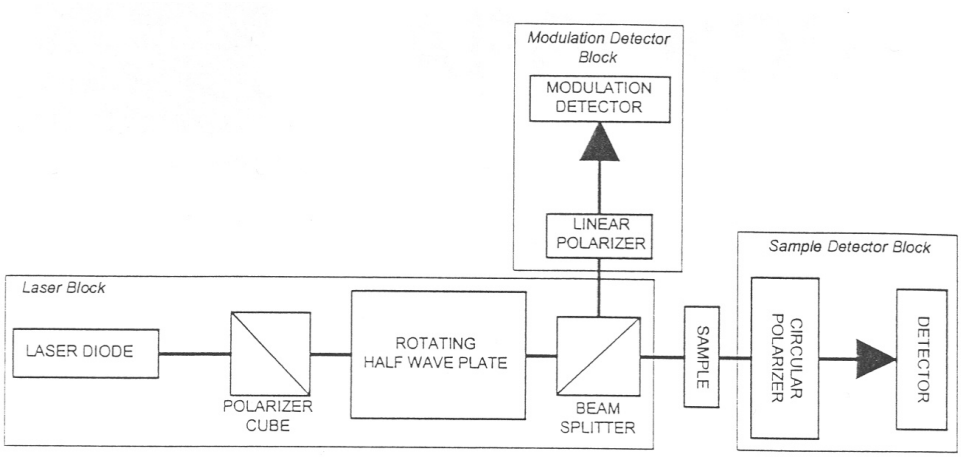

Figure 4.1: Scheme of the optical analysis module (OAM) used for flow birefringence experiments.

4.4 Construction of Searle-type Shear Cell for Rheo-birefringence

Rheo-birefringence measurements using the OAM as it is shown in figure 4.1 were so far only performed with plate-plate or cone-plate geometry. The information obtained from these experiments was thus limited to the flow-neutral plane. In order to detect anisotropies in the flow-velocity gradient direction, the construction of a Searle shear cell was necessary. This was achieved by directing the laser along the neutral direction through the gap of the shear cell.
The construction of this Searle shear cell was done together with C. B. Müller during his Physical Chemistry advanced lab course III. The dimensions of the shear cell were chosen to match those of the Searle-type shear cell, which is used at D11 at the ILL in Grenoble. The rotor (inner

cylinder) is a hollow aluminum cylinder as shown in figure 12.1, which was afterward eloxated to minimize reflection. The stator (outer cylinder, see figure 12.2) was also eloxated and as its bottom an optically improved suprasil glass allows optical experiments.
Birefringence experiments along the neutral direction of a Searle shear cell harbor problems with reflection and distortion of the laser at the meniscus of the fluid. Additionally, evaporation of the solvent has to be minimized. For this purpose a lid with a glass window at the position at which the laser passes was added to the design of the shear cell (see figure 12.3). Thus care has to be taken when filling the cell correctly. The lid has to be in contact with the fluid and it has to be assured that no air is entrapped between the rotor and the lid.
In order to provide good temperature control the cooling liquid (water) passes both, the jacked surrounding the outer cup (stator) of the shear cell (see figure 12.4) and the glass bottom of the cell. The temperature of the sample is measured by a PT-100, placed directly under the glass plate next to the position, where the laser enters the shear cell (see figure 12.5).

4.5 Rheo-Small-Angle Light Scattering (SALS)

Structures on a micrometer scale can be characterized by small-angle light scattering (SALS). The resulting scattering can be described by the formalisms presented in 3.2.2. Using polarized light offers the possibility to characterize anisotropic structures and the orientation with respect to the polarization plane of the incident beam. Two different configurations are possible:

1. The detection of polarized scattering by placing a polarizer, whose polarization plane is parallel to that of the incident beam, between sample and detector.

2. Complementary information can be obtained from depolarized scattering. Here the polarization plane of the polarizer is perpendicular to that of the incident light.

Without a polarizer unpolarized scattering is observed, a superposition of both polarized and depolarized scattering.
The description of scattering from polarized SALS is not straightforward, since it depends on the difference of the radial polarizability of the scatterer and the polarizability of its environment. The latter is in most cases difficult to determine and small changes have drastic consequences for the calculated scattering pattern.[57]
Depolarized small-angle light scattering is of particular use for the characterization of vesicular

structures and a characteristic four-lobe cloverleaf pattern can be observed. This characteristic scattering pattern arises from the difference of the radial and tangential polarizabilities of the MLVs (or spherulites). If the intensity distribution displays a maximum in the studied q-range, the size of the MLVs can be estimated by $R_{MLV} \approx 4.1/q_{max}$.[57,58]

If these multilamellar vesicles (MLVs) are sufficiently monodisperse they may arrange in a close packing and consequently a structure factor dominates the scattering. The size of the MLVs can very easily be extracted from the position of the first maximum of this structure factor by assuming that the MLV radius is half the center to center distance. According to Braggs law $R = \pi/q_{max}$.

Rheo-SALS was performed on the Bohlin CVO-R with an argon-ion laser, supplying a wavelength of 488nm. It was passed through the shear geometry along the gradient direction, thus yielding information in the flow-neutral-plane. An analyzer placed between the sample and the screen can be used to discriminate polarized from depolarized components of the scattered light by orienting it parallel or perpendicular to the polarization direction of the incident light. The setup is shown in figure 4.2.

4.5.1 Data Evaluation

The data were evaluated by sector averaging the scattering patterns to obtain either angular or radial intensity distributions. This is done by a software that was designed by F. Renth for that purpose. Centered SALS images can be averaged over the four quadrants if a four fold symmetry is present, which greatly facilitates the procedure and improves the data quality. From the radial intensity distributions, normally carried out with a 10°-sector oriented along the diagonal of the image ($\Delta\phi = 10°$, $\phi = 45°$), the position of maxima can be extracted by fitting cubic splines to the data. This allows the evaluation of an experimental sequence to yield time resolved information about MLV-size. The angular intensity distributions, evaluated at the position of the intensity maximum, provide information about the symmetry of the aggregates that lead to scattering. This information can be extracted from the angular intensity distributions in a similar fashion as the MLV-size. For this purpose a spline fitting routine was programmed by C. B. Müller.

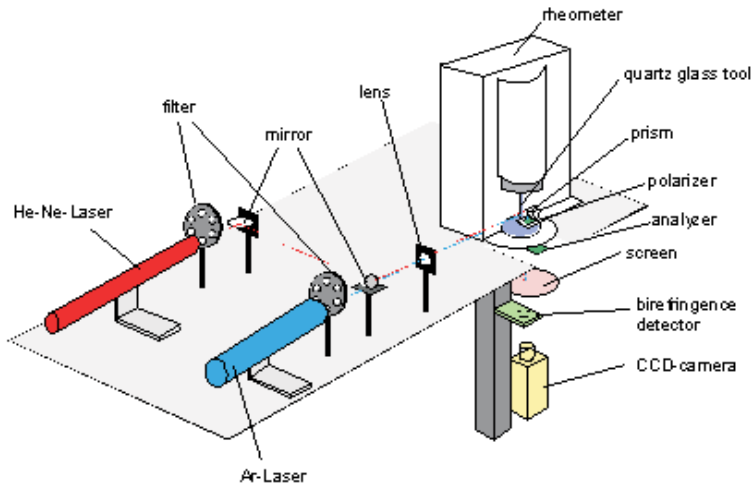

Figure 4.2: Rheo-optics setup as used for depolarized rheo-SALS.

4.6 Rheo-Small-Angle Neutron Scattering (SANS)

Small-angle neutron scattering experiments were performed at the diffractometers D11 and D22 at ILL in Grenoble. A schematic of such an instrument is shown in figure 4.3. Experiments under shear were performed either in a Searle-type shear cell mounted on a stress controlled Bohlin CVO 120 rheometer as in figure 4.4 or in a Couette shear cell figure 4.5(left)[59], where the shear rate can be controlled by a step motor. The two types of shear cells differ with respect to whether the inner (Searle) or the outer cylinder (Couette) rotates. Both types of shear cells consist of concentric cylinders, where the inner one has a radius of 23 and the outer one a radius of 24mm. For the Searle shear cell an inner cylinder with a radius of 23.5mm is also available. This enables experiments with different sample thicknesses and shear gradients.

A translation table allows experiments in the radial and the tangential beam. In the radial beam configuration the neutrons pass the center of the shear cell and thus record information in the

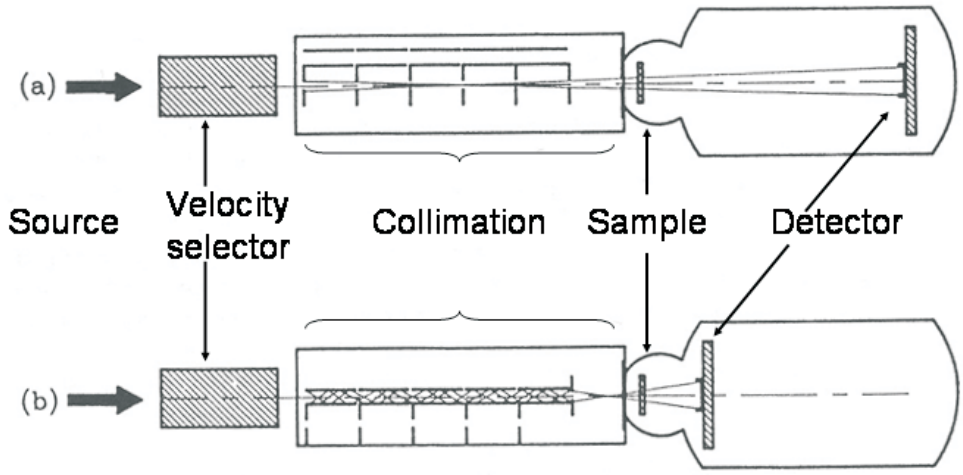

Figure 4.3: A schematic of a SANS instrument. Top: Short detector distance, short collimation. Bottom: Long detector distance, long collimation.

neutral-flow plane, whereas in the tangential configuration they pass the shear cell through the gap along the flow direction, recording information in the neutral-gradient plane (see also figure 4.5). The combination of both configurations is indispensable for an unambiguous characterization of all lamellar orientations with respect to the flow flied (see figure 4.5, right).

The tangential beam experiment is, however, associated with difficulties owing to the asymmetry of the scattering volume. This leads to a more or less pronounced asymmetry of the resulting 2-dimensional intensity distribution manifesting in the gradient direction. This problem is deferred to chapter 9, where it is discussed in detail.

Small-angle neutron scattering is a powerful tool to investigate structures in the range of 1-1000nm. Again the formalisms of scattering theories are applicable. There are, however, a few features specific to neutron scattering.

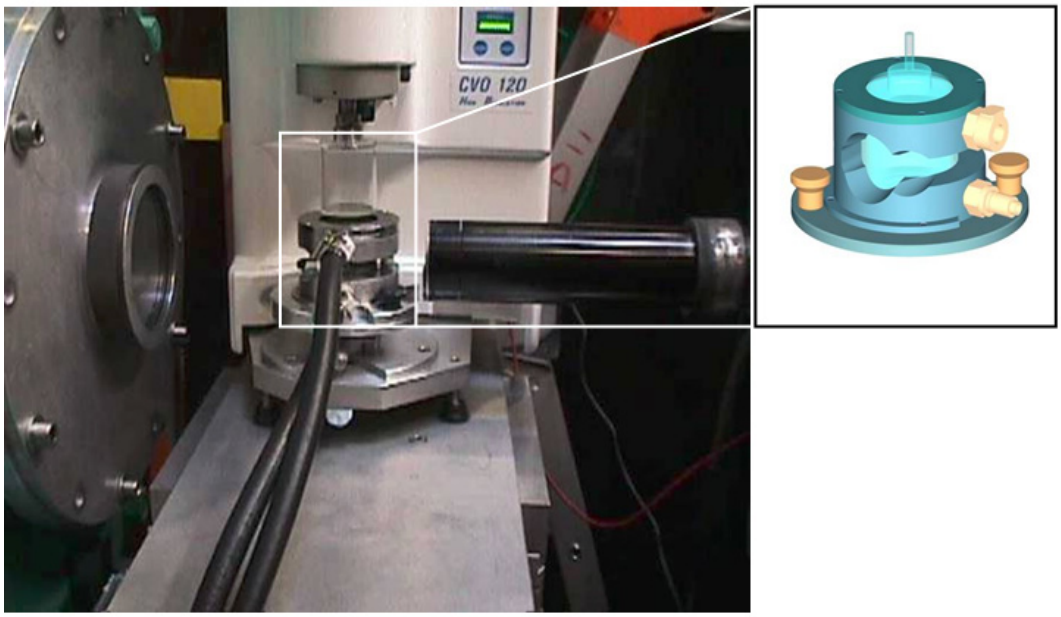

Figure 4.4: Bohlin CVO 120 with Searle type shear cell used for rheo-SANS.

The scattering lengths of the elements, unlike that in X-ray scattering, do not vary systematically with electron density, i.e., atomic number, but rather arbitrarily.[60] It can furthermore differ from one to the next isotope, as is the case for hydrogen and deuterium. This can be exploited to obtain scattering contrast or even vary the contrast between solute and solvent. By those means SANS provides a very elegant method to study the internal structure of particles (such as polymers, colloids, proteins, viruses etc.) in solution without qualitatively changing the chemical properties. Selectively matching the scattering length density of one component in a multi-component system allows studies of intra- and interparticle correlations of one particle kind separately from those of different particle kinds.[61,62]

Absolute calibration is inevitable in the procedure to obtain meaningful information from small-angle neutron scattering. It, among other things, provides an important consistency check and quantities like molecular weight, particle volume, specific surface area and radius of gyration

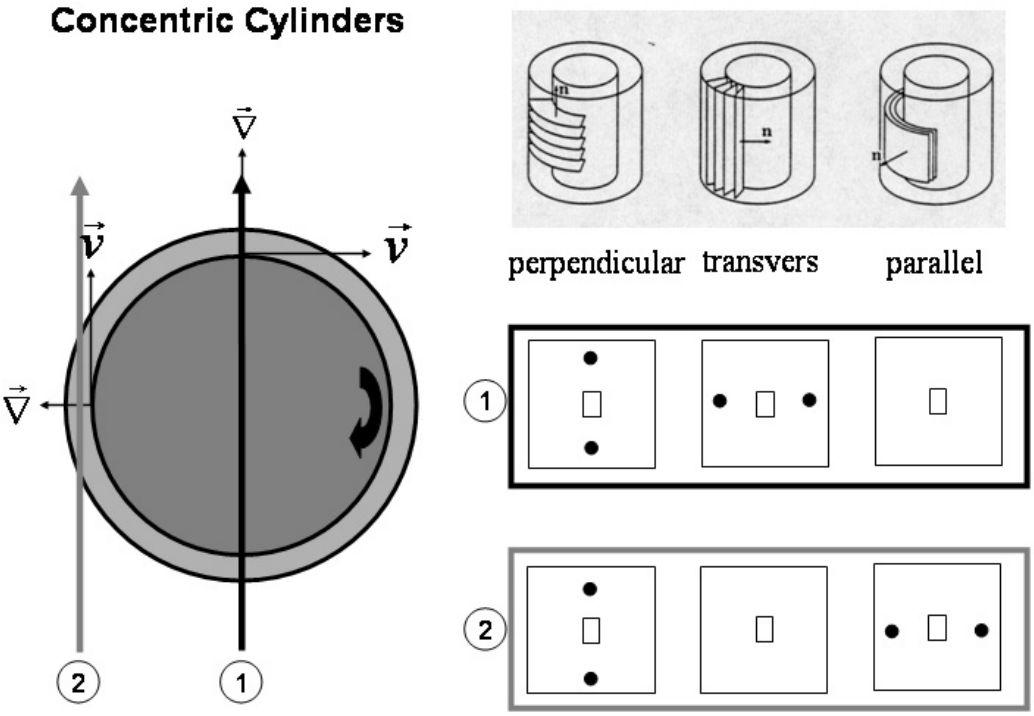

Figure 4.5: Sketch of a couette shear cell with the radial ① and the tangential beam configuration ② and the scattering patterns resulting from a lamellar phase in the parallel, transpose and perpendicular orientation, respectively, on a 2-dimensional detector.

can be calculated.[53,63]

It is thus necessary to measure background scattering originating form the sample holder, solvent and finally inherent background (incoherent scattering owing to the presence of hydrogen in the sample), which all have to be subtracted from the measured intensity distribution.

The instrumental scaling constant can be determined by measuring the scattering cross section of a secondary standard, whose absolute scattering cross section is precisely known. This can be done by recording the scattering of water. Since the scattering of water is dominated by the incoherent contribution of the hydrogens, it is independent of the angle and thus can be used at the same time to map the counting efficiency of every pixel of the position sensitive area detector.[63,64]

Inherent to all (real world) scattering experiments is the question of resolution. The finite resolution of a scattering instrument results from a combination of a finite wavelength distribution, aperture size, collimation of the beam and if necessary radial averaging of a pixelated detector. The finite resolution of the scattering instrument finally leads to a smearing of the ideal scattering cross sections. In the case of X-ray and light scattering these effects are rather small, since a well collimated beam of a monochromatic, coherent source of high intensity passes through an aperture system (smearing is minimal with a pinhole geometry).[65,66]

In neutron scattering, however, one compromises using a certain wavelength spread to yield a higher neutron flux. This leads to strong smearing of the observed scattering profiles. If model calculations of scattering functions are considered, these effects have to be taken into account by convoluting the ideal scattering cross section with an appropriate resolution function.[65,66]

In some cases it is not that important, as it is the case for the scattering of laponite particles. The characteristic features of the radial intensity distribution occur at lower q, where the uncertainty in q owing to the wavelength spread is not noticeable. Consequently the scattering of clay suspensions will be analyzed without taking finite instrumental resolution into account.

Considering the scattering of lamellar phases is rather complex, since the smectic order is perturbed by in plane density fluctuations (especially for nonionic surfactants) and out of plane bilayer undulations.[67] As a consequence the Bragg-peak is broadened and the low-q scattering is increased. The intensity in the vicinity of the Bragg-peak decays with

$$\langle S_{caillé} \rangle (q) \propto |q - q_0|^{-1+\eta_{caille}} \tag{4.1}$$

where $\langle\rangle$ denote an orientational average. Nallet et al. developed a model based on the Caillé-theory for the thermodynamic description of smectic A phases, which accounts for the out–of–plane undulations encountered in a lyotropic lamellar phase.[68,69]

The orientationally averaged scattering intensity can be decomposed in form and structure factor contributions (equation 4.2). While the form factor (equation 4.3) of a lamellae with a Gaussian scattering length density profile, to account for fluctuations in bilayer thickness, is considered for the contribution of a finite bilayer thickness δ to the scattering, the structure factor (equation 4.4) contains the correlation function of the smectic order (equation 4.5). The structure factor in turn contains information about the thermal undulations of the bilayers (equation 4.6). Instrumental resolution predominantly affects the structure factor. And finally

the q-dependence of the uncertainty in q has to be considered as well (equation 4.7).

$$I(q) = 2\pi \frac{V}{q^2 d} P(q) \tilde{S}(q) \tag{4.2}$$

$$P(q) = \frac{2\Delta\rho^2}{q^2} \left[1 - cos\,(q\delta)\, e^{-q^2\sigma^2/2}\right] \tag{4.3}$$

$$\begin{array}{l} \tilde{S}(q) = 1 + 2\sum_1^{N-1} \left(1 - \frac{n}{N}\right) \cos\left(\frac{q_z n d}{1+2\Delta q^2 d^2 \alpha(n)}\right) \\ \times \exp\left[-\frac{2q_z^2 d^2 \alpha(n) + \Delta q^2 d^2 n^2}{2(1+2\Delta q^2 d^2 \alpha(n))}\right] \sqrt{1 + 2\Delta q^2 d^2 \alpha(n)} \end{array} \tag{4.4}$$

with the smectic correlation function

$$\alpha = \frac{\eta_{caille}}{4\pi^2} \left[ln\,(n\pi) + \gamma\right] \tag{4.5}$$

where γ is the Euler's constant and η_{caille} the so-called Caillé-parameter

$$\eta_{caille} = \frac{q_0^2 k_B T}{8\pi\sqrt{K\bar{B}}} \tag{4.6}$$

and

$$\Delta q^2 = q^2 \left[\left(2\sqrt{2ln2}\right)^{-1} \frac{\Delta\lambda}{\lambda}\right] + \left[\left(\frac{4\pi}{\lambda}\right)^2 - q^2\right] \Delta\theta^2 \tag{4.7}$$

In equation 4.2 V is the scattering volume, d the lamellar separation. The Nallet-model describes the shape and width of the first and, if present, higher order Bragg-peaks and their height variation. This is displayed in figure 4.6, where the contribution of the finite bilayer thickness is displayed by a dashed, the structure factor by a dotted and the resulting intensity distribution by a solid line.

In practice, however, one has to be aware of the limitations of this model. It for instance fails to describe the intensity at low q ($q \ll q_0$). Furthermore, one has to be aware that the Caillé-theory uses a harmonic description of the fluctuation spectrum, which is only applicable for small undulation amplitudes. If the fluctuations of the bilayer density and out of plane undulations couple strongly, the simple separation of form and structure factor is not valid anymore. In principle more complex models can be chosen for the description of the form factor.[70]

4.6.1 Data Evaluation

The data obtained from SANS experiments were evaluated using Grasp, a software provided by the ILL, suited for treating anisotropic scattering data.[71] Isotropic data were radially averaged, corrected for background scattering and normalized to the incoherent scattering of water. If

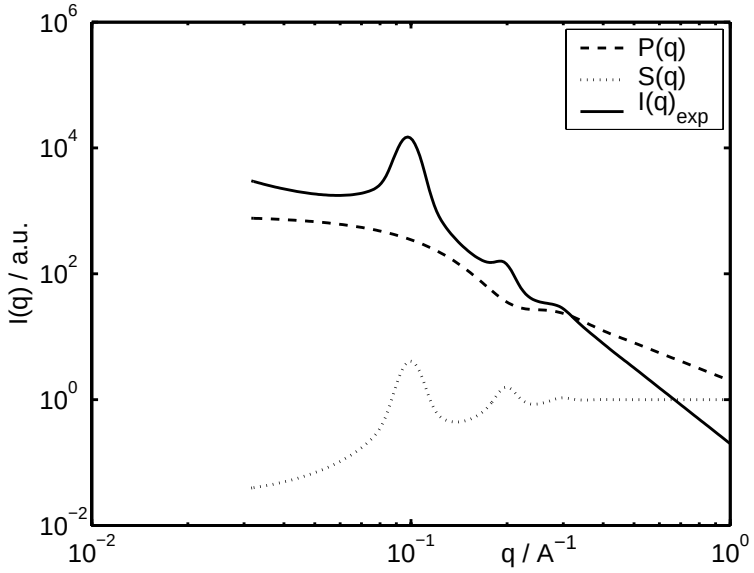

Figure 4.6: Intensity profile of a lamellar phase with a lamellar spacing 63Å and 28Å bilayer thickness. Caillé-parameter $\eta_{caille} = 0.2$, instrumental resolution $\Delta q = 0.006\text{Å}^{-1}$.

necessary the incoherent scattering of hydrogen in the samples was measured at high q and then subtracted from the sample scattering. Anisotropic data were sector averaged to obtain radial or azimuthal intensity distributions. Further evaluation of the data was performed by modeling the scattering of lamellae by the Nallet-model or the scattering of laponite by that of orientationally averaged platelets. Azimuthal intensity distributions obtained from tangential beam experiments can be evaluated in terms of an order parameter, which will be defined later (chapter 6).

4.7 Neutron-Spin-Echo (NSE)

Neutron-Spin-Echo (NSE) is an inelastic scattering technique, where the energy transfer ΔE during a scattering event can be directly measured and thus the dynamics of the system of interest are accessible. NSE makes direct use of the neutron spin and its magnetic moment. Polarized neutrons first pass a $\pi/2$-flipper and then enter a magnetic field where they start to rotate with their Lamor-frequency. This rotation serves as an internal clock.[72]

After exiting the first coil, they interact with the sample and according to the energy transfer their velocity is changed. They now have to pass a π-flipper, which inverts the direction of

rotation (inverting the time of the internal clock), another coil and a $\pi/2$-flipper, the analyzer, before they arrive at the detector. The setup is symmetric with respect to the π-flipper and if there is no sample, the spin-echo condition is fulfilled at the detector.

If a neutron experienced an energy change during a scattering process, the spin-echo condition will not be met. In order to produce an echo at the detector the magnetic field of the second coil can be changed appropriately and thus changing the Lamor-frequency of the neutrons (changing the speed of the internal clock). The resulting phase shift is called the Fourier-time, from which the energy transfer and the intermediate scattering function $S(q, \tau)$ can be calculated.[72]

In the case of lamellar phases NSE directly permits the measurement of the bilayer undulations. The procedure, however, requires a rather complicated theoretical framework.[73,74] The intermediate scattering function $S(q, \tau)$ can be evaluated using stretched exponentials to determine the relaxation rate of the fluctuations and the Zilman-model[73] allows an estimate of the bending elasticity of the bilayer κ_b in the limit of high q.

5 Pathway of the Shear-Induced Transition between Planar Lamellae and Multilamellar Vesicles as studied by Time-Resolved Scattering Techniques

5.1 Introduction

The influence of shear on the structure of complex fluids has attracted a lot of interest in the past for several reasons. Structural changes in complex fluids affect their flow properties and therefore imply consequences for various industrial applications. Closed bilayer structures are also important in biological processes. This results in a variety of pharmaceutical applications such as encapsulating drugs in liposomes made from natural lipid bilayers.

In particular, flow properties of lamellar phases have received a lot of attention.[2] The variety of different structures and structural transitions that can be found in lamellar phases under shear is rich.[75,76] The lamellae can align in the flow field with their layer normal along the velocity gradient or in the vorticity direction; the former is often referred to as the parallel and the latter is termed perpendicular orientation. Another morphology often found in lamellar phases exposed to shear is that of multilamellar vesicles (MLV), multi-layered closed bilayer structures, and a variety of different descriptive names like onions, liposomes, or spherulites can be found in the literature. These shear-induced structures in lamellar phases are often summarized in so-called orientation diagrams first introduced by Roux et al.[9,77–79] A MLV region flanked by regions of planar lamellae dominates these diagrams in many cases. At low shear rates ($\dot{\gamma}$) the parallel orientation is found and the perpendicular orientation often dominates at higher shear rates. In some cases the transition back to lamellae in the parallel orientation was observed at

very high shear rates.[80]

The formation of MLVs is accompanied by a shear thickening. By increasing the shear rate further, shear thinning is caused in the MLV region as the MLVs become smaller.[9,77,78] Shells being stripped off cause this effect.[81] Another reason for the size change can be the compression of the repeat distance of the MLVs shells, where the water, which is expelled from between the bilayers, goes to the interstitial spaces.[26,82]

The interest in MLVs has grown due to their prospective applications in pharmacology for encapsulation of drugs, as viscosity modifiers in pharmaceutical formulations and as micro-reactors.[7] The interest in MLVs has grown due to their prospective applications in pharmacology for encapsulating of drugs, as viscosity modifiers in pharmaceutical formulations, and as micro-reactors.[7] Despite of many studies on shear-induced MLV formation in several systems, including surfactant-[16] and copolymer-based systems,[19,83,84] there is yet no satisfying explanation of how and why MLVs form. These attempts included varying the elastic properties and interactions between the bilayers. On one hand, this can be done by charging the bilayers of a nonionic lamellar phase with ionic surfactant;[82,85,86] on the other hand polymers can be added[28,29,34,87,88] or to a certain degree particles can be incorporated into lamellar phases.[37] Many studies point out that texture defects in the lamellar phase cause instabilities in the flow field and therefore cause MLV-formation.[89] Leon et al.[13] studied the influence of the saddle-splay modulus on MLV formation in an ionic surfactant system and found that the time necessary for shear induced MLV formation increased with increasing salt concentration. By varying the salt concentration in a dilute lamellar phase of AOT, Leon et al. were able to show that the nucleation of MLVs is a random process. This study furthermore correlated the formation of MLVs to the defect density in the lamellar phase. In contrast, Courbin et al. describe a strain-controlled transition in an ionic surfactant system.[23,90] Furthermore, predictions by Zilman and Granek[40] regarding the dependence of the transition from planar lamellae to MLVs on lamellar spacing d and sample thickness D are confirmed in this work.

The formation of multilamellar vesicles from originally undisturbed polydomain lamellar phases was studied by Escalante et al.[91,92] Here the undisturbed polydomain of a L_α phase was produced by a hydrolysis reaction of diethyl oxalate which for its part protonates a C_{14}DMAO (tetradecyldimethylaminoxide). The virgin L_α phase was then subjected to shear. The results indicated that the transition from planar bilayers to MLVs shows a scaling with the strain ($\gamma = \dot{\gamma}t$). This

transition apparently involved a sequence of structural changes from polydomain to parallel to perpendicular to MLVs to small unilamellar vesicles (SUV). Bergenholtz et al.[10] also observed a scaling of the viscosity with strain for the onset of MLV formation in an AOT/brine system. In many cases the MLVs are found to pack densely, having a high volume fraction. This is possible if the MLVs are polydisperse or if they are deformed into polyhedra. As an extreme, they can be hexagonally packed into layers that slide relative to each other in shear flow. In these cases a scattering of hexagonal symmetry is found in small angle neutron scattering (SANS) at rest. An asymmetry in the scattering with respect to the neutral axes is observed if shear is applied to such a dense MLV phase.[93] This is explained by the deformation of the hexagonal packing and layer sliding. Scattering of hexagonal symmetry was also observed in unpolarized SALS.[10,12] Depolarized scattering reveals a typical four-lobe cloverleaf with a structure factor imprinted.[58]

In surfactant systems of wormlike micelles Pine et al. observed that shear induced structural changes start at the rotating wall of the shear cell and propagate through the gap.[94] A similar observation was made by Berghausen et al., who studied the transition from a parallel to the perpendicular orientation of lamellae at different shear rates and different positions in the gap in small angle X-ray scattering (SAXS) measurements. Here the perpendicular orientation occurred at the inner wall of the shear cell when intermediate shear rates were applied.[25]

In many non-ionic surfactant systems of the C_nE_m-type, a lamellar phase stretches over a wide temperature and concentration range, which on its part hosts a region where MLVs can be formed by shear, and another one close to the upper temperature boundary, neighbored by the L_3-phase, where shear causes a transition from MLVs to planar lamellae. This qualifies non-ionic surfactants as model systems, since a reproducible initial state with a defined orientation can be obtained by simply shearing the sample close to the upper temperature phase boundary of the L_α phase. The phase diagrams at rest of several non-ionic surfactants in water have been studied by Mitchell et al.[95] and Jonströmer and Strey.[36] Using binary lamellar phases of non-ionic surfactants of the C_nE_m-type has advantages, as compared to ternary mixtures. With surfactant / cosurfactant mixtures it is possible to achieve different preferred curvatures by a local segregation of surfactant and cosurfactant molecules.[96]

Figure 5.1 shows a phase scheme for $C_{10}E_3$ under shear.[97] A region of pure MLVs at room temperature, a coexistence region between MLV- and L_α-phase and finally the pure L_α-phase

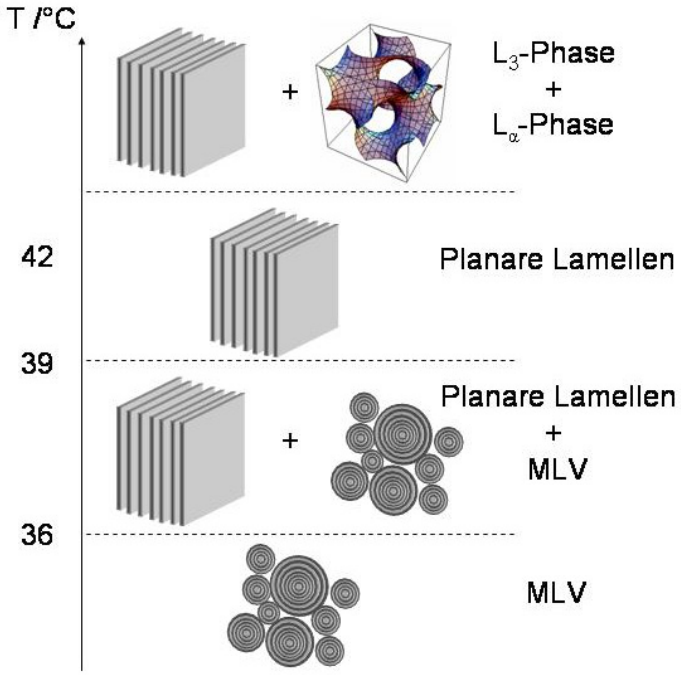

Figure 5.1: Phase scheme under shear, 40wt% $C_{10}E_3$ in D_2O at shear rate of $10s^{-1}$. According to reference[93].

close to the boundary to the L_3-phase are found. The phase diagram of $C_{12}E_4$, also used in this study, is very similar to the one of $C_{10}E_3$, except that the phase boundaries are shifted toward higher temperatures.[93]

In a preceding paper Zipfel et al.[24] described the transition from homogeneously aligned planar lamellae to MLVs by studying three different shear rates in time resolved SANS and SALS-experiments. A scaling of the transition with strain was observed. An intermediate structure with cylindrical scattering symmetry was found, which was interpreted as multilamellar cylinders (MLC). The formation of such multilamellar cylinders fits in the concept of membrane elasticity and curvature, since the curvature of cylinders lies in-between planar bilayers and MLVs.

Nevertheless, it has to be pointed out here that MLCs are not the only structure giving rise to a cylindrical scattering symmetry. The problem is that in a scattering experiment one cannot distinguish between a local, i.e. MLCs, and a global cylindrical symmetry, which can be realized by stripe buckling (figure 5.2). This was already proposed by Zilman and Granek[40] as

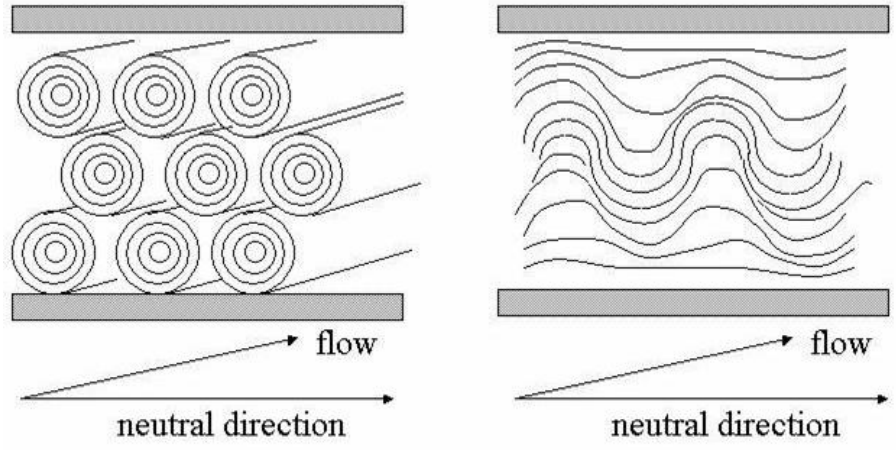

Figure 5.2: Sketch of possible structures leading to cylindrical scattering symmetry. Left: multilamellar cylinders (MLC). Right: coherent stripe buckling according to theory. Note that in order to completely fill space, planar lamellae have to be also present in the case of MLCs, especially in the vicinity of the walls of the shear cell. They were omitted in the sketch for reasons of clarity.

an intermediate state in the transition to MLVs, caused by the suppression of short wavelength thermal undulations. They argue that a buckling of the lamellae is the necessary consequence of a constant geometric projected area, i.e., a finite sample size. Although their model favors a two dimensional buckling over a stripe buckling with its wave-vector in the neutral direction, they conclude that the latter seems more plausible. Shear induced layer undulations were also observed in a theoretical model by Auernhammer et al.[42] using a hydrodynamic description of smectic liquid crystals. Assuming a coupling of the flow with the underlying nematic director of the smectic phase but not with the layer normal, they found undulation instabilities of the layers with their wave vector in the neutral direction. Furthermore, Courbin et al. interpreted a streak found in rheo-SALS at intermediate strain values by an initial stripe buckling.[23,90] Further calculations about the influence of shear on lamellar systems were performed by Marlow and Olmsted.[41] They calculated how a lamellar phase escapes the tension induced by the suppression of thermal undulations by a shear field predicting that impermeable bilayers have to buckle and eventually form closed bilayers (MLVs), whereas permeable lamellae have the possibility to reduce the lamellar spacing by creating new lamellae.

The study presented here aims to investigate the pathway of MLV formation in further detail. The intermediate with cylindrical symmetry found in the preceding study[24], will be examined closer with respect to its stability.

Moreover switching to a different non-ionic surfactant of the C_nE_m series makes it possible to change the membrane thickness and rigidity and thus enables us to study the influence of these parameters on the transition. Another parameter that influences the properties of the bilayers is temperature. A temperature increase results in a decrease in the spontaneous curvature of the surfactant monolayer, thereby increasing the saddle-splay modulus of the bilayer.[98] For this reason the transition was studied at different temperatures.

The techniques used to pursue this task are small angle neutron scattering (rheo-SANS) and small angle light scattering (rheo-SALS), both under shear.

5.2 Experimental Section

5.2.1 Materials

$C_{10}E_3$ (triethylene glycol monodecylether) and $C_{12}E_4$ (tetraethylene glycol monododecylether) were used as surfactants with a concentration of 40wt% in D_2O. Both were purchased from Nikko Chemicals Co., Ltd., and used without further purification. D_2O was purchased from Sigma-Aldrich Chemicals Co. Samples were prepared by simply mixing surfactant and D_2O by gentle shaking over night. Normally this was sufficient to yield a homogeneous lamellar phase. After loading the sample into the shear cell, reproducible starting conditions were obtained by shearing the samples just below the upper temperature boundary of the lamellar phase (42 and 63°C for $C_{10}E_3$ and $C_{12}E_4$, respectively) with a shear rate of $10s^{-1}$ until steady state was reached. At this temperature and shear rate the steady state structure corresponds to planar lamellae, oriented by the flow with their bilayer normal along the velocity gradient direction. This orientation is referred to as parallel orientation. Then shear was stopped and the sample cooled to 25°C, retaining the parallel orientation.

5.2.2 Small-Angle Neutron Scattering

SANS-experiments were performed at the D11 beam line at the Institut-Laue-Langevin in Grenoble, France. A thermostated Couette shear cell consisting of two concentric quartz cylinders with

a gap of 1mm was employed to study SANS under shear. Two scattering configurations were used: The so-called radial beam, where the neutrons pass through the center of the shear cell, i.e. passing the sample along the gradient direction and thus yielding information in the velocity-neutral plane; and the so-called tangential beam, where the neutrons pass through the gap of the shear cell, along the velocity direction and thereby obtaining information in the gradient-neutral plane.In principle two types of experiments were performed:

1. Time resolved neutron scattering experiments were carried out in a q-range of 0.02-0.15Å^{-1}, while the sample was subjected to shear. An aperture of 10mm radius and a slit of 0.3 by 10mm were used in the radial and the tangential beam, respectively.

2. SANS experiments on trapped intermediates at rest were performed in the tangential beam, scanning the gap of the couette shear cell. For this purpose a slit aperture of 0.12 by 12mm was used to produce a narrow beam. These data were scaled to the sample transmission at the given position within the gap.

The latter will be referred to as gap-scan experiments. Data obtained from radial beam experiments were corrected for empty cell scattering and put to absolute scale by calibration with incoherent water scattering. The normalization of tangential data is not straightforward, due to the asymmetric scattering geometry. Therefore most tangential beam data was not corrected in this fashion.

5.2.3 Small-Angle Light Scattering

Depolarized rheo-SALS experiments were performed using a Bohlin- CVO HR rheometer equipped with a quartz 3°-cone/plate shear geometry in the rate-controlled mode. The incident light ($\lambda = 488$nm) was linearly polarized parallel to the flow direction and passed the sample along the gradient direction. The analyzer was aligned perpendicular to the polarization of the incident light, i.e., perpendicular to the flow direction. The accessible **q**-range in SALS was ca. 0.5-3 μm^{-1}. For the evaluation of the scattering a program for radial and angular averaging of centered SALS-images allowing for a sector analysis suited for anisotropic data, was used.

5.3 Results and Discussion

The following section will be structured according to the different techniques used to elucidate the transition from planar lamellae to MLVs. First, this process will be discussed briefly as it was already described by Zipfel et al.[24] Details will be given concerning the pathway of this transition, the symmetry of the intermediates occurring and their stability. Temperature dependence will be addressed as well. Finally, the effect of increasing the bilayer thickness by changing to a higher analogue nonionic surfactant, $C_{12}E_4$, on the transition from planar lamellae to MLVs will be discussed.

5.3.1 Transition from Planar Lamellae to MLVs

The surfactant concentration was 40wt% $C_{10}E_3$ in D_2O. The sample was prepared following the procedure outlined above.

Subsequently, simultaneous rheological and time-resolved scattering experiments were performed. Figure 5.3a summarizes the transient viscosities during the transition from the planar lamellae to MLVs measured at five different shear rates in cone and plate geometry at 25°C. The viscosity of the L_α phase is below 1 Pa·s. Shear thickening is observed as shear is turned on, which is typical of shear induced MLV-formation.[9] Up to a strain of about 6000 the viscosity evolution of the shear rates 5 to 20s^{-1} is very similar. After approximately 6000 strain units, the increase in the viscosity slows down, a shoulder is observed for the shear rates 5 and 10s^{-1} and the viscosity finally approaches a steady state value at high deformations (above 2×10^4 strain units). The steady state viscosity depends on shear rate. The viscosity evolution of $\dot{\gamma} = 1s^{-1}$ deviates from the other shear rates over the whole strain range. Already at γ= 6000 a steady state is reached. The steady state viscosities are plotted vs. shear rate in figure 5.3b, where a weak shear thickening regime at low shear rates and a stronger shear thinning regime at higher shear rates can be distinguished. The maximum in the steady state viscosity is found around $\dot{\gamma} = 10s^{-1}$.

Depolarized small-angle light scattering was carried out simultaneously with the viscosity measurements. The scattering patterns are summarized in figure 5.4. The evolution of these series is very similar up to a strain of 3000. Prior to shear a diffuse small angle scattering is found, where a higher intensity is found in the former flow direction and characterizes a parallel orientation of lamellae with few texture defects. After 3000 strain units scattering intensity is mainly found in

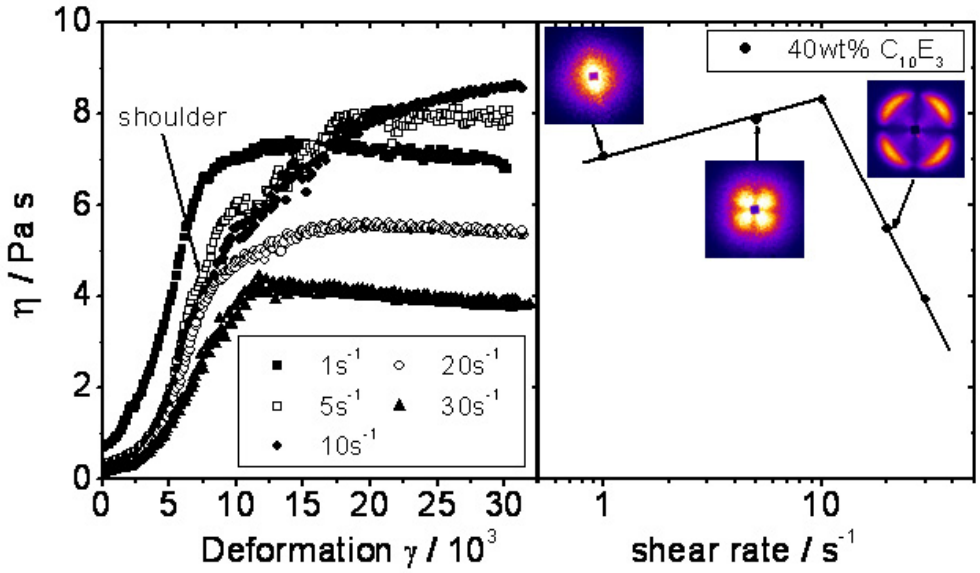

Figure 5.3: Left: Evolution of viscosity vs strain for shear rates 1, 5, 10, 20 and 30s^{-1} as measured in cone and plate geometry. Right: According steady-state viscosities and final SALS patterns plotted vs shear rate. the line is to guide the eye.

the neutral direction. This streak in depolarized rheo-SALS was already found in the previous study by Zipfel et al., who explained this scattering with multilamellar cylinders (MLC). Such a scattering was also observed by Courbin et al., who attributed this scattering pattern to an initial stripe buckling of the lamellae in neutral direction.[23,90] Basically both structures have the same spatial refractive index variation. A four-lobe pattern evolves at strain values of 6000. The only difference between the different shear rates, except 1s^{-1}, is the higher q-values at which the maximum of the four-lobe cloverleaf pattern is found for increasing shear rates. This pinpoints the shear rate dependence of the MLV size.[9]

Above $\gamma = 6000$, differences between the series become evident. The scattering patterns at $\dot{\gamma} \geq 10s^{-1}$ develop a structure factor peak at strain values of about 12000.[16] For the highest

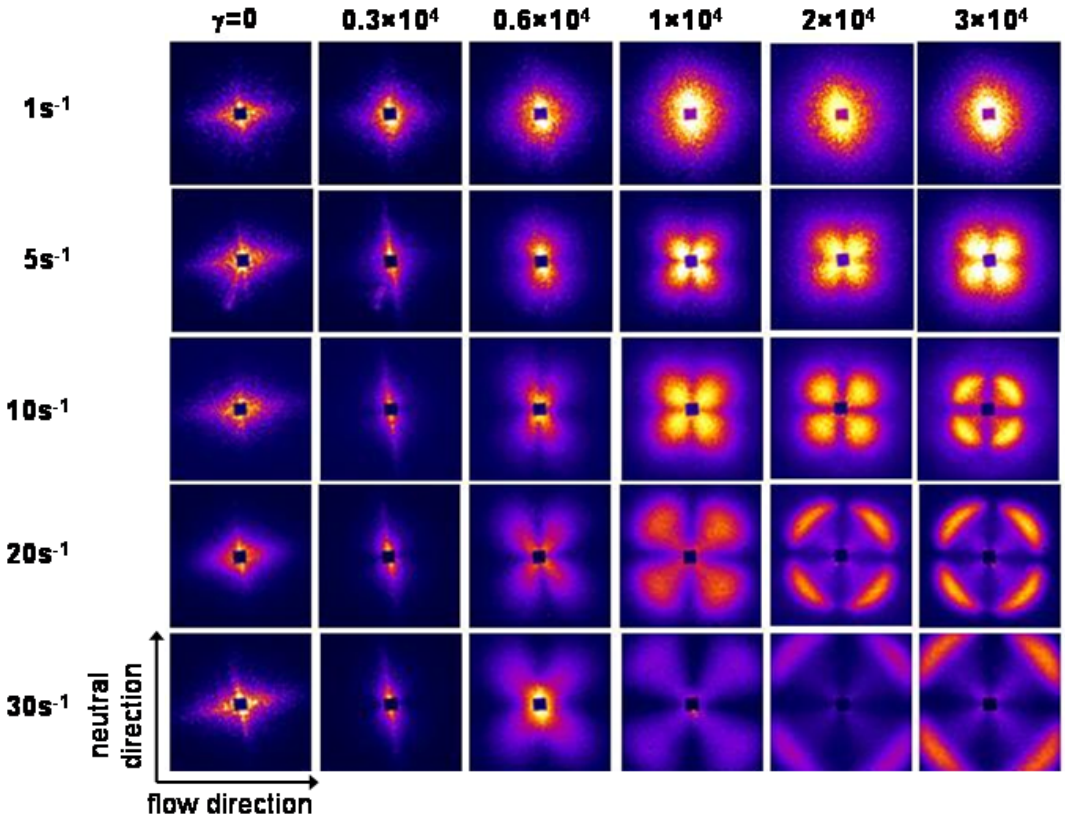

Figure 5.4: Comparison of the evolution of scattering patterns recorded in depolarized SALS for shear rates of 1, 5, 10, 20, and 30 s^{-1}.

shear rate ($30s^{-1}$) this structure factor is visible already at lower strain values (8000 strain units). A narrowing of the peak and a shift to higher **q**-values can be observed with increasing strain. It has to be noted here, that two types of four-lobe scattering patterns occur. On one hand, there is the pattern known as cloverleaf, corresponding to the form factor of MLVs (figure 5.4, $\dot{\gamma} = 10s^{-1}$ and $\gamma = 1 \times 10^4$). Here the size can be determined by the relationship $q_{max} \times R \approx 4.1$. This relationship has been used in the determination of spherulite sizes in films and semi-crystalline polymers.[58] On the other hand a structure factor evolves at higher deformation (figure 5.4, $\dot{\gamma} = 10s^{-1}$ and $\gamma = 3 \times 10^4$) and therefore the center-to-center distance $2R_{MLV}$ of the MLVs can be measured from the position of the intensity maximum using $R_{MLV} = \pi/q_{max}$. It should be pointed out that a ring at the same q-value is observed in unpolarized scattering.[12]

The evolution of the structure factor can be understood to arise from a decrease in polydisper-

sity resulting in an increased ordering of the packing of the MLVs. Figure 5.5 (left) shows the evolution of the peak during the transition at a shear rate of $10s^{-1}$. A narrowing of the peak

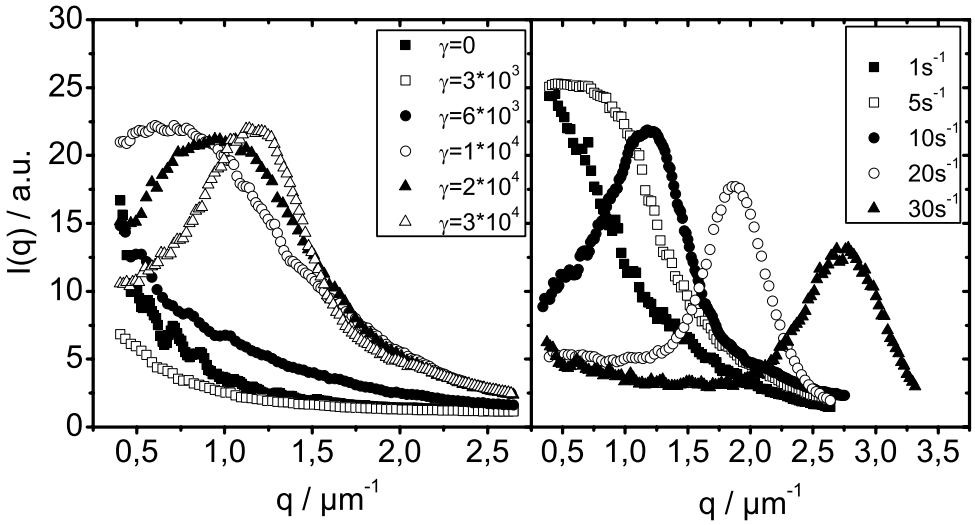

Figure 5.5: Left: Radial intensity distribution at shear rate 10 s^{-1} and different strain values. Right: Radial intensity distribution at shear rates 1-30 s^{-1} and a strain of 3×10^4.

and a shift to higher q-values can be observed. The MLV size decreases during the transition from $7\mu m$ to the final size of $2.6\mu m$, while the size distribution becomes narrower. Interestingly, such an evolution of the MLV size with increasing deformation was also observed by Courbin et al.[23,90] This can be expected since the initial size of the MLVs should be of the order of the wavelength of the stripe buckling, as pointed out by Zilman and Granek[40] and Auernhammer et al.,[42] yet the final MLV sizes are much smaller. Figure 5.5 (right) shows the scattering intensity obtained at large deformations ($\gamma = 3 \times 10^4$) for different shear rates. This corresponds to the last column in figure 5.4. The steady state size of the MLVs can be estimated to be 5.8, 2.6, 1.7 and $1.2\mu m$ for the respective shear rates between 5 and $30s^{-1}$.

The depolarized SALS reveals three distinct states characterized by three different SALS patterns: One is found at a shear rate of $1s^{-1}$, where the pattern is slightly elongated along the neutral direction. The second is found at $5s^{-1}$, where the steady state structure gives rise to a

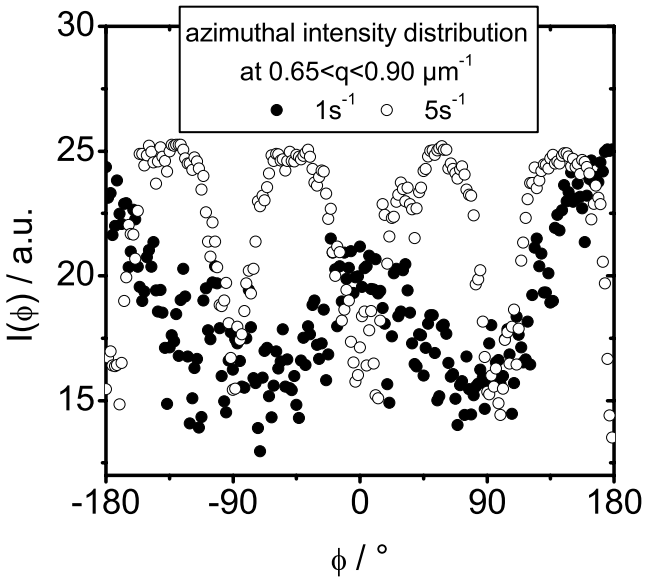

Figure 5.6: Comparison of the angular intensity distribution of the shear rates 1 and 5 s^{-1} at a strain of 3×10^4. Flow direction is at (90°, neutral at 0°. Radial averaging was performed in four 20° sectors along the diagonal axis of the picture. The azimuthal average was performed in a q-band at 0.65 <q <0.90 μm^{-1}.

diffuse cloverleaf pattern characteristic for MLVs with a rather broad size distribution. Third, a structure factor is observed at high shear rates (10 to 30s^{-1}). The first and second region correspond to the shear thickening regime in the steady state viscosities. The third region corresponds to the shear thinning region, where MLVs are already densely packed and their size decreases. Since the depolarized SALS reveals that the size of the MLVs decreases in the second as well as in the third region (see above), the shear thickening at low shear rates can only be explained by an increase in the MLV number density (or narrowing of the size distribution). Already at a strain of 3000 the difference between 1s^{-1} and the higher shear rates becomes evident. The scattering changes from a diffuse small-angle scattering to an almost isotropic scattering pattern. The intensity in the flow direction is slightly lower than in neutral direction, an indication for an increased defect density in neutral direction. Figure 5.6 shows the azimuthal intensity distribution, where 90° represent the flow direction, performed at $0.65\mu m^{-1} \leq q \leq 0.90\mu m^{-1}$

for $\gamma = 3 \times 10^4$ and $\dot{\gamma} = 1$ and $5s^{-1}$, respectively. The transition from a 2- to a 4-fold symmetry is observed, when increasing the shear rate from 1 to $5s^{-1}$.

Figure 5.7 gives an overview of the transition from planar lamellae to MLVs as obtained from rheo-SANS in the radial and the tangential configuration and rheo-SALS experiments carried out at 25°C and a shear rate of $10s^{-1}$. The scattering at the start of the experiment, obtained from SANS, clearly shows a pronounced Bragg peak in the gradient direction. Hence the parallel orientation dominates.

If shear is then applied, an increased intensity of the Bragg peak in the neutral direction of the radial beam is observed, which reaches a maximum after 300s. Here, essentially isotropic scattering is found in the tangential beam, and the rheo-SALS reveals enhanced scattering intensity in the neutral direction close to the beam stop. As already discussed previously these scattering patterns are of cylindrical symmetry.[24] In thermotropic liquid crystals Panizza et al. already described such scattering and interpreted this as multilamellar cylindrical structures. They found them as steady state structures forming as a function of shear rate.[99] As already pointed out, there is no possibility to distinguish between MLC (local cylindrical symmetry) and stripe buckling (global cylindrical symmetry) in a scattering experiment (figure 5.2). A stripe buckling (undulation) along the neutral direction was proposed by different theoretical models.[40,42] At 1000s, isotropic scattering in SANS and a diffuse four-lobe cloverleaf pattern in depolarized SALS is found, a typical signature of MLVs with a broad size distribution. Finally, when steady state is reached in the viscosity evolution, the four-lobe cloverleaf pattern developed a pronounced structure factor peak at ca. $1.2\mu m^{-1}$. These observations are consistent with the evolution of viscosity as observed in rheology.

To study the strain dependence of this process, further experiments applying several shear rates ranging from 1 to $100s^{-1}$ were carried out in the radial beam. The shear rate $10s^{-1}$ was also studied in the tangential beam. The intensity at the Bragg peak in the flow and neutral directions was followed during the shear experiment. Figure 5.8 displays the evolution of the Bragg peak intensity with the deformation of the sample for eight different shear rates. For all shear rates the intensity in the neutral direction reveals a maximum at about 3000 strain units. At $\gamma = 6000$ the intensity in the neutral direction reaches a steady value, and finally, at a strain of 10^4 the scattering is isotropic.

Now let us examine the details of this transition more closely. All shear rates above $3s^{-1}$ have

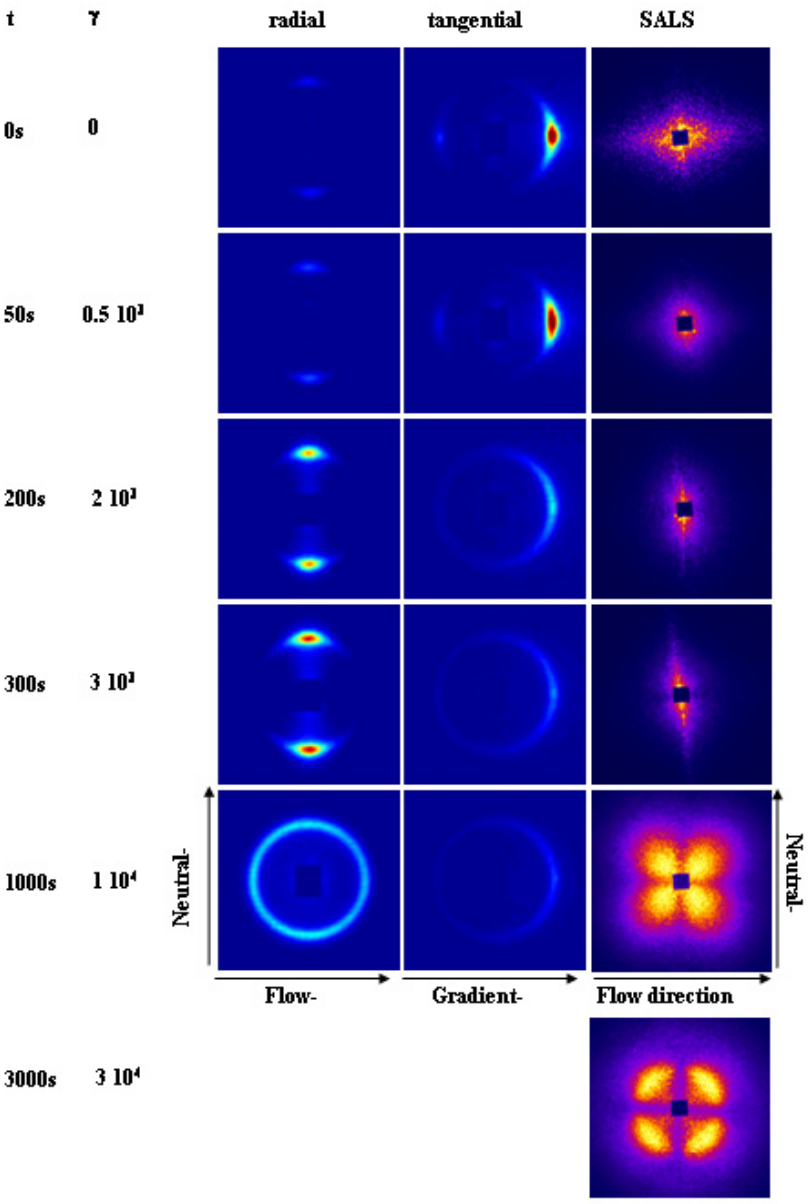

Figure 5.7: Evolution of SANS patterns during a startup experiment at $\dot{\gamma}$=10 s^{-1} and 25°C as recorded in the radial and the tangential beam in comparison with depolarized SALS.

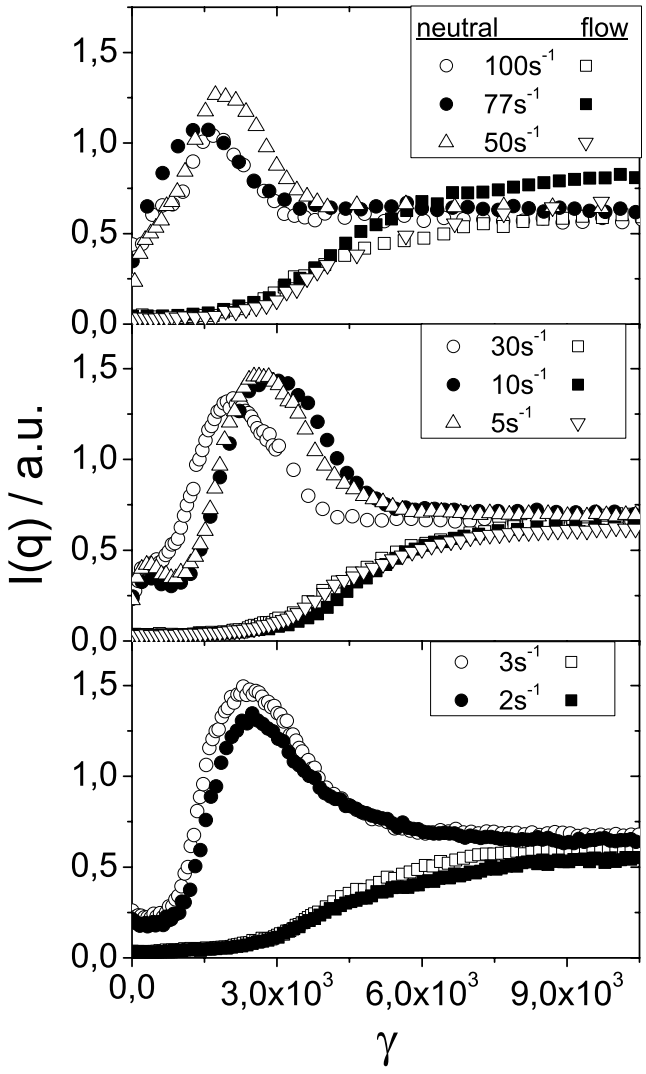

Figure 5.8: Evolution of SANS intensity at the lamellar Bragg-peak in neutral and flow direction recorded in the radial beam for eight different shear rates from 2 to 100 s^{-1}.

a more or less pronounced wiggle of the intensity in the neutral direction at strains below 300. Actually, this modulation of the intensity evolution is most pronounced for $5s^{-1}$ and least visible for the highest shear rates, probably due to the fact that the number of points recorded in this strain range decreases with increasing shear rate.

The major intensity maximum in the neutral direction is shifted toward slightly lower strain

values for $\dot{\gamma} \geq 30s^{-1}$. Even if one considers the increasing experimental difficulties of starting the shear experiment simultaneously to recording the scattering data and other instrumental imponderableness such as the acceleration of the rotor at the start of the rheological experiments, this shift to lower strain values is still significant. If the position of the intensity maximum in the neutral direction is plotted vs. the shear rate, one can distinguish between two regimes (figure 5.9). The first is found from 1 to $10s^{-1}$. Here the strain value, at which the intensity maximum

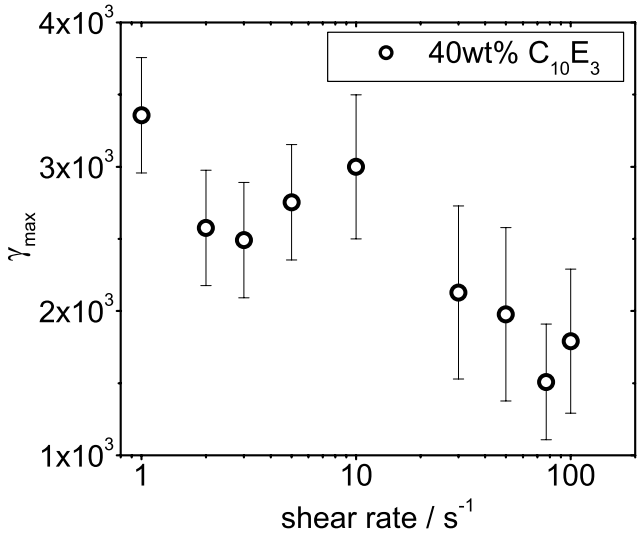

Figure 5.9: Strain at intensity maximum along neutral direction plotted vs shear rate.

in neutral direction occurs, is almost constant. The highest strain value for this intensity maximum is found at a shear rate of $10s^{-1}$. Above shear rates of $10s^{-1}$ this strain value decreases. These two regions correlate with the shear thickening and shear thinning regions found for the steady state viscosity. In other words we observe two regimes in the steady state viscosity (figure 5.3b) and in the transient behavior (figure 5.9). However, the latter correspond to a transient structure whereas the data in figure 5.3b correspond to steady state properties. This can be rationalized by the assumption, that the wavelength of the stripe buckling is of the same order as the initial size of the MLVs. Therefore there is a correlation between the transient and the steady state properties and hence they show similar behavior.

It remains to discuss the different intensity evolution for the shear rate of $1s^{-1}$ (Figure 5.10). The most striking difference is that, even at very high strain values, the scattering remains

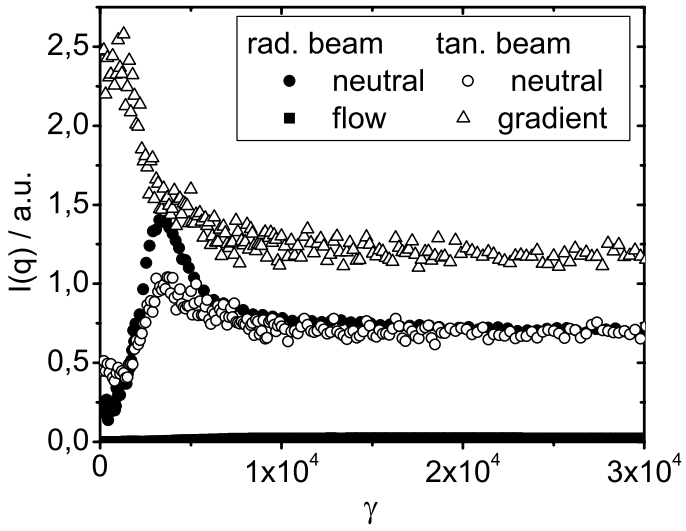

Figure 5.10: Evolution of SANS intensity at the lamellar Bragg peak in neutral, flow, and velocity gradient direction recorded in the radial and tangential beam at $\dot{\gamma} = 1s^{-1}$ and 25°C.

anisotropic. Thus we can exclude that a pure MLV state is reached at $\dot{\gamma} = 1s^{-1}$. The intensity along the flow direction levels off at $\gamma = 6000$ and is much lower as compared to the higher shear rates. Obviously, only few vesicles have been formed. In the tangential beam the intensity in gradient direction decays monotonically. At $\gamma = 3500$ the neutral direction of the tangential beam shows a maximum. Even at high strain values the scattering in the tangential beam stays anisotropic, although the anisotropy is less pronounced as in the radial beam. The remnant anisotropy in the tangential beam suggests the presence of lamellar fragments that are preferentially aligned in the parallel orientation. The anisotropy in the radial beam, which is more pronounced compared to the tangential beam, however, can be explained by stripe buckling (or MLCs). Hence, the steady-state structure at this shear rate probably consists of buckling lamellae (or MLC) and few MLVs. These few MLVs are not observed in depolarized rheo-SALS, since they can be expected to be very large and scatter to very low angles, which are not resolved with the setup used in this study. Hence the scattering is dominated by a structure with two-fold

scattering symmetry.

5.3.2 Trapping of Intermediates

To study the stability of these intermediates, discontinuous startup experiments were carried out, where shear was interrupted after a certain strain for half an hour. Figure 5.11 (top) shows a comparison of the viscosities of a continuous experiment with those of a discontinuous one. The discontinuous experiment consists of three parts with deformations of 3500. The same viscosity is found in both types of experiments. Simultaneously time resolved neutron scattering was recorded (figure 5.11 bottom).

No change in the intensity of the Bragg-peak was observed during the rest phases. Hence there is no difference in the evolution of intensities, either in the flow or in the neutral direction, between a discontinuous and a continuous startup experiment. This experiment was repeated with shorter deformation steps of 2000 strain units resulting in the same scattering intensity as well as viscosity evolution. This proves that the intermediate structures are stable, as long as they are not exposed to deformation. The fact that the intermediates are stable over long rest times makes it possible to conduct SANS-experiments on trapped intermediates, and gap-scan experiments were performed in order to investigate how the transition evolves over the gap of the shear cell.

5.3.3 Gap-Scan Experiments

For this purpose SANS measurements employing the tangential beam at different positions within the gap of the shear cell were conducted using a slit aperture of 10 by 0.12mm. The evolution of the Bragg peak intensity during a startup of $\dot{\gamma} = 10s^{-1}$ at three positions in the gap is shown in figure 5.12. The intensities are normalized to the transmission at the corresponding position, i.e., the intensities are scaled to the path length of the neutrons passing the sample. The path length decreases to the outside of the gap. The three data sets are very similar indicating that the structural transition is homogeneous throughout the gap.

A closer inspection of the SANS data reveals more details of the transition from planar bilayers to MLVs. As soon as the intensity along the neutral direction, as probed by the radial beam,

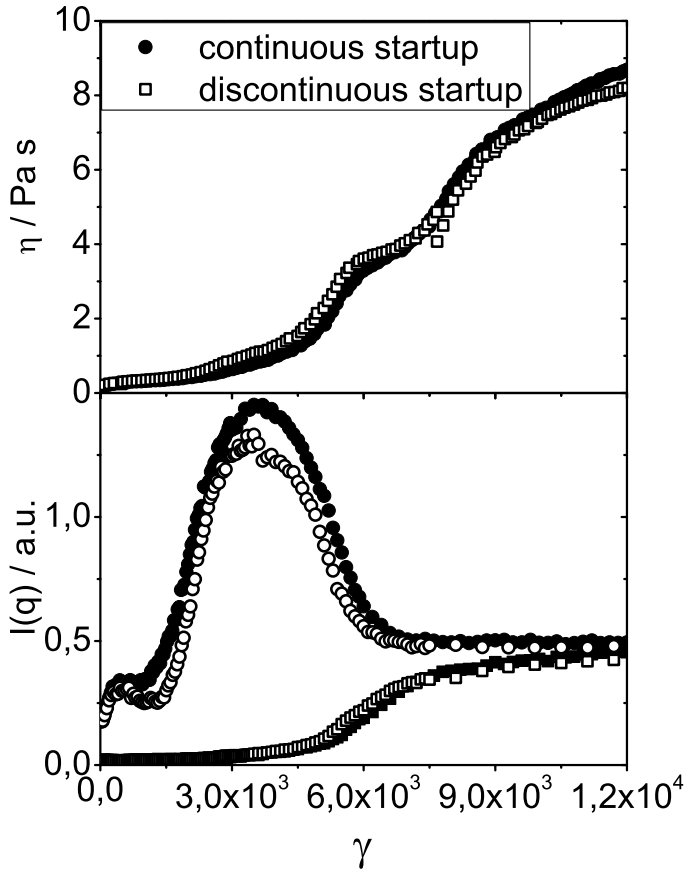

Figure 5.11: Top: Comparison of the evolution of the viscosities recorded during a discontinuous and a continuous startup experiment both carried out with a shear rate of 10 s^{-1} in a couette shear cell. Bottom: Comparison of the evolution of scattering intensity at the Bragg peak of a continuous and a discontinuous startup experiment at a shear rate of 10 s^{-1} and 25°C.

passes the maximum, the intensity along the flow direction starts to increase and simultaneously the viscosity rise becomes steeper. The intensity along the flow direction indicates the formation of closed bilayers. The tangential SANS pattern which was isotropic at 3000 strain units becomes anisotropic again. The intensity along the velocity gradient direction increases whereas that along the neutral direction decreases (figure 5.12 and 5.13). Thus the MLVs reside in a matrix of lamellae. As already mentioned above the isotropic tangential SANS pattern at 3000 strain units is compatible with either MLCs or buckling lamellae. The enhanced anisotropy

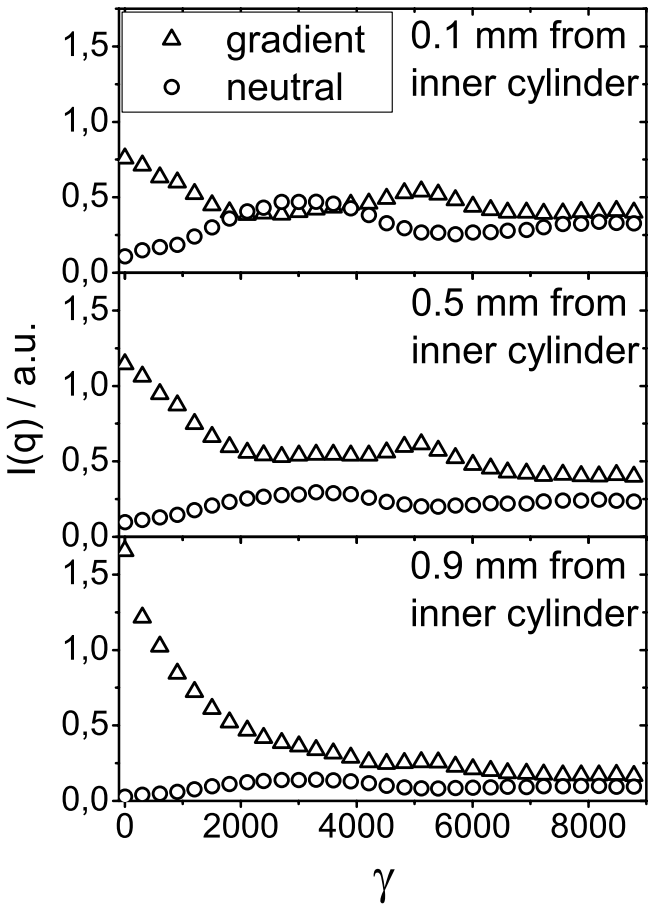

Figure 5.12: Evolution of the Bragg peak intensities during a startup experiment at shear rate 10 s^{-1} and 25°C recorded in the tangential beam at three different positions in the gap, i.e., 0.1, 0.5, and 0.9 mm from the inner cylinder of the couette shear cell. In the tangential beam a slit aperture of 0.12 mm width was used.

observed at larger strains indicates, that either MLCs transform into MLVs and planar lamellae or the buckling lamellae transform into MLVs and lamellae with less pronounced undulations. These lamellae, preferentially in parallel orientation, give rise to the increased anisotropy in the tangential beam.

Towards the end of the transition the tangential and also the radial SANS pattern becomes isotropic. Finally, all lamellae are transformed into closed bilayers. In SALS the four-lobe cloverleaf pattern is found and the shoulder is observed in the viscosity curve. Obviously, MLVs

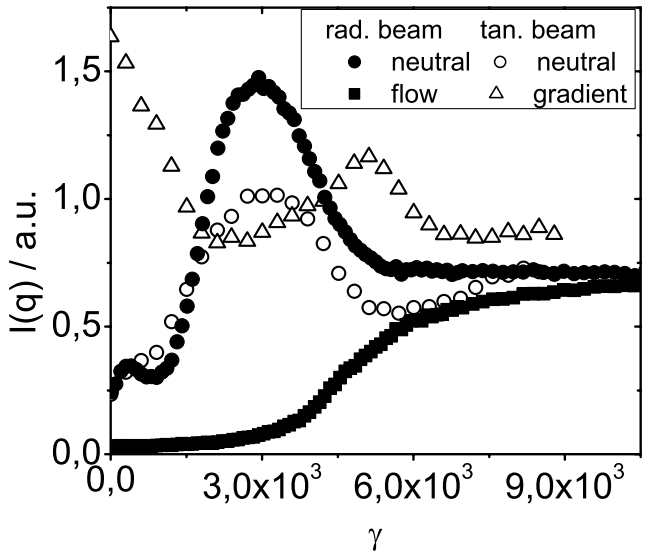

Figure 5.13: Evolution of scattering intensities at the lamellar Bragg peak recorded in the radial and the tangential beam (positioned at 0.1 mm from the inner cylinder of the shear cell) with a shear rate of 10 s^{-1}.

are now the dominating structure in the sample. Upon further shear flow the MLV size distribution becomes narrower and a closer packing is achieved, as evident from the SALS patterns.

5.3.4 Temperature Dependence

For non-ionic surfactants the monolayer spontaneous curvature changes strongly with temperature.[100] Therefore increasing the temperature should influence the transition from planar lamellae to MLVs and additional startup experiments at 32°C and 38°C have been carried out. At 32°C the transition at $10s^{-1}$ is very similar to what was found at 25°C. At 38°C, however, the rheo-SANS results were different.

Up to $\gamma = 2500$ - 3000 the evolution of viscosities at 38°C for $\dot{\gamma} = 6$ and $7s^{-1}$ (figure 5.14) are still very similar to the $10s^{-1}$ experiments at 25°C but a plateau is reached at 6000 strain units, its viscosities being 1.5 and 1Pa s for shear rate 6 and $7s^{-1}$, respectively. Superposed oscillations in the viscosity are observed.

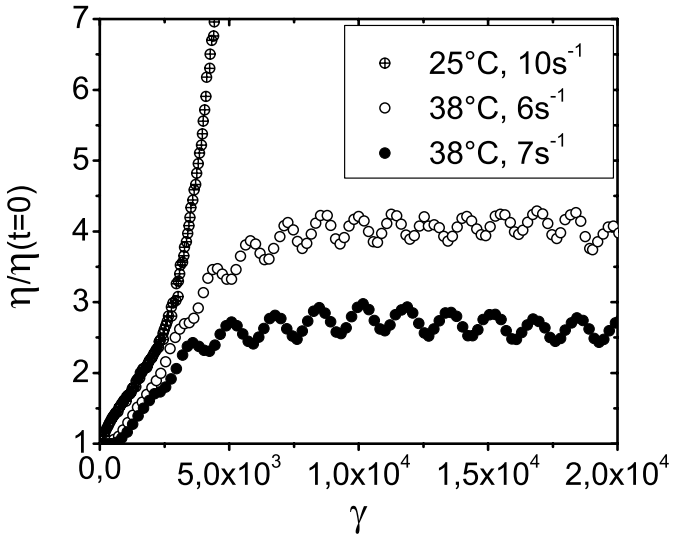

Figure 5.14: Evolution of viscosities for startups at 38°C at shear rates of 6 and 7 s^{-1} in comparison with the viscosities measured at 25°C and a shear rate of 10 s^{-1}. Note that the viscosities are scaled to η(t=0s) .

Viscosity oscillations have been observed already in wormlike micelle systems[101] and concentrated lamellar phases[102] under shear flow. Recently, Wunenburger et al.[103] reported of such viscosity oscillations for a MLV system. They associated this phenomenon with periodic structural changes between two states of comparable stabilities, namely, a disordered and an ordered state of MLVs. Wunenburger et al. excluded the possibility of an instrumental origin by studying different sample compositions at different temperatures. They also argued that the period of the oscillations found is too long to be due to instrumental influences.

In our case the period of the oscillations corresponds to about 10 rotations of the couette shear cell's rotor. The time associated is ca. 230s. This is sufficiently long for a stress-controlled rheometer to set a certain shear rate. The deviations in the shear rate stay below 0.5%. Thus it is the stress that builds up and at a certain point drops again, causing the viscosity to oscillate. Probably the viscosity oscillations are caused by structural oscillations between planar lamellae and buckled lamellae (or MLCs). Up to $\gamma = 2500$ the Bragg peak intensities in neutral and in flow directions, which were recorded simultaneously to the viscosities, are identical to what

was found at 25°C (figure 5.15 top). But the evolution differs above $\gamma = 2500$ and steady state

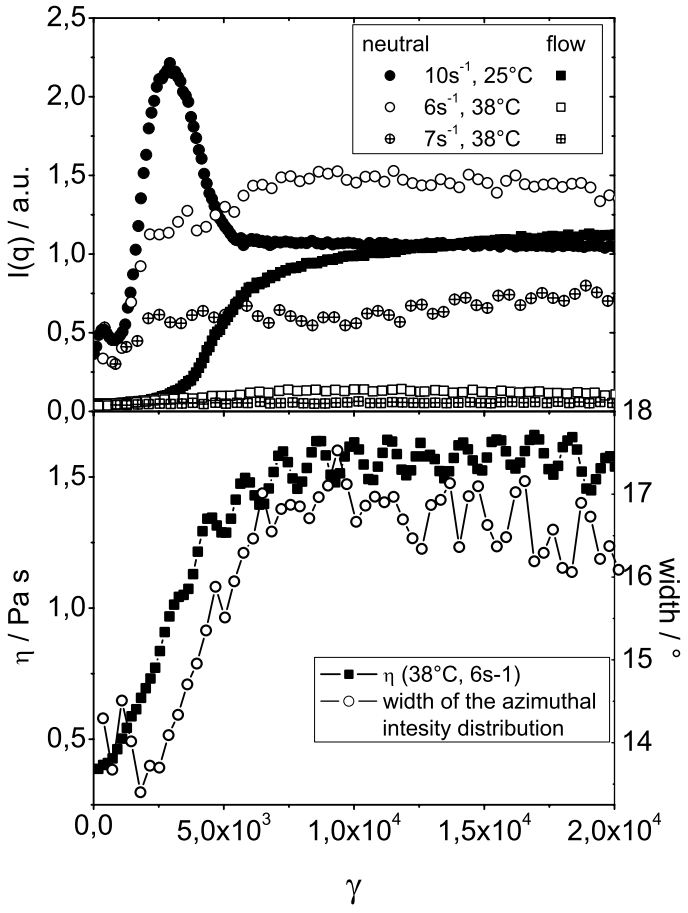

Figure 5.15: Top: Evolution of the respective intensities in neutral and flow direction in comparison with the intensities at 25°C. Bottom: Evolution of the width of the azimuthal intensity distribution is plotted vs strain. The widths were obtained from Gaussian fits to the azimuthal data in a sector from -45°$\leq \phi \leq$ +45°, where 0° represents the neutral direction.

reveals strong anisotropy in the scattering. The Bragg intensity along flow direction does not reveal any further increase, leading to the conclusion that only very few MLVs could have been formed.

Oscillations of the peak width, obtained from fitting a gaussian distribution to the data, with the

same period as the oscillations found in the viscosity were observed in the radial SANS pattern (figure 5.15 bottom). Hence the oscillations in the viscosity originate from oscillations of the width of the orientation distribution of the lamellae. The viscosity has a maximum shortly after the width of the orientation distribution. The increased disorder causes a higher viscosity and thus a higher stress is required to keep a constant shear rate. As a consequence a higher order is realized, which causes shear thinning. Again a lower stress is needed to guarantee the desired shear rate and the disorder increases again. A periodical change in the fraction of planar and curved lamellae is most likely responsible for this behavior. In addition to the oscillations in the width of the orientation distribution, the orientation of the lamellar director itself shows small oscillations of the same period with an amplitude of about $\pm 1°$ (not shown here).

The tangential beam data, recorded after the respective shear experiments, reveal further details. Figure 5.16 summarizes the data of the experiments using shear rates of 6 and $7s^{-1}$ at 38°C. The scattering pattern recorded at 25°C prior to shear, i.e. for a sample of planar lamellae with a parallel orientation, is also shown for comparison. The images are scaled to the same intensity.

In contrary to the SANS pattern recorded at 25°C (I), the patterns II and III reveal a Bragg-peak along the neutral direction, although it is small compared to that found along the gradient direction. The comparison of the tangential beam patterns obtained at 38°C after shear (II and III) with that of fully aligned lamellae (I) show that a fraction of layers were tilted out of the parallel orientation. In figure 5.16b the azimuthal intensity distributions of the respective experiments are shown. One can see that the full width at half height (fwhh) is broader at 38°C. Also the fwhh of the Bragg peaks found in the gradient direction are larger than that found for the parallel planar lamellae at 25°C. This indicates, that the lamellae become less ordered in respect to their orientation as well as their lamellar spacing. This could be due to the coexistence of curved and planar lamellae. Additionally a small difference in the Bragg peak position along gradient and neutral directions is seen at 38°C after shearing with $\gamma = 6s^{-1}$. After a shear rate of $7s^{-1}$ is applied, this difference becomes more pronounced (figure 5.16c). The position of the Bragg-peak along the velocity gradient is found at 0.114 $Å^{-1}$, whereas along the neutral direction it is at 0.105 $Å^{-1}$. This corresponds to a d-spacing of 55 and 60 Åalong the gradient and the neutral directions, respectively. These observations lead to the conclusion that the transition at 38°C leads to stripe undulations, which are more or less pronounced.

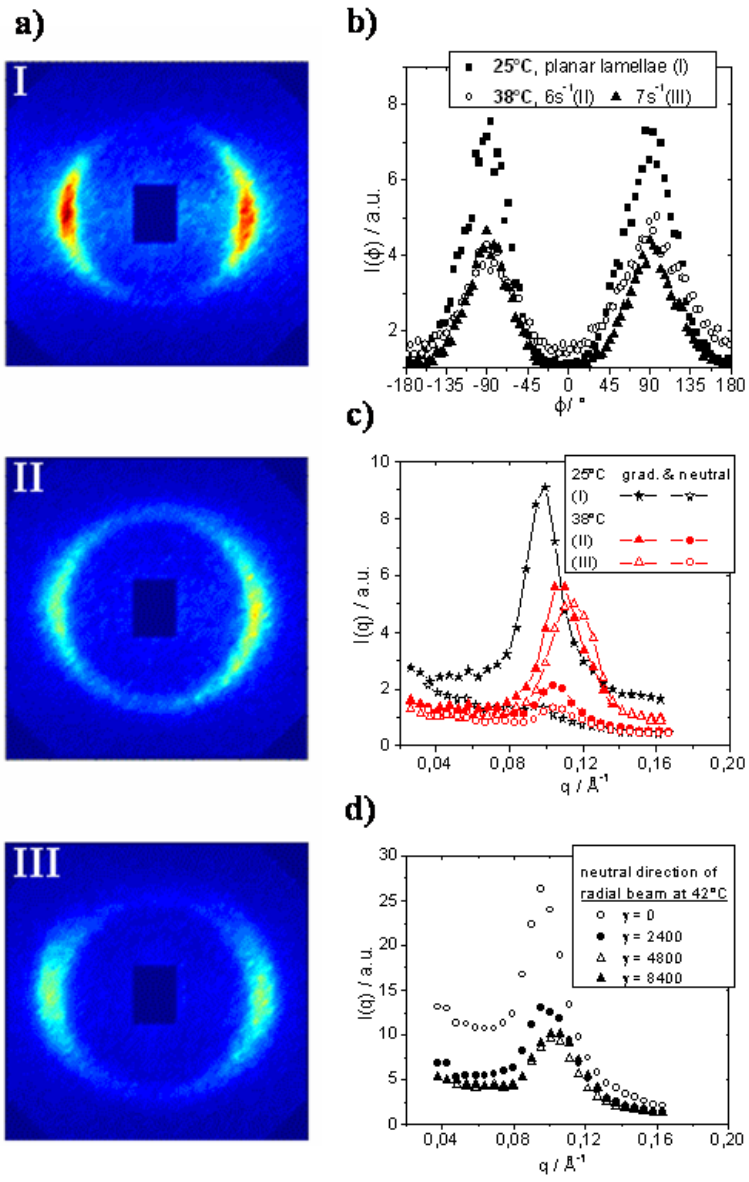

Figure 5.16: (a) Tangential SANS patterns taken at 25°C of planar lamellae with parallel orientation (I) and scattering patterns found after shearing at 38°C with $\dot{\gamma}$=6 (II) and 7 s^{-1} (III). (b) Azimuthal intensity distributions recorded at the Bragg peak position of the three respective experiments. (c) Corresponding intensities in neutral and gradient direction recorded at 25 and 38°C after shearing with $\dot{\gamma}$=6 and 7 s^{-1}, respectively. (d) Evolution of the scattering in the neutral direction of the radial beam at 42°C and a shear rate of 10 s^{-1}.

Furthermore, the average layer spacing is squeezed along the gradient direction most likely because of the coexistence of lamellae with different amplitudes of undulation. The squeezing of the layer spacing also explains the surprisingly low viscosity at 38°C and $7s^{-1}$ compared to that at $6s^{-1}$. The water squeezed out from between the bilayers serves as a lubricant, and this effect is hence more pronounced for the shear rate of $7s^{-1}$. The lower anisotropy found for $7s^{-1}$ in the radial beam is also a direct consequence of the lubrication. Accordingly, the stress is lower and the resulting undulation has a lower amplitude.
One can speculate that this is also the reason for the oscillations in the viscosity. As working hypothesis we suggest that two processes are possible:

1. The lamellae buckle (or build MLCs) and eventually MLVs are formed.

2. The lamellae can change their layer spacing and this way reduce the tension exerted on them.

The former and latter could correspond to the non-permeable and permeable case, respectively, in the model developed by Marlow and Olmsted.[41] They calculated how a shear field influences the orientation of lamellae. The non-permable case is what happens at 25°C, the permeable case can describe the mechanism for the opposite transition from MLVs to lamellae at 42°C. Here a shift of q_{max} in the neutral direction of the radial beam to higher values is observed (figure 5.16d). In the coexistence region the two paths seem to be degenerate and the moderate permeability of the lamellae allows both mechanisms for tension relaxation depending on the actual stress.
Additionally, gap-scan experiments were conducted for both experiments at 38°C after steady state was reached. These experiments revealed an increasing anisotropy towards the outer wall of the shear cell. After closer inspection of the azimuthal data, it seemed plausible to attribute this increase to a small fraction of parallel lamellae, which give rise to a very sharp peak on top of the broader scattering arising from curved lamellae. The contribution of the parallel lamellae to the scattering is dominant for the two outer positions in the gap, although their fraction is rather small. This arises from a very good alignment, probably due to wall effects. The underlying broad peak does not change intensity or width significantly, so that one can conclude that a homogeneous distribution of defects throughout the gap is found.
Additionally, the position of the Bragg peak shifts to slightly higher values within the first

0.5mm from the inner cylinder and is then constant. In this respect the situation differs from that found at 25°C and a shear rate of $10s^{-1}$, where there was no change in the peak position throughout the gap. It was argued earlier that a mixture of curved and planar lamellae leads to the rather broad Bragg peak. As one moves closer to the outer wall of the shear cell, the sharp peak characteristic of parallel lamellae increases in intensity at slightly higher q-values. Regardless, the shift of the peak position is only due to the increasing dominance of the parallel lamellae towards the outer wall of the shear cell. As mentioned above their fraction is low and therefore this observation is of minor importance.

5.3.5 Comparison with $C_{12}E_4$

To investigate how the surfactant chain length influences the transition between planar lamellae and MLVs, we have studied a sample containing 40wt% $C_{12}E_4$ in D_2O. At this concentration of $C_{12}E_4$ the Bragg peak is found at 0.093 A^{-1}, corresponding to a d-spacing of 68Å. The sample was prepared in a very similar fashion to the $C_{10}E_3$ sample, only a temperature of 63°C had to be chosen here in order to gain a parallel orientation of planar lamellae upon shearing with $10s^{-1}$.[93] The transition from planar lamellae to MLVs was studied at 25°C for shear rates of 5 and $10s^{-1}$. The rheological experiments show a similar evolution of viscosities as compared to the $C_{10}E_3$ sample. The data of experiments at 5 and $10s^{-1}$ are compared in figure 5.17. The steady state viscosity at a shear rate of $10s^{-1}$ is 5 Pa·s higher than the one of the $C_{10}E_3$ sample. Also the initial incline of the viscosities is much steeper in the startup experiment with $C_{12}E_4$. The viscosity evolution at a shear rate of 5 shows a shoulder at about 2500 strain units. It is more difficult to unambiguously identify this shoulder in the viscosity at $10s^{-1}$. The difference is the much steeper incline at the beginning resulting in fewer data points. This incline levels off at a strain value of about 6000 and steady state is reached after about 10 000 strain units. The shoulder in the viscosity evolution was also observed for the $C_{10}E_3$ system at shear rates lower than $10s^{-1}$, there at a strain value of about 6000. The overlap of the viscosity evolution with strain indicates strain dependence for this transition, as was the case for $C_{10}E_3$.
Neutron scattering data recorded in the radial (figure 5.18 top) and the tangential beam (figure 5.18 bottom) support the observations made in the rheological experiment. In the case of $C_{12}E_4$, the intensity maximum in the neutral direction is found at $\gamma \approx 700$ or 900 for shear

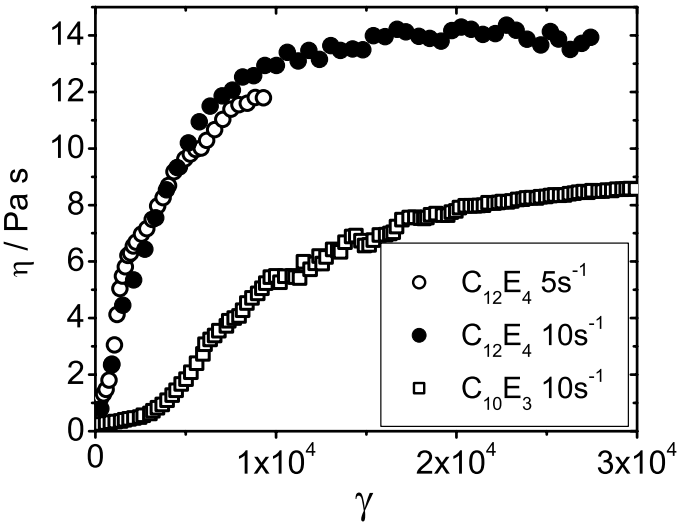

Figure 5.17: Evolution of viscosities during the transition from planar lamellae to MLVs at 25°and shear rates of 5 and 10 s^{-1} for a 40wt% C12E4 sample in comparison with the evolution of viscosities of the $C_{10}E_3$ system at a shear rate of 10 s^{-1}.

rates of 10 and 5s^{-1}, respectively. A shift of this maximum towards smaller strain values is observed already at these comparatively low shear rates. A similar observation has been made for the $C_{10}E_3$ sample, but only at shear rates above 30s^{-1}. The evolution of intensities in the flow direction also closely resembles that found for $C_{10}E_3$, except that the increase takes place earlier. The scattering is almost isotropic after about 6000 strain units. From the comparison of the viscosity and the intensity evolution one can conclude, that for $C_{12}E_4$ the transition from planar lamellae to MLVs follows a similar path but requires less strain compared to $C_{10}E_3$.

The tangential beam experiment reveals some residual anisotropy in the steady state, but nevertheless it very much resembles the evolution of intensities found for the $C_{10}E_3$ sample in the tangential beam. For this surfactant a fraction of lamellae close to the outer, not rotating cup, seems to remain in the parallel orientation, while the rest of the sample undergoes the transition to MLVs.

The deformation, where the scattering in the radial beam becomes isotropic, coincides with the point in the viscosity evolution where the incline becomes less steep. In the case of $C_{10}E_3$ this

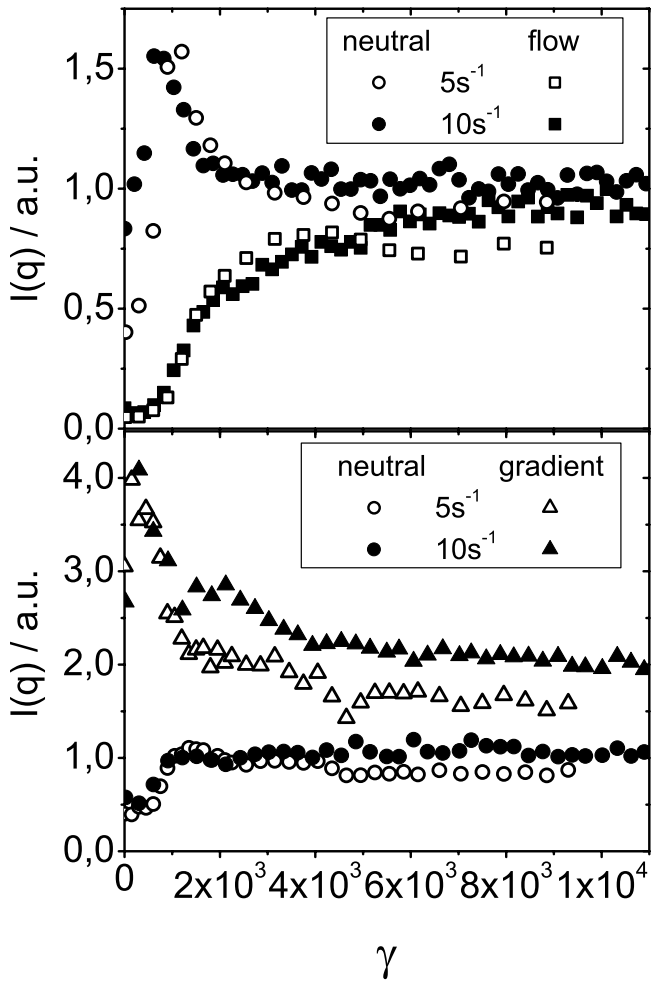

Figure 5.18: Top: Evolution of intensities in neutral and flow direction of the radial beam, recorded at the Bragg peak during a startup at 25°C and shear rates of 5 and 10 s^{-1} for a 40 wt% $C_{12}E_4$ sample. Bottom: Intensities in neutral and gradient direction recorded in the tangential beam.

point was identified with the last step of the transition, i.e. the formation of a pure MLV phase. This interpretation seems also plausible here.

In comparison with the $C_{10}E_3$ sample the transition from planar lamellae to MLVs only about half the strain is needed and the range where the cylindrical intermediate is observed is much narrower. The intensity maximum along the neutral direction is observed at about a third of the deformation.

Recently, Müller et al. studied the steady-state properties of the 40wt% $C_{12}E_4$ system in detail[16] and observed a shear-thickening and a shear-thinning regime as a function of shear rate as we find it for $C_{10}E_3$. A comparison of the findings presented here with the study of Müller et al. is very useful. In the case of the $C_{12}E_4$ system first a shear thinning region is found at shear rates below $0.3s^{-1}$, which is probably correlated with the polydomain to monodomain transition. The shear thickening region stretches from 0.3 to ca. $3s^{-1}$, where a maximum in the steady state viscosity was found. Above $3s^{-1}$ a second shear thinning regime is entered and scattering in depolarized SALS shows a structure factor, as was the case in our study of the $C_{10}E_3$ system. Obviously the shear-thickening and the second shear-thinning regime occur at shear rates about 3 times smaller as in the case of the $C_{10}E_3$ system.

The characteristics of the transition in the case of the $C_{12}E_4$ system at a shear rate of $10s^{-1}$ occur at deformations three times lower than in the case of $C_{10}E_3$, whereas the steady state viscosity of the $C_{12}E_4$ sample is by a factor of 1.7 higher than that of $C_{10}E_3$. Most striking is that the radius of the MLVs taken from the position of the intensity maximum (q_{max}) found in depolarized SALS shows a linear dependence upon the square root of the shear rate for both systems, however, for the $C_{10}E_3$ the values are ca. 1.7 times higher compared to $C_{12}E_4$ (figure 5.19 left). The MLV size at the maximum in viscosity is identical for both systems. Since the same shear thinning law applies to both systems, the sizes of the MLVs in the second shear thinning region can be expected to be very similar for the two systems.

A nice agreement between the two data sets is found, if R_{mlv} for the two systems is plotted vs. shear stress. This comparison is shown in figure 5.19 (right). The values for $C_{12}E_4$ are taken from reference 11. The MLV sizes are very similar and show the same stress dependence. Deviations from a power law behavior are found at stresses above 100 Pa for both systems. In the case of $C_{10}E_3$ this is the region, where the MLVs form a dense packing. This deviation from the power law behavior can probably be attributed to an increasing influence of layer sliding,

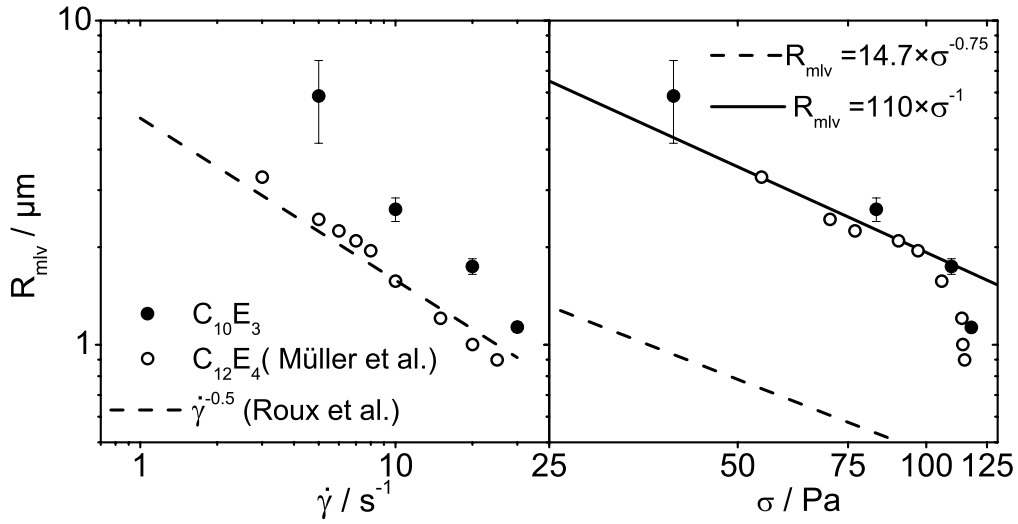

Figure 5.19: Left: R_{mlv} obtained from the position of the intensity maximum in sector averaged depolarized SALS pictures is plotted vs shear rate for $C_{12}E_4$ (∘) and $C_{10}E_3$ (•). Here the dashed line represent the relation given by Roux et al. ($R_{mlv} \propto \dot{\gamma}^{-0.5}$). The data for $C_{12}E_4$ are taken from ref 11. Right: R_{mlv} is plotted vs shear stress. The straight line represents a fit to the $C_{12}E_4$ data. The dashed line is an extrapolation of the shear thinning behavior found by Bergenholtz and Wagner for the ionic surfactant system AOT/brine to higher stresses.

as it is observed in hexagonally packed MLV systems. As a comparison an extrapolation of the shear thinning behavior found by Bergenholtz and Wagner to higher shear stress is also plotted in figure 5.19 (right). They studied MLV formation in the AOT / brine system at much lower stress (1^{-1}5Pa) and found comparable MLV sizes. Hence, the critical stress for MLV formation in this system is much lower compared to nonionic surfactants. We interpret this as a strong indication, that the MLV size is controlled by the stress, as it was found by van der Linden et al., who also proposed that the vesicle size is controlled by the balance between viscous and surface forces.[39]

Furthermore, a comparison with the shear thinning law deduced by Roux et al. is shown in figure 5.19 (left). Here the dashed line represents the relation given by Roux et al. ($R_{MLV} \propto \gamma^{0.5}$). One can see, that while it describes the data of Müller et al. very well, the $C_{10}E_3$ system shows

a stronger dependence of R_{MLV} on the shear rate.

There is an apparent contradition in the strain control observed in SANS and the stress control of the MLV size observed in depolarized SALS. The apparent strain control of the transient behavior only holds for the intermediate range of shear rates (5 to $20s^{-1}$) at strains below 6000. Here the viscosities and the scattering patterns are similar for the different shear rates. On small length scales, i.e., in neutron scattering, only the reorientation of lamellae is observed, which undergoes a transition from planar lamellae to MLVs. Reorganization and reorientation of bilayers are completed before the transitions that take place on larger length scales, i.e., MLV-size changes and the narrowing of the size distribution. The latter do not affect the scattering observed in SANS but lead to different scattering patterns in depolarized SALS. Therefore the SANS intensities much earlier reach a steady state as compared to SALS and rheology. Here the strain control is true for a wider range of shear rates, i.e., from $2s^{-1}$ up to $100s^{-1}$.

Furthermore it is possible, that the viscosity evolution at low strain, depolarized SALS patterns and also the Bragg-intensities of the SANS data show a scaling with strain despite the stress control indicated by the comparison of the $C_{10}E_3$- with the $C_{12}E_4$-system. Note that at shear rates $\geq 30s^{-1}$ the transition monitored by rheo-SALS and even rheo-SANS took less deformation compared to the lower shear rates. This is expected for a stress-controlled transition. Nevertheless, at shear rates below $30s^{-1}$ up to a strain of 6000 the transition seems to be controlled by deformation only. It is very likely, that two effects compensate in the range of moderate shear rates. At higher stress (as is built up at higher shear rate) the transition should require less deformation. At the same time the sample undergoes a structural change and the size of the aggregates formed sensitively depends on the stress itself.

Bergenholtz and Wagner also reported about a strain-controlled transition in an AOT/brine system. Here the strain control regarded the onset of MLV formation as well as the transition of MLVs to an ordered structure revealing a hexagonal symmetry in depolarized SALS. They found that a certain critical stress is necessary to invoke this transition to an ordered state. From that they concluded that the governing parameter is the stress and not the shear rate. Nevertheless the strain dependence was observed for both transitions, below and above this critical stress.

Apparently, the observations made in this study are very similar, but even at the highest shear rates that were studied, an ordered state with hexagonal symmetry was not observed. This suggests, that the critical stress that is needed to reach such an ordered state is much higher in our

case. Anyhow, the shear thinning behavior at shear rates above $10s^{-1}$ indicates that eventually a hexagonal packing will be reached and the so-called layer sliding should be observable at very high shear rates.

5.4 Conclusion

The transition from the L_α-phase to MLVs was studied by small-angle neutron and light scattering and rheology for two nonionic surfactant systems, namely 40wt% $C_{10}E_3$ and 40wt% $C_{12}E_4$ in D_2O. For the $C_{10}E_3$ system, a scaling with the strain for shear rates ranging from 2 to $100s^{-1}$ was observed for the MLV formation at 25°C.

In figure 5.20 we have illustrated the structural evolution of the transition, as interpreted from rheology, rheo-SANS and rheo-SALS experiments. The transition can be subdivided into five regions. First the initial state of planar lamellae in parallel orientation (I), followed by the intermediates with cylindrical symmetry (MLCs or coherent stripe buckling of the lamellae) (II). As theoretically suggested these lamellae start breaking into MLVs, and a state consisting of a mixture of undulating lamellae and MLVs is obtained (III). Upon further shear flow a pure MLV-state (IV) is reached, which finally becomes ordered (V).

Now the different experiments can be discussed according to this scheme, especially the question of what the governing parameter for the transition from planar lamellae to MLVs is.

When applying a shear rate $1s^{-1}$ the transition only reaches the intermediate state with few MLVs present (state III). This assumption is supported by the SANS and additionally by the SALS data. SANS data from the radial and the tangential beam revealed a remaining anisotropy. Especially the anisotropy in the tangential beam inferred the presence lamellar fragments, that preferentially adopt the parallel orientation. SALS data where essentially two fold, also supporting the presence of cylindrical symmetry. Also the viscosity evolved differently compared to the higher shear rates. Hence, the stress exerted on the sample was not big enough to complete the transition to a pure MLV phase.

Applying shear rates between 2 and $5s^{-1}$ leads to isotropic SANS-patterns, i.e., the pure MLV-state can be obtained. But SALS revealed, that an ordered structure could not be gained with a shear rate of $5s^{-1}$. Thus state IV is reached at the intermediate shear rates. Only at $\dot{\gamma} \geq 10s^{-1}$, as indicated by the structure factor in SALS, were MLVs with a narrow size distribution and hence a closer and better packing obtained (state V). The deviation of the radii from the power

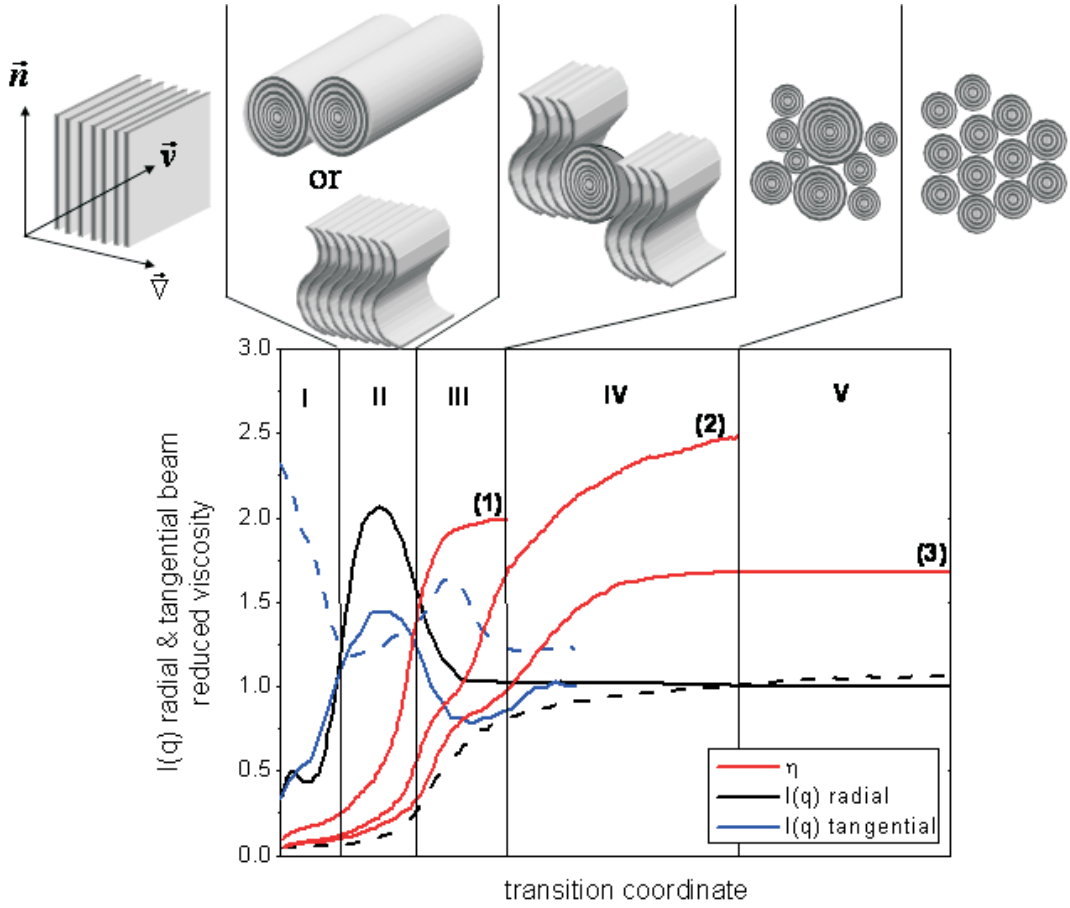

Figure 5.20: Sketch of the process, showing the initial state (state I), the coherent stripe buckling or MLCs (state II), a region where buckled lamellae and MLVs coexist (state III), and finally the MLV state (states IV and V). The intensity evolution in the radial (neutral direction, solid black line; flow, dashed black line) and the tangential beam (neutral direction, solid blue line; gradient, dashed blue line) are schematically shown together with three flow curves (red lines). Flow curves represent the viscosity evolution (1) at $\dot{\gamma} \leq 1s^{-1}$, (2) between 1 and $10s^{-1}$, and finally (3) at $\dot{\gamma} \leq 10s^{-1}$.

law behavior at higher stress is probably due to layer sliding as it occurs in hexagonally packed MLV-phases. The transition at 38°C stops even earlier than that at 25°C and $1s^{-1}$. In this case only a state between state I and II is reached, i.e., a fraction of lamellae starts to buckle while the other fraction escapes the tension by a permeation mechanism as proposed by Marlow and Olmsted, leading to a reduced d-spacing.

The final state viscosities reveal a shear thickening and a shear thinning regime as a function of shear rate (Figure 5.3b). The MLV size decreases in both regimes and therefore the shear thickening was attributed to an increase in the number density of MLVs and their increasingly narrow size distribution. The shear thickening regime includes state II, III and IV, whereas shear thinning only takes place, if state V is present. The transition from planar lamellae to MLVs at deformations $\gamma \leq 6000$ appears to be controlled by strain. The fact that eventually different final states (above $\gamma = 6000$) are reached at different shear rates is a strong indication for a stress control of the transition.

In time-resolved SANS similar regions could be distinguished for the position of the intensity maximum in neutral direction. Although this is not a steady-state property, it very well agrees with the conclusions presented above. It can be argued, that this transient behavior correlates with the steady-state properties, since the MLVs that form from the initial stripe buckling (state II to III) have the same size as the wavelength of the undulation. The two properties are therefore correlated and a similar behavior can be expected. The position is almost constant until a shear rate of $10s^{-1}$ and decreases at higher shear rates.

Intermediate structures occurring during the transition are stable after cessation of shear allowing scattering studies on trapped intermediate structures. So-called gap-scan experiments revealed that the transition at 25°C is homogeneous throughout the gap. Additionally the tangential beam experiments revealed that the transition from the state II to the pure MLVs involves a state with MLVs in a matrix of lamellae, preferentially in the parallel orientation.

Increasing temperature to 32°C essentially does not influence the strain dependence of the process. The start of the transition is very similar even in the coexistence region at 38°C. However, SANS remains anisotropic in the steady state. Here the steady state consists of weakly buckled lamellae or of MLCs residing in a matrix of planar lamellae. The d-spacing in gradient direction was found to be smaller than that in neutral direction, in accordance the predictions of Marlow and Olmsted for permeable lamellae under shear.

The startup experiment at 25°C and shear rate $1s^{-1}$ raises the question of how the aggregates are distributed throughout the gap at steady state. However, gap-scan experiments have not been performed in this case. Therefore a comparison with the gapscan experiments 38°C using shear rates 6 and $7s^{-1}$ as well as the one at 25°C and a shear rate of $10s^{-1}$ is helpful. The gap-scan experiments at 38°C revealed that, with the exception of a small fraction of parallel lamellae at the outer wall of the shear cell, the aggregates are evenly distributed throughout the gap. Furthermore, the gap-scan experiment at 25°C and $10s^{-1}$ revealed the same for the entire transition. It therefore seems plausible to assume that the situation found at 25°C and $1s^{-1}$ is essentially the same as at 38°C. Upon changing the surfactant to $C_{12}E_4$, essentially the same transition as with $C_{10}E_3$ at 25°C and $10s^{-1}$ is observed. The intermediate with cylindrical scattering symmetry is already found at ≈ 900. This is roughly at a strain 3 times smaller compared to the $C_{10}E_3$ system. The steady state revealed some anisotropy in the tangential beam, leading to the conclusion that a certain fraction of lamellae remains in the parallel orientation. One possible explanation for the shift of the transition to lower deformation is the increased the membrane stiffness. The other is the higher viscosity of the $C_{12}E_4$ sample. The transition requires less strain since a higher stress has to be applied to obtain the desired shear rate. The stress is about a factor of 1.7 higher compared to the $C_{10}E_3$ sample (compare the shear rate dependence of q_{max}). The intermediate with cylindrical symmetry especially is found at a strain value about three times lower than for the $C_{10}E_3$ sample. The comparison of the steady-state viscosities and MLV sizes of the $C_{12}E_4$ system as studied by Müller et al. and those of the $C_{10}E_3$ system indicates, that the stress is the parameter governing the transition from planar lamellae to MLVs.

Temperature and the surfactant chain length were the two parameters that were changed in order to determine which factors control the transition from planar lamellae to MLVs. One can see that while temperature does not change the position of the maximum in intensity found in the neutral direction it does affect whether the transition is completed. Upon increasing the temperature (changing the spontaneous curvature of the bilayer) at a constant shear rate a coexistence region of MLVs and planar lamellae is entered (see also figure 5.1).

5.4.1 Acknowledgement

We thank the Deutsche Forschungsgemeinschaft, the Fonds der chemischen Industrie and the Swedish research council for financial support. F. N. especially wishes to thank the Marie Curie Fellowship association and the Deutscher Akademischer Austausch Dienst.

6 Effect of Flow Reversal on the Shear-Induced Formation of Multilamellar Vesicles

6.1 Introduction

The influence of shear on lyotropic lamellar phases is of fundamental interest to industrial application as well as for mere scientific reasons. In particular a control over the kinetics of multilamellar vesicle (MLV) formation would be useful. In view of their morphology they are interesting for applications as micro reactors and for drug encapsulation.[7,104,105] The inherent non-equilibrium nature of MLVs poses problems for technological realization and understanding the time scales and specific conditions under which MLVs are formed is indispensable for a better control over the formation process.

It is well known, that multilamellar vesicles (MLV, also termed torical focal conic defects, spherulites or onions) can be formed by shearing a lamellar phase.[9] Earlier studies focused on the steady state behavior of the L_α-phase. In this context so-called orientation diagrams were established, where areas of lamellar orientation in a shear field are mapped in a shear rate vs surfactant volume fraction diagram.[9] These orientation diagrams display a central region, where MLVs are present, neighbored by lamellae with parallel orientation. In certain regions of the orientation diagram transitions from planar lamellae in parallel orientation to perpendicular orientation and back have been observed as a function of shear rate.[9,17,18,25]

In the low shear region a defect ridden L_α-phase is present. It has been proposed, that such defects play a central role in MLV-formation.[9] Leon et al.[13] describe the process of MLV formation as a randomly activated process.

Within the MLV-region, the steady state size of the MLVs is expected to scale with σ^{-1}.[39] This dependence is derived by balancing the surface tension of a droplet with bulk stress. Expressing the bulk stress by viscosity times shear rate and baring in mind that the viscosity itself is shear

rate dependent with a shear thinning exponent of -1/2 the proportionality of MLV size to $\dot{\gamma}^{-1/2}$, as often found in rate controlled experiments, can be rationalized.[9,15,16] However, a proportionality with $\sigma^{-0.75}$ was reported in the case of stress controlled experiments.[10] The evolution of the structure as displayed by physical properties, such as viscosity, conductivity, birefringence and the evolution of the scattering pattern, during the transition from planar lamellae to MLVs was found to scale with strain.[10,23,24,90,106,107]

Several different theoretical approaches have been proposed to model the mechanism of MLV-formation. Zilman et al. proposed a coupling of strain with short wavelength thermal undulation, leading to a coherent stripe buckling of lamellae that will eventually lead to MLV-formation.[40] The MLVs are expected to be of comparable size as the wavelength of the buckling instability. Further calculations about the influence of shear on lamellar systems were performed by Marlow and Olmsted.[41] They calculated how a lamellar phase escapes the tension induced by the suppression of thermal undulations by a shear field predicting that impermeable bilayers have to buckle and eventually form closed bilayers (MLVs), whereas permeable lamellae have the possibility to reduce the lamellar spacing by creating new lamellae. For both proposed mechanisms a strain dependence of the process should be expected.

Courbin et al. found a $\dot{\gamma}^{1/3}$ dependence of the q-vector, at which the intensity maximum of the first formed MLVs occurs, a strong evidence for the buckling mechanism proposed by Zilman et al.[23,90] Furthermore they found the same scaling exponent for the dependence of the lamellar spacing d and the inverse sample thickness $1/D$. The strain needed to induce the initial buckling, however, was only found to scale with the inverse of the lamellar spacing d.

Auernhammer et al.[42] proposed a hydrodynamic model based on the formalism of the description of thermotropic smectics, where the underlying nematic and smectic directors couple differently to the shear field.

Lyotropic lamellar phases and thermotropic smectic liquid crystals share most of the above described features, except MLV-formation. Large amplitude oscillatory shear (LAOS), however, has only been studied for thermotropic smectics and it was found to drive out defects, if the strain amplitude was close to unity. Thus LAOS produces a defect free, oriented lamellar phase.[43]

Little is known about the effect of oscillatory shear on MLV-formation itself. If lyotropic lamellar systems showed the same response to oscillatory shear as thermotropic smectics, namely the

healing of focal conic defects, this would be an intriguing aspect.

Very recently an interesting study in this regard was pursued by Fritz et al.[27] They investigated the effect of an oscillating shear field on the formation kinetics of MLVs. Varying the stress amplitude of the oscillation, they were able to controll the kinetics of the transition and to determine a minimum strain amplitude needed to trigger MLV-formation. The steady state size was, however, controlled by the stress amplitude, according to continuous shear experiments.[10] This study mainly relies on rheological information. The only structural information therein comes from rheo-SALS experiments, i.e., probing length-scales of a few μm. Furthermore, the starting conditions are less well defined, since in the AOT-brine system, an orientation of the lamellae prior to shear is not possible. Consequently, the experiment was carried out with a polydomain sample.

Nonionic surfactant systems of C_nE_m-type have proved to be particularly useful for studying the transition from planar lamellae to MLVs under the influence of shear.[24,107] These systems are advantageous in two respects. On one hand they are binary systems, and therefore problems with different preferred curvature caused by a segregation of components, as is possible in ternary systems, are avoided; on the other hand the bilayer saddle-splay modulus $\bar{\kappa}_b$ varies with temperature and thus offers a convenient way to study the transition as $\bar{\kappa}_b$ changes. Zipfel et al.[24] and Nettesheim et al.[107] studied the transition from planar lamellae to MLVs for continuous shear, varying shear rates, temperature and surfactant chain length. The results from these studies will serve as references in the investigation presented here.

There are three major differences between the study of Fritz et al. and the one presented here. First, Fritz et al. use stress-controlled oscillatory experiments, whereas we use a zigzag strain profile (for details see section 6.3.1). Second, as pointed out above, Fritz et al. mainly rely on rheological information. We, however, will present structural information on two different length scales from small angle neutron and small angle light scattering experiments. Third, the initial state is in our case well defined by preparing a lamellar phase in a parallel orientation, where the layer normal is parallel to the velocity gradient direction.

6.2 Experimental

The system contains the nonionic surfactant triethylene glycol monodecylether $C_{10}E_3$ (40wt% in D_2O). A lamellar phase with predominant parallel orientation was prepared by continuously shearing the sample with $\dot{\gamma} = 10s^{-1}$ at 42°C as described previously.[24] SANS-experiments were performed at the D11 beam line at the ILL in Grenoble, France. A thermostatted couette shear cell consisting of two concentric quartz cylinders with a gap of 1mm was employed to study SANS under shear. The step motor enabled an easy inversion of the direction of shear by simply reversing the polarity. Two scattering configurations were used: The radial beam, where the neutrons pass along the gradient direction and the tangential beam, where the neutrons pass along the flow direction. The sample was studied at 0.02 $Å^{-1} < q < 0.15$ $Å^{-1}$. Data correction for background and solvent scattering, absolute calibration dividing as well as radial and azimuthal averaging was performed on the anisotropic data using Grasp, a standard ILL software. Radial averaging was performed in 30°-sectors along the flow, neutral and gradient directions whereas the azimuthal average was performed in a 360°-sector at the Bragg-peak position ($0.084Å < q < 0.12Å^{-1}$).

Depolarized rheo-SALS experiments were performed using a Bohlin-CVO HR rheometer equipped with a quartz 3°-cone/plate shear geometry. The incident light ($\lambda_0 = 488nm$) was linearly polarized parallel to the flow direction and passed the sample along the gradient direction. The analyzer was aligned perpendicular to the polarization of the incident light. The accessible q-range in SALS was ca. 0.5-3 μm^{-1}. The evolution of the SALS-patterns was captured by a CCD-camera and saved in tiff-format. For the evaluation of the depolarized scattering rheo-SALS-patterns were selected in equal intervals along the strain axis.

6.3 Results

The presentation of the results will be divided into three sections. First, a description of the experimental protocol will be given. Second, we present the response of lamellar orientation as observed by SANS. Finally, the response on larger length scales will be discussed in connection to SALS data.

6.3.1 Procedures

Using a lamellar phase initially in the parallel orientation where the layer normal is parallel to the velocity gradient direction (for the preparation of this initial state see[24]) flow reversal experiments were performed, employing shear rates of $\dot{\gamma} = 10s^{-1}$ and $5s^{-1}$ and varying strain amplitudes $\Delta\gamma$. Here, the strain amplitude is defined as $\Delta\gamma = \dot{\gamma}\Delta t$, with Δt the duration of half a shear cycle. This was accomplished by

1. shearing in one direction for a certain time at the given shear rate yielding the desired strain

2. then shearing in the opposite direction for the same period of time and at the same shear rate.

In between 1) and 2) shear was stopped to give time for the recording of SANS-spectra. The duration of the rest phase was chosen to yield scattering data with reasonable statistics. For the shear experiment itself, the duration of the rest phase is unimportant, since no structural changes take place, while shear is stopped.[107] Consequently, neutron scattering was only recorded at rest. This procedure was repeated until a total strain of $\gamma_a = 3 \cdot 10^4$ was reached. The resulting strain profile is as sketched in figure 6.1.

To simplify comparison the same procedure was also used in rheo-SALS, except that scattering patterns were recorded during all phases of the experiment. Unless specified differently the data (either SANS or SALS) are presented as a function of the absolute deformation $\gamma_a = \sum \gamma_{forward} + \sum \gamma_{backwards}$, hence simply adding the values of the forward and backward shearing phases together. Figure 6.2 (left) displays a typical scattering pattern of an oriented lamellar phase recorded in the radial beam. The sectors for radial and azimuthal averaging are depicted with solid and dotted lines, respectively.

The evolution of the scattering pattern during continuous shear was studied in previous experiments,[24,107] which now serve as a reference (Figure 6.2, right). To follow the progress of the transition with time or deformation the intensity at the Bragg-peak $I(q_0)$ was followed in the respective directions of the rheological experiment. This intensity evolution is termed an intensity trace.

Before the scattering in such a start-up experiment becomes isotropic due to MLV formation, the intensity in neutral direction passes a maximum at $\gamma = 3000$, while the intensity in flow direction

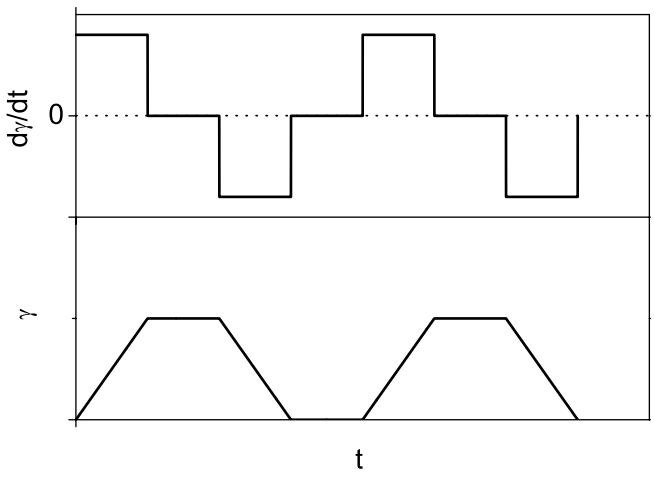

Figure 6.1: Profile of the flow reversal experiment.

is still very low. Tangential beam experiments at the same deformations revealed isotropic scattering symmetry. These two observations led to the conclusion, that the anisotropy observed in the radial beam at $\gamma = 3000$ is indicative for the presence of a cylindrical symmetry in lamellar orientation.[24,107] This maximum in the neutral intensity trace will in the later experiments serve as the reference point for establishing reduced and relative strain axes.

Another point at much lower strain seems to be significant as well. A local maximum in the neutral intensity trace is observed at $\gamma \approx 300$. A temporary enhancement of the residual perpendicular orientation of lamellae causes this local maximum. The reproducibility of the starting point was checked in the tangential beam directly after preparing the oriented lamellar phase at 42° and at 25° just before starting the flow reversal experiment. Furthermore, the low viscosity of about 0.5 Pas was indicative for a good parallel orientation of lamellae. The intensity found in the radial beam along the neutral direction prior to shear results from a small fraction of lamellae in the perpendicular orientation (where the layer normal is parallel to the vorticity direction). However, only about 10% of the lamellae reside in this orientation, which results in the initial anisotropy in the radial beam experiment.[24,107]

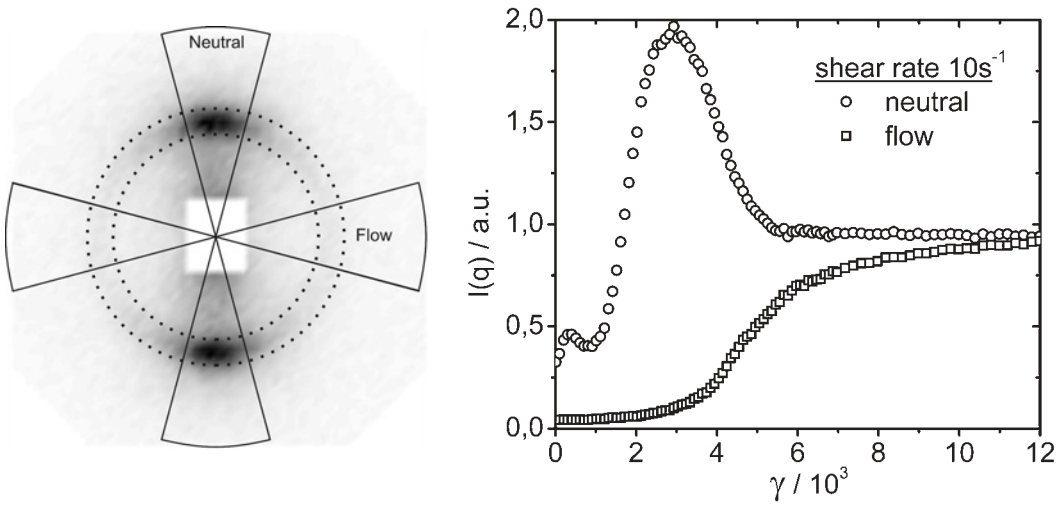

Figure 6.2: Left: Neutron scattering of an aligned lamellar phase recorded in the radial beam. Solid lines are 30°radial sectors in neutral and flow directions, respectively. The dotted lines show the azimuthal sector at the Bragg-peak position. Right: Intensity trace along neutral and flow directions from a continuous shear experiment with $\dot{\gamma} = 10s^{-1}$ vs strain γ. The intensities are normalized to the intensity of the isotropic state. For two-dimensional SANS data of the continuous experiment see supporting information or in ref.[107]

6.3.2 Small Length Scales

Using a shear rate of $\dot{\gamma}$=10s^{-1}, strain amplitudes $\Delta\gamma$ = 10, 20, 30, 50, 100, 200, 300, 500 and 3000 were realized. Strain amplitudes 30 and 200 were studied in both beam configurations, the others only in the radial beam. The results of radial beam experiments are shown in figure 6.3.

It can clearly be seen that the maximum of the neutral intensity trace, earlier identified with a cylindrical scattering symmetry[24,107], shifts to higher absolute deformations as the strain amplitude of the flow reversal is decreased. At strain amplitudes below 30 passing the maximum was not accomplished within the course of the experiment. Here the position of the maximum was estimated by the intensity in neutral direction, that was reached at the end of the experiment. This intensity was compared to that of a continuous experiment and by extrapolation it was estimated how much more strain would be needed to reach the maximum in the neutral intensity trace assuming that the shape of the intensity traces are similar.

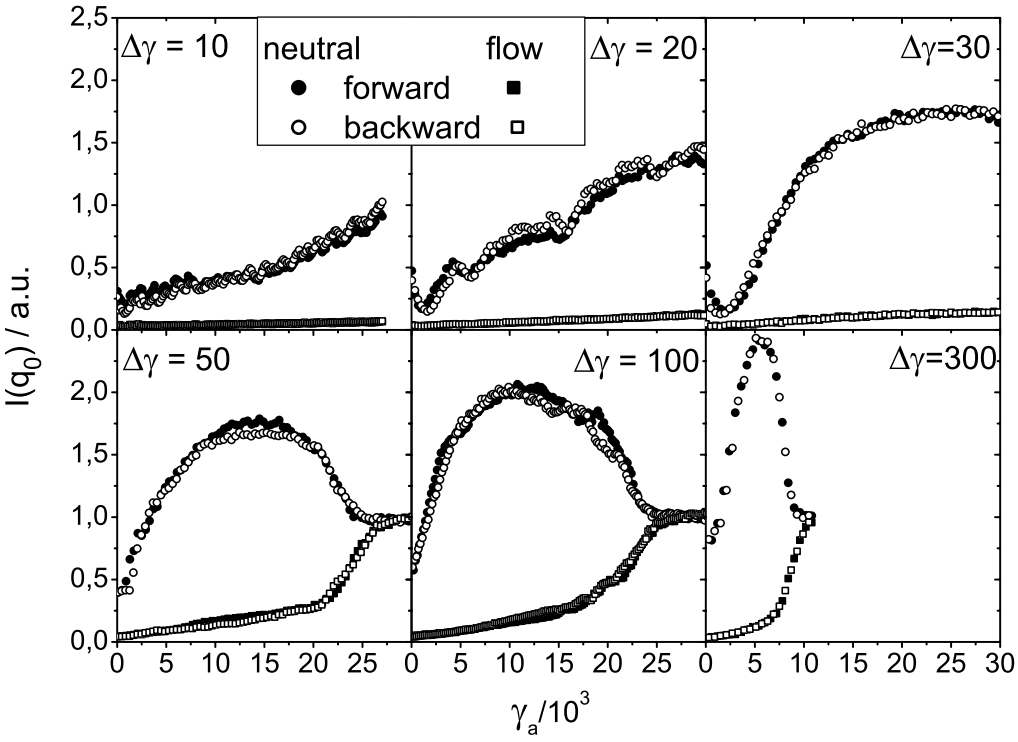

Figure 6.3: Intensity traces at q_0 along neutral and flow directions as a function of absolute strain for strain amplitudes 10, 20, 30, 50, 100 and 300 with shear rate $10s^{-1}$. The intensity traces of forward and backward shear are shown separately.

Nevertheless, contrary to what is typically found for the effect of large amplitude oscillatory shear on defect evolution in thermotropic smectic liquid crystals, MLVs (focal conic II defects) are still formed. Additionally a broadening of the maximum in neutral direction with respect to absolute strain is found for decreasing $\Delta\gamma$ and the hight of the maximum decreases as well. The latter indicates, that the intermediate structure is different, i.e., the buckling of the lamellae is less pronounced.

Interestingly, irregular oscillations of the intensity in the neutral direction with a period of 1300 to 5000 absolute strain units are observed for strain amplitudes 20 and 10, respectively. These oscillations become more regular with smaller $\Delta\gamma$. It can be assumed that these oscillations correspond to the first local maximum of the intensity trace in neutral direction at γ=300, that was found in preceding experiments with continuous shear (compare figure 6.2b). However, they

are not observed at higher strain amplitudes. It is so far not understood, why these oscillations disappear at higher strain amplitudes. Moreover, the absence of the first wiggle in the neutral intensity trace for $\Delta\gamma \geq 30$ remains unclear.

In order to study the influence of the shear rate, $5s^{-1}$ was used aiming for strain amplitudes of $\Delta\gamma$=30 and 300, shown in figure 6.4. Qualitatively the same evolution of Bragg-peak intensities

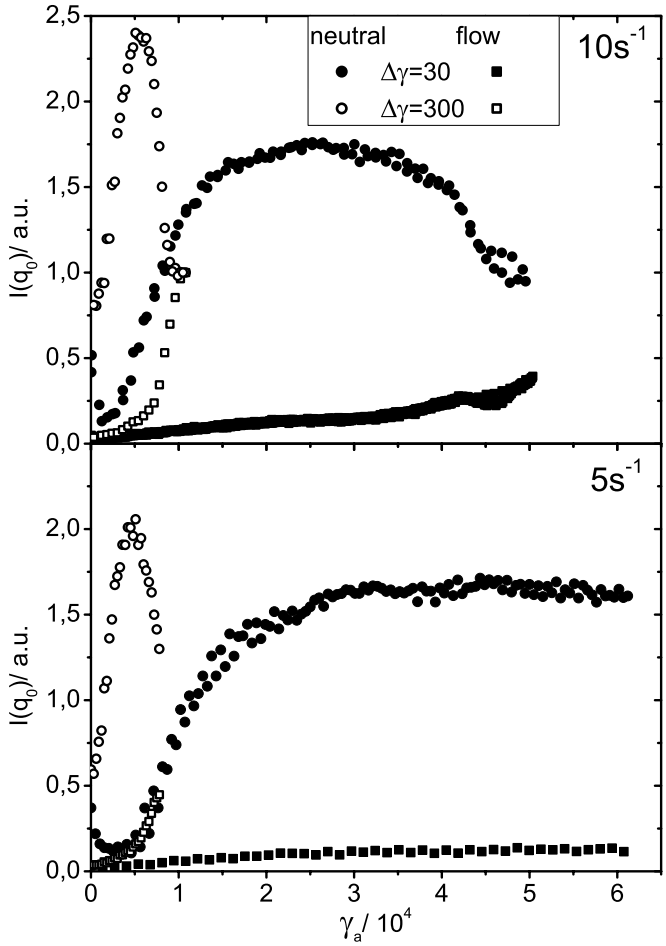

Figure 6.4: Intensity traces along neutral and flow directions as a function of absolute strain for strain amplitudes 30 and 300 with shear rates $10s^{-1}$ (top) and $5s^{-1}$ (bottom).

is found as for the experiments conducted with $10s^{-1}$. The slowing down of the process with decreasing $\Delta\gamma$ is also observed. Even the absolute strain values at which the maximum of the neutral intensity trace is found, are quite similar. However, at $\Delta\gamma$=300 the maximum is passed

if $10s^{-1}$ are applied, whereas the neutral intensity remains at a plateau value in the case of the $5s^{-1}$-experiment.

So far the results of the flow reversal experiments display a certain loss of strain as can be concluded from the shift of the intenisity maximum of the neutral trace to higher absolute strain values in comparison to a continuous experiment. Let us define a quantity similar to the loss factor of Fritz et al.[27] To quantify this loss, the maximum along the intensity trace in neutral direction was taken as a reference point for establishing a master curve. This was accomplished by shifting the neutral intensity traces of the flow reversal experiments onto that of a continuous one. Since in every experimental cycle there is a certain fraction of the strain that contributes to MLV formation (irreversible dissipation) and, if shear is inverted, a certain part of strain that restores, at least partially, an earlier state the resultant state, with respect to a continuous experiment is given by:

$$X = \frac{\gamma_{max,cont}}{\gamma_{max}} \tag{6.1}$$

Here X is the fraction of strain that irreversibly contributes to MLV formation and γ_{max} and $\gamma_{max,cont}$ are the deformations at which the intensity maximum in neutral direction is found in a flow reversal and a continuous experiment, respectively. This quantity will be called a shift factor and it quantifies the irreversible part of the strain, that in every experimental cycle contributes to MLV-formation .

It has to be mentioned, that X is only representative for one point in the course of the whole experiment, i.e., the occurrence of the maximum anisotropy in the neutral intensity trace. This will also become evident at a later point of the discussion. Nevertheless it is a feasible criterion for determining the progress of and the average reversible and dissipative contributions to the transition. The result of this calculation is presented in figure 6.5.

In this representation X=0 means that the reversible part of the strain dominates and hence there will be no transition from planar lamellae to MLVs. As can be seen from this representation of the data, the slowing down of the transition can be described by an exponential function of the form $X = 1 - exp(-A\Delta\gamma)$ over the whole strain range. Taking a closer look reveals, that the data at low strain amplitudes are not well represented by the overall scaling with $1 - exp(-A\Delta\gamma)$. Yet a determination of a minimum strain amplitude γ_{min}, below which a transition would not take place is difficult owing to the large error bars. The exponential scaling would for all finite values of $\Delta\gamma$ lead to positive values for the loss factor. The inset in figure

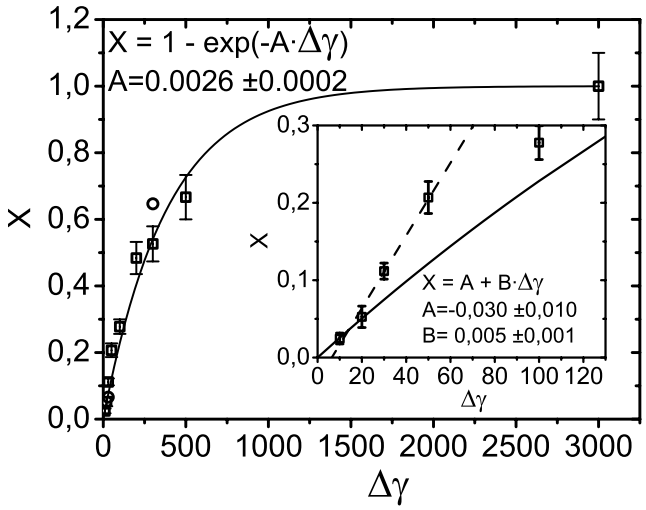

Figure 6.5: Shift factor X as defined in equations 1 as a function of strain amplitude for $\dot{\gamma} = 10^{-1}$ (squares) and 5^{-1} (circles). Solid line represents a best fit to the data using $X = 1 - exp(-A \cdot \Delta\gamma)$ as a test function. The inset shows $\Delta\gamma$ <130 for which a linear fit was chosen (dashed line). For comparison $X = 1 - exp(-A \cdot \Delta\gamma)$ is included (solid line)

6.5 displays a linear fit to the shift factor X for $\Delta\gamma$ <50 and consistently $\Delta\gamma_{min}$ is found to be $\approx$ 6.5 strain units. However, this fit only describes the lowest strain amplitudes better and deviates substantially at higher values. We can thus conclude here, that the minimum strain amplitude $\Delta\gamma_{min}$ is to be found in the range of $0 \leq \Delta\gamma_{min} \leq 6.5$.

Although only 2 points are available for the experiment with $5s^{-1}$, the slope is steeper and hence $\Delta\gamma_{min}$ larger. The transition at $5s^{-1}$ from planar lamellae to MLVs, as studied in a continuous experiment,[107] does not yield the final state of densely packed, but that of polydisperse MLVs. Thus it seems plausible, that also the minimum strain required for MLV formation is larger.

However, the representation of the data in figure 6.5 does not give information about the whole transition. Therefore the intensity trace along the neutral direction of the different experiments is plotted vs the absolute deformation γ_a normalized to the position of the respective maxima along the absolute strain axis, i.e., γ_{max}. For a better comparison the intensity is normalized to 1 (figure 6.6).

It can clearly be seen, that the traces of the flow reversal experiments do not superimpose

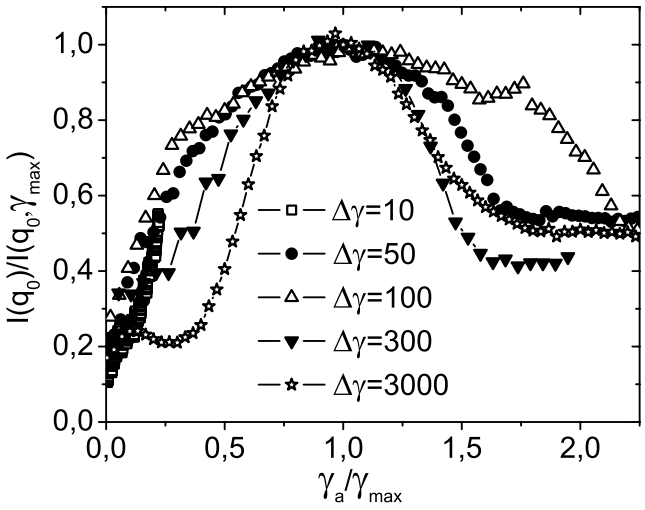

Figure 6.6: Neutral intensity traces for different strain amplitudes at $\dot{\gamma} = 10s^{-1}$ normalized to one vs absolute strain normalized to γ_{max}

over the entire experiment. Before the intensity maximum the traces of the flow reversal experiment display an immediate increase on the normalized strain axis, contrary to the trace of the continuous experiment. As was proposed by Zipfel et al. the transition involves two steps, the formation of cylindrical intermediates, multilamellar cylinders or coherently buckled lamellae. Consequently, the situation after the maximum, i.e., for $\gamma_a/\gamma_{max} \geq 1$, differs from the for $\gamma_a/\gamma_{max} \leq 1$. The fact, that the traces do not superimpose over the entire strain range for $\gamma_a/\gamma_{max} \leq 1$ is not unexpected and is congruent with the observations made in the tangential beam experiment as will be discussed in the section below.

Envisioning the transition from planar lamellae to MLVs as a process of successive lamellar fission, reorientation and fusion, one can assume that the observed oscillation in the intensity trace of the neutral direction are due to slight reorientation processes of lamellae. These reorientations seem to be partially reversible. The irreversible part contributes in each cycle to the formation of MLVs.

This was further investigated in a tangential beam experiment using $\Delta\gamma$=30 and 200. Since this beam configuration is especially sensitive to the parallel orientation of lamellae, one could

expect distinct influences of the lamellar reorientation on the intensity distribution (figure 6.7). Qualitatively the traces of the intensities in gradient and neutral directions are similar to those

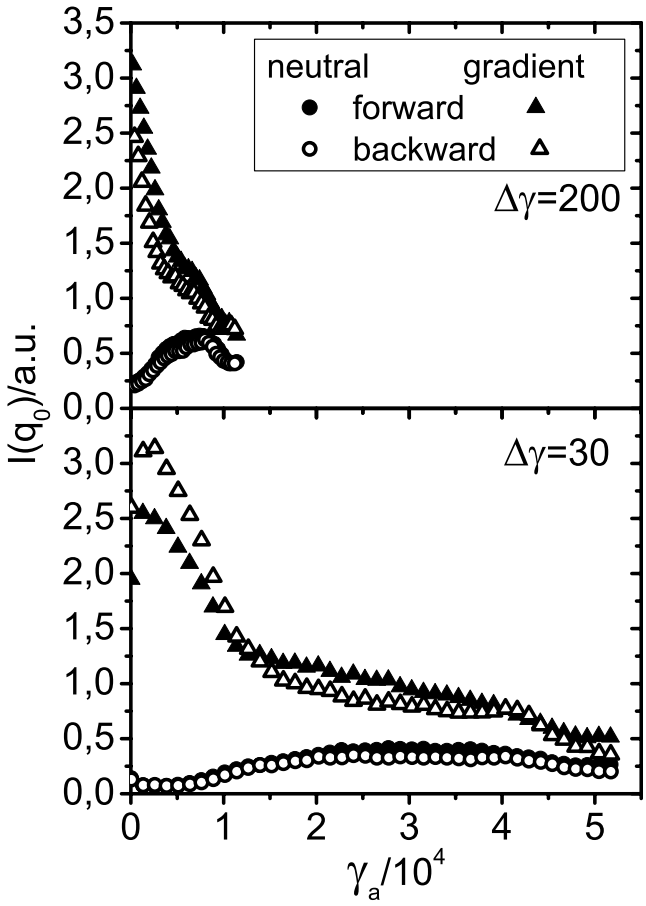

Figure 6.7: Intensity traces along neutral and gradient directions from tangential beam experiments for strain amplitudes 30 and 200, $\dot{\gamma} = 10s^{-1}$

of a continuous experiment, only that it takes much larger absolute strain. The data recorded after shearing forward (closed symbols) or backward (open symbols) are shown separately. It is evident, that up to absolute deformations of about $1 \cdot 10^4$ shearing backwards leads to a partial recovery of Bragg-peak intensity in gradient direction. In the course of the experiment the forward and backward shearing result in increasingly similar lamellar orientations.

For a better quantification of this observation the angular intensity distributions (figure 6.8, bottom) were fitted to a model, since then the information of the whole azimuthal intensity

distribution is taken into account, and not only the peak intensities. For this purpose a Mayer-Saupe description for the azimuthal intensity distributions of rod-like scatterers, as proposed by Piken et al., was employed.[108]

$$I(q_0, \phi) = I_0 \cdot exp\left[\alpha \cdot P_2\left(sin\phi\right)\right] + I_b \tag{6.2}$$

Here I_0 and I_b are intensity amplitude and isotropic scattering contribution, respectively and P_2 the second Legendre polynomial. A phase of $\pi/2$ was subtracted from the orientation angle ϕ to account for the parallel alignment of lamellae. Additionally α is proportional to the probability of finding a parallel lamellar orientation and thus accounts for the width of the angular intensity distribution. More details about this and other models for the calculation of the azimuthal intensity distribution of anisotropic scatterers can be found in ref.[109]. Figure 6.8 (top, left) displays the evolution of α for tangential beam experiments of continuous and flow reversal experiments calculated up to absolute strains of $1.5{\cdot}10^4$. As expected, α decreases with increasing absolute strain in the course of MLV-formation until it reaches a steady state value. In the experiment with $\Delta\gamma = 30$ and in the continuous one an ordering is observed in the beginning ($\gamma_a \leq 1000$), i.e., α displays a maximum at $\gamma_a \approx 3000$. In both flow reversal experiments α oscillates as long as steady state is not reached and the amplitude of this zigzag is of comparable magnitude. For comparison the evolution of α of the corresponding continuous experiment is supplemented.

In the shear experiment with $\Delta\gamma = 200$ scattering was recorded every cycle after both, the forward and backward shear, whereas for $\Delta\gamma = 30$ only every 20 cycles after both, forward and backward shear periods. The more astonishing is the fact, that the oscillations in the latter case are still so prominent and regular.

Figure 6.8 (top, right) shows the scaling of the three experiments on a strain axis normalized to the respective strains at which the maximum of the neutral intensity trace from a radial beam experiment occurs. Again it becomes evident, that the strict scaling with $1 - exp(-A\Delta\gamma)$ does not apply over the entire strain range. Nonetheless, the experiments show parallel behavior, as for instance steady state is reached at $\gamma_a/\gamma_{max} \approx 0.5$, just about where the oscillations of α in the flow reversal experiments damp. Figure 6.8 (bottom) shows the fits of the intensity distributions according to Piken et al. for a continuous experiment (left) and the flow reversal experiment (right) with $\Delta\gamma = 30$, both using $\dot{\gamma} = 10s^{-1}$. The fits show a good agreement with the data and the widening of the intensity distributions proceeds symmetrically around

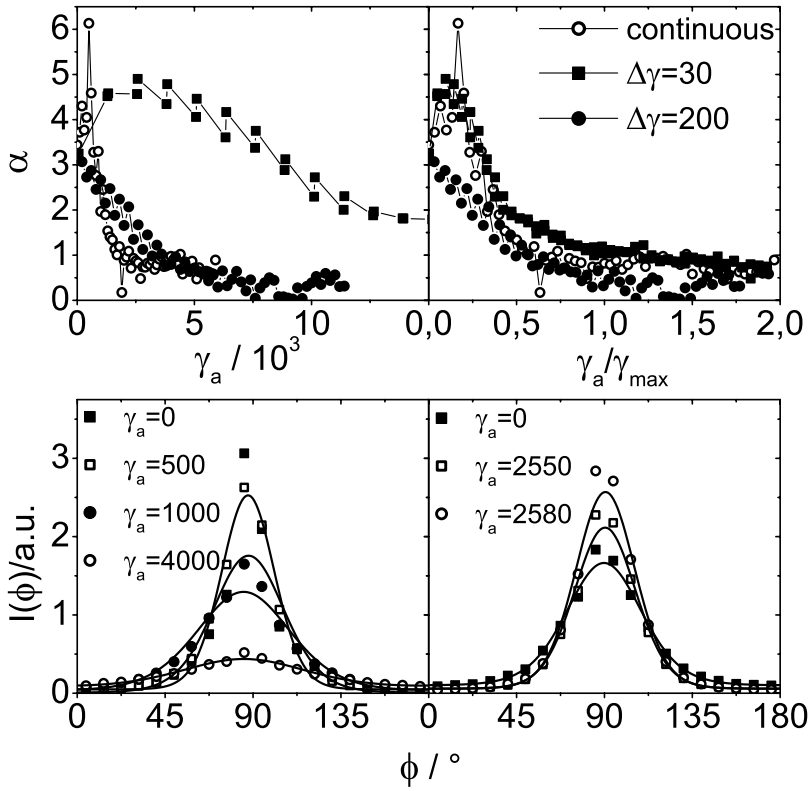

Figure 6.8: Top left: α as a function of absolute strain for strain amplitudes $\Delta\gamma$=30, 200 and a continuous experiment, $\dot{\gamma} = 10s^{-1}$. A higher α implies a better alignment of the lamellae. Top right: Scaling of the three respective experiments on a normalized strain axis. Bottom: Azimuthal intensity distributions including fits according to Piken et al. for a continuous (left) and a flow reversal experiment $\Delta\gamma = 30$ (right).

90°, i.e. the distribution of lamellar orientations is symmetric throughout the entire transition. Hence, the material transport in gradient direction that has to occur in order to bend or reorient lamellae, is symmetric as well. Clockwise flow in the neutral-gradient plane would lead to an asymmetry of the intensity distribution and consequently is compensated by a counter clockwise flow. Admittedly the azimuthal intensity distributions are affected by the asymmetry of the tangential beam and thus systematic errors are introduced, impeding a more detailed discussion of this observation.

6.3.3 Large Length Scales

Rheo-SALS-experiments were performed with a strain amplitude of $\Delta\gamma = 50$ and a shear rate of $\dot{\gamma} = 10s^{-1}$. The transient viscosities of this experiment are compared with those of a continuous one up to an absolute strain of $\gamma_a = 3 \cdot 10^4$ in figure fig:flowrev9.

Most striking are the much lower viscosities during the entire experiment. The final viscosity

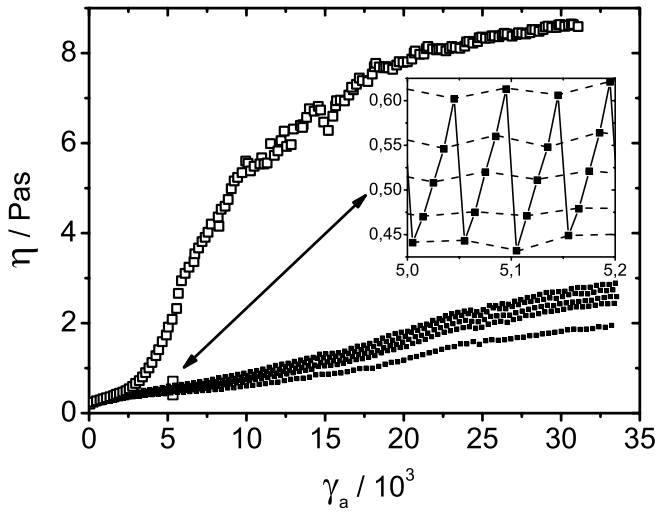

Figure 6.9: Transient viscosities of a flow reversal experiment with $\Delta\gamma$=50 (closed squares) compared to a continuous one (open squares), both conducted with $\dot{\gamma} = 10s^{-1}$. Inset shows a zoom of the flow reversal experiment into the region just above $\gamma_a = 5 \cdot 10^3$.

is by a factor of ca. 3 smaller. Furthermore the display of five distinct branches is somewhat peculiar. A closer look (inset in figure 6.9) reveals, that these are not separate branches, but a saw-tooth pattern of the viscosity evolution. Each upwards trend of the viscosity, comprising five points, corresponds to a forward or backward shearing phase, respectively. Hence, inverting the direction of shear first decreases the viscosity, and then it increases again. Overall this results in a net increase of the viscosity. It has to be mentioned, that the decrease in the viscosity is not due to a relaxation of the structure upon cessation of flow. This was studied in earlier experiments, where step-strain experiments were performed, recording SANS-patterns during the phases of rest.[107] The decrease in viscosity observed here are therefore merely due to the flow reversal.

These observations indicate that the process of MLV-formation in a flow reversal experiment is not only slowed down, but the mesoscopic structures at the end of the flow reversal experiment most likely differ substantially in comparison to the continuous experiment. The terminal viscosity of the flow reversal experiment is equivalent to the transient viscosity of the continuous experiment at strain values of ca. 6000. This would result, in analogy to the treatment of the neutron scattering data, in a shift factor $X = 0.18$. Recall, the value for $\Delta\gamma = 50$ calculated from the SANS-experiments is 0.21 and the fit to the data yielded ca. 0.12.

The depolarized SALS patterns of the flow reversal experiment are arranged in figure 6.10. Scattering patterns for deformations larger than 13500 were not available in the flow reversal experiment, since gradual sample loss impeded recording meaningful data.

As a function of absolute strain the scattering symmetry changes from two- to fourfold at about

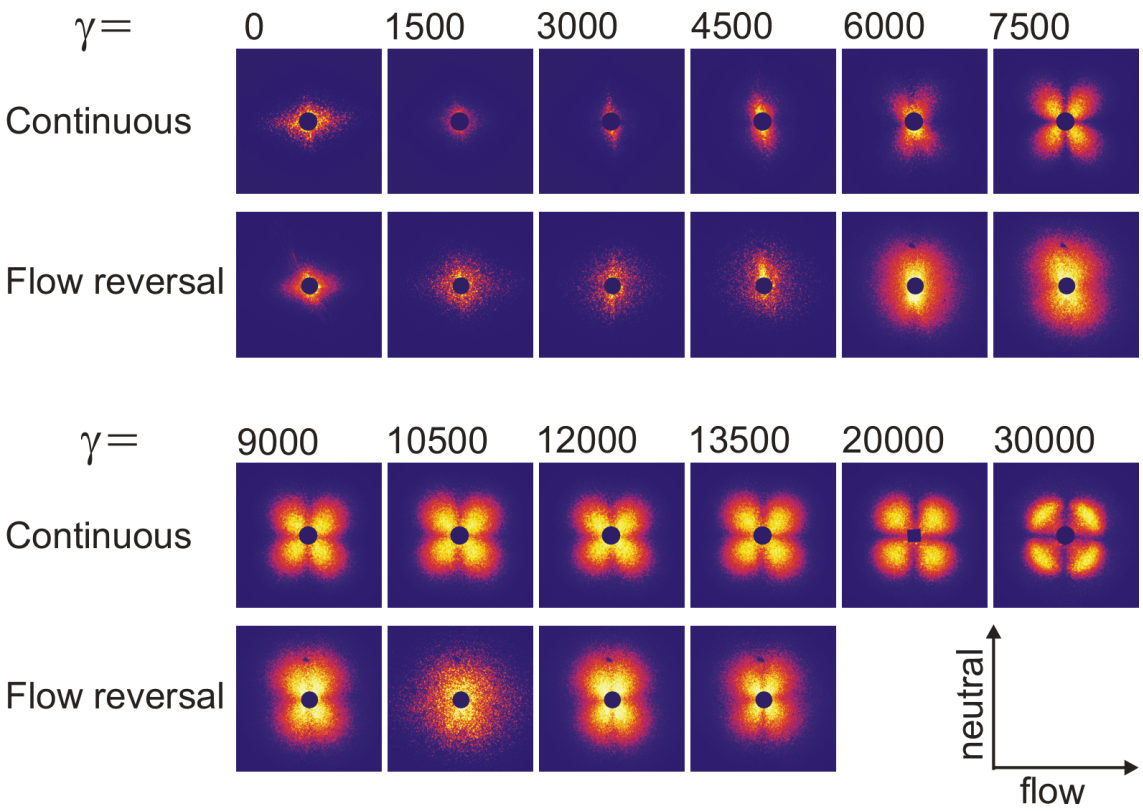

Figure 6.10: Depolarized SALS-patterns recorded during the flow reversal experiment with a strain amplitude of $\Delta\gamma = 50$ at different absolute strain values compared to the scattering found during a continuous shear experiment with a shear rate of $10s^{-1}$ at the respective deformations.

5500 absolute strain units. However, the cloverleaf pattern is elongated in neutral direction, thus indicating that the MLVs are elongated in flow direction. In these stages of the experiment, the fourfold symmetry can disappear again as shear is inverted. At higher deformation the fourfold symmetry is maintained, however, the orientation can vary slightly. The MLVs are still slightly elongated along the flow direction and the size of the aggregates can be estimated from the position of the intensity maximum with $R = 4.1/q_{max}$ [58,110] to ca. 8μm. The steady state structure of the continuous experiment at a shear rate of $\dot{\gamma} = 10s^{-1}$, on the other hand, is a densely packed MLV phase, displaying a structure factor in depolarized SALS, from which a MLV size of 2.6μm can be deduced.

Thus findings in the flow reversal differ fundamentally from those in the continuous experiments. First the size of the MLVs is much larger (about threefold, comparable to the decrease in viscosity) and about what is found at strain values of 6000 in a continuous experiment.

The cloverleaf displays an elongation in both cases, indicating elliptically deformed MLVs with an aspect ratio of about 1.5. Additionally the intermediate vanishing and reoccurring of the fourfold symmetry is unique to flow reversal.

6.4 Discussion

Flow reversal has a profound influence on the transition from planar lamellae to MLVs. The most obvious is the slowing down of the process. The neutron scattering data were compared to those of a continuous shear experiment with the respective shear rate and an exponential scaling of the shift factor X with the strain amplitude $\Delta\gamma$ was observed. This scaling was found to hold for other length scales as well, namely it was possible to relate the terminal viscosity of the flow reversal experiment with $\Delta\gamma$=50 to the transient viscosity of a continuous experiment. Also the data from depolarized SALS show a retardation of the process comparable to that observed by SANS and rheology. First evidence of MLVs is, however, already found at absolute strain values of $\approx$ 6000, comparative to the continuous experiment. The MLVs formed in this phase of the experiment can vanish again or deform in such a way, that their scattering loses its fourfold symmetry. This observation was also made by Fritz et al.[27] Presumably the MLVs are stretched in flow direction such that the characteristic cloverleaf pattern is not resolved by the SALS setup anymore.

The experiments in SANS and rheo-SALS give information about different length scales that

are relevant for the process. Using these techniques, it should be possible to unravel the origin of the scaling of X with $1 - exp(-A \cdot \Delta\gamma)$.

Shearing a lamellar phase leads to a structural change which above certain deformations is irreversible. At deformation amplitudes of 3000 an inversion of shear direction did not have a noticeable influence on the process; flow reversal with $\Delta\gamma$=500 already led to a slowing down of the process. At all strain amplitudes below 3000 there has to be a reversible and an irreversible component, the latter contributing to the formation of MLVs in each experimental cycle. At $\Delta\gamma$=3000 the irreversible part is assumed to dominate completely.

To shed more light on this observation we would like to compare these results with those obtained by Fritz et al. Their definition of the absolute strain is very similar to our's, although they applied oscillatory stress rather than a zigzag strain profile at a given shear rate. They calculate the loss factor by shifting the complex viscosity of an oscillatory onto that of a creep experiment, i.e. using rheological information to establish a mastercurve. This is different from our approach, where structural information from SANS-experiments is used to establish a relative strain axis. The shift or loss factor, obtained by either of these methods, is not identical to the loss modulus G", since it only gives information about the strain that leads to dissipation contributing to MLV formation. There are, however, other dissipation modes such as solvent viscosity that contribute to the loss modulus.[27]

The minimum deformation amplitude for shear rate $10s^{-1}$ necessary to induce the transition from planar lamellae to MLVs (γ_{min}) is in our study found to be ≈6.5. This is of comparable magnitude to the value found by Fritz et al. for the AOT/Brine system. However, the use of different experimental procedures and even more the use of different surfactant systems, forbids a direct comparison. The AOT/Brine system used by Fritz et al. is a screened ionic lamellar phase, essentially representing a Helfrich stabilized system as is also the case for the nonionic surfactant lamellar phase used in our study. However, the lamellar spacing is more than two times larger than in the $C_{10}E_3/D_2O$-system studied here (≈ 135Åand 60Å, respectively).

The order parameter analysis of the tangential beam data revealed periodic changes of the width of the azimuthal intensity distributions with the absolute strain. This, to our knowledge, is a new aspect. These oscillations can be explained by changes of the lamellar order, e.g. building up coherent buckling of the lamellae. Upon flow reversal a previous state is at least partially restored and thus a lamellar phase with a higher degree of order is recovered. We speculate,

that only the part of the process that involves braking lamellae while changing its orientation is irreversible and consequently leads to MLV-formation.
The question of the influence of shear rate is, however, still unresolved, although the experiments with $5s^{-1}$, as expected, indicate a slightly larger γ_{min} (Figure 5).
The minimum strain needed to induce irreversible changes in the sample is much smaller in the beginning and accordingly increases in the course of the experiment. This conclusion is nicely supported by the oscillations in the lamellar orientation distribution α in the beginning of the experiment, which vanish before γ_{max} is reached. It is also the reason why even at the smallest strain amplitudes used in the experiment a transition takes place.

6.5 Conclusion

In the study presented here it was possible to show the effect of successive flow reversals on the transition from planar lamellae to MLVs. A slowing down of the process was observed, which scaled with $1 - exp(-A\Delta\gamma)$. From establishing master curves we were able to distinguish a reversible from an irreversible contribution to the transition.
Tangential beam experiments and the order parameter analysis revealed, that the change of the lamellar orientation distribution is partially reversible. A strong indication for such a process, namely partially reversible reorientations of lamellae, are the oscillations observed early during the transition from planar lamellae to MLVs in the order parameter. The part of the process that involves breaking lamellae and not just bending them might represent the irreversible contribution to the transition.
A minimum strain required to induce irreversible changes in the sample was deduced from the irreversible contribution to the transition, yielding $0 \leq \gamma_{min} \leq 6.5$ strain units, comparable to the value found by Fritz et al. in stress controlled oscillatory experiments with an AOT/brine system. However, the systems and experimental techniques used, are too different to draw any conclusions from a comparison of the two studies. We, however, for a given low shear rate, here $10s^{-1}$, expect a minimum strain amplitude from the fact, that the lamellar phase is a viscoelastic liquid at small enough strain amplitudes, i.e., in the linear viscoelastic regime. This value, in fact, can be very small.
An investigation of the dependence of γ_{min} on the lamellar spacing was not the scope of this study, but could be subject to future work. This would be of particular interest with respect to

the studies of Courbin et al.

Current theories describe the formation of MLVs from planar lamellae with parameters like the strain or the strain rate. These descriptions are able to predict the strain control[40] that is also found experimentally or give estimates of a critical shear rate required for MLV-formation.[42] Both approaches also yield estimates of the initial size of the MLVs. The experimental data gathered here are not discussed in terms of current theories, because the influences of the various parameters (strain, shear rate and stress) seem not to be independent of one another. A verification or falsification of the theories is not possible, since they apparently do not capture the interdependency of the variable parameters. We are confident that the data presented here will be useful to refine the current theoretical descriptions of this transition.

6.5.1 Acknowledgments

We thank the Deutsche Forschungsgemeinschaft (DFG), the Fond der Chemischen Industrie and the Swedish Research Council for financial support.

6.5.2 Supporting Information

Two-dimensional SANS-patterns in the radial and the tangential beam of $C_{10}E_3$ (40wt% in D_20) at three different strain values in a continuous shear experiment with a shear rate of $10s^{-1}$. This material is available free of charge via the Internet at http://pubs.acs.org.

7 Shear-Induced Morphology Transition and Micro Phase Separation in a Lamellar Phase doped with Clay Particles

7.1 Introduction

Recently, there has been an increasing interest in lamellar phases with particles included. These may have applications as stable pastes which may form delivery systems for abrasives or other cleaning agents and can be used to track the mechanism of MLV-formation by optical means.[37] Additionally these particles may influence the equilibrium properties of the lamellar phase as well as those under shear. For instance a mixture of a lamellar phase and latices with a radius larger than the d-spacing should phase separate. However, under shear a stable dispersion can be obtained and the latices were found to reside in the center of the MLVs.[111] Guest particles influence the properties of the MLV-phase in several ways. A pure MLV-phase without dopant particles has to fill space entirely. Therefore, MLVs have to deform to polyhedra, forming a foam-like structure. This comes along with a curvature energy penalty. As was shown by Arrault et al. spherical guest particles help to reduce this frustration by occupying the sites with highest curvatures, i.e., the interstices and / or the MLV-cores and therefore rendering the particles more spherical. Surprisingly, the addition of spherical particles does not change the rheological properties significantly.

The properties of the lamellar phase can also be altered significantly by adding polymers.[28,29,32,33,112–114] In these cases the membrane properties are changed by the presence of additional osmotic, steric and if so coulomb interactions. The latter can also be introduced by adding ionic surfactant to a nonionic lamellar phase.[26,85]

Steady state properties of undoped lamellar phases under shear have been studied for numerous

surfactant systems and normally the orientation diagram is well established.[9] In very few studies a shear induced change in the local structure, i.e., in the bilayer repeat distance d has been observed. Yamamoto and Tanaka[82] observed a change in the lamellar spacing upon shear in a dilute solution of $C_{12}E_5$ (1.8wt% in H_2O). They related the change in d to the applied stress and found a linear dependence. The change ranged between 1 and 5% of the lamellar spacing at rest. Nettesheim et al.[26] observed a change of d of up to 15% in a semidilute nonionic surfactant mixture (10wt% $C_{12}E_4$ in D_2O) weakly charged by the anionic surfactant SDS.

In general shear is thought to suppress short wavelength thermal undulations and thus leads to an increase in the projected area.[40,41] According to Zilman and Granek this leads to a coherent buckling of the lamellae since they are refined to a finite sample volume and the phase is incompressible. Marlow and Olmsted distinguish two cases in this context: (1) In the non-permeable case, shear leads to an increase in the local curvature of the bilayers (coherent stripe buckling) and finally to the formation of MLVs. (2) In the permeable case material transport perpendicular to the bilayers is possible and new bilayers can be created leading to a decrease in the lamellar spacing d. In an alternative approach Auernhammer et al.[42] derived a smectic model introducing a coupling of the flow field to the underlying nematic director of the lamellar phase, which essentially leads to the same observations. The suppression of thermal undulations in a system solely stabilized by Helfrich interactions has consequences for its stability as was shown by Ramaswamy.[115] For the presence of weak attractive interactions he predicts a segregation into two regions, one with a decrease in d, the other devoid of bilayers.

The addition of anisotropic clay particles to a lamellar phase seems especially intriguing, since these particles reside in the water layer in-between the bilayers. Depending on their size, the tumbling of laponite particles under shear is in conflict with the spatial confinement in the lamellar phase. Additional long range interactions perpendicular to the bilayers mediated by lamellar order were predicted.[116,117]

The binary nonionic lamellar phase of $C_{12}E_4$ in water was studied under shear by Müller and co-workers.[16,118] A shear thinning behavior in the MLV region as well as the dependence of the MLVs' radius on $\dot{\gamma}$ were found to be consistent with theory.[9] Grillo et al.[38] studied the quiescent state properties of lamellar phases hosting laponite clay particles (radius=15nm, thickness=1nm). These systems should in principle differ from the ones studied by Arrault et al.[37] since the particles are anisotropic and as such cannot lead to a relief of the curvature energy frus-

tration. From a shape analysis of the SANS Bragg peak using a structure factor model proposed by Nallet et al.[68] no noteworthy changes in the Caillé-Parameter η_{caille} were observed. Only very small clay concentrations can be incorporated into a lamellar phase, as was shown by Grillo et al.

7.2 Experimental Part

The system contains the nonionic surfactant tetraethyleneglycol mono-dodecylether ($C_{12}E_4$) and the synthetic hectorite laponite RD with a radius of about 15nm and a thickness of 1nm. Aqueous mixtures of a surfactant volume fraction $\Phi = 0.365$ were prepared from stock solutions of laponite with a clay volume fraction of $\Phi_{lap} = 0.00157$, where we used the densities of H_2O, D_2O, surfactant and laponite as 1, 1.107, 0.95 and 2.65g/cm^3, respectively. A pH of 8 to 9 was employed to ensure a stable dispersion. The laponite volume fraction of $\Phi_{lap} = 0.00157$ was chosen, since it was the highest possible clay content for a sample with a surfactant volume fraction of $\Phi = 0.365$.[38]

SANS experiments were conducted in lamellar as well as with clay contrast. For this purpose an H_2O/D_2O mixture of 0.327 (w/w) and 0.9 (w/w) were used used for lamellar and clay contrast, respectively, was used.[38]

In order to keep a constant volume fraction of surfactant and clay platelets, the concentration of the sample with lamellar contrast was 33.3wt% surfactant and S/L=0.39% and that of the sample with laponite contrast was 35.15wt% with S/L of 0.4%. S/L is defined as the mass of dried solid per mass of the aqueous stock solution.

SANS-experiments were performed at D11 at the ILL in Grenoble, France. At D11 a thermostatted Searle shear cell consisting of two concentric quartz cylinders with a gap of 0.5mm was employed to study SANS under shear. Two scattering configurations were used for the samples with lamellar contrast: The radial beam, where the neutrons pass along the gradient direction and the tangential beam, where the neutrons pass along the flow direction. The samples were studied at 0.02 Å^{-1} $\leq q \leq$ 0.15 Å^{-1}. Data correction for background and solvent scattering, absolute calibration dividing and radial averaging was performed using a standard ILL software provided. Anisotropic data were averaged in 30°-sectors along the flow, neutral and gradient directions.

Depolarized rheo-SALS experiments were performed using a Bohlin-CVO HR rheometer equipped

with a quartz 3°-cone/plate shear geometry. The incident light ($\lambda_0 = 488nm$) was linearly polarized parallel to the flow direction and passed the sample along the gradient direction. The analyzer was aligned perpendicular to the polarization of the incident light. The accessible q-range in SALS was ca. 0.5-3 μm^{-1}. In this setup, MLV-sizes can be determined from either the maximum of the MLV form factor, which occurs at $R_{MLV}q_{max} \approx 4.1$,[57,58,110] or from the maximum of the structure factor using $D = 2\pi/q_{max}$, with D the center-center distance of MLVs.

7.3 Results

The viscosities show a shear thinning regime at small shear stress (figure 7.1). Filling the Couette shear cell results in a polydomain sample. Steady shear flow leads to a better orientation and therefore to a smaller viscosity. At stresses above $5Pa$ a shear thickening regime is entered followed by a second shear thinning regime at $\sigma \geq 20Pa$ (Figure 7.1, top). In cone / plate geometry (SALS) a shear thinning of $\eta = \sigma^{0.55}$ and in a Couette geometry (SANS) $\eta = \sigma^{0.3}$ are found. $\eta = \sigma^{0.75}$ was reported in AOT/brine.[10] If plotted vs. shear rate one finds exponents of 0.36 (cone/plate geometry) and 0.24 (Couette), which are smaller than the value of 0.5 found for the pure system (40wt% $C_{12}E_4$ in water).[16]

The size of the MLVs was measured by depolarized small-angle light-scattering under shear (rheo-SALS) and determined from the maximum of the structure factor which arose in the second shear thinning regime. Assuming densely packed MLVs, the size can be determined from the Bragg-condition, i.e., $R_{MLV} = \pi/q_{max}$. The variation of the MLV-size with stress differs from literature values. If MLV-radius is plotted vs. shear rate ($\dot{\gamma}$) a powerlaw exponent of 0.89 results. This value is higher than that found in the binary $C_{12}E_4$/water system, where 0.5 was found.[16]

7.3.1 Rheo-Small-Angle Neutron Scattering

Now the results from SANS-experiments will be presented. Figure 7.2 shows the radial intensity profiles in the three respective directions of the shear experiment, namely neutral (left), flow (middle) and gradient directions (right). These were obtained from radial averages in 30° sectors

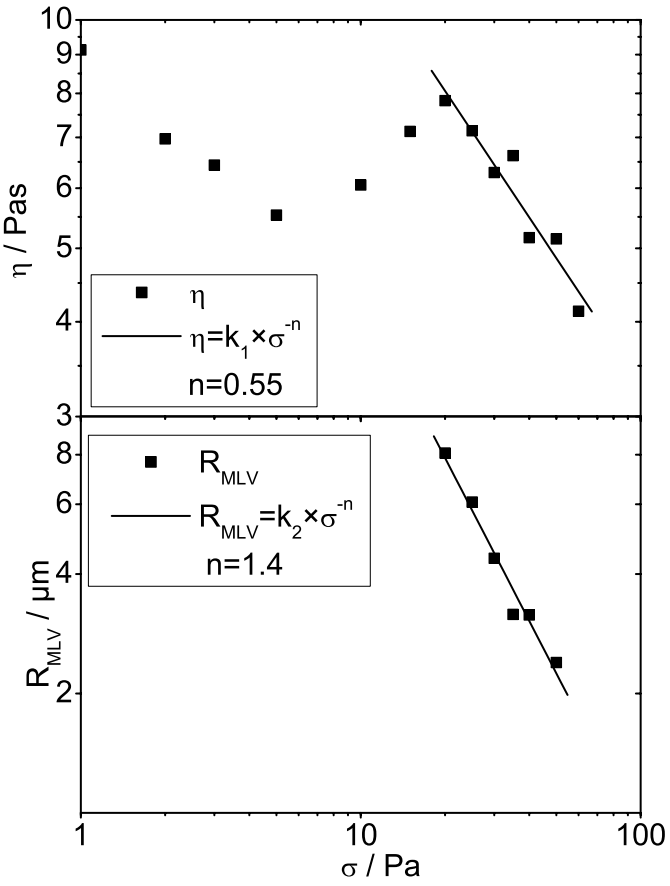

Figure 7.1: Top: Viscosity as a function of stress. Bottom: Corresponding R_{MLV} as a function of stress measured in depolarized rheo-SALS in the second shear thinning regime.

oriented along the vertical or the horizontal axis of the 2-dimensional intensity distribution from a radial beam experiment (neutral and flow directions) or along the horizontal axis of the tangential beam scattering (gradient direction). At low stress there is a noticeably higher intensity at the Bragg-peak in the neutral direction as in the flow direction and hence a fraction of lamellae is oriented with its layer normal along the neutral direction, i.e., these lamellae remain in the so-called perpendicular orientation. This anisotropy decreases with increasing shear, yet it does not vanish completely. Hence, there is a certain fraction of lamellae which is not incorporated in MLVs and is perpendicularly oriented.

Most important, SANS experiments revealed a drastic change of q_0 and thus the lamellar spacing

with stress. Accordingly, the repeat distance d changes from 79 to 56Å, a relative change of 30% (figure 7.4). Several szenarios that lead to such a change in lamellar spacing are conveivable.

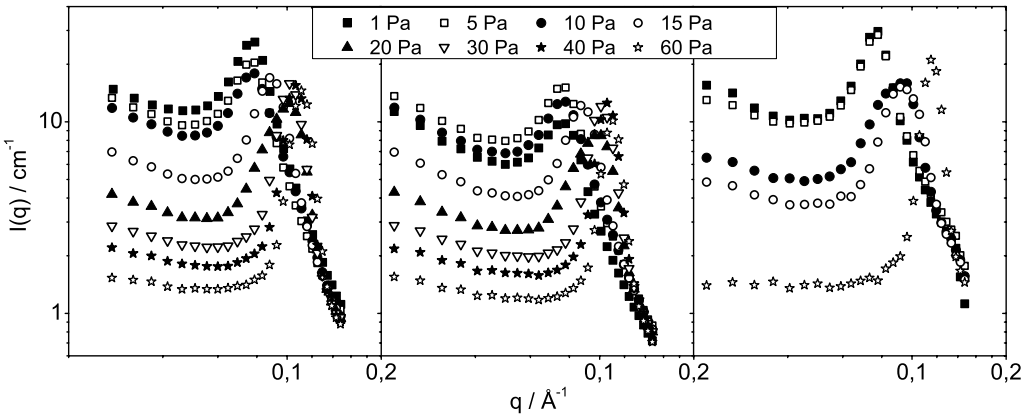

Figure 7.2: Radial SANS intensity distributions of $C_{12}E_4$ with Laponite RD along the neutral (left), flow (middle) and gradient directions (right) as a function of stress.

1. The first being the change of projected bilayer area owing to a suppression of thermal undulations as it was discussed in the introduction.[82] This effect is normally of the order of a few percent.

2. Another scenario would be a thinning of the bilayer, leading to an increase of the bilayer area concomitant with a considerable decrease of the Caillé-parameter as discussed by Castro-Roman et al.[113] This mechanisms could very well lead to the observed magnitude of change in lamellar spacing, however, it requires a component which attached to the membrane such as an amphiphilic block copolymer exerting a strain on the bilayer.

3. Furthermore, one could imagine a perforation of the bilayer[113], which would lead to a decrease of the bilayer separation without decreasing its thickness δ.

4. Finally, a phase separation into a clay rich and a surfactant rich phase would lead to a decrease in bilayer separation in the lamellar domains while the bilayer thickness should stay constant. The change of d depends on the amount of water expelled from the lamellar domains.

Considering, that the clay probably resides in the water regions, the last scenario is most likely. A thorough discrimination of the different scenarios, however, is only possible if data at higher q yielding more detailed information about the bilayer thickness, were available. Owing to the design of the shear cell, the maximum q available in rheo-SANS experiments at D11 is 0.17Å^{-1}, which is not sufficient to determine the membrane thickness.

With the premises of a constant bilayer thickness, the change in d leads to a change of the volume of the lamellar domains of about 35%. Thus, 35% of the water has to be expelled from the inter bilayer space. Also width and height of the Bragg-peak itself change due to a better correlation of layers. This is partially due to the decrease in d, but other contributions play a role as well as will be shown later on.

The SANS data were further analyzed by fitting the data to a structure factor model for lamellar phases proposed by Nallet et al.[68], where the intensity is given by a resolution limited structure factor $\tilde{S}(q)$ and the form factor $P(q)$ of a lamellar sheet according to:

$$I(q) = 2\pi \frac{V}{d} \frac{P(q)\tilde{S}(q)}{q^2} \tag{7.1}$$

where the form factor is given by:

$$P(q) = 2\frac{\Delta\rho}{q^2}\left[1 - \cos(q\delta)\exp\left(\frac{-q^2\sigma^2}{2}\right)\right] \tag{7.2}$$

with σ the width of the Gaussian excess scattering length density profile of the lamellar sheet. The structure factor reads:

$$\begin{aligned}\tilde{S}(q) = 1 + 2\sum_{n=1}^{N-1}\left(1 - \tfrac{n}{N}\right) cos\left(\tfrac{qdn}{1+2\Delta q^2 d^2 \alpha(n)}\right) \\ \times \exp\left(-\tfrac{2q^2d^2\alpha(n)+\Delta q^2 d^2 n^2}{2(1+2\Delta q^2 d^2\alpha(n))}\right)\tfrac{1}{\sqrt{1+2\Delta q^2 d^2\alpha(n)}}\end{aligned} \tag{7.3}$$

It includes the correlation function $\alpha(n) = \eta_{caille}/(2\pi^2)\,[ln(\pi n) + \epsilon]$, where η is the Caillé-parameter and ϵ Euler's constant. The Caillé-Parameter, that enters the expression for the structure factor of a lamellar phase, is defined as:

$$\eta_{caille} = \frac{q_0^2 \cdot k_B T}{8\pi\sqrt{\bar{B}\kappa/d}} \tag{7.4}$$

Here, κ and $\bar{B}$ are the the bilayer bending and the osmotic compression modulus, respectively. Instrumental resolution was taken into account by the appropriate uncertainty in q, according to:

$$\Delta q^2 = q^2\left[\left(\frac{1}{2\sqrt{2ln(2)}}\frac{\Delta\lambda}{\lambda}\right)^2\right] + \left[\left(\frac{4\pi}{\lambda}\right)^2 - q^2\right]\Delta\theta^2 \tag{7.5}$$

The wavelength spread $\Delta\lambda/\lambda$ is 10% at D11 and the uncertainty of θ, which arises from the finite collimation of the neutron beam, was determined by taking the fwhm of a Gaussian function fitted to an empty beam measurement performed with the same instrument configuration as the experiments ($\Delta\theta = 0.246°$). The number of layers N used for the calculation of the structure factor, does not influence the width of the Bragg-peak as long as $N\Delta q/q_0 \gg 1$. The Bragg-peak for the highest stress is found at 0.12Å and thus N=20 was used for all stresses. The lamellar spacing d was taken from q_0 and total bilayer thickness can be calculated from the position of the first order Bragg-peak and the volume fraction of surfactant ($\Phi_s = 0.365$) to $\delta = 30.2$Å. The hydrophobic bilayer thickness is smaller and was determined in the first fit (data of 2Pa) to $\delta_t = 23.2$Å and thereafter kept constant. The width of the excess scattering length density profile σ introduced in the form factor[68] was kept constant at $\delta_t/4$. In principle these two quantities, σ and δ_t, could be used as free fit parameters if high q data were available and the relevant features of the form factor (intensity maximum in a $I(q)q^4$ representation) were not obscured by the structure factor.[70]

This model requires isotropic scattering data, which were not available in this study owing to residual planar surfactant bilayers in perpendicular orientation. However, the scattering in flow direction can only originate from bilayers that are incorporated in MLVs, and therefore this was taken as the isotropic contribution to the spectra. The resulting fits are shown in figure 7.3 together with the radial sector averages of the intensity distribution. The quality of the fits is comparable to that found in the literature for different systems.[29,32,68,114] As one can see, very good agreement between data and fit is obtained at stresses below 20Pa. It more or less fails at 20Pa, a circumstance that will be discussed later. Fairly good agreement is reached at the higher stresses again. At the highest stresses, however, the fit seems to underestimate the intensity at high q. This can either be due to a decrease in bilayer thickness and thus shifting the form factor minimum to higher q or an increasingly sharp interface, which would lead to a slower decay of the intensity in this region.[86] But as pointed out above, the data presented here do not allow conclusions about this issue.

The results can nevertheless be discussed in terms of the bilayer bending and osmotic compression modulus, which can be calculated from the Caillé-parameter:

$$\bar{B}\kappa = \frac{q_0^3 \cdot (k_b T)^2}{32\pi\eta_{caille}^2} \tag{7.6}$$

The results for d and $\kappa \cdot \bar{B}$ are summarized in figure 7.4. The values for d and η_{caille} at low

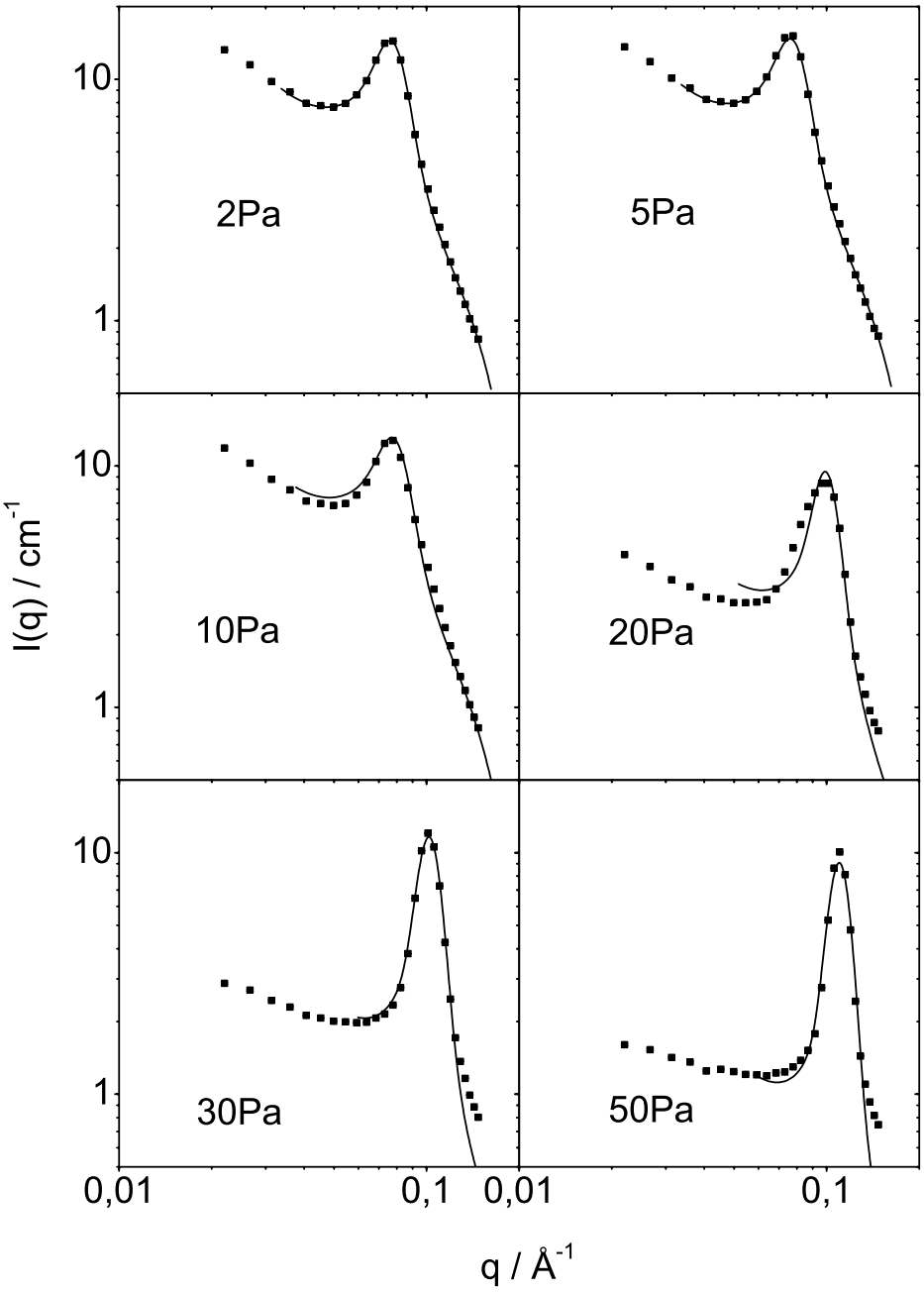

Figure 7.3: Comparison of the Nallet-fits and the intensity distributions in flow direction for different stresses.

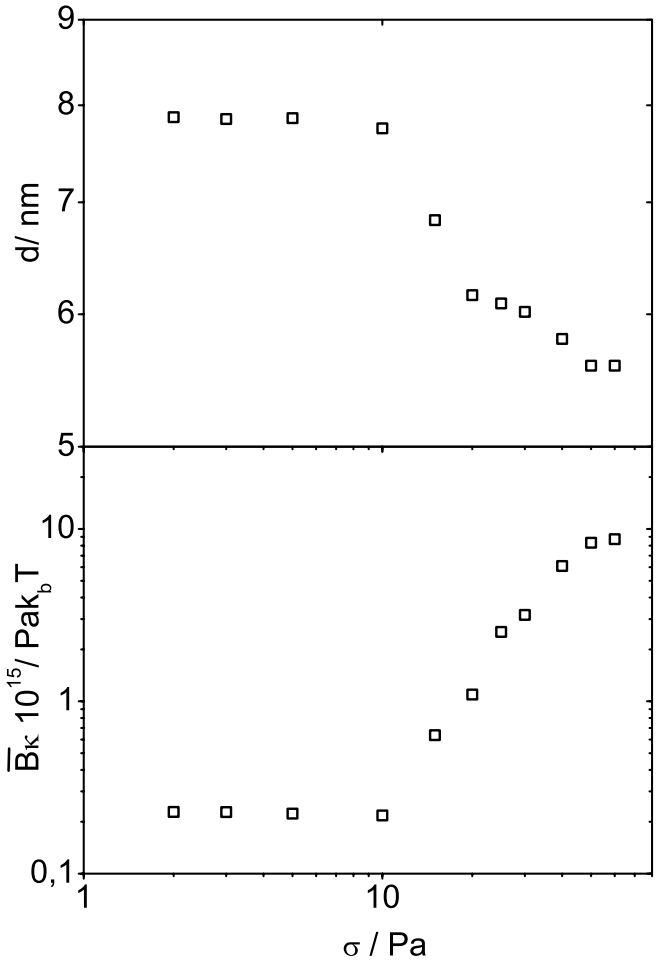

Figure 7.4: Lamellar spacing d (top) and $\kappa \cdot \bar{B}$ (bottom) as a function of stress.

stress agree well with the ones found by Grillo and co-workers[38] and stay constant at $\sigma \leq 10Pa$. However, lamellar spacing decreased and $\kappa \cdot \bar{B}$ increased (η_{caille} decreased), as soon as the shear thickening regime was entered, i.e., when MLV-formation started.

The change in the lamellar spacing observed here is qualitatively different from the change observed by Yamamoto and Tanaka.[82] They observed a linear relationship between the relative change in repeat distance and stress over the whole applied stress range. Furthermore, the change they observed is much smaller compared to the one observed in this study. Most important, the d-change in our study is only observed at $\sigma \geq 10Pa$, coinciding with the beginning of

shear thickening and hence with MLV-formation. In other words the change in d is somehow a consequence of MLV-formation. Conversely, MLV-formation itself does not seem to be induced by the presence of clay, since it is observed in the corresponding pure system at about the same stress. Another strong indication for a morphology induced phase separation is, that the position of the first order Bragg-peak does not relax back to its initial position after the cessation of flow.

Since κ and $\bar{B}$ cannot be determined independently, the product is presented. One can, however, assume that κ stays unchanged (literature values for κ in lamellar phases range from 1 to 4 k_BT) or decreases only slightly owing to the suppression of the lamellar undulations. Consequently, the increase of $\kappa \cdot \bar{B}$ has to be mainly due to an increase in $\bar{B}$. Similarly, Yamamoto and Tanaka[82] discuss the influence of the stress on $\bar{B}$ and κ. However, they find η unchanged and argue on grounds of the peak shape analysis, that $\bar{B}$ decreases and κ increases. This leads us to conclude, that the observed effect of stress on the lamellar phase with clay particles is essentially different from a mere suppression of bilayer undulation. The latter would also not be able to explain the drastic changes in the quantities (d and $\kappa \cdot \bar{B}$), that were observed here.

If one takes a closer look at the intensity profiles of 10, 20 and 30Pa as they evolve with time, i.e., in the shear thickening and the beginning of the shear thinning regime, one observes a transition region from 10 to 20Pa, where two lamellar Bragg-peaks coexist (figure 7.5). The Bragg-peak at 10Pa after 30s is still sharp and occurs at 0.08Å^{-1}, the position at which it also occurs at the lower stresses. After having sheared the sample with 10Pa for 5000s, a shoulder at 0.1Å^{-1} evolves. This shoulder becomes the main Bragg-peak at 20Pa, revealing the change of relative fractions of coexisting phases. At 30Pa the transition is over, the Bragg-peak position does not change with time, and more importantly no coexisting Bragg-peaks are observed. Thus, there is a single lamellar phase with a lamellar spacing of 60Å. The coexistence of two lamellar phases is the reason why the Nallet-fits do not yield very reliable results in this stress range between 10 and 20Pa.

As outlined above the clay containing system shows a few intriguing features if compared to the binary $C_{12}E_4/D_2O$ system. First, the shear thinning behavior is less pronounced as compared to the binary system.[16] Also the radii show a different stress dependence, however, it is stronger than commonly observed. Commonly, the dependence of MLV-radius on stress is explained by a stripping off of MLV-shells. The general scaling of MLV-size with stress can be explained by

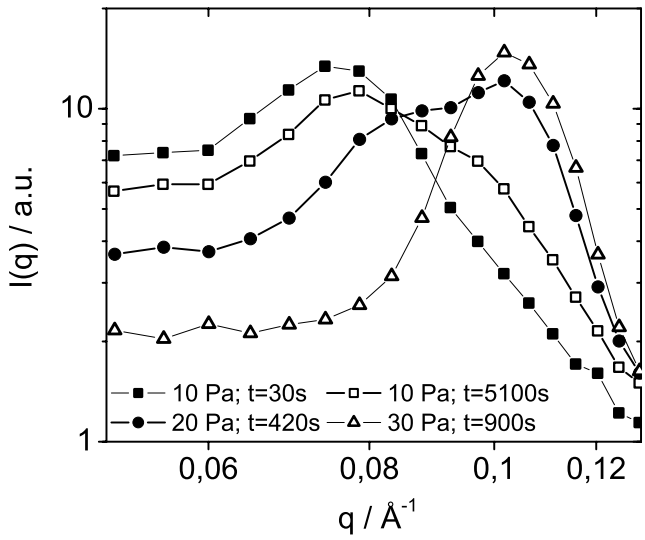

Figure 7.5: Intensity profiles of shear experiments at 10, 20 and 30Pa at certain times during the time resolved experiment.

a balance of the surface tension of a droplet and the bulk stress.[39] In the case presented here, the stress dependence of MLV-size is, however, stronger than what is commonly observed. The decrease in bilayer separation above a stress of 10Pa in fact is an additional contribution to the MLV-size and consequently a stronger stress dependence results.

A closer look at figure 7.4 reveals, that there are two regions where d shows different dependencies on σ. These correspond to the shear thickening and shear thinning regions. The strongest change in d is observed in the shear thickening region, but the change in the shear thinning region is still remarkable. The decrease of d in this region thus might explain the stronger stress dependence of the MLV-radius.

7.3.2 Laponite Contrast

In this section the results from scattering experiments of the lamellar phase with laponite contrast under shear are presented. Figure 7.6 shows I($\mathbf{q}$) vs $\mathbf{q}$ on an absolute scale, where the incoherent background and the contribution of imperfectly matched lamellae was substracted. All 2-dimensional scattering patterns are isotropic in the velocity-neutral plane, even at the

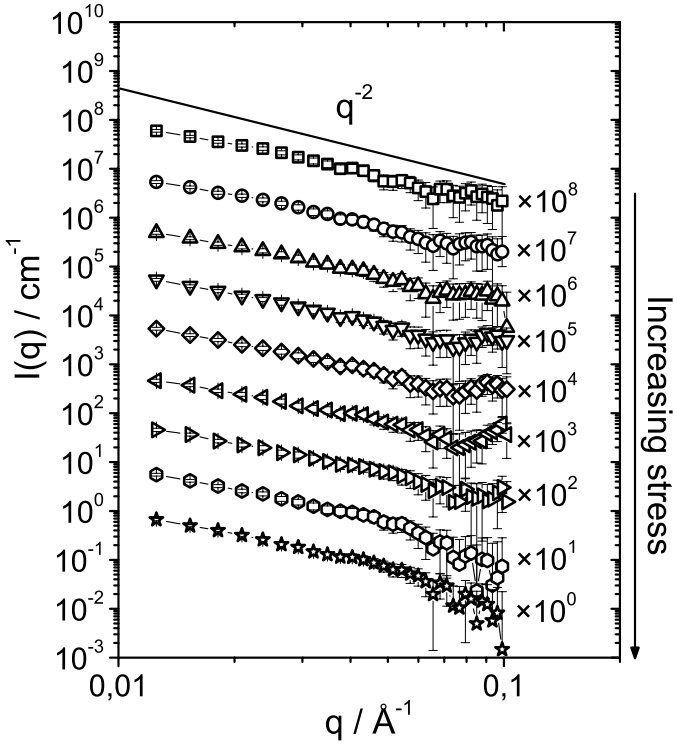

Figure 7.6: Scattering of the sample with laponite contrast at shear stresses of 1 (top), 3, 5, 10, 15, 20, 30, 50 and 60Pa (bottom).

highest stress applied to the sample. The radial intensity profiles (figure 7.6) are almost independent of shear stress. For isotropically oriented platelets of 150Å radius and 10Å thickness one would expect a slope of $\mathbf{q^{-2}}$ in the q-range of interest. The slope of the data is, however, $\mathbf{q^{-1.5}}$, which can in principle result from different weights of the platelet orientations in the orientational average.

Additionally the radial intensity distributions display subtle minima in the intermediate q-range, which are more pronounced at lower stresses. As a function of stress, slight variations of the intensity distribution, i.e., the slope and also of the subtle intensity oscillations in the range of $0.3 \leq q \leq 0.8 \text{Å}^{-1}$, can be observed, but these variations do not seem to be systematic with stress. These observations suggest, that the orientation distribution is not isotropic in the velocity gradient-neutral plane, while it is in the velocity-neutral plane. Consequently, this anisotropy would only be visible in the tangential beam experiment, which, owing to the high incoherent

background of the sample, was not a feasible one. Nevertheless, the slope of the radial intensity distribution from radial beam experiments is sensitive to these changes of the orientation distribution and thus orientations of the platelets in the velocity-neutral plane are favored under shear.

The intensity increase at $q \geq 0.7\text{Å}^{-1}$, observed for intermediate stresses, might be due to imperfections in the matching. This is an intrinsic problem of contrast matching a surfactant bilayer, since the headgroups have a different scattering length density than the hydrophobic tails of the surfactant. Therefore, SANS-experiments with a pure lamellar phase of the same surfactant volume fraction in a 0.9 (w/w) mixture of H_2O/D_2O were performed at rest to accurately determine this contribution. The situation is more complex, since the position of the lamellar Bragg-peak in the samples containing laponite depends on the applied stress.

However, the contributions to the scattering from the imperfect matching were found not to be as drastic as expected from model calculations.[68] It only yielded to a background contribution which in the relevant q-range had a positive slope. Moreover, the problem of over subtracting the incoherent background is delicate. Since the contribution of the imperfectly matched lamellae was measured at rest, no data for the higher stresses, where the position of the first order Bragg-peak might change, are available. Thus the scattering at rest was taken as the background contribution for all laponite scattering profiles under shear.

Modeling of clay spectra is helpful for elucidating the orientation distribution of the laponite particles under shear. This was done by using the form factor of isotropically oriented platelets (see equation 7.7).[38]

$$P_p(q) = (F_p(q))^2 = \int_0^{\pi/2} \left(\frac{sin\,(q\epsilon cos\alpha)}{q\epsilon cos\alpha} \frac{2J_1\,(qRsin\alpha)}{qRsin\alpha} \right)^2 \sin\alpha d\alpha \tag{7.7}$$

Here, ϵ is the thickness and R the radius of the platelets, whereas α denotes the angle between the normal on the basal plane of the platelet $\mathbf{n}$ and the scattering vector $\mathbf{q}$ (figure 7.7). $J_1(x)$ is the first order Bessel function. A selection of different intensity profiles, obtained from performing the orientational average over a limited range of orientation angles α, is shown in figures 7.8. The limitation of the orientation angle α is done in the velocity gradient-neutral plane, since $\mathbf{q}$ is defined from azimuthal averaging of the scattering vector in the velocity-neutral plane. Prerequisite is, that the 2-dimensional scattering data itself is isotropic.

The figures display, how limiting the platelet orientation angle α affects the scattering function and in particular the slope in the intermediate $\mathbf{q}$-range. As shown in figure 7.8a, suppressing

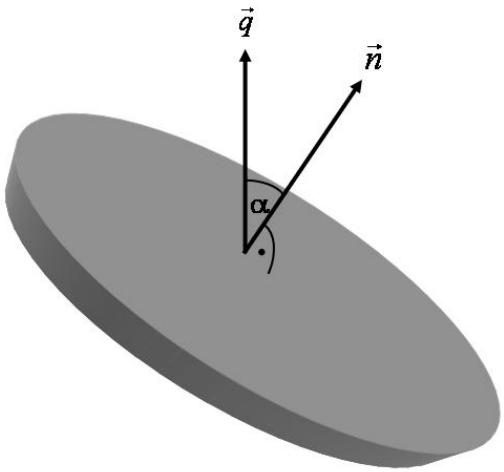

Figure 7.7: Definition of the orientation angle α with respect to the scattering vector $\vec{q}$ and $\vec{n}$ the normal on the basal plane of the platelet.

orientations with a large orientation angle α, corresponding to orientations where the platelet is oriented parallel to the walls of the shear cell, leads to a drastic decrease in the slope in the intermediate **q**-range. At high scattering vectors the minimum corresponding to the platelet thickness is observed. In the **q**-range, where also the measurements were performed, slight oscillations of the intensity are observed. Omitting small orientation angles (figure 7.8 b), the minimum at high **q** quickly vanishes, but strong oscillations, corresponding to the radius of the platelet, occur. However, the slope of the envelope increases beyond q^{-2}.

A full analysis of the data in terms of the platelets scattering is, however, hampered by several shortcomings of the data. The most obvious one is the limited q-range. The low-q and the high-q regions are especially sensitive to a change in the orientation distribution of the platelets. As can be seen in figure 7.8 the minimum of the orientationally averaged form factor for a platelet with 10Å thickness is expected at $q = \pi/\epsilon \approx 0.314\text{Å}^{-1}$. Despite the sensitivity of this region to changes in the orientation distribution, high-q measurements were discarded. The window in the cooling jacket of the Searle shear cell limits the scattering angle θ to below 8°and thus to a maximum accessible **q** of 0.2Å^{-1}. The low q-region, where the plateau in the scattering intensity of a platelets with a radius of approximatly 150Åcan be expected, would have been a time costly experiment with very poor counting statistics.

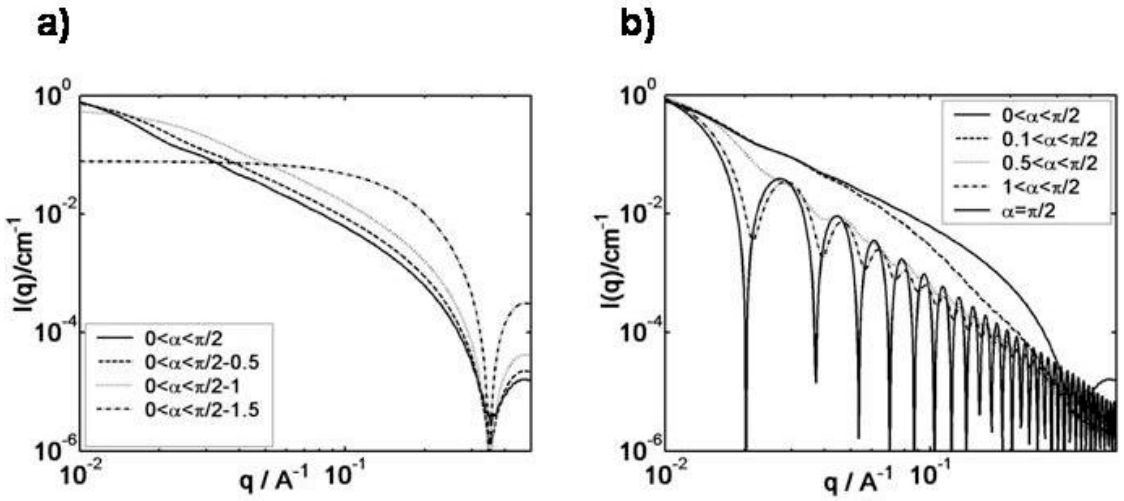

Figure 7.8: Different orientation averages of a platelet form factor. a) The integration is performed from zero to $\pi/2$ and smaller values, corresponding to suppressing platelets where the normal on the basal plane and the gradient direction enclose angles smaller than $\pi/2$. b) The integration is performed from values between zero and $\pi/2$ to $\pi/2$. This corresponds to suppressing the orientations where the platelet normal and the flow direction enclose angles smaller than $\pi/2$.

Less obvious, but equally important, are the uncertainties in the determination of the sample inherent incoherent background. In the multi component system the background originates from the H_2O/D_2O mixture used as solvent, the surfactant and the clay itself. The main contribution to the incoherent background comes from the solvent and the surfactant owing to their high hydrogen content and their relatively high concentrations. These contributions were determined experimentally in a regular scattering cell, in order to get to the high-q where the incoherent background dominates the sccattering, i.e., without shear. An error in the background transmission of typically 5% leads to a very large error. Furthermore, the contribution of unperfecltly matched lamellae, as mentioned before, is difficult to determine, especially if the position of the Bragg-peak might depend on stress. Unfortunately, only scattering data at rest of a matched lamellar phase was available.

Most importantly, the incoherent background inherent to the clay scattering itself was not available. It was therefore estimated from the composition and concentration of the clay in solution. These experimental difficulties lead to large errors of the data and especially the slope

in the intermediate region will be affected by over- or underestimation the different background contributions. Furthermore, the low instrumental resolution inherent to a neutron scattering experiment masks the rather subtle features of the laponite scattering in the investigated q-range. Performing the integration in equation 7.7 with different boundaries, i.e., not over the full range of $0 \leq \alpha \leq \pi/2$, allows a first estimate of preferred orientations of the platelets in the shear field. This is a rather crude estimate, since assuming an orientation distribution would be the more rigorous approach. But the quality of the data is affected by the difficulties in correctly accounting for the different contributions to the background scattering, and thus a simple approach is sufficient. Apparently, platelets, where the platelet normal points along the gradient direction, are at least underrepresented under shear.

7.4 Discussion

The system under study is distinctively different from its pure binary counterpart. Although MLV-formation is observed in both systems as evidenced by depolarized rheo-SALS, the scaling of the viscosity and the MLV-radius with stress are different. A drastic change of the lamellar repeat distance is observed in the clay containing system, as soon as MLV-formation starts, i.e., in the shear thickening region. Apparently, the change in repeat distance is connected to the formation of MLVs. On the contrary, such a change of d upon MLV-formation was not observed in the pure system.

The possible reasons for such a change in the lamellar repeat distance d were already mentioned in the previous section. A thinning or a perforation of the bilayers seem unlikely, since the clay probably resides in the water regions of the lamellar phase and therefore is not able to exert a strain on the bilayer. However, a clear falsification of these mechanisms can not be made on the basis of the presented SANS-data. Data at higher q values would be necessary to obtain good information about the thickness and also the blurriness (σ) of the bilayer.

The suppression of undulations on the other hand is an effect that is normally much less pronounced and more importantly its stress dependence should be linear. Moreover, such small effects are difficult to be observed in concentrated lamellar phases. Additionally, a relaxation of the lamellar spacing to its quiescent state should take place as soon as shear is stopped, which was not observed in our case.

The situation is very similar to that observed by Ligoure et al.[112], who incorporated a water soluble polymer into a lamellar phase of ionic surfactant and then tuning the bilayer interactions by the addition of screening salt. The samples with low salinity (electrostatic stabilization) were homogeneous, whereas at high salt (Helfrich stabilization) phase separation occurred. The observation of two Bragg-peaks in the transition region was clear evidence for a phase separation. Here, the stabilization mechanism of the lamellar phase was not sufficient to overcome the energy penalty owing to the confinement of the polymer and consequently the sample separated into a polymer rich and a surfactant rich phase.

In the presented case, the energy penalty owing to the confinement of the clay platelets is artificially increased by creating curvature and it thus seems to be a matter of the sample's morphology. As a working hypothesis we suggest micro phase separation in order to explain the drastic change in d. The coexistence of two Bragg-peaks is observed in the transition regime from 10 to 20Pa, a strong indication for a micro phase separation. Excluded volume effects impose increasing restrictions on the stiff clay platelets as lamellae become more curved. As increasing lamellar spacing is not possible, areas with high curvature will deplete of laponite and clay rich areas evolve that drain water from the lamellar domains. Water drain decreases d leading to a smaller η_{caille}, which might further enhance the tendency of phase separation.

The most convenient places for the laponite particles, which had to leave the unfavorable sites in areas with high curvature, are the outer shells of the MLVs, which are less curved. Since increasing stress leads to a decrease in the number of shells per MLV, this scenario is less and less likely. Another site, where clay can gather are the focal conic defects of the lamellar phase with MLV-morphology. Once the clay concentration in these areas increases above the average clay concentration, the difference in osmotic pressure between clay rich and clay poor domains leads to a water drain from the lamellar region. The MLVs become more spherical and their lamellar spacing further decreases as it is depicted in figure 7.9.

This exclusion of clay platelets from the lamellar domains should only be possible as long as the bilayers are not closed, i.e., early during the transition from planar lamellae (polydomain at low stress) to MLVs. During this transition from planar lamellae to MLVs an intermediate structure with cylindrical symmetry was observed earlier.[23,24,107] During this state an extrusion of the clay platelets is still reasonable, while it is unlikely to occur during a later state of the experiment, when MLVs are already formed. The only event where clay could be released from

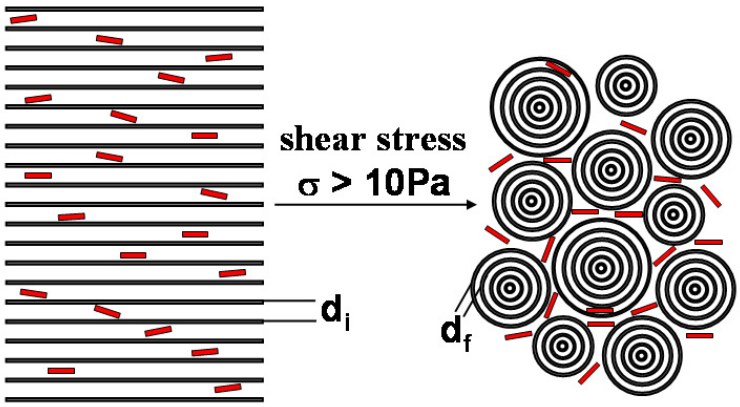

Figure 7.9: Sketch of the proposed shear induced phase separation with d_i and d_f the initial and final repeat distance, respectively. Please, note that the right hand side is not really to scale, since the typical MLV-radius is several μm and thus a vesicles contains several hundred bilayers.

a MLV is when a shell is being stripped off.

Using the interpretation of a micro phase separation one can calculate the water which is expelled from the lamellar domains from the change in d. It follows that about 35% of the water is expelled from the lamellar domains. This volume change agrees well with the volume that the interstitial space occupies in a random closed packing of undeformed MLVs, namely 36% of the total volume. A structure factor that is observed at higher stresses in depolarized SALS supports the assumption of closely packed MLVs (see supporting information).

Conclusively, one might state, that micro phase separation occurs as a consequence of MLV formation and renders the MLVs more spherical.[37] Thus interstitial space filled with water and clay platelets is created. This resembles the structure of an alloy as described by Arrault et al.[37] with spherical dopant particles.

The results indicate that micro phase separation caused by MLV formation leading to a water drain and thus to a decrease in d is the mechanism for the unusual behavior of a lamellar phase doped with clay platelets under shear. The coincidence of the change in d and the onset of MLV-formation is a strong indication for a morphology driven transition. Thus the underly-

ing mechanism for the change in d is completely different to that discussed by Yamamoto and Tanaka.[82] As mentioned above, if the change of repeat distance was due to the suppression of bilayer undulations, a relaxation back to the quiescent state should be observable upon cessation of flow, which was not the case in our study.

In contrary, it displays similarities to the model of Ramaswamy[115], who argues that a phase separation occurs in Helfrich stabilized systems in the presence of weak attractive forces. Such attractive forces could be differences in osmotic pressure in clay rich and clay poor areas. However, in his model a critical shear rate has to be exceeded to lead to a collapse of the lamellar phase. This shear rate is rather high and was not reached in our studies. Furthermore, the decrease of layer spacing is coupled to the increase in viscosity, i.e., MLV formation, which in general is thought to be controlled by stress.[10]

The observation of a coexistence of two lamellar phases with different membrane separations in the transition regime from 10 to 20Pa is a further strong indication for a micro phase separation, where the lamellar domains with the smaller d-spacing are depleted of clay platelets. Additionally, the decrease in d-spacing itself might accelerate the extrusion of the laponite from the lamellar phase, since the insertion limit of clay particles might be exceeded.[38] This became even more obvious for a sample with higher surfactant concentration. The sample with 40wt% surfactant and S/L=0.5% turned turbid and eventually seperated macroscopically, when it was subjected to a stress of 50Pa (data not shown here, see supporting information). This sample is closer to the inversion point of the insertion limit[38], so that a decrease in layer spacing and thus local increase in surfactant volume fraction, leads to the stronger tendency to phase separation.

7.5 Conclusions

In summary, the presented study on the influence of clay platelets incorporated into a lyotropic lamellar phase on its behavior under shear revealed a few new aspects. The formation of MLVs is observed concomitant with shear thickening, as it is the case for the corresponding pure binary system. The shear thinning behavior at higher stress, however, is weaker. Furthermore, the dependence of MLV-radius on stress in this region is more pronounced as that of the pure system.

Rheo-SANS experiments revealed a drastic change in the lamellar repeat distance d along with a

change of the properties of the lamellar phase characterized by the product of the bilayer bending and the osmotic compression modulus κ and $\bar{B}$, respectively. The change is only observed above a stress of 10Pa and once this change took place a relaxation to the quiescent state was not observable. Thus, the observed decrease of d is qualitatively different from the change that is due to the suppression of thermal bilayer undulations. The observations from rheo-SALS and SANS led us to conclude, that the presence of clay, in contrast to the clay free lamellar phase, leads to a micro phase separation as soon as MLVs are formed.

Clay platelets do not noticeably change the membrane properties and interactions at rest, e.g., no change of the Caill*é*-parameter and no change of dynamics of lamellar undulations[119] is noticeable, yet a significant difference between the pure binary and the clay containing nonionic lamellar phase was observed under shear.

The following scenario is proposed: Applying a shear field leads in both cases, namely in the pure binary and in the clay containing lamellar phase to MLV-formation. In the presence of laponite, a conflict arises between the stiff clay platelets and curved lamellae as they are present in MLVs. Especially in the MLV cores the curvature is too high to accommodate the clay platelets, which consequently leave those areas. They may reside in the outer shells of the MLVs, which are essentially flat or in the focal conic defects of the MLV-phase. There the osmotic pressure difference between clay rich and surfactant rich domains leads to a water drain, which manifests in the drastic decrease of d.

7.5.1 Acknowledgements

We thank the "Deutsche Forschungs Gemeinschaft" for financial support and S. Egelhaaf for useful discussions.

Supporting Information Available: Intensity profiles of the 40wt% $C_{12}E_4$ sample in H_2O/D_2O (0.327 w/w) with a laponite content of S/L=0.5% at three different shear stresses in the radial beam, i.e. in flow and in the velocity direction and depolarized rheo-SALS images for the 33wt% sample with a laponite content of S/L=0.39% for different stresses are available free of charge via the Internet at http://pubs.acs.org.

8 Shear-Induced Sponge–to–Lamellar Phase Transition studied by Rheo-birefringence

8.1 Introduction

Lyotropic surfactant systems display a rich phase behavior. Phase diagrams of nonionic surfactants, as for instance of the C_nE_m-type, where n is the number of carbons in the hydrocarbon chain and m the number of ethylene oxide units in the headgroup of the surfactant, display a large temperature and concentration range, with micellar aggregates organized as bilayers. These themselves can arrange in stacks (L_α-phase) or divide the sample volume into two bicontinuous, interpenetrating subvolumes (L_3- or sponge-phase).

Of particular interest is the behavior of these phases under shear, since detailed knowledge of the influence of shear is relevant for industrial applications.[2,76] The L_3-phase itself is known to be flow birefringent and small-angle neutron scattering (SANS) experiments revealed, that a transition from the sponge-phase to a shear aligned lamellar phase takes place above a critical shear rate $\dot{\gamma}_c$, that strongly depends on membrane volume fraction.[51]

Such a transition from an isotropic to the L_α-phase was discussed on theoretical grounds by Cates and Milner.[120] They found the following relation of the critical shear rate with membrane volume fraction Φ_m,

$$\dot{\gamma}_c \propto \frac{k_b T}{\eta_s \xi^3} \propto \frac{k_b T}{\eta_s} \left(\frac{\Phi_m}{\delta} \right)^3 \tag{8.1}$$

where k_b is the Boltzmann's constant, ξ the correlation length of the L_3-phase, η_s the solvent viscosity and δ the thickness of the bilayer. Furthermore, they predicted that the critical temperature (L_3 to L_3+L_α) and spinodal should have different shear rate dependencies leading to an increasingly narrow two-phase region and consequently to a weakening of the first order character of the transition.

A different behavior of the L_3-phase under shear was predicted by Bruinsma and Rabin.[121]

Based on the Reynolds effect, an enhancement of concentration fluctuations is found, which stabilizes the L_3- over the L_α-phase.

More recently, Porte et al.[98,122,123] studied the shear induced isotropic to nematic transition in wormlike micellar systems in rate controlled experiments and concluded, that it displays all the characteristics of a first order phase transition. The transition involves shear bands in the two-phase region accompanied by a stress plateau. Within the framework of a first order transition it was possible to scale the rheological data of different concentrations and temperatures onto a mastercurve using reduced variables $\dot{\gamma}^* = \dot{\gamma}\tau_r$ and $\sigma^* = \sigma/G_0$. Here τ_r is the terminal relaxation time of a Maxwell fluid and G_0 its plateau modulus. Such a behavior can also be assumed for the L_3-phase, although there are some fundamental differences between the L_3-phase and wormlike micellar systems, as for instance the L_3-phase in contrast to wormy micelles (above the overlap concentration c*) is not viscoelastic.[124]

In order to investigate the underlying mechanisms more closely, a variety of L_3-phase systems was studied on length scales of the order of ξ, commonly using SANS and SAXS.[51,86,125–130] Larger length scales were studied by dynamic light scattering (DLS), where the collective diffusion can be measured.[51,93,131] Temperature jump (T-jump) experiments were conducted by Le et al.[93,131] and Schwarz et al.[132] to study the relaxation from a disturbed state back to equilibrium. All these studies aimed at correlating the dynamics of the system, i.e. membrane strangling, passage fission and membrane fusion, to the observed transition under shear.

A systematic study in this respect was performed by Porcar et al. who used rheo-small-angle neutron scattering to investigate the structural changes in situ. Moreover, they used different membrane volume fractions and controlled the dynamics of the system by adding sugar to the L_3-phase. Thus the solvent viscosity of the "sweetened" sponge phase, which also enters equation 1, was varied over more than a decade. They found a scaling of the normalized sample viscosities (η/η_0 where η_0 is the solvent viscosity) as well as the anisotropy parameters from radial and tangential beam SANS-experiments with $\dot{\gamma}\eta_s/\Phi_m^3$, in very nice agreement with the predictions from theory.[128]

Different experiments, however, probe different relaxation processes, and therefore different Φ_m-dependences are found in the literature. Le et al. for instance found that the relaxation of a perturbation by temperature-jump in case of the $C_{12}E_5$/decane/water system displayed a very strong Φ_m-dependence (if fitted to a powerlaw an exponent of -11 resulted).[93,131] They

concluded, that the relaxation is dominated by topology changes. However, this strong concentration dependence of the topological relaxation at low Φ_m can only be explained by a very high activation barrier of $350 k_b T$ attributed to the formation of passages by membrane fusion. This high activation barrier, however, is in disagreement with current theories.[120,133]

Yamamoto et al.[82] studied the shear rate dependence of the transition temperature to the shear aligned L_α-phase of a dilute $C_{12}E_5$/water-sample (c=1.8wt%) using small-angle light scattering under shear and found reasonable agreement with the respective predictions of Cates and Milner.

A flow-birefringence study was performed by Mahjoub et al.[125], who raised the question of the role of defects in the shear-induced transition for the L_3–to–lamellar transition. Additionally, they found a weaker Φ_m-dependence than Porcar et al., raising the question whether the viscosity entering equation 8.1 is that of the sample and not the solvent.

Here, we present data of a study using $C_{12}E_5$, decane and water at a fixed surfactant to oil ratio, varying the membrane volume fraction. The critical temperature and the transition to the aligned L_α-phase was recorded as a function of shear rate. In order to study the critical shear rate more closely isothermal shear ramps were performed. The relaxation kinetics were studied in shear quench experiments. The transitions from L_3 to L_3+L_α to L_α were tracked using birefringence and transmission measurements under shear.

8.2 Experiment

The sample under study consisted of the nonionic surfactant pentaethylene mono-dodecyl-ether ($C_{12}E_5$), n-decane and water. The decane to surfactant weight ratio was kept constant at 0.481:0.519 and only the water content was changed. Thus membrane thickness remained constant at 5nm,[131] while membrane volume fraction Φ_m was varied between 0.0388 and 0.31. Samples were prepared by diluting a stock solution of decane and $C_{12}E_5$ with water and mixing over night to assure equilibration.

Flow-birefringence experiments were performed in a stress controlled Bohlin CVO-R rheometer, equipped with a transparent plate-plate shear geometry. Birefringence and transmission were recorded by a commercially available optical analysis module (OAM) purchased from Rheometrics, which is mounted on the optical bench such that the laser passes the sample along the velocity gradient direction. A sample thickness of 0.2 mm was chosen for all experiments.

In a first series of experiments, the temperature was gradually increased at different constant shear rates. The temperature gradient was $dT/dt = 10K/h$. The L_3-phase was identified at rest and also at low shear rates as the isotropic state, i.e., its birefringence $\Delta n \approx 0$.
In a second set of experiments the influence of shear on the sponge phase was studied at constant temperature. For this purpose a shear ramp was applied to the sample at a temperature, which was, at rest, slightly above the upper L_3-phase boundary.
Finally, shear quench experiments were conducted, tracing the birefringence and transmission signal, to study the relaxation from the shear aligned back to the isotropic state.
Since the stability of the L_3-phase is very delicate with respect to composition and temperature, reversibility experiments were performed. The transition temperatures were checked in a temperature dependent experiment at a shear rate $10s^{-1}$ performing successive heating and cooling cycles using the same sample filling. One temperature ramp took about one hour. Water evaporation was suppressed by a solvent trap situated around the shear geometry covered with lids. The transition temperatures of the heating and cooling experiment were found to be very similar. Thus we assume, that selective evaporation of one component did not play a significant role during one experiment, which never took longer than two hours. For the following experiments samples were always freshly refilled. The problem of temperature gradients within the sample is also not of importance, since the sample thickness was 0.2mm in the plate–plate–geometry.

8.3 Results

The phase boundaries of the system at rest used in this study were examined beforehand in a temperature bath equipped with crossed polarizers in a temperature range from 25 to 50°C in order to localize the very narrow region of the L_3-phase. Figure 8.1 displays the phase diagram as it was obtained from the inspection in the temperature bath.
Figure 8.2 displays transmission and birefringence data in addition to transient viscosities for a sample with a membrane volume fraction of $\Phi_m = 0.155$ representative for the experimental procedure used in this study. The L_3-phase was identified as the isotropic region following the L_α-phase (which itself can be isotropic due to parallel (homeotropic) orientation of the lamellae). The critical shear rate is determined as the drop of birefringence and transmission upon increasing the shear rate. The plate–plate geometry used throughout the investigation implies that the shear field is inhomogeneous, i.e., the shear rate increases with the radius toward the

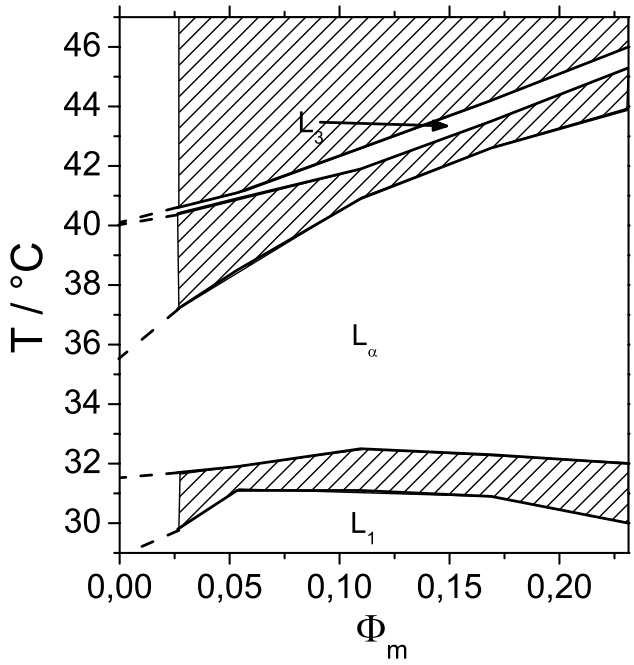

Figure 8.1: Phase boundaries between L_1-, L_α- and L_3-phase. Hatched areas display the two phase regions.

outside. Hence the viscosities are average values over the whole volume of the shear geometry. If a transition takes place at a given shear rate (and thus a given radius) the viscosities of that particular volume can be different from the rest of the sample.

Nevertheless, the use of the plate–plate geometry has certain advantages. First, sample loss at high temperatures is much less pronounced than in a cone–plate geometry. Second, the cone–plate geometry bears the problem of viscoelastic meniscus distortions[134] at high shear rates, which can impede the birefringence experiments. Third, the sample thickness can be varied in a plate–plate geometry, which can be advantageous for the birefringence experiment. Finally, a shear induced transition can be directly visualized as shown in figure 8.3. The nominal shear rate is determined at 3/4 of the radius of the shear geometry, the position at which also the laser for birefringence measurements passes the sample. Hence the birefringence corresponds to the shear rate selected in the control software.

In the following three sections we will present the results of the three different types of experi-

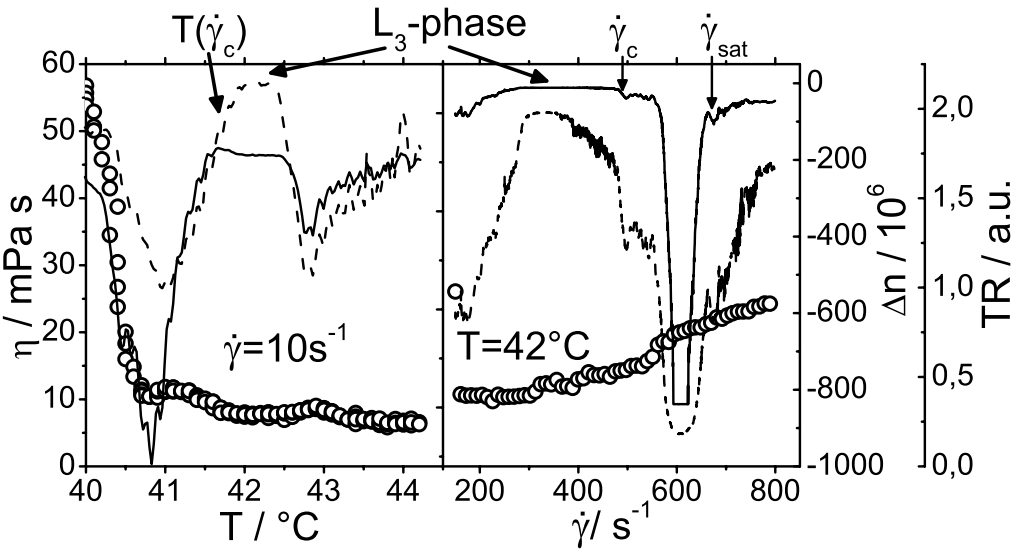

Figure 8.2: Transmission (dashed line), birefringence (solid line) and transient viscosities (open circles) in a temperature ramp experiment (left) and an isothermal shear ramp (right) for Φ_m= 0.155. T($\dot{\gamma}_c$), $\dot{\gamma}_c$ and $\dot{\gamma}_{sat}$ are the temperature for the transition (L_3+L_α) $\rightarrow$ L_3 under shear, the critical shear rate (onset of birefringence) and the saturation shear rate, respectively.

ments performed in this study following the outline given in the experimental part.

8.3.1 Temperature Dependent Experiments

In the temperature scan experiments a constant shear rate was applied, while the sample was heated starting from the L_α-phase as found in the phase diagram at rest. At low shear rates this was usually 39°C. The results of these temperature scan experiments are summarized in a phase diagram under shear for three different membrane volume fractions in figure 8.4. The lower and upper phase boundaries of the L_3-phase display a sudden shift to higher temperatures at a characteristic shear rate $\dot{\gamma}_c$. This shear rate shifts toward higher values as Φ_m increases. Additionally, the magnitude of the shift of the phase boundaries to higher temperature increases with concentration. Figure 8.5 displays the results of Φ_m=0.0775 along with the upper phase boundary of the L_α-phase, which seems to follow parallel to the lower L_3-phase boundary. The

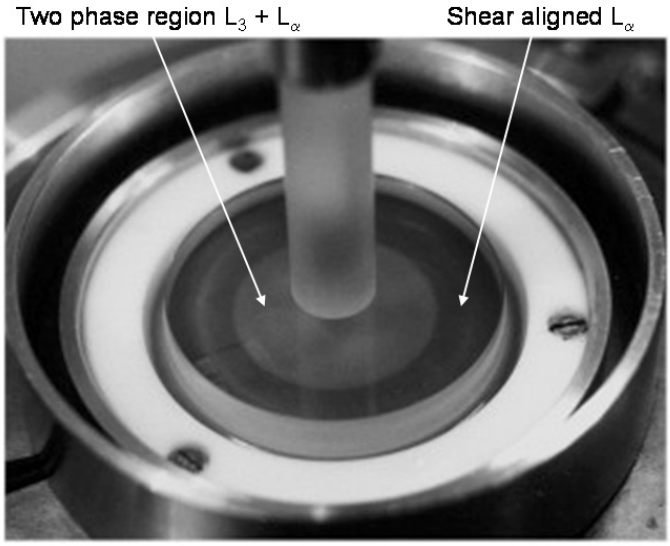

Figure 8.3: L_3-Phase under shear. Due to the inhomogeneous shear field in the plate–plate shear-geometry, the shear induced L_α-phase is visible at the outside, the two-phase region as a ring.

same behavior is found for the other samples. Thus there is always a two phase region separating the L_3-phase from the shear induced L_α-phase, an indication for the first-order nature of the transition. The data, however, do not allow any conclusion whether its first-order nature becomes weaker, as was predicted by Cates and Milner.[120]

8.3.2 Isothermal Experiments

The determination of the critical shear rate by the method used above bears the problem that it is not very accurate and these measurements thus only served as a means to map the phase region. The inaccuracy became most apparent when studying the lowest volume fraction Φ_m=0.0388. Owing to the low membrane volume fraction the signal in birefringence and the decrease in transmission were hardly detectable. Therefore, a correct determination of the critical shear rate was not possible in that case.

Isothermal measurements were performed with a wide range of volume fractions between Φ_m=0.058 and 0.31, where the shear rate was incrementally increased from $10s^{-1}$ well into the shear-induced L_α-phase. For volume fraction Φ_m=0.0388 the lowest shear rate was chosen to be $4s^{-1}$, since from the preliminary experiments $\dot{\gamma}_c$ could be estimated to be ca. $10s^{-1}$.

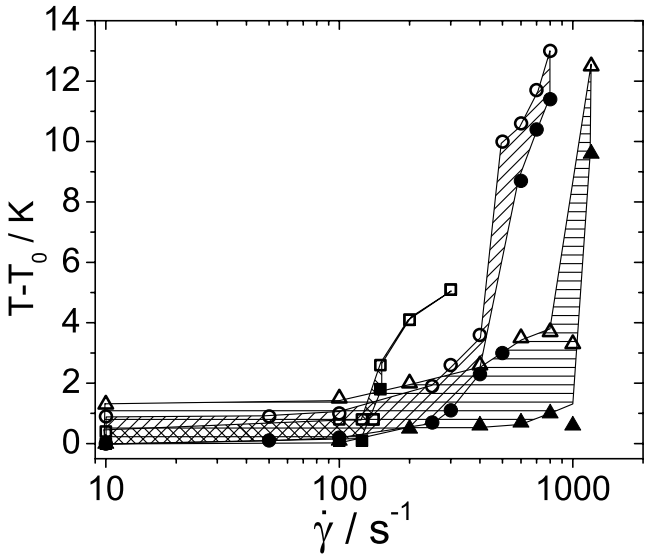

Figure 8.4: Transition temperatures from $(L_\alpha + L_3)$ to L_3 to $(L_3 + H_2O)$ at different shear rates and three different membrane volume fractions Φ_m=0.0775 (squares), 0.155 (circles), 0.2325 (triangles). Closed and open symbols depict the lower and upper L_3-phase boundaries, respectively.

In the isothermal experiments the critical shear rate was identified with the abrupt increase of the magnitude of birefringence accompanied with a decrease in transmission, thus with the transition from L_3 to the coexistence of L_3 and L_α (see figure 8.2). These shear rates are very similar to $\dot{\gamma}_c$ from the temperature scan experiments.

The critical shear rates determined for different volume fractions using this procedure are presented in figure 8.6. The critical shear rate displays a Φ_m-dependence with an exponent of 1.7. The transition to the pure shear-induced L_α-phase, however, displays Φ_m^2-dependence (see figure 8.6). These exponents are not in good agreement with equation 8.1. On the other hand, deviations from the expected behavior have been reported previously by Mahjoub et al.,[125] who also found an exponent smaller than 3. They argue, that the viscosity entering equation 8.1 is not the solvent but rather the sample viscosity, which itself can be Φ_m-dependent. Additionally, the exponent of approximately 2 found here for the critical shear rate happens to be similar to the scaling of the transition temperatures at rest.[131]

The two fits (solid and dashed lines) meet at lower volume fractions (at $\Phi_m \approx 0.03$), which

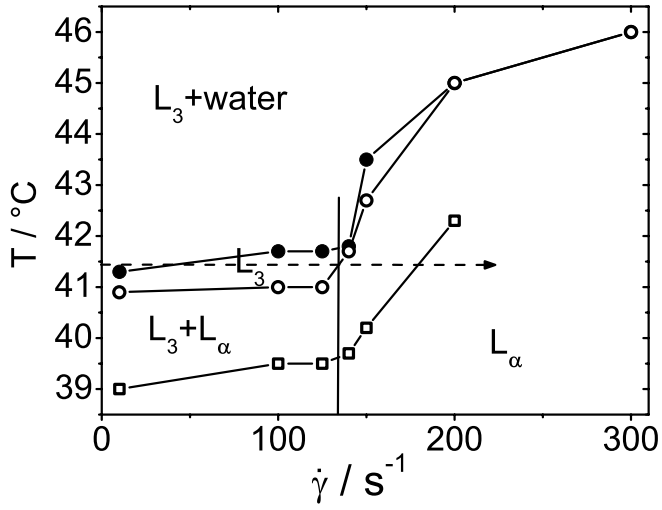

Figure 8.5: Transition temperatures at different shear rates and Φ_m=0.0775. The vertical lines mark the critical ($\dot{\gamma}_c$) and the saturation shear rate ($\dot{\gamma}_{sat}$), respectively. The horizontal arrow describes how an isothermal shear ramp experiment was performed.

might be an additional reason, why an accurate determination of $\dot{\gamma}_c$ was not possible at the lowest membrane volume fraction. The respective data point is therefore omitted from the presentation.

Again the existence of a two-phase region between L_3 and L_α (shear-induced) indicates the first-order nature of the transition. As mentioned earlier, the birefringence of the shear-induced L_α-phase is zero due to its parallel orientation in the shear field. The two-phase region in between L_α and L_3, aside from the increased turbidity, displays birefringence (figure 8.2). This can either be attributed to the presence of deformed droplets of L_α-phase that consequently display form birefringence or to a perpendicular orientation of lamellae in the shear field. The latter was already observed in similar systems and was predicted by theory as well.[121,135]

8.3.3 Shear Rate Quench

In a last set of experiments we studied the relaxation of the shear aligned L_α- back to the isotropic state by performing a shear quench using birefringence and transmission to trace the

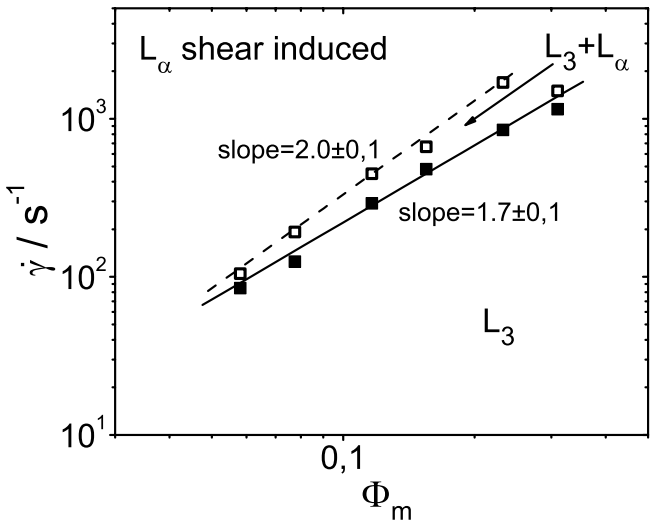

Figure 8.6: Shear rates for the transition to the two-phase region (critical shear rate $\dot{\gamma}_c$, solid squares) and to the fully shear-aligned L_α-phase (saturation shear rate $\dot{\gamma}_{sat}$, open squares) as a function of volume fraction Φ_m taken from the shear ramp experiment.

transition. The quench was performed from a shear rate about 30% higher than $\dot{\gamma}_c$ to 10s^{-1} and hence the relaxation in all cases started from the fully shear aligned state. Only for the lowest volume fraction the sample was quenched to 0.4s^{-1}.

Transmission and birefringence initially drop abruptly upon decreasing the shear rate to $10s^{-1}$. This might be due to a disturbance of the homeotropic alignment of bilayers upon stopping shear.

Eventually a fully isotropic distribution of bilayers will be reached and consequently the birefringence converges to zero. This relaxation of the signals seems to obey an exponential form (see figure 8.7). A time t=0 was defined at the minimum of the transmission and birefringence signals, respectively. Note that the nucleation of the L_3-phase is not considered by omitting the first part of the signal, since data evaluation starts in the two phase region and thus L_3-phase has already nucleated. The underlying process for the relaxation of birefringence and transmission might be the formation of handles.

The results of one relaxation experiment with a sample of Φ_m=0.1163 are shown in figure 8.7 along with best fits from an exponential (transmission) and a biexponential decay (birefringence).

The relaxation times τ_{slow} from transmission and birefringence are very similar, whereas τ_{fast}

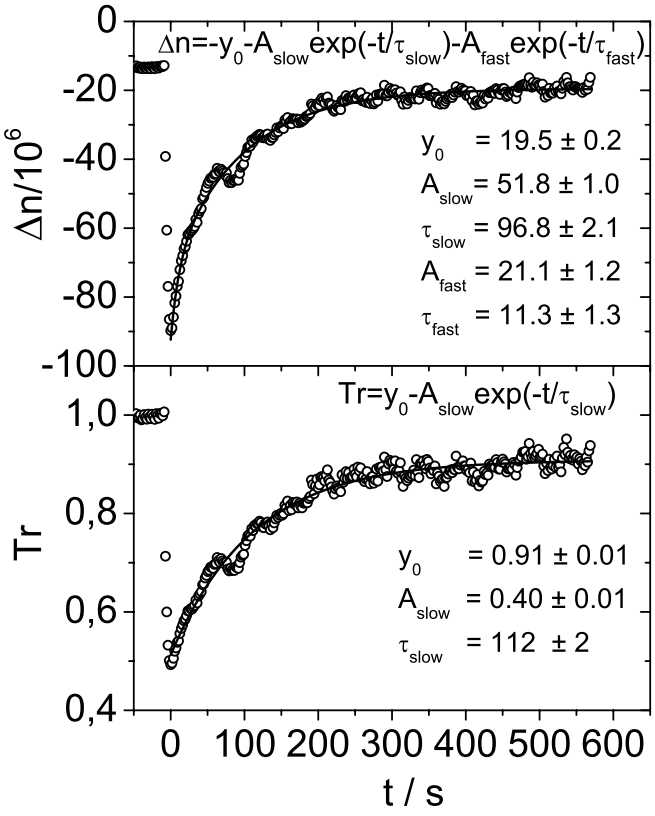

Figure 8.7: Measurement of the characteristic relaxation time studied by a shear rate quench from $\dot{\gamma} > \dot{\gamma}_c$ to $\dot{\gamma}=10s^{-1}$. Here Φ_m=0.1163 and T=42°C, and the quench was performed from $350s^{-1}$. Lines represent exponential and biexponential fits to the transmission and the birefringence, respectively.

from birefringence is about one order of magnitude smaller. The results for all volume fractions are summarized in figure 8.8 and compared with the inverse of the critical shear rate from shear ramp experiments, which should correspond to the topological relaxation time of the system. The inverse critical shear rate is neither identical to τ_{slow} nor to τ_{fast}. One reason is of experimental nature. The detection of relaxation times on the order of microseconds or milliseconds is impossible in a relaxation experiment as it was carried out here. This would, however, be necessary if one wanted to observe the relaxation of the bilayer fluctuations, which were suppressed by shear. It is nevertheless interesting that a relaxation is observed on longer time

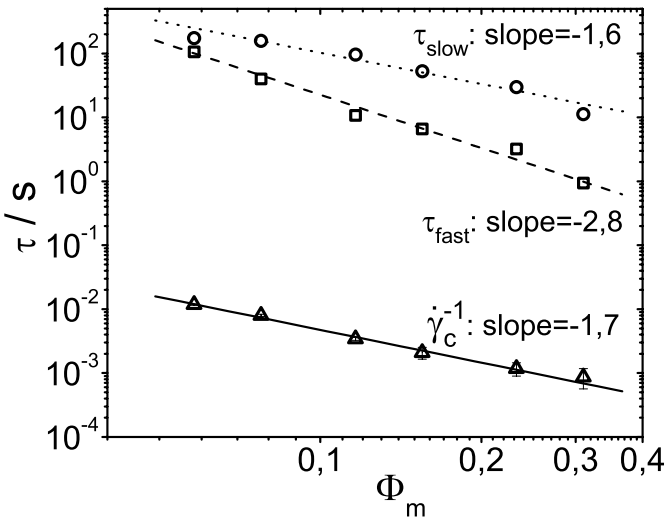

Figure 8.8: Comparison of the relaxation times obtained from the different experiments. τ_{slow} and τ_{fast} are the relaxation times obtained from fitting a biexponential function to the birefringence data of the relaxation experiment. The inverse of the critical shear rate obtained from shear ramp experiments is compared with the above mentioned relaxation times.

scales, which in addition has a similar scaling with membrane volume fraction. Thus the relaxation back to the isotropic state has a different time constant. Baring in mind that the shear alignment is a process in the presence of a field, whereas the relaxation to the isotropic state is almost field free, this asymmetry is not necessarily contradictory. On the other hand, processes on larger length scales, where domains of bilayer material rearrange might be involved, lead to different magnitudes of the relaxation times and inverse critical shear rates. Interestingly, at low membrane volume fractions the values found in T-jump experiments using the same system are of similar magnitude as the relaxation times observed in the shear quench experiments, they however display a different scaling behavior.[135]

Since the birefringence revealed two relaxation times, there have to be two processes involved. One mechanism might be a local process involving the formation of handles and the relaxation of the distorted lattice, which is a necessary consequence of the transition from a one to a three dimensional arrangement of bilayers. This is associated with a change of the lattice constant,

i.e., the correlation length ξ of the L_3-phase, which is about 1.5 times the lamellar spacing of the L_α-phase with the same membrane volume fraction. Thus an intermediate state could be a distorted L_3-phase, which relaxes to the fully isotropic L_3-phase. The other might be a shape relaxation of the initially deformed L_3-domains. Both contributions lead to a decrease in the birefringence signal. The fast relaxation most likely comprises the rearrangement of bilayer material and the relaxation of the distorted lattice, whereas the slow relaxation is probably connected to the growth of the L_3-domains.

Additionally, the evolution of transmission displays a single relaxation time very similar to τ_{slow}, indicating again that the slow relaxation time might be associated with the growth of L_3-domains. These two mechanisms, rearrangement of bilayer material and growth of the L_3-domains, might explain the biexponential behavior of the relaxation process as it is observed in the birefringence. The growth of the L_3-domains is probably associated with a shape relaxation of initially deformed L_3-droplets.

A video sequence of such a shear quench experiment is added as supporting information to illustrate this relaxation process. The video displays the process for a sample with Φ_m=0.31. As one can see, the turbidity in the center of the shear geometry vanishes quickly upon the shear rate quench. However, the initial drop in transmission, as it is observed in the shear quench experiments (see figure 8.7), cannot be observed visually, since it is not pronounced enough to be resolved by the naked eye.

8.4 Discussion

Three types of experiments were conducted to study the influence of shear on the L_3-phase, namely temperature dependent experiments at different constant shear rates, isothermal shear ramps and shear quench experiments. The Φ_m-dependence of the critical shear rate reveals discrepancies to current theories. The origin of this discrepancy is, however, yet not fully understood. It could very well be a dependence of the viscosity on membrane volume fraction that alters the general scaling predicted by equation 8.1.

The shear quench experiments on the other hand, yielded interesting information about the relaxation back to the undisturbed, isotropic state. A careful control of the starting conditions, however, was necessary. This experiment can be compared to the temperature-jump experiments, where also a relaxation from a perturbation back to the isotropic state is observed. As

mentioned before, the relaxation times at low Φ_m are of comparable magnitude, but the overall scaling is different. In both cases the underlying process leading to the relaxation is the formation of handles and hence a similar scaling should be observed. Yet the starting conditions are different, i.e., here we start from a well aligned anisotropic state and Le et al. started from the L_3-water coexistence. In this respect it would be interesting to study the Φ_m-dependence of the relaxation times in temperature-jump experiments starting from the L_α-phase.

Relaxation experiments similar to the ones presented here, were also performed by Mahjoub et al.[125] They however, found a dependence of the relaxation times on shear rate as well as shearing time, i.e., shear history effects. These influences were not found in the study presented here, since care was taken to guarantee identical starting conditions for the different relaxation experiments.

The relaxation times found in the shear quench experiments differ by orders of magnitude from the inverse critical shear rate. Most likely, other processes are involved on different length scales, i.e., the topological relaxation involved in the relaxation of the shear aligned back to the isotropic state is much slower that the bilayer fluctuations, which are suppressed by shear. At least for τ_{fast} the general Φ_m^3-scaling applies and the scale invariance argument seemingly holds for these processes as well, which as such is a striking observation.

The L_3-phase is a very delicate system for experimentalists, owing to its narrow concentration and temperature range in the phase diagram of nonionic surfactants. Especially problematic is the selective evaporation of components. This has in some cases proved to be the reason for unreasonably low critical shear rates.[126,127] In our case, however, the component with the lowest vapor pressure is water (32 mbar at 25°C and 73 mbar at 40°C[136]). The boiling point of n-decane is 174°C and its vapor pressure at 25°C is 1.7mbar. Thus the only parameter that can change in our system during the experiment is the membrane volume fraction, not the membrane thickness. This would, however, lead to a higher critical shear rate than expected and thus is contrary to our findings. We are confident that the sample composition was constant during one experiment and that there were no temperature gradients within the sample (see experimental part).

There is a fundamental difference of our system to that studied by Porcar et al. Our system is constituted of a swollen bilayer and as such it is more complex. In the case of the system studied by Porcar et al. a pure surfactant/water L_3-phase was used, whereas in our case the

swollen bilayer may imply a more complex velocity gradient profile across the bilayer. It is possible that the general scale invariance argument of Porte et al.[137] for L_3-phases that leads to the Φ^3-scaling of the free energy per unit volume is still applicable, but the solvent viscosity needs to be replaced by that of the sample, which itself depends on membrane volume fraction and therefore would lead to a different scaling of $\dot{\gamma}_c$.

Again, we want to point out the difference of our experiments to the T-jump experiments performed by Le et al. on the same system.[93,131,132] The T-jump is performed starting from the L_3-phase, heating into the L_3 + water two phase region. The relaxation of the disturbed L_3-phase back to its equilibrium state is observed. Increasing the shear rate in our experiments yields a L_α-phase and the relaxation in the shear quench experiments is observed from this shear aligned state back to the isotropic phase. This might explain the different scaling with Φ_m as found in the two studies.

The scaling of the critical shear rate with Φ_m found here resembles the Φ_m^2-dependence of the phase boundaries at rest.[131] We thus suggest that in our case the transition from the L_3- to the shear aligned L_α-phase should be discussed in terms of an underlying first order phase transition, as it is also found in the case of wormlike micelles.[98,122,123]

8.5 Summary

In conclusion, this study showed that the L_3–to–lamellar transition under shear can be examined by rheo-birefringence. This study revealed a weaker Φ_m-dependence of the critical shear rate than expected from theory (equation 8.1) or in comparison to the experiments performed by Porcar et al. However, it has been argued that the viscosity entering equation 8.1 should be the sample viscosity, which itself is Φ_m-dependent, and smaller powerlaw exponents for the critical shear rate were fond in other studies as well.[125] Furthermore, the relaxation experiments from the shear aligned state back to the isotropic, were possible by a careful control of the starting conditions.

Interestingly, the relaxation from the shear aligned back to the isotropic state displayed a different scaling with membrane volume fraction than that studied in temperature jump experiments. Although the process leading to the relaxation, namely the topological relaxation by formation of handles, is probably identical in both cases, the starting conditions are different. This might explain the different findings.

8.5.1 Acknowledgments

We thank the Deutsche Forschungsgemeinschaft, the Fond der Chemischen Industrie and the Swedish Science Council (VR) for financial support.

9 Correction Method for the Asymmetry of the Tangential Beam in Couette (or Searle) Geometry used in Rheo-SANS

9.1 Introduction

Shear experiments of complex fluids are often carried out in a Couette shear cell combined with optical methods for determining the structure-property relationship in situ. Small-angle neutron scattering has proven to be a very powerful technique in this respect.[2,76,138] Especially with the 2D-position sensitive area detectors available it is possible to characterize anisotropic media under shear.

To obtain full information about the orientation of the anisotropic structures under shear, two beam configurations are used. In the so-called radial beam configuration the neutrons pass the center of the Couette shear cell and thus reveal structural information in the neutral-flow-plane. In the tangential beam configuration the beam passes through the gap of the shear cell, i.e., along the flow direction and thus reveal structural information in the gradient-neutral-plane.[59]

For the radial beam configuration, standard data treatment (normalization to absolute units) is straightforward.[63] This is, however, more difficult for the tangential beam, and thus most of such data presented in the literature is not properly normalized and background corrected.

Porcar et al. and Zipfel et al.[19,139] presented simple methods, which just take into account the pathlength of the transmitted beam. This way they are able to use the water calibration and sample transmission from the radial beam and scale the tangential beam data to absolute units. This calibration method, however, neglects a central problem of tangential beam experiments, namely the asymmetry of the pathlength of neutrons that are scattered inwards (towards the axis of rotation of the shear geometry) or outwards (away from the axis of rotation). The

pathlength of an unscattered neutron may differ significantly from that of a scattered neutron. Moreover, the lengths of the respective paths of inwards and outwards scattered neutrons may also differ significantly. This results in an asymmetry of the recorded scattering pattern. Considerations to quantify this asymmetry might be helpful in establishing a standard calibration routine for tangential beam data. We will therefore start with a detailed description of the tangential beam configuration and the difficulties associated with it. This description of the asymmetry is necessary to justify the correction procedure that we propose.

9.1.1 The Tangential Beam

Figure 1 shows a sketch of a Couette shear cell, as it is used at the D11-beamline at the ILL in Grenoble, France.[59] The difference in pathlengths of the inwards and outwards scattered neutrons is obvious. As mentioned above, inwards and outwards is defined with respect to the axis of rotation of the shear cell (see also figure 9.1).

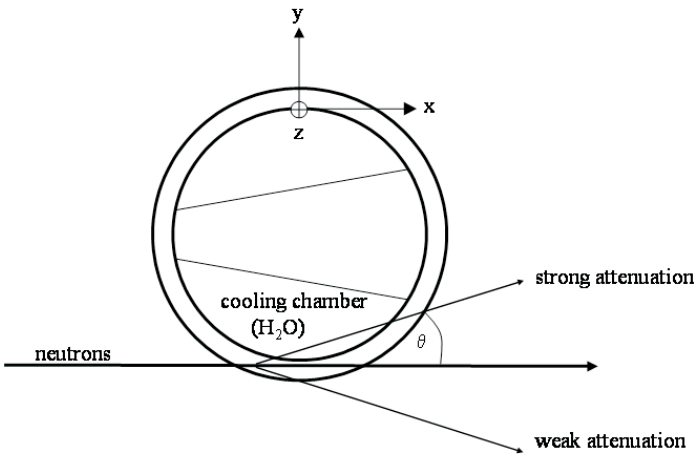

Figure 9.1: Geometry of a Couette shear cell. Typical dimensions of such a shear cell are: 48mm diameter, 1mm gap width. A slit-aperture with a neutron beam cross-section of 0.3 by 10mm was used for this set-up.

Additionally, a shadow problem occurs in this Couette design due to the cooling liquid in the inner chamber of the inner cylinder (here being the stator). This problem is not so pronounced

at smaller angles or if a Searle type shear cell is used, as is the case for the Bohlin CVO 120, also available at D11.[59] In this design the cell is thermostatted from the outside by a cooling jacket, and thus the inner cylinder (the rotor of the Searle-type shear cell) is hollow.
The asymmetry will be more pronounced at short detector distances, since the difference in pathlength for large scattering angles θ consequently becomes more drastic. Furthermore, lower transmission will lead to a stronger asymmetry. The factors influencing the asymmetry are listed below:

1. the detector distance strongly influences the asymmetry.
2. the total scattering cross-section of a sample plays an essential role. Consequently, a low total scattering cross-section of the sample is advantageous, i.e., high transmission.
3. Since the transmission and also the total scattering cross-section is normally wavelength dependent, owing to the wavelength dependence of the incoherent scattering cross-section, and higher for shorter wavelength, the wavelength also influences the asymmetry of the SANS-pattern.

However, the situation is more complex if anisotropic samples are studied, as will be discussed later. Let us first proceed with a description of the shear cell's geometry.

9.2 Theoretical Considerations

A geometrical representation of the problem is represented in figure 9.2. There are several questions to answer in order to correctly describe the asymmetry of the tangential beam. (For the following considerations the possibility of multiple scattering will be neglected, although it may play an essential role owing to the long pathlength of the scattered neutrons in the tangential beam.)

1. How long is the path from A to Ξ and from Ξ to Y or Z for any possible θ along ξ ?
2. What is the intensity of the respective rays?
3. What is the angular dependent intensity integrated over all possible scattering events along $\overline{AB}$?

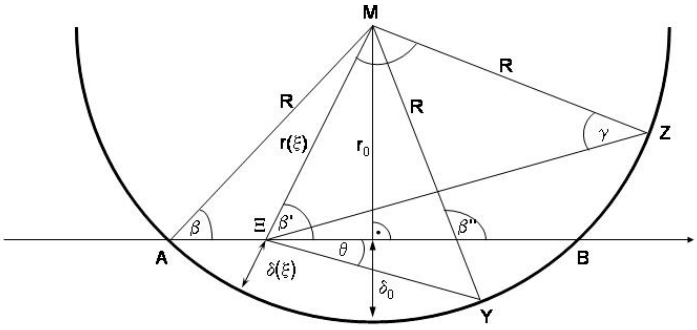

Figure 9.2: Geometry of shear cell in a top view, i.e, the flow-gradient plane is represented. M is the center and R the radius of the outer cup. A beam intersects the circle at A and is transmitted along ξ to B. Consider scattering events at Ξ where a neutron is scattered with an angle θ in the flow-gradient plane. The scattered beams exit the cell at Y or Z. The distance from the center M to the transmitted beam ($\overline{AB}$) is called r(ξ) with the special case r_0, where it is perpendicular to the beam. The distance from the beam to the wall of the cup is called $\delta(\xi)$ with the special case of δ_0. The coordinate along $\overline{AB}$ is ξ. Angles between R, r(ξ) and $\overline{AB}$ are called β' and β", respectively.

4. Is it possible to treat anisotropic data (as for instance the scattering of a lamellar phase where the layer normal is parallel to the gradient direction) with this method?

Consider a neutron beam that enters a Couette shear cell at point A (see figure 9.2) and exiting it at B. A scattering event can take place somewhere along $\overline{AB}$ at point Ξ, where the neutrons are scattered under the scattering angle θ. Thus, an outwards scattered neutron (away from the axis of rotation) will exit the cell at point Y, whereas an inwards scattered neutron (toward the axis of rotation) will leave the cell at point Z. The path of a scattered neutron is thus described by $\overline{A\Xi Y}$ or $\overline{A\Xi Z}$. The position of the beam intersecting the shear geometry is defined by r_0, the distance from the center of the cell M to the intersecting beam, where r_0 is perpendicular to $\overline{AB}$. The coordinate along $\overline{AB}$ is called ξ.

9.2.1 Geometry

As can be seen, the inner cylinder is omitted in order to simplify the considerations. Hence the problem of the shadow of the inner cylinder, which in the case of the Couette shear cell contains the cooling fluid whereas it is hollow in the Searle geometry, is neglected. The distance from the intersecting beam to the outer wall of the shear geometry at point Ξ is given by:

$$\delta(\xi) = R - r(\xi) \tag{9.1}$$

In equation 9.1 R is the radius of the shear geometry and $r(\xi)$ is the distance from the center to the point Ξ. $r(\xi)$ itself is given by:

$$r(\xi)^2 = r_0^2 + (s - \xi)^2 \tag{9.2}$$

where $s = \overline{AB}/2 = \sqrt{R^2 - (R - \delta')^2}$ and $\xi = \overline{A\Xi}$.
Since $r_0 = R - \delta_0$ equation 9.2 can be rewritten as

$$\begin{aligned} r(\xi)^2 &= (R - \delta_0)^2 + (s - \xi)^2 \\ &= (R - \delta_0)^2 + (\sqrt{R^2 - (R - \delta_0)^2} - \xi)^2 \end{aligned} \tag{9.3}$$

The length of the path after the scattering event $\overline{\Xi Z}$ or $\overline{\Xi Y}$ can be calculated by:

$$\overline{\Xi Z} = x + y = r(\xi)\cos\alpha + R\cos\gamma \tag{9.4}$$

with the known $r(\xi)$ and

$$\gamma = \arcsin\left[\frac{r(\xi)\sin(\alpha)}{R}\right] \tag{9.5}$$

A full geometric expression for the length of $\overline{\Xi Z}$ is available. The angle $\alpha = \beta \pm \theta$, where β can be calculated by:

$$\begin{aligned} \beta &= \arcsin\left[\tfrac{r_0}{r(\xi)}\right] = \arcsin\left[\frac{r_0}{\sqrt{(R-\delta_0)^2+(s-\xi)^2}}\right] \quad \Big| \; \xi \le s \\ \beta &= \pi - \arcsin\left[\tfrac{r_0}{r(\xi)}\right] = \pi - \arcsin\left[\frac{r_0}{\sqrt{(R-\delta_0)^2+(s-\xi)^2}}\right] \quad \Big| \; \xi \ge s \end{aligned} \tag{9.6}$$

Finally the full expression for the angle dependent pathlength of a neutron entering the cell at A, being scattered at Ξ and exiting the cell at Z or Y, $S(\xi, \theta_{gf})$ for neutrons that are scattered in the gradient-flow plane, is:

$$S(\xi, \theta_{gf}) = \xi + \overline{\Xi Z} = \xi + r(\xi)\cos\alpha + R\cos\gamma \tag{9.7}$$

The angle θ_{gf} describes the scattering angle in the gradient-flow plane. The respective pathlengths in the flow-gradient plane are shown in figure 9.3 as a function of the position of the scattering event ξ and the scattering angle θ.

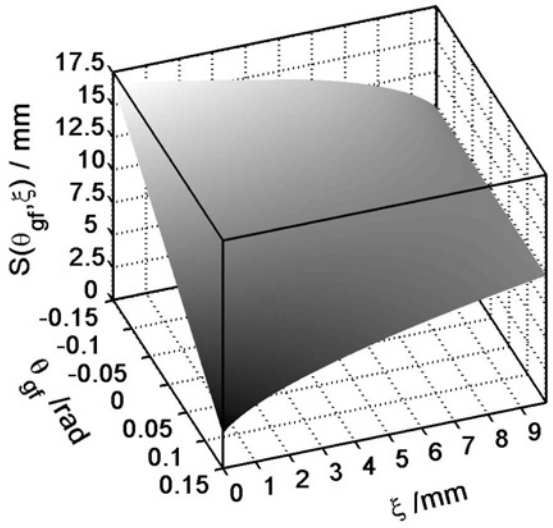

Figure 9.3: Pathlength of a scattered neutron as a function of the position of the scattering event along the transmission path and the scattering angle. As a convention, negative angles describe a scattering event toward the inside (toward the axis of rotation) of the Couette shear cell. The beam is positioned 0.15mm away from the inner cylinder of the shear geometry.

So far we were only concerned with the pathlengths in the gradient-flow plane. Taking this a step further to construct the function for the pathlength in two dimensions one needs to define the azimuthal angle $0 \leq \phi \leq 2\pi$. One then needs to combine the expression 9.7 with that for the pathlength in the neutral direction (equation 9.8) where the angle θ_{nf} is the scattering angle in the neutral-flow plane.

$$S(\xi, \theta_{nf}) = \frac{\overline{AB} - \xi}{cos\theta} + \xi \tag{9.8}$$

Equations 9.7 and 9.8 can be combined in a linear combination as long as the scattering angle θ is small, so that the curvature of the shear cell does not play a role. At a detector distance of 2.5m, which is the shortest distance that is used at D11 in rheo-SANS experiments, the maximum scattering angle is 7°. The error that is introduced to the pathlength in the neutral-flow plane (azimuthal angle $\phi = 90°$) is 20%. But for an angle of 4° the error is down to

6%. Note that the error is also smaller for azimuthal angles between 0° and 90°. From the linear combination of the pathlength in the gradient-flow with that in the neutral-flow plane one obtains the full expression for pathlength of neutrons that entered the cell at A, are scattered at Ξ and exit the cell at Z or Y, including the change of pathlength if a neutron is scattered out of the gradient-flow plane:

$$S(\xi,\theta,\phi) = cos(\phi)\cdot S(\xi,\theta_{gf}) + cos\left(\frac{\pi}{2}-\phi\right)\cdot S(\xi,\theta_{nf}) \tag{9.9}$$

9.2.2 Implications for Scattering

The transmission is defined as:

$$T_s = exp\,(-\mu d) \tag{9.10}$$

where μ is the total scattering cross-section and d the sample thickness. The scattered intensity is a function of q and is no more independent of the position at which the scattering event takes place, since the pathlengths of scattered neutrons are asymmetric with respect to the path that an unscattered neutron travels ($\overline{AB}$).

The assumption that is often made in small-angle scattering for thin and symmetric samples, namely that $\overline{AB} = \overline{A\Xi Z} = \overline{A\Xi Y}$, does not apply anymore. The measured intensity is a sum of all the scattering events that take place along ξ. Therefore, the scattering intensity that one would obtain from an experiment in a regular scattering cell $I(\theta,\phi)$ enters the integral $I(\theta,\phi)_{tan}$ over the respective paths of each scattered neutron.

$$\begin{aligned} I(\theta,\phi)_{tan} &= \int_0^{\xi} T_s(\theta,\phi,\xi) I(\theta,\phi) d\xi \\ &= I(\theta,\phi)\int_0^{\xi} T_s(\theta,\phi,\xi) d\xi \\ &= I(\theta,\phi)\int_0^{\xi} e^{-\mu\cdot cos(\phi)\cdot S(\xi,\theta_{gf})}\cdot e^{-\mu\cdot\cos\left(\frac{\pi}{2}-\phi\right)\cdot S(\xi,\theta_{nf})} d\xi \\ &= I(\theta,\phi)A(\theta,\phi) \end{aligned} \tag{9.11}$$

Equation 9.11 finally yields the expression to establish a correction routine for the asymmetry of the tangential beam. Here, $A(\theta,\phi)$ summarizes the asymmetry due to the tangential beam geometry. How exactly the correction procedure needs to be conducted will be deferred to section

9.3. Figure 9.4 displays the resulting asymmetric scattering as a function of q in the gradient direction (i.e., as a function of q_{gf}) calculated for a flat scatterer (e.g. H_2O/D_2O sample) with a scattering cross section of $3.8cm^{-1}$. This calculation is based on equation 9.11, i.e., merely on the asymmetry in pathlength of inward and outward scattered neutrons.

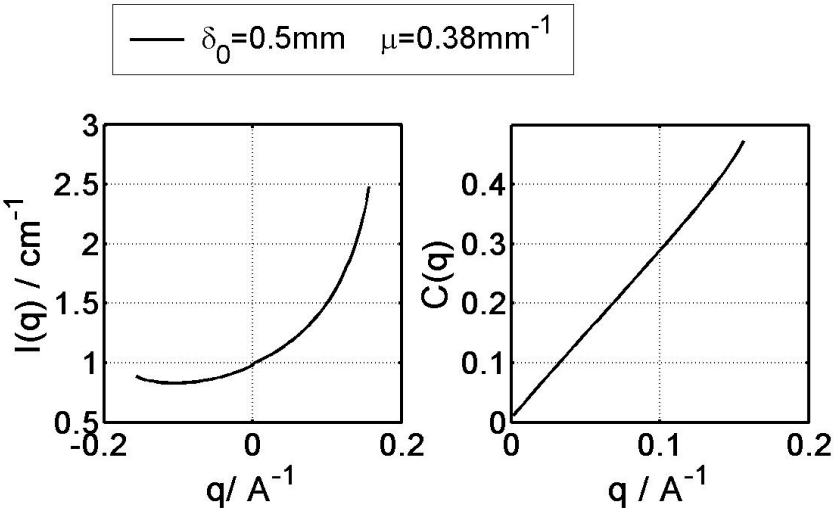

Figure 9.4: Left: Asymmetric scattering of a flat scatterer (e.g. an H_2O/D_2O mixture) based on equation 9.11 in the gradient direction. Here δ_0 is the position of the neutron beam away from the outer cylinder of the Couette geometry and μ the total scattering cross-section of the sample. Right: Asymmetry raitio $C(q) = [I(q_+) - I(q_-)] / [I(q_+) + I(q_-)]$.

If this dependence on q is observed for a D_2O/H_2O sample with a similar total scattering cross-section as the sample, the problem can be reduced to a pathlength effect and the data treatment can greatly be facilitated by just measuring the asymmetry in pathlengths with the respective D_2O/H_2O sample. It should then be possible to correct the asymmetry of a sample scattering pattern by dividing it by $A(\theta, \phi)$.

Details of this procedure and experimental results will be presented in section 9.3 Before focusing on the experimental aspects the important issue of the effect of anisotropic media on the asymmetry of a scattering pattern has to be addressed.

9.2.3 Anisotropic Samples

Figure 9.5 displays the more complex situation for anisotropic samples. Lets assume a parallel orientation of planar lamellae, as sketched in figure 5. At short detector distances an additional

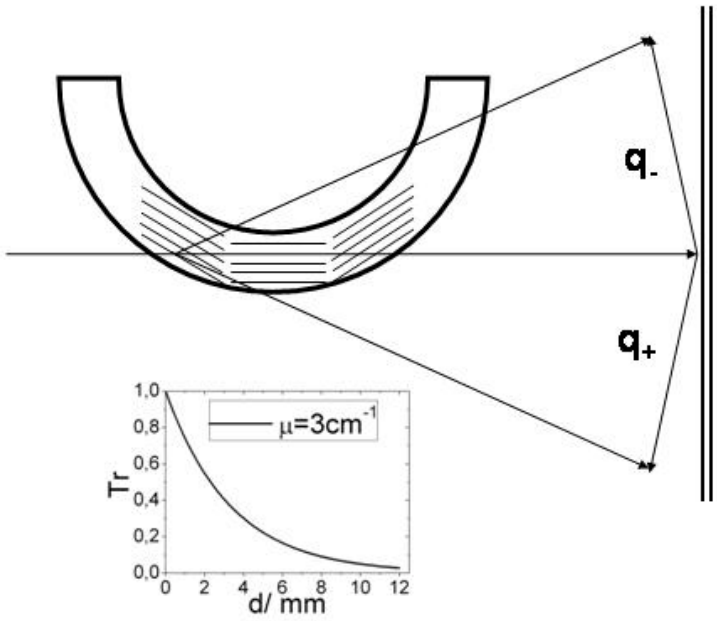

Figure 9.5: Geometry of a Couette shear cell filled with an anisotropic sample8e.g. lamellae in a parallel orientation).

reason for the asymmetry comes into play. As soon as the radius of the Ewald-sphere becomes too small, the scattering vector q cannot be assumed to lie in the detector plane anymore. Therefore we distinguish between q_+ and q_- for outwards and inwards scattered neutrons, respectively. The Bragg-condition is fulfilled for lamellae, whose layer normal is parallel to q. This is the case in the first part of the scattering volume. In this case the outwards scattering events are favored, since q_+ is parallel to the layer normal of lamellae in this volume, whereas q_- is not. Additionally the inwards scattered neutrons have a very long way through the sample and are thus attenuated much more.

As the neutron beam passes through the sample, it is, for a given scattering cross-section μ of the sample, attenuated, as shown at the bottom of figure 9.5. Thus the contribution to the

scattering, when the Bragg-condition is fulfilled for q– is of minor importance and thus the asymmetry is not compensated by this condition. Consequently, this origin of the asymmetry contributes less to the overall skewness of the scattering pattern, if the scattering cross-section of the sample is small and the correction procedure described above, will work better for more dilute samples.

This problem is not present for an orientation of the bilayer normal along the neutral direction. In this case, the asymmetry leading to a skewness of the Bragg-peaks along the azimuth is only due to the difference in pathlengths and should be accounted for so that peak-shape analysis, for instance in terms of an order parameter, would be possible with a corrected scattering pattern. In addition to the asymmetry, the tangential beam is more and more "polluted" by radial beam components the closer the beam is positioned to the inner cylinder. In other words, one averages over different orientations of lamellae, and if there is for instance banded flow, where different orientations of lamellae exist at different positions within the gap, one will not be able to clearly distinguish between them.

All these complications, however, are sample inherent features and may as well be regarded as useful information about the state of the sample (e.g. banded flow, parallel orientation of lamellae or wall effects etc.).

9.3 Correction Procedure and Experimental Results

The asymmetry is predominantly caused by the difference in pathlengths of inward and outward scattered neutrons. Having analyzed the geometry, we propose a simple procedure to experimentally account for the asymmetry: A H_2O/D_2O mixture with the same scattering cross-section as the investigated sample displays a flat scattering intensity. The scattering intensity is thus q-independent and we call it a featureless scattering pattern. If such a H_2O/D_2O-mixture is investigated in the tangential beam, an asymmetry is observed, originating from the asymmetry of pathlength with respect to the flow-neutral plane as is described in section 9.2 in detail. Thus, $A(q,\phi)$ can be obtained by dividing $I(q,\phi)_{tan}$ by $I(q,\phi)$. The latter can be obtained from a scattering experiment in a regular scattering cell or directly from the radial beam experiment. The resulting $A(q_{gf})$ ($A(q,\phi)$ evaluated in the gradient direction) for a H_2O/D_2O (51.12/48.88 w/w) with a scattering cross section of 3.795cm^{-1} at a beam position 0.2mm away from the inner cylinder of the Searle shear cell is shown in figure 9.6 and compared with the calculated

asymmetry in the gradient direction. As can be seen the scattering of the H_2O/D_2O is very

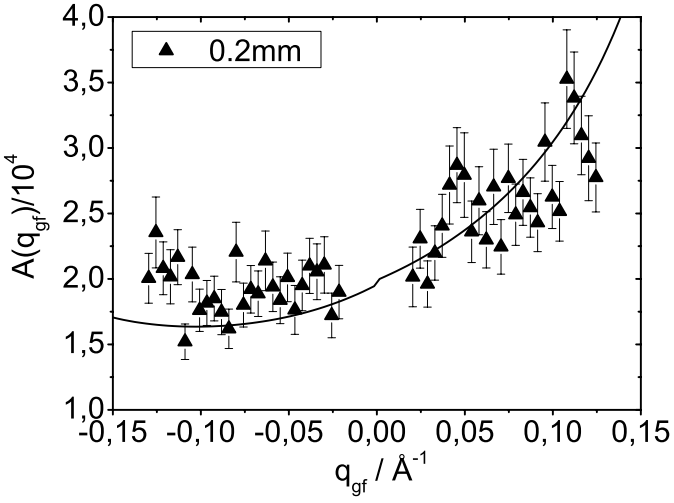

Figure 9.6: A(q, ϕ) obtained from a H_2O/D_2O sample (51.12/48.88 w/w) with $\mu = 3.795cm^{-1}$ measured at 0.2mm away from the inner cylinder of the Searle shear cell. The wavelength used was λ=6Åat a detector distance of 2m. The line represents the calculated A(q, ϕ).

well described by the asymmetry factor $A(q_{gf})$. This justifies the procedure chosen here, i.e., a flat scatterer captures the pathlength problem correctly. $A(q, \phi)$ can then be used to correct the scattering of the sample of interest.

The precision of the positioning is of utmost importance of the correction procedure. Thus the transmissions of a H_2O/D_2O sample (51.12/48.88 w/w) with a total scattering cross section of $\mu = 3.795cm^{-1}$ were measured at different positions of the translation table. From the minimum in transmission, the reference position, namely where the neutron beam is closest to the inner cylinder of the shear cell, can be determined as was described by Zipfel et al.[19]. This procedure is shown in figure 9.7. The largest error in the calculation of the pathlength from the transmission originates from the transmission itself. The transmission can be measured with a precision of 5%[63] and thus the calculated pathlength is associated with a rather large error which does not come from unprecise positioning of the translation table.

The result of the correction of the asymmetric scattering of an isotropic scattering pattern, here

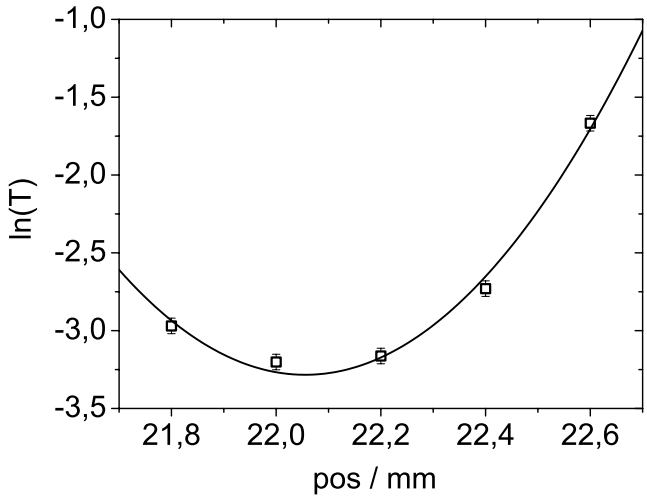

Figure 9.7: Natural logarithm of the transmission of a H_2O/D_2O sample (51.12/48.88 w/w) with $\mu = 3.795 cm^{-1}$ measured at different positions of the translation table. The fit is a polynomial of second order, which describes the pathlength of a neutron beam intersecting the shear cell as a function of its distance to the center of the shear cell and the minimum of it is the zero-position of the tangential beam.

multilamellar vesicles (MLVs) prepared from a 40wt% sample of $C_{10}E_3$ in D_2O with a shear rate of $10s^{-1}$ at 25°C, with the asymmetry factor $A(q, \phi)$ scattering of the H_2O/D_2O sample is shown in figure 9.8. Proper transmission and background scattering measurements at the given position have to be made.

In the uncorrected case (figure 9.9, left) the asymmetry ratio C, defined as $C = [(I(q_+) - I(q_-))] / [(I(q_-) + I(q_+))]$, is clearly q-dependent. Note that the kink at q_0 is due to a slight mismatch of q_+ and q_-. The asymmetry ratio C is almost constant at high q ($C = 0.5$). In the asymmetry corrected case (figure 9.9, right) C is nearly q-independent. It is, however, not zero, as was expected after having done the correction. An almost q-independent asymmetry means, that there is a residual and almost linear slope in the scattering pattern. The average value of 0.21 is an intrinsic contribution to the asymmetry probably due to the mismatch of the respective total scattering cross sections of the sample and the H_2O/D_2O mixture.

As pointed out before, the anisotropy of a medium can pose a problem for the correction method presented here (see section 9.2.3). This is depicted in figure 9.10. The asymmetry is still con-

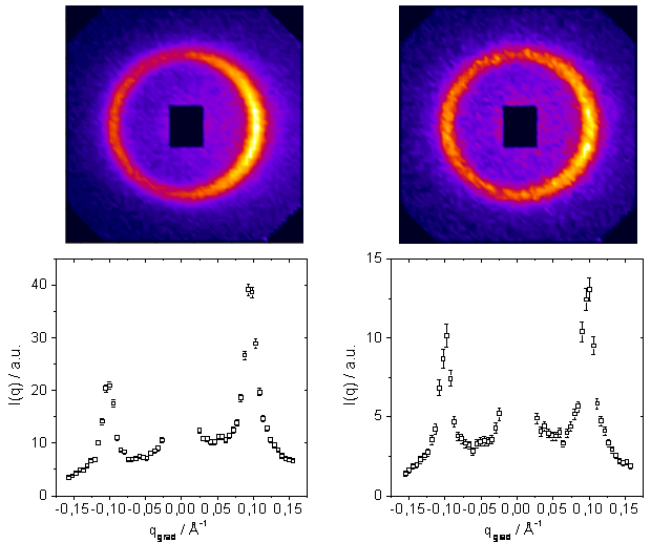

Figure 9.8: left (top): Scattering of (MLV from a 40wt% $C_{10}E_3$ sample in D_2O, detector distance=2m, λ=6Å) ($\mu = 3.945 \pm 0.063 cm^{-1}$) at 0.2mm away from the inner cylinder of the Searle shear cell, background corrected and normalized to H_2O. The pathlength of an unscattered neutron was calculated from the transmission to $8.571 \pm 0.26 mm$. right (top): The same data divided by $A(q, \phi)$ obtained from the scattering from a H_2O/D_2O sample (51.12/48.88 w/w) with $\mu = 3.795 cm^{-1}$ recorded at the same position. The transmission at this position is 0.0423 and the pathlength calculated from it is $8.335 \pm 0.270 mm$. Please note that the images are not on the same scale, since otherwise the characteristic features and the result of the correction procedure would not be visible. Bottom: Corresponding intensity profiles along q_{gf}. Here the intensity scales correspond to the images above.

siderable as can be seen from the asymmetry ratio C in figure 9.11). The residual anisotropy is still q-dependent and therefore the pathlength approach does not capture the asymmetry for highly anisotropic data entirely. This is not only true for the scattering at the Bragg-peak, but also for the regions, which are not dominated by the structure factor. This can be attributed to the situation discussed in section 9.2.3 and depicted in figure 9.5, where different orientations of the lamellae exist at different coordinates along the $\overline{AB}$ that favor in- or outwards scattering, respectively. The asymmetry of the whole pattern is probably due to an anisotropic form factor that has essentially the same effect for the whole investigated q-range. But since these features

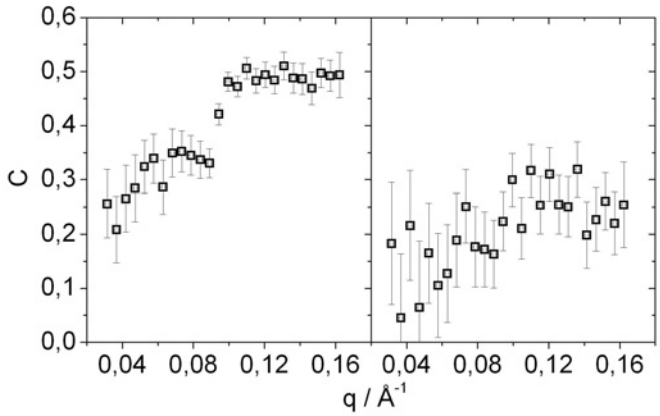

Figure 9.9: Left: Asymmetry ratio C for the background corrected and H_2O normalized intensity profiles of MLV (same sample as above). Right: Respective asymmetry ratio for the background corrected and H_2O normalized intensity profiles, which were additionally divided by $A(q, \phi)$ obtained from the corresponding H_2O/D_2O sample.

are sample inherent they contain valuable information about the system, as was already pointed out in section 9.2.3.

After the correction for the asymmetry, a calibration to an absolute standard can be conducted following standard procedures. The larger transmission path, however, has to be taken into account.

In order to prevent errors in matching the scattering cross-sections of the sample and the H_2O/D_2O mixture as well as minimizing the errors in beam positioning, which are introduced if the sample has to be changed, it would be even better if one did the correction for the asymmetry with the sample itself. This is possible for samples, where an isotropic phase is present at a different temperature. Then one can record the asymmetry with the sample under study heated or cooled to the isotropic phase (e.g. L_1 or L_3-phase). The intensity distribution, $I(q, \phi)$, can be determined directly from a radial beam experiment. A necessary prerequisite is, that the sample is entirely isotropic so that one can be sure that the structures that are detected in the radial beam are the same as those in the tangential beam experiment. The asymmetry map $A(q, \phi)$ can be calculated as described above using equation 9.11. An example of such an experiment is shown in figure 9.12 using the L_3-phase of a 40wt% $C_{10}E_3$-sample obtained at 48°C. The scattering of the L_3-phase from the tangential beam is shown on the top, to the left, the isotropic reference from the radial beam to the right. The bottom shows $A(q_{gf})$ (left) and

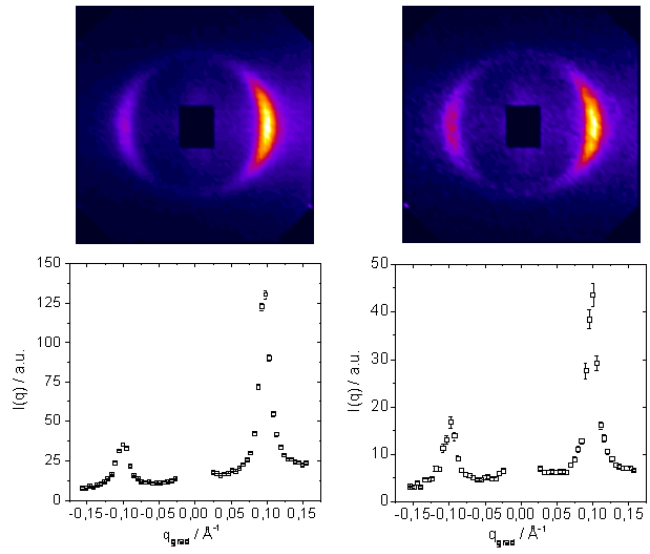

Figure 9.10: left (top): Scattering of lamellae in the parallel orientation (obtained from the same sample by shearing with a shear rate of $10s^{-1}$ at 42°C, scattering cross-section $\mu = 3.945cm^{-1}$) at 0.5mm away from the inner cylinder of the Searle shear cell background corrected and normalized to a H_2O standard. right (top): The same data corrected with a scattering pattern from a H_2O/D_2O sample (51.12/48.88 w/w) with $\mu = 3.795cm^{-1}$ recorded at the same position. Bottom: Corresponding intensity profiles along q_{gf}.

the comparison of the uncorrected with the corrected scattering of a lamellar phase in parallel orientation from the very same sample recorded under the same conditions as $A(q_{gf})$ (i.e., beam position, wavelength and detecctor position). As one can see, $A(q_{gf})$ displays the characteristic trough like feature of the calculated asymmetry (see figures 4 and 6) and moreover, the statistics are much better than in the case using the H_2O/D_2O-mixture for similar recording times. The correction seems to work equally well compared to the H_2O/D_2O-method.

9.4 Conclusion

A calibration of tangential beam data is possible by dividing the sample scattering by $A(q_{gf})$ obtained from the otherwise featureless scattering of a H_2O/D_2O-mixture with the same scattering

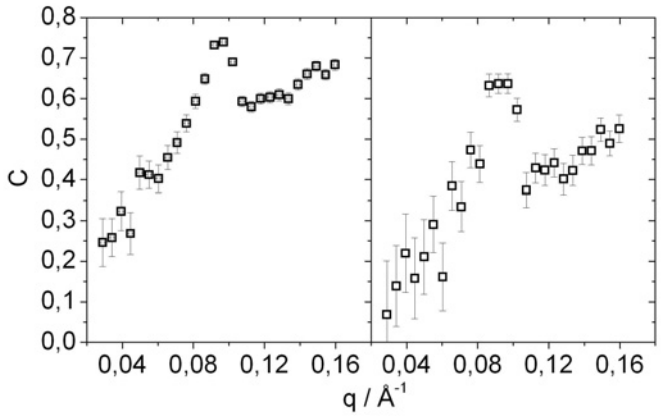

Figure 9.11: Left: Asymmetry ratio for the background corrected and H_2O normalized intensity profiles of a parallel orientation of lamellae. Right: Respective asymmetry ratio for the background corrected and H_2O normalized intensity profiles, which were additionally divided by $A(q, \phi)$ obtained from the corresponding H_2O/D_2O sample.

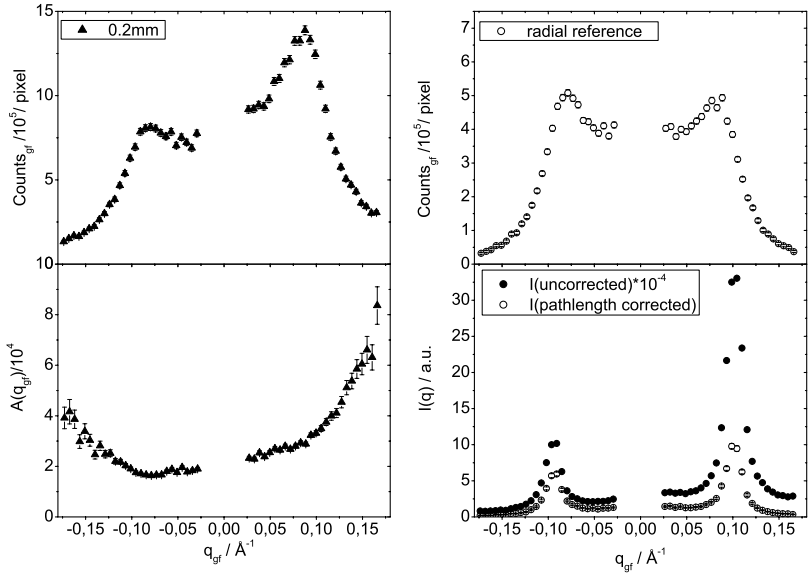

Figure 9.12: $A(q_{gf})$ obtained from an isotropic scatterer (L_3-phase of a 40wt% sample) with a wavelength of 4.5Å and a detector distance of 2.5m. The plots on the top panel depict the procedure and the bottom panel shows the reulting $A(q_{gf})$.

cross-section as the sample under study. This is possible, since the dominating contribution to the asymmetry originates from a pathlength asymmetry with respect to the neutral-flow plane. A nice alternative is at hand if an isotropic phase is available in the phase diagram of the sample under study. In this case the difficulties arising from exact positioning after changing the sample and matching the scattering length densities of sample and flat scatterer can be circumvented. Thus, if such an isotropic phase is available in the phase diagram of the sample under study, the latter method should be favored above the treatment with a flat scatterer. For both methods difficulties can, however, arise for anisotropic samples with high scattering cross-sections. In such a case point 1 to 4 of section 9.1.1. have to be considered. However, the remaining asymmetry in such a case is sample inherent and thus contains information about the orientation state and homogeneity of the sample.

Special care has to be taken about the exact positioning of the shear cell in the respective calibration experiments. The calibration has to be carried out at the same position as the measurement of the sample of interest, since small offsets create rather large variations in the pathlength. It is therefore inevitable to work with a precision in the positioning of the shear cell of less than 0.01mm.

9.4.1 Acknowledgments

We thank the Deutscher Akademischer Austausch Dienst (DAAD) and the Deutsche Forschungsgemeinschaft (DFG), the Swedish Research Council (VR) and the Marie-Curie-Foundation (MCF) for financial support.

10 Conclusions and Perspectives

10.1 Conclusions

The influence of shear on bilayer systems was studied using a variety of time-resolved scattering techniques. Nonionic Surfactants of the ethylene glycol homologous series ($C_{10}E_3$, $C_{12}E_4$ and $C_{12}E_5$) were chosen, since these systems display a lamellar phase over a wide temperature and concentration range. By these means, a variation membrane properties (by changing temperature of surfactant type) and volume fraction was possible.

Furthermore, nonionic surfactants are advantageous, because no cosurfactants are needed to obtain stable bilayer systems. Thus, problems with a local segregation of components, which may lead to different local spontaneous curvatures of the film, can be avoided.[97]

The transition from planar lamellae to MLVs was examined in detail using the nonionic sufactants $C_{10}E_3$ and $C_{12}E_4$. The systematic variation of experimental conditions such as shear rate, temperature, surfactant type and flow pattern provided detailed insight of transient morphologies, the parameters that reign the transition as well as stability of intermediates and their behavior upon flow reversal. The latter proved to reveal more detail about the early stages of transformations and in particular a distinction between reversible and irreversible parts, which thus contribute to MLV-formation, of the transition was possible.

Conversely, the study of doped systems revealed insight into the interaction of clay platelets in a lamellar phase under shear. Above all, the observation of a drastic change of lamellar spacing is a striking and somewhat puzzling result.

The study of the shear induced L_3–to–lamellar transition of a nonionic microemulsion, representing a different topology, raised questions about the general scaling behavior of bilayer fluctuations with membrane volume fraction.

Before discussing the results in detail, a quick review of the theoretical framework of the flexible

surface model is necessary. According to Helfrich[67] the free energy of a film can be written as:

$$G_f = \int \left[2\kappa \left(H - H_0\right)^2 + \bar{\kappa} K\right] dA \tag{10.1}$$

In this equation κ and $\bar{\kappa}$ are the bending and the Gaussian modulus of the surfactant monolayer, respectively, H_0 is the spontaneous and H the actual curvature of the film, evaluated in the two principal directions. The two respective principle curvatures are $H_1=1/R_1$ and $H_2=1/R_2$. H_0 is dictated by surfactant geometry, which can be strongly temperature dependent, as it is the case for nonionic surfactants. Its temperature dependence can be described by an expansion around the phase inversion temperature (PIT), leading to the following expression:

$$H_0 \approx \left|\frac{dH_0}{dT}\right|_{T_0} (T_0 - T) \approx \beta \left(T_0 - T\right) \tag{10.2}$$

Thus, increasing temperature leads to a decrease in spontaneous curvature and at the PIT to an inversion of its sign. A description for bilayer structures can be obtained by rewriting equation 10.1 in terms of the mean bilayer $\langle H \rangle$ and the mean Gaussian bilayer curvatures $\langle K \rangle$.

$$\frac{G_f}{A} = 2\kappa_b \langle H \rangle + \bar{\kappa} \langle K \rangle \tag{10.3}$$

where the Gaussian curvature is given by:

$$\langle K \rangle = 4\pi \frac{(n_c - n_h)}{A} \tag{10.4}$$

From equation 10.4 it becomes evident that the Gaussian bilayer curvature is independent of the actual bilayer geometry and only depends on the connectivity (n_c) and the number of handles (n_h). Bending κ and Gaussian modulus $\bar{\kappa}$ introduced in equation 10.1 are related to their bilayer counterparts by:

$$\begin{aligned} \kappa_b &= 2\kappa_{mono} \\ \bar{\kappa}_b &= 2\bar{\kappa}_{mono} - \kappa_{mono} l_0 H_{0,mono} \end{aligned} \tag{10.5}$$

As is apparent from equation 10.5 the Gaussian bilayer modulus $\bar{\kappa}_b$ is temperature dependent. Thus, temperature can be used to fine tune the bilayer properties (the Gaussian bilayer modulus) to yield the different bilayer topologies, namely MLV, planar lamellae, and L_3-phase. A simple phase diagram can be constructed from these considerations, which qualitatively reflects the phase sequence found experimentally (see figure 10.1).

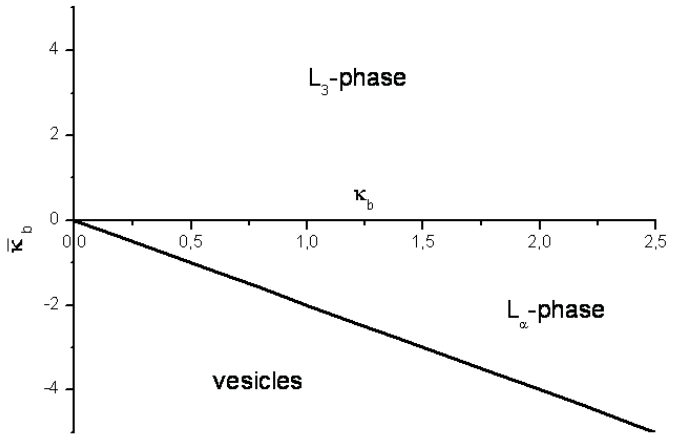

Figure 10.1: Schematic phase diagram of bilayer structures as a function of the bending moduli κ_b and $\bar{\kappa}_b$.

10.1.1 Continuous Experiments

Continuous shear experiments in combination with time-resolved small-angle light and neutron scattering revealed five intermediates with different symmetries (see figure 5.20). State II is most distinct, since it displays a cylindrical scattering symmetry, as such being intermediate between a planar bilayer and a spherical MLV (see also 10.1). Scattering methods do not allow the distinction between a local cylindrical symmetry as for instance multilamellar cylinders (MLC) or a global cylindrical symmetry, which could be a coherent buckling of lamellae.[23,90]

Different models for this dynamic lamellar–to–MLV transition have been devised, which, however, do not completely describe all details of this transition. One first attempt to explain MLV-formation is based on the argument that gap-inhomogeneities lead to defects, which in a flow field proliferate and consequently MLVs are formed.[9] The transition presented here is, however, reproducible in different shear geometries and thus this explanation does not seem to be valid.

More recent attempts to describe the transition involve the suppression of short wavelength thermal undulations, which lead to an increase in projected bilayer area. An incompressible fluid can escape the tension by either buckling or by a change in bilayer separation (in case of permeable bilayers).[40,41] These descriptions lead to the conclusion, that the transition occurs at

a certain strain or strain rate, respectively.

Reasoning involving thermal undulations, however, refers to dilute lamellar phases, which were not considered in this thesis. The mechanism proposed by Zilman et al. and also by Marlow et al. does not necessarily lead to a coherent undulation of the lamellae, whereas at higher concentrations it is a collective phenomenon, which is observed on a μm scale. Otherwise the observation of a cylindrical symmetry on these length scales by SANS and SALS would not have been possible.

Moreover, a strain control was observed only during the early stages of the transition. Already the cylindrical intermediate displayed a shear rate dependence, and clear indications for a stress control were found in experiments at different temperature and by using a different nonionic surfactant of the homologous series, as will be specified later.

Also the model proposed by Auernhammer et al.[42], although based on a hydrodynamic description of a lyotropic smectic and the different coupling of the smectic and the underlying nematic director with the flow field, arrives at similar conclusions as the models by Zilman et al. and Marlow et al. In summary it can be said that, although the different models manage to grasp certain details of the transition, they do not describe the lamellar–to–MLV transition entirely. In particular, all of them fail to describe the apparent stress control of this transition.

As it was emphasized above, the transition is apparently controlled by stress. A critical stress was determined for $C_{10}E_3$, above which a transition to the well ordered state V takes place. States II-IV occur as intermediate states. At lower stress, however, these states may at a given stress be the steady state structures, i.e., the transition to state V is not completed. This observation is additional support for a stress control of the transition.

The transition coordinate in figure 5.20 is left unspecified, since a clear decision as to which, strain or stress, is the appropriate parameter is ultimately not possible. The neutron scattering data on one hand seemingly support a strain control, although a slight variation of the position of the intensity maximum along the neutral intensity trace with shear rate (and thus with stress) is indicative for a stress control; rheo-small-angle light scattering on the other hand supplies evidence for a stress control of the transition. This is not further surprising: small-angle neutron scattering yields information on length scales of the lamellar correlation and about their orientation distribution, whereas rheo-SALS probes length scales of several micrometers, and thus about the vesicle shape and their spatial arrangement. The spatial arrangement may still

change although the orientation distribution of lamellae is already isotropic.

Figure 10.2 nicely supports the assumption of a stress control of the transition. The transient

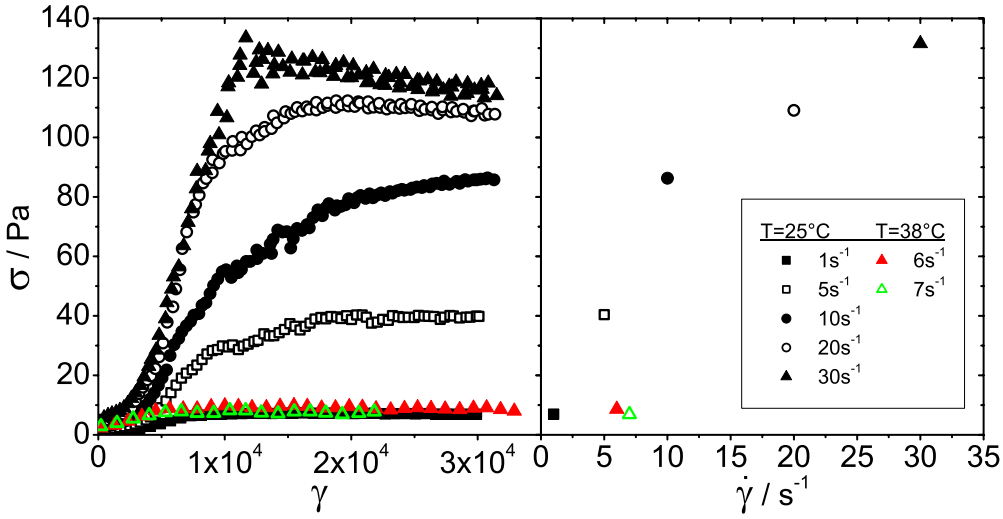

Figure 10.2: Data of startup experiments from chapter 5 for shear rates 1, 5, 10, 20, 30s^{-1} at 25°C and 6, 7s^{-1} at 38°C replotted. Left: Transient stress as a function of deformation. Right: Corresponding steady state values of the stress as a function of shear rate.

stresses increase with deformation until they reach a steady state value (see figure 10.2, left). In conjunction with rheo-SANS and rheo-SALS it became clear that these steady state stresses correspond to distinct microstructures. The steady state stresses reveal two regimes (figure 10.2, right). First a strong increase of the stress is observed at low shear rates. This is the region where states II-IV are the steady state structures. At higher shear rates, corresponding to the regime where state V is the steady state structure, the stress increase is weaker.

Above all, the experiments at 38°C show a very similar stress evolution as the shear rate 1s^{-1}, with very similar structures involved, as revealed by SANS. By increasing temperature the mean curvature and concomitantly the bilayer splay modulus $\overline{\kappa}_b$ is tuned. The strain dependence of the transition does not seem to be affected, but the critical stress of MLV-formation is increased. It is apparently increasingly difficult to create a spherical deformation. Thus, by increasing $\bar{\kappa}_b$, the critical stress for MLV-formation is increased as well. Consequently, a shear rate of 7s^{-1}

or more precisely the corresponding stress at 38°C cannot induce a spherical deformation of the bilayer and a substantial fraction of the lamellae remains planar or buckled and also the transition state itself is less pronounced. Even more, at 42°C a shear rate of $10s^{-1}$ leads to a completely planar, well oriented lamellar phase, a fact that was the prerequisite for all startup experiments. In fact shear rates well above $30s^{-1}$ have to be applied to produce MLVs at 42°C. Further evidence for the stress control of this transition came from the comparison of two different surfactants of the homologous series C_nE_m, namely $C_{10}E_3$ and $C_{12}E_4$ samples with the same membrane volume fraction. Since the bilayer rigidity of $C_{12}E_4$ can be expected to be higher, more energy has to be introduced to increase the curvature of the bilayers. Consequently, the critical stress for the transition will be higher. Rheo-SANS experiments revealed, that the transition is about three times faster and the steady state viscosities are by a factor of 1.7 higher compared to $C_{10}E_3$. In rate controlled experiments the higher viscosity leads to higher stresses and consequently the transition to MLVs is faster.

10.1.2 Flowreversal Experiments

After confirming the stability of any state along the transition coordinate upon cessation of flow, flowreversal experiments were performed. These experiments lead to the next level of understanding in particular the transitions of lamellar orientations at short times (small deformations), which have remained elusive in the continuous shear experiment.

The structural information from rheo-SANS and rheo-SALS was furthermore used to establish a masterplot of the transition from experiments with varying strain amplitudes. A clear slowing down of the transition with decreasing the strain amplitude was observed. From this slowing down it was concluded that there have to be reversible and irreversible contributions to the transition. These contributions can be expressed by a loss factor similarly defined as by Fritz et al.[27], which shifts the intensity maximum found along the neutral intensity trace in a flowreversal onto that of a continuous experiment.

Despite the overall scaling with reduced accumulated strain (strain of the maximum along the neutral intensity trace relative to the position of the maximum in a continuous experiment), clear deviations are observed in the early and the late stages of the transition. Apparently, the magnitudes of the reversible and irreversible contributions to the transition change along the

transition coordinate. This observation is not surprising, since the viscosity and the elasticity of the sample change during the transition as well, which is an additional indication for the stress control of the transition. This observation was also made by Fritz et al. who used rheological data from stress controlled creep experiments to shift their data from oscillatory shear experiments onto a single mastercurve. As a reference point they defined the minimum in the complex and, respectively, the steady shear viscosity. The rest of the transient complex viscosities does not entirely collapse on one curve. Thus, there have to be additional changes, that lead to the different scaling at the different stages of the transition.

More details about the reversible and irreversible parts of the transition, especially during the early stages of the experiment, were revealed in tangential beam experiments. The tangential beam is in comparison to the radial beam more sensitive to changes of the lamellar orientation distribution, since the initial state is a parallel orientation of the bilayers. The analysis in terms of a Mayer-Saupe intensity distribution gave insight into the change of bilayer orientation distribution and a partial recovery of earlier states of the transition was detected upon every inversion of shear direction. This partial recovery was identified with the reversible part of the transition.

A slowing down of the transition was also observed on larger length scales in rheo-SALS experiments. Viscosities as well as the scattering displayed a similar evolution as in a continuous experiment, but slower. The slowing observed here was comparable with that determined from rheo-SANS measurements.

10.1.3 Laponite Inclusion

The inclusion of laponite clay particles into a lamellar phase is to a small extent possible. Phase studies at rest[38] reveal an insertion limit of clay in lyotropic bilayer systems (L_α and L_3-phase) that is dependent on surfactant concentration, type and bilayer arrangement. The bilayer properties themselves are not changed at the low clay concentrations as was apparent from a peak shape analysis according to Nallet et al.[68] This was additionally affirmed in neutron spin-echo experiments on the same system (see Appendix). It can be argued that a change of the membrane properties of detectable magnitude is a frustration of the system and thus would lead to phase separation. It is nevertheless surprising that even close to the insertion limit no changes

of the fluctuations are observed.

Conversely, shear represents a totally different situation as the system is forced to undergo morphology transitions. Creating curvature may result in conflicts of the stiff laponite particles, whose diameter is several times the bilayer separation, with its environment. These studies revealed that the shear thinning was less pronounced as compared to the pure system. Additionally, a strong dependence of the MLV-radius of the shear stress was found, much more pronounced than it is commonly observed in the corresponding binary system.

A unique observation was made when studying the stress dependence of the lamellar order in rheo-SANS experiments. A sudden decrease in the bilayer separation, so far unparalleled in its magnitude, was observed above $\sigma = 10Pa$; rheo-SALS indicated the start of MLV-formation at this stress. In parallel the membrane properties underwent a drastic change, an observation that is in contrast to the findings at rest.

This transition is unique with respect to the magnitude of the change of bilayer separation, which is of the order of 30%. Furthermore, this change only takes place above a citical stress of 10Pa. This distinguished the change of d observed here from that observed by Yamamoto et al.[82], which was linear with stress and of the order of a few percent, only. They attributed this change to the suppresion of bilayer undulations and to the associated increase in projected area. On the conditions presented above, a micro phase separation seems a plausible explanation for this change in d. As soon as curved areas are created the clay platelets residing in the highly curved centers of the MLVs would be in conflict with their environment. Consequently, laponite platelets reside either in the outer shells of or between the MLVs. There their presence leads to an osmotic pressure difference between clay rich areas and the lamellar domains. This leads to water drain from the lamellar domains. As a consequence MLVs are most likely spherical and the interstitial volume filled with water takes about 35% of the total volume, comparable to a random closed packing of spheres.

Clay contrast experiments were also performed in SANS. Those experiments did not reveal any changes of platelet orientation with increasing stress. The 2-dimensional scattering patterns were isotropic, the radially averaged intensity distributions, however, displayed a slope of $q^{-1.5}$ at low q. A fully isotropic distribution of platelet orientations would lead to a q^{-2} behavior in this q-range and thus the platelet orientation distribution is not fully isotropic. This anisotropy would be visible in a tangential beam experiment, which, however, is not feasible, owing to the

high incoherent background of the contrast conditions used in this case.

10.1.4 L_3-Phase under Shear

The L_3-phase can be described in terms of the stability plot for the different bilayer topologies as shown in figure 10.1. The same parameters that stabilize the L_α-phase, namely the bilayer bending and the Gaussian modulus, govern the stability of this phase. It was thus interesting to compare the influence of shear on the L_3- with that on the L_α-phase.

Details of the transitions between the isotropic L_3- to the shear aligned L_α-phase were studied for different membrane volume fractions by increasing the shear rate and thus determining the critical shear rate for the shear induced alignment of bilayers, as well as in shear quench experiments, i.e., the relaxation from the shear aligned back to the isotropic state.

In conclusion, this study showed that the L_3–to–lamellar transition under shear can be examined by rheo-birefringence. This study revealed a weaker Φ_m-dependence of the critical shear rate than expected from theory (equation 8.1) or in comparison to the experiments performed by Porcar et al. However, it has been argued that the viscosity entering equation 8.1 should be the sample viscosity, which itself is Φ_m-dependent, and smaller powerlaw exponents for the critical shear rate were fond in other studies as well.[125] Furthermore, the relaxation experiments from the shear aligned state back to the isotropic were possible by a careful control of the starting conditions.

Interestingly, the relaxation from the shear aligned back to the isotropic state displayed a different scaling with membrane volume fraction than that studied in temperature jump experiments. Although the process leading to the relaxation, namely the topological relaxation by formation of handles, is probably identical in both cases, the starting conditions are different, which might explain these different findings.

10.1.5 The Tangential Beam

Many small-angle neutron scattering studies of anisotropic materials subjected to shear involve the use of the so-called tangential beam configuration. Also in the presented study on the influence of shear on lyotropic lamellar phases extensive use of this configuration was made. A central problem often encountered in rheo-SANS studies is the asymmetry of the 2-dimensional

intensity distribution in tangential beam experiment, which is normally ignored. As a consequence most of the tangential beam data is not presented on absolute scale or even without the proper background correction. This gap was closed by the instrumental study performed in the last part of this thesis. As a result of a geometrical description a rather simple experimental approach to account for the asymmetry of tangential beam data is now available.

10.2 Comparison of the Different Systems

In conclusion, various systems were studied with respect to their shear induced transitions and their transient and steady state behavior. So far, the different systems were discussed separately, which was necessary to achieve an understanding of the different problems investigated in this thesis. To gain a more global understanding of the influence of shear on these systems, it will be discussed in the context of the membrane properties. Two categorizations will be useful for this purpose.

1. The shear induced transitions in the L_α- and L_3-phases can be discussed together.

2. An attempt to compare the pure binary and doped systems by these means is useful.

Both L_α and L_3-phases have zero mean curvature. They can only be distinguished with respect to their Gaussian bilayer curvatures, which are either zero in case of the lamellar or negative in case of the L_3-phase.
In both cases a shear induced change in topology takes place. Apparently, increasing shear rate or respectively shear stress favors structures with a smaller Gaussian bilayer curvature. Additionally, the critical stress for such a transition, especially in case of the lamellar–to–MLV transition, intimately depends on the the Gaussian bilayer modulus (see figure 10.1).
Since spontaneous curvature of the monolayer enters the Gaussian bilayer modulus it is temperature dependent and the correct sequence of phases (MLV–planar lamellae–L_3-phase) is picked up. However, a quantitative analysis of the stability diagram in figure 10.1 reveals that thermodynamically stable MLVs should have a spontaneous curvature, which is comparable to that of spherical micelles. Using equation 10.5, the condition $2\kappa_b = -\bar{\kappa}_b$, which defines the separation line of lamellar and MLV stability regions, with the bending energy for a MLV being $4\pi(2\kappa_b+\bar{\kappa}_b)$,

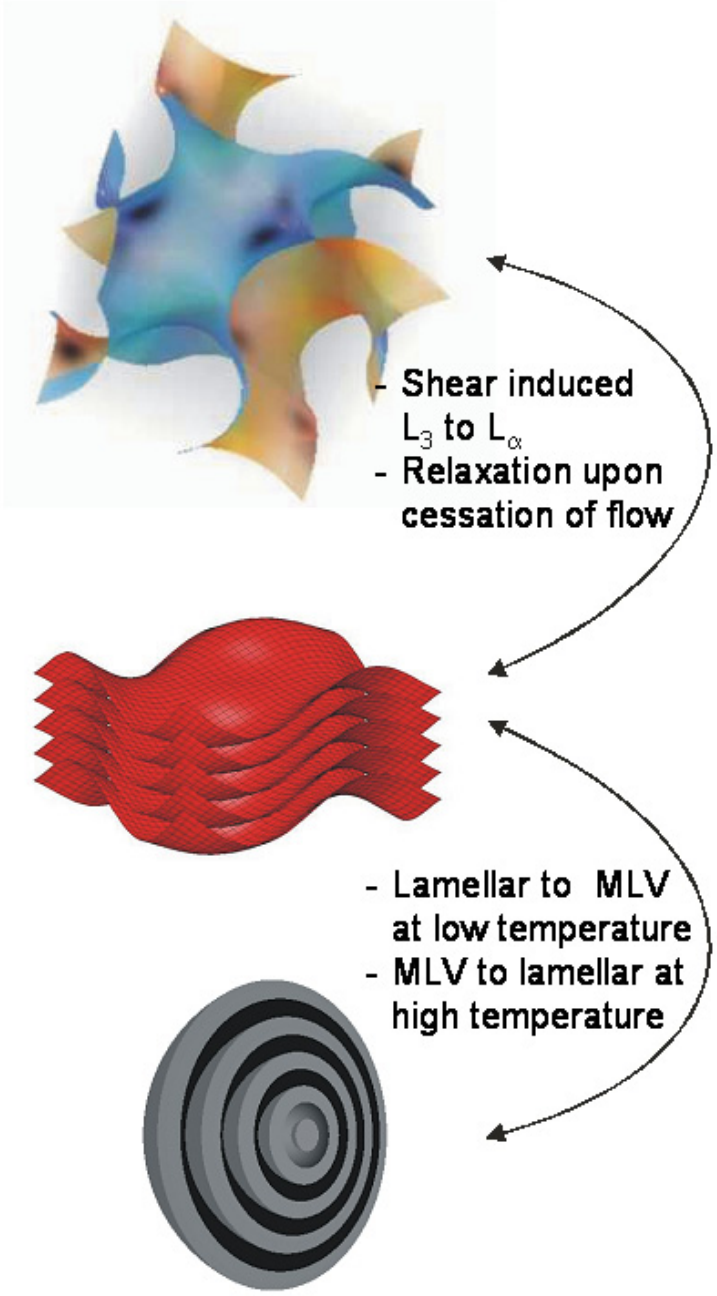

Figure 10.3: Schematic of the sequence of structures found, when subjecting bilayer systems to shear. The arrows describe the transitions that were studied in the presented thesis.

and assuming that $\bar{\kappa}_{mono} = -\kappa_{mono}$, one can write:

$$\begin{aligned} 2\kappa_b + \bar{\kappa}_b &= 4\kappa_{mono} - 2\bar{\kappa}_{mono} - \kappa_{mono} l_0 H_0 \\ 0 &= 4\kappa_{mono} + 2\kappa_{mono} - \kappa_{mono} l_0 H_0 \\ 2\kappa_{mono} &= \kappa_{mono} (6 - l_0 H_0) \\ H_0^{-1} l_0 &= 2 \end{aligned} \tag{10.6}$$

Thus $H_0 l_0$ is of the order of unity, which is the value found for spherical micelles. In such a situation the micelles lead to a gain in entropy, and consequently MLVs would be unstable, at least in binary surfactant/water systems. Nevertheless, MLVs appear as shear induced, metastable aggregates in the lower temperature region of the L_α-phase. These aggregates can be stable for very long times.

The origin of this extraordinary stability of the metastable MLV-state was discussed in terms of the surface free energy by Olsson and Wennerström[140] using higher order corrections in curvature. Depending on the specific correction used, a ripening of the MLVs, which are initially of a broad size distribution, toward either a monodisperse MLV-dispersion with a mean size equivalent to that of the initial size distribution or to a bimodal distribution with mostly small MLVs and a few large ones, is predicted. They argue that for the case that membrane fusion is a rare event, MLVs are thus trapped in such a metastable state, which can be stable up to month or even years.

These predictions are in good agreement with our observations. Once MLVs of a certain size are formed by applying a shear field, they are stable for long times. The result of shearing a nonionic lamellar phase of for instance 40wt% $C_{10}E_3$ in D_2O with a high shear rate ($\dot{\gamma} \geq 10 s^{-1}$) is a monodisperse MLV-sample, which is stable for very long times. Such MLV-dispersions can even become as monodisperse that the spatial confinement requires a hexagonal packing of the MLVs in a foam like structure. This was observed before[12,93,103] and an example for the 40wt% $C_{10}E_3$-system is included in the appendix (see figure 12.14).

Figure 10.3 shows the bilayer structures and the respective transitions, which were of interest to the presented work. The transition from planar lamellae to MLVs has been discussed extensively in chapters 5 and 6. The reverse transition, however, was not addressed so far. The transition from MLV to planar lamellae is less reproducible, but nevertheless interesting to study. The reasons for the difficulties are two-fold.

1. The specific transition path seems to depend delicately on sample history, i.e., the prepa-

ration of MLVs, and thus size and size distribution, strongly influence the results.

2. A radial rheo-SANS experiment only gives information about the decay of the vesicular structure, not about the evolving parallel lamellae. Thus, additional tangential beam experiments yield more meaningful observations.

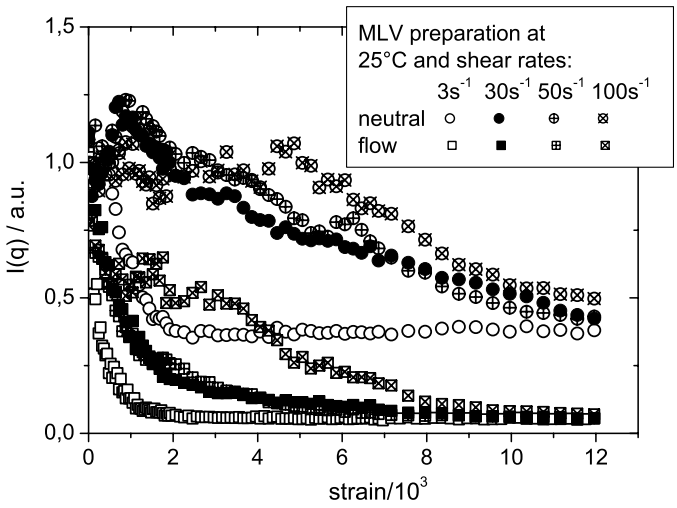

Figure 10.4: Intensity traces evaluated at the Bragg-peak position along the neutral and flow directions of radial beam experiments for the transition MLV–to–lamellar at 42°C and a shear rate of $10s^{-1}$. The MLVs were prepared at 25°C with different shear rates until steady state was reached.

Figures 10.4 and 10.5 display such experiments. One can see that the evolution of the intensities in radial beam experiments is not very reproducible. MLV-size seems to have an influence on the transition path as is evident from figure 10.4. Larger MLVs (preparation at $3s^{-1}$) seem to be more readily transformed into planar lamellae and a clear steady state is reached within the course of the experiment. Smaller MLVs (preparation at shear rates 30 - 100^{-1}) display a slower decay as evident from the intensity trace in flow direction and the neutral direction displays a qualitatively different evolution. Since no tangential beam data are available, one can only speculate at this point whether this is the signature of a cylindrical scattering symmetry or if it is simply that of perpendicular lamellae.

Even with identical starting conditions, i.e., preparation at 25°C and $100s^{-1}$ (see figure 10.5,

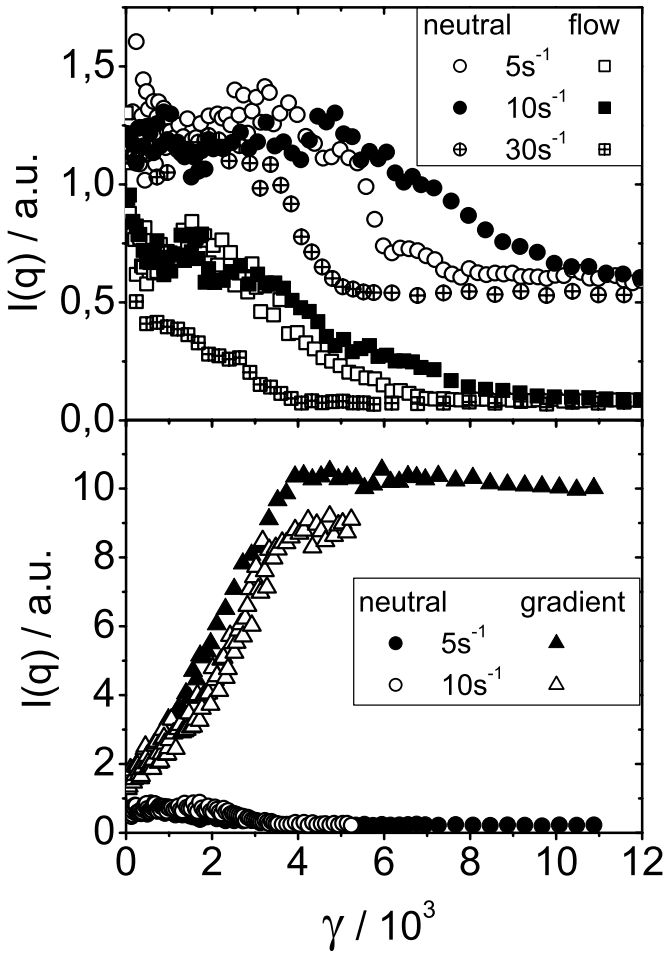

Figure 10.5: Top: Intensity traces along the neutral and flow directions for the same transition with different shear rates, radial beam. Bottom: Intensity traces along the neutral and gradient directions for shear rates 5 and $10s^{-1}$, tangential beam. MLV-preparation was performed at 25°C with a shear rate of $100s^{-1}$.

top), the neutral intensity trace, which contains information about lamellae in perpendicular orientation, does not display a scaling with strain as it was observed for the reverse transition. This is not surprising, since the perpendicular orientation under these conditions is not exposed to a torque and thus the factors that might influence the specific reorientation of these lamellae will depend on subtle disturbances of the flow field. These disturbances may originate from MLVs that pass and thus cause neighboring perpendicular lamellae to tilt out of the flow–velocity

gradient plane. As soon as all MLVs are turned into planar lamellae, these disturbances are not present anymore and the remaining perpendicular lamellae are stuck in this orientation.

A coherent picture is obtained in tangential beam experiments (see figure 10.5, bottom), where the transition is compared for shear rates 5 and $10s^{-1}$ with the same starting conditions as the corresponding radial beam experiments. The transition is dominated by a monotonous increase of the intensity along the gradient direction. Hence, MLVs are successively transformed into planar lamellae, which immediately acquire the parallel orientation. Additionally, there is an apparent scaling of the transition with strain as was already observed for MLV-formation. The evolution of the neutral intensity trace is of minor importance.

As is also evident from figure 10.5, no state with cylindrical symmetry is involved in the transition from MLVs to planar lamellae, at least not after a preparation with $\dot{\gamma} = 100s^{-1}$, i.e. rather small MLVs ($R_m lv \approx 600nm$). In summary, the transition from MLVs to planar lamellae is far more complex as the reverse transition, since numerous parameters define the starting conditions.

The evolving picture for this transition bears similarities to the predictions for the ripening process of MLVs at rest. Despite the obvious difference, namely the presence of a shear field, which in the discussion of the Ostwald ripening process of MLVs is explicitly excluded by considering a situation, where no tension is exerted on the surfactant bilayers,[140] the analogy is tempting. Apparently, the transition from large, polydisperse MLVs (preparation at $3s^{-1}$) to planar lamellae is quicker than that from monodisperse, small MLVs.

Thus, the attempt to study the different shear induced transitions in a bilayer system, namely planar lamellae–MLV and L_3–planar lamellae in both directions (see figure 10.3), yields to a coherent picture of bilayer systems under shear. Both transitions can be discussed in terms of the flexible surface model as presented above. This approach has proved successful in describing MLV-formation qualitatively but also the L_3–to–L_α-transition is well described by this formalism.

Within this formalism the bilayer topologies studied in this thesis are qualitatively reproduced and the controlling parameter seems to be the spontaneous curvature. Not only MLV, lamellar and L_3-phase, but also the intermediate morphologies found in startup experiments fit into this picture. However, a quantitative analysis reveals, that MLVs are not stable (equation 10.6). They are rather a metastable morphology that displays extraordinary longtime stability. Thus,

other properties that depend on spontaneous curvature need to play a role in defining the stability regions of the respective topologies (MLV or lamellar, figure 10.1).
An additional common aspect of the two different transitions presented here, is the similarity to phase transitions at rest. In the case of MLVs this transition is expected at negative $\bar{\kappa}_b$, but it is not observed owing to the competition with the entropically favored spherical micelles. The analogy is more obvious for the L_3–L_α transition under shear, where the underlying equilibrium phase transition is accessible in the phase diagram. Such comparisons were also drawn in the case of the shear alignment of wormlike micelles and characteristics of a first order phase transition were discussed in this respect.[98,137,141] Indications for the first order nature of the L_3–L_α transition and its relaxation were observed in the experiments presented in chapter 8.

The major conclusions from the comparison of pure with clay containing lamellar phase are that the clay introduces subtle interactions between bilayer and laponite platelets. These interactions do not affect the equilibrium properties of the lamellar phase at rest to a measurable extend. Neither SANS nor NSE experiments revealed the influence of the clay platelets on the fluctuation dynamics, wavelength and amplitude of the bilayers.[38,119]
It is possible that the influence is negligible up to the insertion limit and above it the perturbations of the lamellar stabilization mechanism are so strong, that phase separation occurs. Another possibility is, that the local perturbation of the undulation by the clay is not visible owing to the low clay content. In both cases it is still puzzling that the separation occurs at such low clay content or small perturbations of the lamellar phase.
As soon as shear is imposed on the clay containing sample the difference becomes more evident. The change that the environment of the clay undergoes above a certain stress imposes stronger conflicts on the clay as the planar lamellae. As soon as MLVs are formed highly curved areas evolve, in which the clay would experience strong excluded volume effects. It is in much less conflict with its environment if it moves to the outer shells of the MLVs or in the space between them.
Thus the difference between pure binary and clay containing lamellar phases is not found in their behavior at rest but it lies in their behavior under shear.

11 Outlook

The recent instrumental improvement of the rheo-SALS joined with improved data reduction routines as the sector averaging software for the treatment of anisotropic data, kindly provided by Dr. Falk Renth and a number of fitting routines that were developed during this PhD-thesis using Matlab 6.5©The Mathworks Inc., will greatly facilitate the handling of time-resolved measurements in rheo-SALS and rheo-SANS. The extraction of relevant parameters from a series of experiments taking the whole scattering information into account is no longer a time consuming task.

Furthermore, the Nallet-model, taking into account instrumental resolution, is used to put the analysis of isotropic lamellar scattering on firm ground. An example of such a fit for a 10wt% $C_{12}E_4$-sample in D_2O doped with 0.5mol% SDS is shown in figure 11.1. The model can be fitted to data obtained from different detector distances, yielding one parameter set, namely the hydrophobic bilayer thickness δ_t, the width of the excess scattering length density profile σ, and the Caillé-parameter η_{caille}. A detailed describtion of such a fit is provided in a separate manual.

Where there are results there are also questions and hopefully this thesis has risen some interesting ones. There are a number of aspects worth continuing to study.

1. Completion of start-up experiments

    - Thinking the flowreversal experiments uncompromisingly to the end, the next step would be performing stress-controlled oscillatory shear experiments on the well aligned lamellae, where both, stress amplitude and frequency have to be varied systematically. Creep experiments starting from the parallel alignment could complete this series. Preliminary test measurements performed in the rheo-SALS setup can be found in the appendix.
    - Furthermore, a variation of the surfactant volume fraction should be performed over

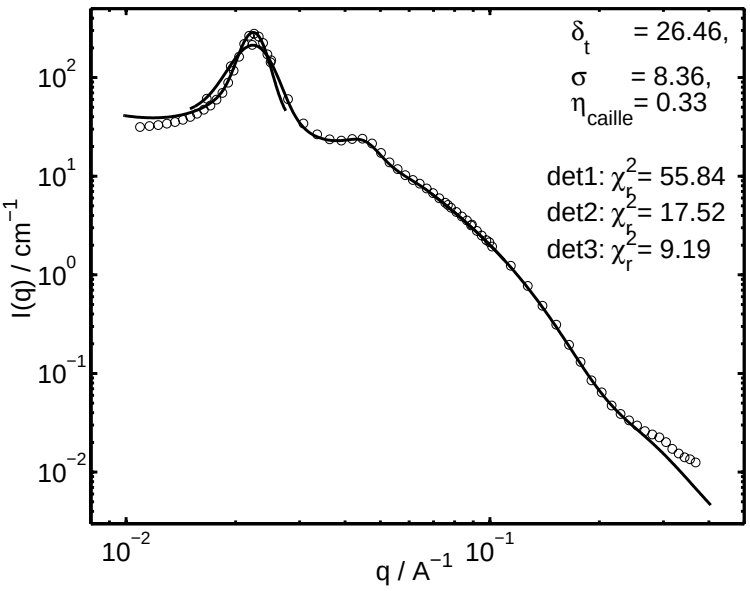

Figure 11.1: Nallet model[68] (see equations 4.2-4.7) fitted to the scattering data of a 10wt% $C_{12}E_4$-sample in D_2O doped with 0.5mol% SDS measured at D22 at three different detector positions. The fits to the different detector settings yield the same parameter set. However, they do not overlap, since the resolution function is different for the different instrumental configurations. The deviation at high q is due to the difficulty of determining the incoherent background. At lower q deviations result, since the model only describes the undulations in a stack of planar lamellae. Thus, the scattering of a system of MLVs reveals deviations at larger length scales (low q).

a reasonable range of lamellar spacing. One problem in the case of the $C_{10}E_3$ samples has been the lack of correlation at concentrations below 30wt% (here see Appendix for more details). This problem could be by-passed by using a slightly charged system, so that spanning a range of concentrations from about 10 up to 40wt%, and thus a fourfold increase in the lamellar spacing, is possible. Also changing the gap size of the shear geometry should be considered in this context, since then a quanititative comparison with the study by Courbin et al.[23,90] is possible.

- Changing the solvent viscosity or using different surfactants (e.g. $C_{16}E_4$) may help to settle the debate as to whether the shear rate or the shear stress governs the transition from planar lamellae to MLVs.

2. The inclusion of laponite into a lamellar phase, leading to the micro-phase separation under shear, does surprisingly not change the dynamics of the bilayer fluctuations. Furthermore, it is yet not clear, where exactly the laponite platelets reside at rest as well as under shear.

   - The first issue could be addressed with a series of NSE-experiments, where the clay content is systematically varied. In that case it might be advisable to use the $C_{12}E_5$/laponite system, since it is apparently easier to handle and its bilayer rigidity is considerably lower.[38] Consequently, the fluctuations may be easier to affect. Additionally, a range of laponite concentrations up to S/L=2% is accessible in a surfactant concentration range between 10 and 30wt%. Lower surfactant concentrations will also lead to slower dynamics and esure a better quality of the spin-echo data. Furthermore, one can ensure that the limit of high-q, required for the complete analysis of the NSE-data, is reached.[73,74]
   - Fluorescence labeling may help localizing the clay platelets in the lamellar phase at rest and under shear in fluorescence microscopy experiments.

3. The influence of shear on the L_3–to–lamellar transition was studied in flow birefringence experiments and, although very extensively examined, many questions remain. One key point crystallized: The unexpected behavior may be due to the complex nature of the swollen bilayer of the L_3-phase used in our study and if so, does this behavior prevail on other length scales as well? Therefore a whole agenda of experiments should be followed up on, including SANS and SAXS at rest as well as under shear.

   - The experiments performed here, should be repeated using rheo-SANS. Special care has to be taken of the temperature control and preventing evaporation of the solvent.[126,127,139]
   - Additionally one could consider SANS and SAXS experiments at rest to use the different contrast situations for the full characterization of the dependence of the membrane properties as a function of membrane volume fraction. Models for this venture are available in the literature.[129,130,142,143]

Bibliography

[1] Schrödinger, E. *What is life;* Cambridge at the University Press: Cambridge, 1944.

[2] Butler, P. *Curr. Opin. Colloid Interface Sci.* **1999,** *4,* 214-221.

[3] Balzer, D.; Varwig, S.; Weihrauch, M. *Colloid Interface Sci. A* **1995,** *99,* 233-246.

[4] Schubert, B.; Kaler, E.; Wagner, N. *Langmuir* **2003,** *19,* 4079-4089.

[5] Pencer, J.; Hallett, F. R. *Phys. Rev. E* **2000,** *61,* 3003.

[6] Stauch, O.; Schubert, R.; Savin, G.; Burchard, W. *Biomacromolecules* **2002,** *3,* 565.

[7] Bernheim-Grosswasser, A.; Ugazio, S.; Gauffre, F.; Viratelle, O.; Mahy, P.; Roux, D. *J. Chem. Phys.* **2000,** *112,* 3424-3430.

[8] Richtering, W. *Curr. Opin. Colloid Interface Sci.* **2001,** *6,* 446-450.

[9] Roux, D.; Nallet, F.; Diat, O. *Europhys. Lett.* **1993,** *24,* 53.

[10] Bergenholtz, J.; Wagner, N. *Langmuir* **1996,** 3122-3126.

[11] Diat, O.; Roux, D.; Nallet, F. *J. Phys. IV* **1993,** *3,* 193-200.

[12] Diat, O.; Roux, D.; Nallet, F. *Phys. Rev. E* **1995,** *51,* 3296.

[13] Leon, A.; Bonn, D.; Meunier, J. *Phys. Rev. Lett.* **2000,** *84,* 1335.

[14] Panizza, P.; Roux, D.; Vuillaume, V.; Lu, C.-Y. D.; Cates, M. E. *Langmuir* **1996,** *12,* 248.

[15] Panizza, P.; Colin, A.; Coulon, C.; Roux, D. *Eur. Phys. J. B* **1998,** *4,* 65.

[16] Müller, S.; Börschig, C.; Gronski, W.; Schmidt, C.; Roux, D. *Langmuir* **1999,** *15,* 7558.

[17] Zipfel, J.; Berghausen, J.; Lindner, P.; Richtering, W. *Europhys. Lett.* **1998,** *43,* 683-689.

[18] Zipfel, J.; Berghausen, J.; Lindner, P.; Richtering, W. *J. Phys. Chem. B* **1999,** *103,* 2841-2849.

[19] Zipfel, J.; Berghausen, J.; Schmidt, G.; Lindner, P.; Alexandridis, P.; Tsianou, M.; Richtering, W. *Phys. Chem. Chem. Phys.* **1999,** *1,* 3905.

[20] Zipfel, J.; Lindner, P.; Richtering, W. *Physica B* **1998,** *241-243,* 1002-1004.

[21] Zipfel, J.; Lindner, P.; Richtering, W. *Progr. Colloid Polym. Sci.* **1998,** *110,* 139-143.

[22] Zipfel, J.; Lindner, P.; Tsianou, M.; Alexandridis, P.; Richtering, W. *Langmuir* **1999,** *15,* 2599-2602.

[23] Courbin, L.; Delville, J. P.; Rouch, J.; Panizza, P. *Phys. Rev. Lett.* **2002,** *89,* 8305.

[24] Zipfel, J.; Nettesheim, F.; Lindner, P.; Le, T. D.; Olsson, U.; Richtering, W. *Europhys. Lett.* **2001,** *53,* 335.

[25] Berghausen, J.; Zipfel, J.; Diat, O.; Naranayan, J.; Richtering, W. *Phys. Chem. Chem. Phys.* **2000,** *2,* 3623-3626.

[26] Nettesheim, F.; Zipfel, J.; Lindner, P.; Richtering, W. *Coll. Surf. A* **2001,** *563,* 183.

[27] Fritz, G.; Wagner, N. J.; Kaler, E. W. *Langmuir* **2003,** *19,* 8709.

[28] Berghausen, J.; Zipfel, J.; Lindner, P.; Richtering, W. *J. Phys. Chem. B* **2001,** *105,* 11081.

[29] Bouglet, G.; Ligoure, C. *Eur. Phys. J. B* **1999,** *9,* 137.

[30] Gompper, G.; Richter, D.; Strey, R. *J. Phys.: Condens. Matter* **2001,** *13,* 9055.

[31] Endo, H.; Allgaier, J.; Gompper, G.; Jakobs, B.; Monkenbusch, M.; Richter, D.; Sottmann, T.; Strey, R. *Phys. Rev. Lett.* **2000,** *85,* 102.

[32] Yang, B.-S.; Lal, J.; Kohn, J.; Huang, J. S.; Russel, W. B.; Prud'homme, R. K. *Langmuir* **2001,** *17,* 6692-6698.

[33] Yang, B.-S.; Lal, J.; Mihailescu, M.; Monkenbusch, M.; Richter, D.; Huang, J. S.; Kohn, J.; Russel, W. B.; Prud'homme, R. K. *Langmuir* **2002,** *18,* 6-13.

[34] Yang, B.-S.; Lal, J.; Richetti, P.; Marques, C. M.; Russel, W. B.; Prud'homme, R. K. *Langmuir* **2001,** *17,* 5834-5841.

[35] Yang, Y.; Prudhomme, R.; McGrath, K.; Richetti, P.; Marques, C. *Phys. Rev. Lett.* **1998,** *80,* 2729-2732.

[36] Jonströmer, M.; Strey, R. *J. Phys. Chem.* **1992,** *96,* 5993-6000.

[37] Arrault, J.; Grand, C.; Poon, W.; Cates, M. E. *Europhys. Lett.* **1997,** *38,* 625.

[38] Grillo, I.; Levitz, P.; Zemb, T. *Eur. Phys. J. E* **2001,** *5,* 377.

[39] van der Linden, E.; Hogervorst, W. T.; Lekkerkerker, H. N. W. *Langmuir* **1996,** *12,* 3127.

[40] Zilman, A. G.; Granek, R. *Eur. Phys. J. B* **1999,** *11,* 593.

[41] Marlow, S. W.; Olmsted, P. D. *Eur. Phys. J. E* **2002,** *8,* 485.

[42] Auernhammer, G.; Brand, H.; Pleiner, H. *Phys. Rev. E* **2002,** *66,* 1707.

[43] Horn, R. G.; Kleman, M. *Ann. Phys.* **1978,** *3,* 229.

[44] Cates, M. E.; Milner, S. T. *Phys. Rev. Lett.* **1989,** *62,* 1856.

[45] Gradzielski, M. . In *Soft matter: complex materials on mesoscopic scale*; Dhont, J. K. G.; Gompper, G.; Richter, D., Eds.; Forschungszentrum Jülich GmbH: Jülich, 2002.

[46] Israelachvili, J. N.; Mitchell, D. J.; Ninham, B. *J. Chem. Soc. Faraday Trans. II* **1976,** *72,* 1525.

[47] Strey, R.; Schomäcker, R.; Roux, D.; Nallet, F.; Olsson, U. *J. Chem. Soc. Faraday Trans.* **1990,** *86,* 2253-2261.

[48] Porte, G. Surfactant Micelles and Bilayers: Shapes and Interactions. In *Neutrons, X-rays and Light: Scattering Methods Applied to Soft Condensed Matter*, 1st ed.; Lindner, P.; Zemb, T., Eds.; North-Holland Delta Series Elsevier: Amsterdam, 2002.

[49] Evans, D. F.; Wennerström, H. *The Colloidal Domain: Where Physics, Chemistry, Biology and Technology meet;* Advances in Interfacial Engineering Series Wiley-VCH: New York, 2nd ed.; 1999.

[50] Daicic, J.; Olsson, U.; Wennerström, H.; Jerke, G.; Schurtenberger, P. *Phys. Rev. E* **1997,** *56,* 1278-1279.

[51] Diat, O.; Roux, D. *Langmuir* **1995,** *11,* 1392.

[52] Macosko, C. W. *Rheology: Principles, Measurements and Applications;* Advances in Interfacial Engineering Series Wiley-VCH: New York, 1st ed.; 1994.

[53] Spalla, O. General Theorems in Small-Angle Scattering. In *Neutrons, X-rays and Light: Scattering Methods Applied to Soft Condensed Matter*, 1st ed.; Lindner, P.; Zemb, T., Eds.; North-Holland Delta Series Elsevier: Amsterdam, 2002.

[54] Glatter, O. Fourier Transformation and Deconvolution. In *Neutrons, X-rays and Light: Scattering Methods Applied to Soft Condensed Matter*, 1st ed.; Lindner, P.; Zemb, T., Eds.; North-Holland Delta Series Elsevier: Amsterdam, 2002.

[55] Rayleigh, L. *Proc. Roy. Soc. London Series A* **1911,** *84,* 25-46.

[56] Fournet, G. *Bull. Soc. Fr. Mineral. Crist.* **1951,** *74,* 39-113.

[57] Samuels, R. J. *J. Polym. Sci. Part A* **1971,** *9,* 2165.

[58] Stein, R. S.; Wilkes, G. L. . In *Phisico-chemical approaches to the measurement of anisotropy*; Ward, I. M., Ed.; Appl. Sci. Publ.: London, 1975.

[59] Lindner, P. Scattering Experiments under External Constraints: SANS and Shear Flow. In *Neutrons, X-rays and Light: Scattering Methods Applied to Soft Condensed Matter*, 1st ed.; Lindner, P.; Zemb, T., Eds.; North-Holland Delta Series Elsevier: Amsterdam, 2002.

[60] Munter, A. *http://www.ncnr.nist.gov/resources/n-length* .

[61] Schurtenberger, P. Contrast and Contrast Variation in Neutron, X-ray and Light Scattering. In *Neutrons, X-rays and Light: Scattering Methods Applied to Soft Condensed Matter*, 1st ed.; Lindner, P.; Zemb, T., Eds.; North-Holland Delta Series Elsevier: Amsterdam, 2002.

[62] May, R. Biological Applications of Small-Angle Neutron Scattering. In *Neutrons, X-rays and Light: Scattering Methods Applied to Soft Condensed Matter*, 1st ed.; Lindner, P.; Zemb, T., Eds.; North-Holland Delta Series Elsevier: Amsterdam, 2002.

[63] Lindner, P. Scattering Experiments: Experimental Aspects, Initial Data Reduction and Absolute Calibration. In *Neutrons, X-rays and Light: Scattering Methods Applied to Soft Condensed Matter*, 1st ed.; Lindner, P.; Zemb, T., Eds.; North-Holland Delta Series Elsevier: Amsterdam, 2002.

[64] Lindner, P. *J. Appl. Cryst.* **2000,** *33,* 807.

[65] Pedersen, J. *J. Physique I* **1993,** *3,* 491.

[66] Pedersen, J. S. Instrumentation for Small-Angle X-ray and Neutron Scattering and Instrumental Smearing Effects. In *Neutrons, X-rays and Light: Scattering Methods Applied to Soft Condensed Matter*, 1st ed.; Lindner, P.; Zemb, T., Eds.; North-Holland Delta Series Elsevier: Amsterdam, 2002.

[67] Helfrich, W. *Z. Naturforsch. A* **1978,** *33A,* 305.

[68] Nallet, F.; Laversanne, R.; Roux, D. *J. Phys. II France* **1993,** *3,* 487.

[69] Caillé, M. A.; Seances, C. R. . In *Acad. Sci., Ser. B*, Vol. 274; 1972.

[70] Lemmich, J.; Mortensen, K.; Ipsen, J. H.; Hønger, T.; Bauer, R.; Mouritsen, O. G. *Mol. Cryst. Liq. Cryst.* **1999,** *332,* 531.

[71] Dewhurst, C. *http://www.ill.fr/lss/grasp/grasp_main.html* .

[72] Zorn, R. Inelastic Neutron Scattering: Dynamics of Polymers. In *Neutrons, X-rays and Light: Scattering Methods Applied to Soft Condensed Matter*, 1st ed.; Lindner, P.; Zemb, T., Eds.; North-Holland Delta Series Elsevier: Amsterdam, 2002.

[73] Zilman, A. G.; Granek, R. *Phys. Rev. Lett.* **1996,** *7,* 4788.

[74] Mihailescu, M.; Monkenbusch, M.; Allgaier, J.; Frielinghaus, H.; Richter, D.; Jakobs, B.; Sottmann, T. *Phys. Rev. E 66,*.

[75] Mortensen, K. *Curr. Opin. Colloid Interface Sci.* **2001,** *6,* 140.

[76] Richtering, W. *Progr. Colloid Polym. Sci.* **1997,** *104,* 90-96.

[77] Diat, O.; Nallet, F.; Roux, D. *J. Phys. II* **1993,** *3,* 1427.

[78] Diat, O.; Roux, D.; Nallet, F. *J. Phys. II France* **1994,** *3,* 1427.

[79] Soubiran, L.; Coulon, C.; Sierro, P.; Roux, D. *Europhys. Lett.* **1995,** *31,* 243.

[80] Berghausen, J.; Zipfel, J.; Lindner, P.; Richtering, W. *Europhys. Lett.* **1998,** *43,* 683.

[81] Bergmeier, M.; Gradzielski, M.; Hoffmann, H.; Mortensen, K. *J. Phys. Chem. B* **1999,** *103,* 1605.

[82] Yamamoto, J.; Tanaka, H. *Phys. Rev. Lett.* **1995,** *74,* 932.

[83] Mortensen, K. *J. Phys. Condens. Matter* **1996,** *8,* A103.

[84] Mortensen, K.; Talmon, Y.; Gao, B.; Kops, J. *Macromolecules* **1997,** *30,* 6764.

[85] Schomäcker, R.; Strey, R. *J. Phys. Chem. 98,* 3908- 3912.

[86] Strey, R. *Ber. Bunsenges. Phys. Chem.* **1996,** *100,* 182 -189.

[87] Bouglet, G.; Ligoure, C.; Bellocq, A. M.; Dufourc, E.; Mosser, G. *Phys. Rev. E* **1998,** *57,* 834.

[88] Prud´homme, R. K.; Wu, G.; Schneider, D. K. *Langmuir* **1996,** *12,* 4651-4659.

[89] Dhez, O.; Nallet, F.; Diat, O. *Europhys. Lett.* **2001,** *55,* 821.

[90] Courbin, L.; Pon, R.; Rouch, J.; Panizza, P. *Europhys. Lett.* **2003,** *61,* 275-281.

[91] Escalante, J. I.; Hoffmann, H. *J. Phys. Condens. Matter* **2000,** *12,* A483.

[92] Escalante, J.; Hoffmann, H. *Rheol. Acta* **2000,** *39,* 209-214.

[93] Le, T. D.; Olsson, U.; Mortensen, K. *Phys. Chem. Chem. Phys.* **2001,** *3,* 1310-1316.

[94] Boltenhagen, P.; Yuntao, H.; Matthys, E. F.; Pine, D. *Europhys. Lett.* **1997,** *38,* 389.

[95] Mitchell, D. J.; Tiddy, G. J. T.; Waring, L.; Bostock, T.; McDonald, M. P. J. *J. Chem. Soc. Faraday Trans. 1* **1983,** *79,* 975-1000.

[96] Hendrikx, Y.; Charvolin, J.; Rawiso, M. *J. Colloid Interface Sci.* **1984,** *100,* 597.

[97] Le, T.; Olsson, U.; Mortensen, K.; Zipfel, J.; Richtering, W. *Langmuir* **2001,** *17,* 999.

[98] Porte, G.; Appell, J.; Bassereau, P.; Marignan, J. *J. Phys. France* **1989,** *50,* 1335-1347.

[99] Panizza, P.; Archambault, P.; Roux, D. *J. Phys. II* **1995,** *5,* 303.

[100] Olsson, U.; Wennerström, H. *Adv. Colloid Interface Sci.* **1994,** *49,* 113.

[101] Hu, Y. T.; Boltenhagen, P.; Pine, D. J. *J. Rheol.* **1998,** *42,* 1185.

[102] Meyer, C.; Asnacios, S.; Bourgaux, C.; Kleman, M. *Mol. Cryst. Liq. Cryst.* **1999,** *332,* 531.

[103] Wunenburger, A. S.; Colin, A.; Leng, J.; Arneodo, A.; Roux, D. *Phys. Rev. Lett.* **2001,** *86,* 1374.

[104] Gauffre, F.; Roux, D. *Langmuir* **1999,** *15,* 3738.

[105] Colin, A.; Roux, D. *Eur. Phys. J. E.* **2002,** *8,* 499-506.

[106] Escalante, J. I.; Gradzielski, M.; Hoffmann, H.; Mortensen, K. *Langmuir* **2000,** *16,* 8653.

[107] Nettesheim, F.; Zipfel, J.; Olsson, U.; Renth, F.; Lindner, P.; Richtering, W. *Langmuir* **2003,** *19,* 3603.

[108] Piken, S. J.; Aerts, J.; Visser, R.; Northolt, M. G. *Macromolecules* **1990,** *23,* 3849.

[109] Hoekstra, H.; Vermant, J.; J., M. *Langmuir* **2002,** *18,* 5695.

[110] Läuger, J.; Weigel, R.; Berger, K.; Hiltrop, K.; Richtering, W. *J. Colloid Interface Sci.* **1996,** *181,* 521-529.

[111] Arrault, J.; Poon, W.; Cates, M. *Phys. Rev. E* **1999,** *59,* 3242-3252.

[112] Ligoure, C.; Bouglet, G.; Porte, G. *Phys. Rev. Lett.* **1993,** *71,* 3600-3603.

[113] Castro-Roman, F.; Porte, G.; Ligoure, C. *Phys. Rev. Lett.* **1999,** *82,* 109.

[114] Castro-Roman, F.; Porte, G.; Ligoure, C. *Langmuir* **2001,** *17,* 5045.

[115] Ramaswamy, S. *Phys. Rev. Lett.* **1992,** *69,* 112.

[116] Daoud, M.; De Gennes, P. G. *Journal de Physique* **1977,** *38,* 85.

[117] Groenewold, J.; Frederickson, G. H. *Eur. Phys. J. E* **2001,** *5,* 171.

[118] Weigel, R.; Läuger, J.; Richtering, W.; Lindner, P. *J. Phys. II France* **1996,** *6,* 529-542.

[119] Nettesheim, F.; Monkenbusch, M.; Biehl, R. *unpublished results, see appendix figures 12.6–12.9* .

[120] Cates, M. E. *Macromolecules* **1987,** *20,* 2289-2296.

[121] Bruinsma, R.; Rabin, Y. *Phys. Rev. A* **1992,** *45,* 994-1008.

[122] Porte, G.; Berret, J.-F.; Harden, J. L. *J. Phys. II France* **1997,** *7,* 459-472.

[123] Porte, G.; Delsanti, M.; Billard, I.; Skouri, M.; Appell, J.; Marignan, J.; Debeauvais, F. *J. Phys. II France* **1991,** *1,* 1101-1120.

[124] Porte, G.; Ligoure, C. *J. Chem. Phys.* **1995,** *102,* 4290.

[125] Mahjoub, H. F.; McGrath, K. M.; Kleman, M. *Langmuir* **1996,** *12,* 3131-3138.

[126] Mahjoub, H. F.; Bourgaux, C.; Sergot, P.; Kleman, M. *Phys. Rev. Lett.* **1998,** *81,* 2076-2079.

[127] Butler, P. D.; Porcar, L.; Hamilton, W. A.; Warr, G. G. *Phys. Rev. Lett.* **2002,** *88,* 9601.

[128] Porcar, L.; Hamilton, W. A.; Butler, P. D.; Warr, G. G. *Phys. Rev. Lett.* **2002,** *89,* 8301.

[129] Strey, R.; Glatter, O.; Schubert, K.-V.; Kaler, E. W. *J. Chem. Phys.* **1996,** *105,* 1175-1188.

[130] Lei, N.; Safinya, C. R.; Roux, D.; Liang, K. S. *Phys. Rev. E* **1997,** *56,* 608.

[131] Le, T. D.; Olsson, U.; Wennerström, H.; Schurtenberger, P. *Phys. Rev. E* **1999,** *60,* 4300.

[132] Schwarz, B.; Moench, G.; Ilgenfritz, G.; Strey, R. *Langmuir* **2000,** *16,* 8643.

[133] Waton, G.; Porte, G. *J. Phys. II France* **1993,** *3,* 515-530.

[134] Larson, R. G. *Rheol. Acta* **1992,** *31,* 497.

[135] Le, T.; Olsson, U.; Wennerström, H.; Uhrmeister, P.; Rathke, B.; Strey, R. *J. Phys. Chem. B* **2002,** *106,* 9410.

[136] C., W. R.; J., A. M.; Beyer, W. H., Eds.; *CRC Handbook of Chemistry and Physics;* CRC Press, Inc: Boca Raton, Florida, 67 ed.; 1986-1987.

[137] Porte, G. *Current Opinion in Colloid & Interface Science* **1996,** *1,* 345.

[138] Lindner, P.; Oberthür, R. C. *Rev. Phys. Appl.* **1984,** *19,* 759.

[139] Porcar, L.; Hamilton, W. A.; Butler, P. D.; Warr, G. G. *Rev. Sci. Instrum.* **2002,** *73,* 2345.

[140] Olsson, U.; Wennerström, H. *J. Phys. Chem. B* **2002,** *106,* 5135-5138.

[141] Porte, G.; Appell, J.; Bassereau, P.; Marignan, M.; Skouri, M.; Billard, I.; Delsanti, M.; Candau, S. J.; Strey, R. e. a. *Progress in Colloid & Polymer Science* **1991,** *84,* 264.

[142] Strey, R.; Winkler, J.; Magid, L. *J. Phys. Chem.* **1991,** *95,* 7502-7507.

[143] Teubner, M.; Strey, R. *J. Chem. Phys.* **1987,** *87,* 3195-3200.

12 Appendix

12.1 Construction of a Searle Shear Cell

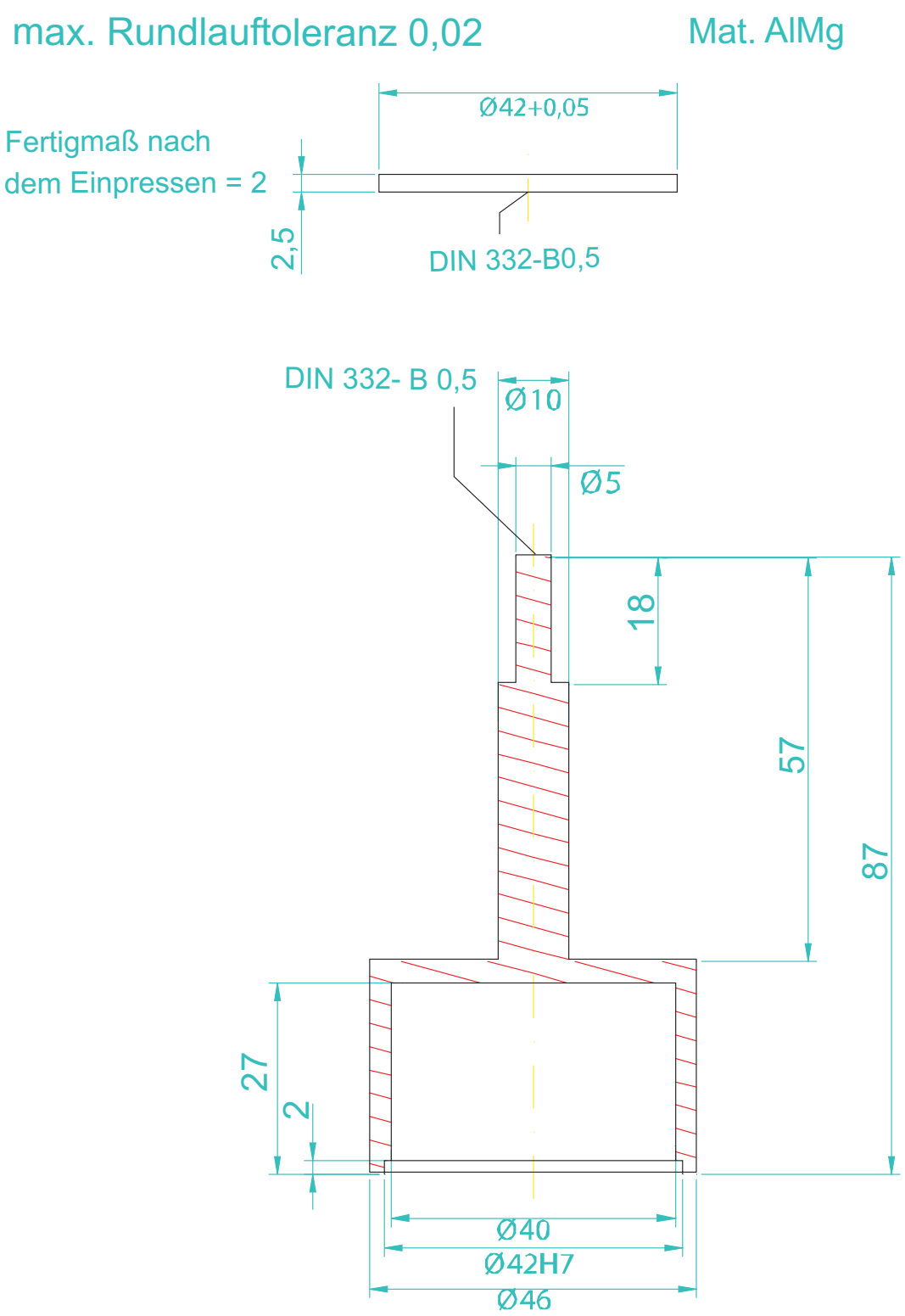

Figure 12.1: Inner cylinder of the Searle shear geometry consisting of a hollow aluminum cylinder.

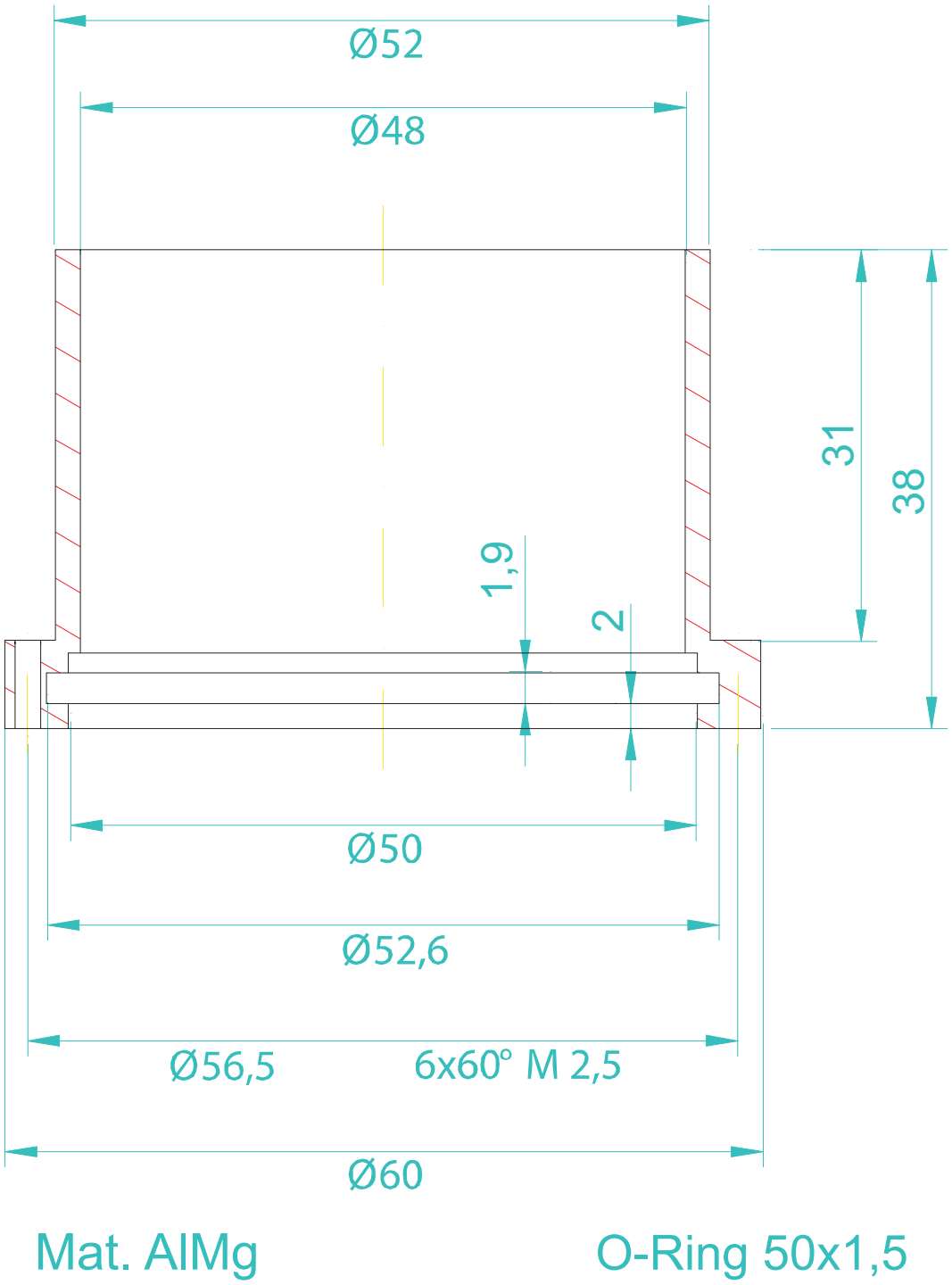

Figure 12.2: Outer cylinder of the Searle shear cell consisting of eloxated aluminum and a suprasil glass bottom.

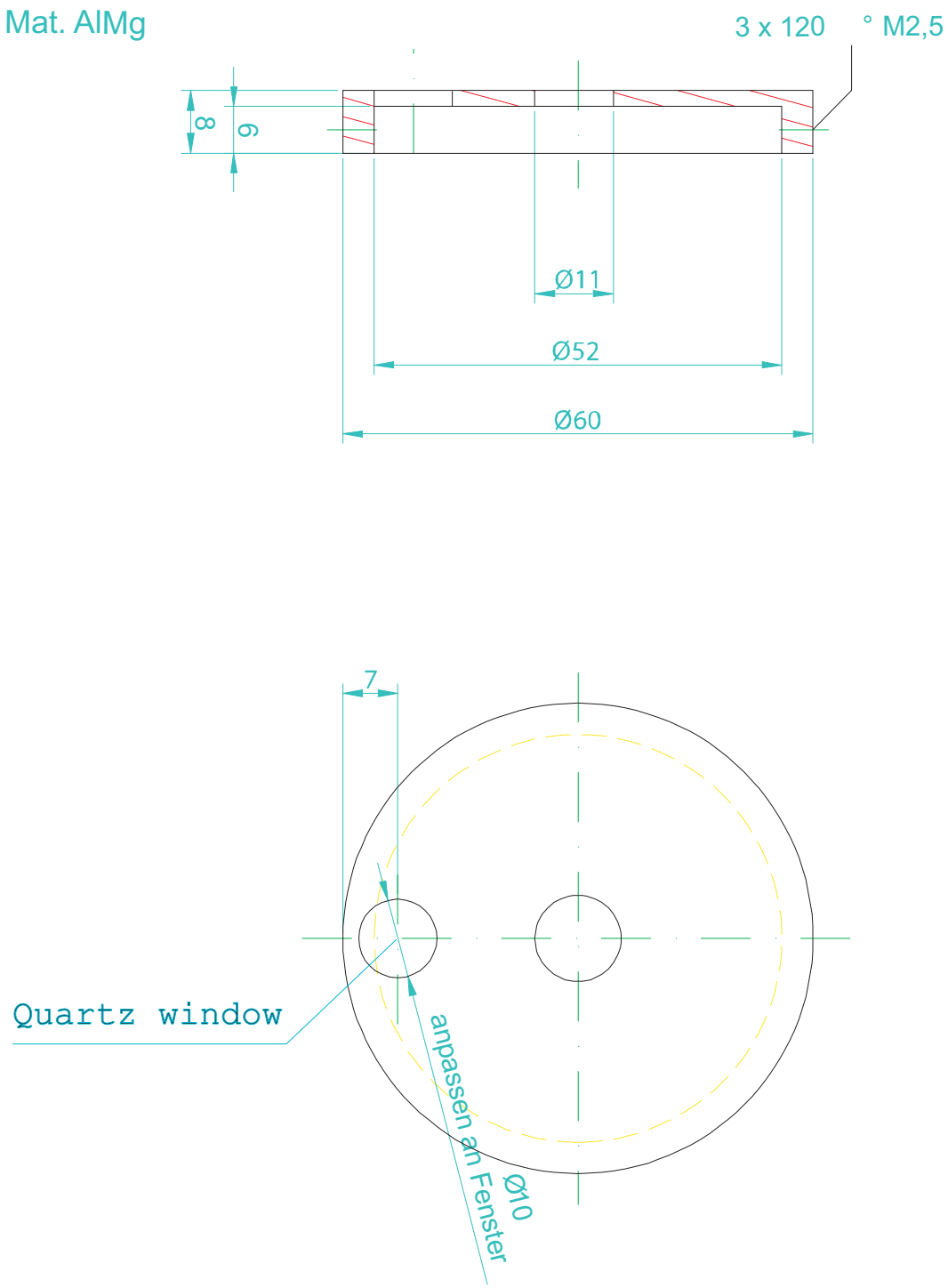

Figure 12.3: Lid for preventing evaporation of solvent and distortion of the laser beam at the meniscus of the fluid.

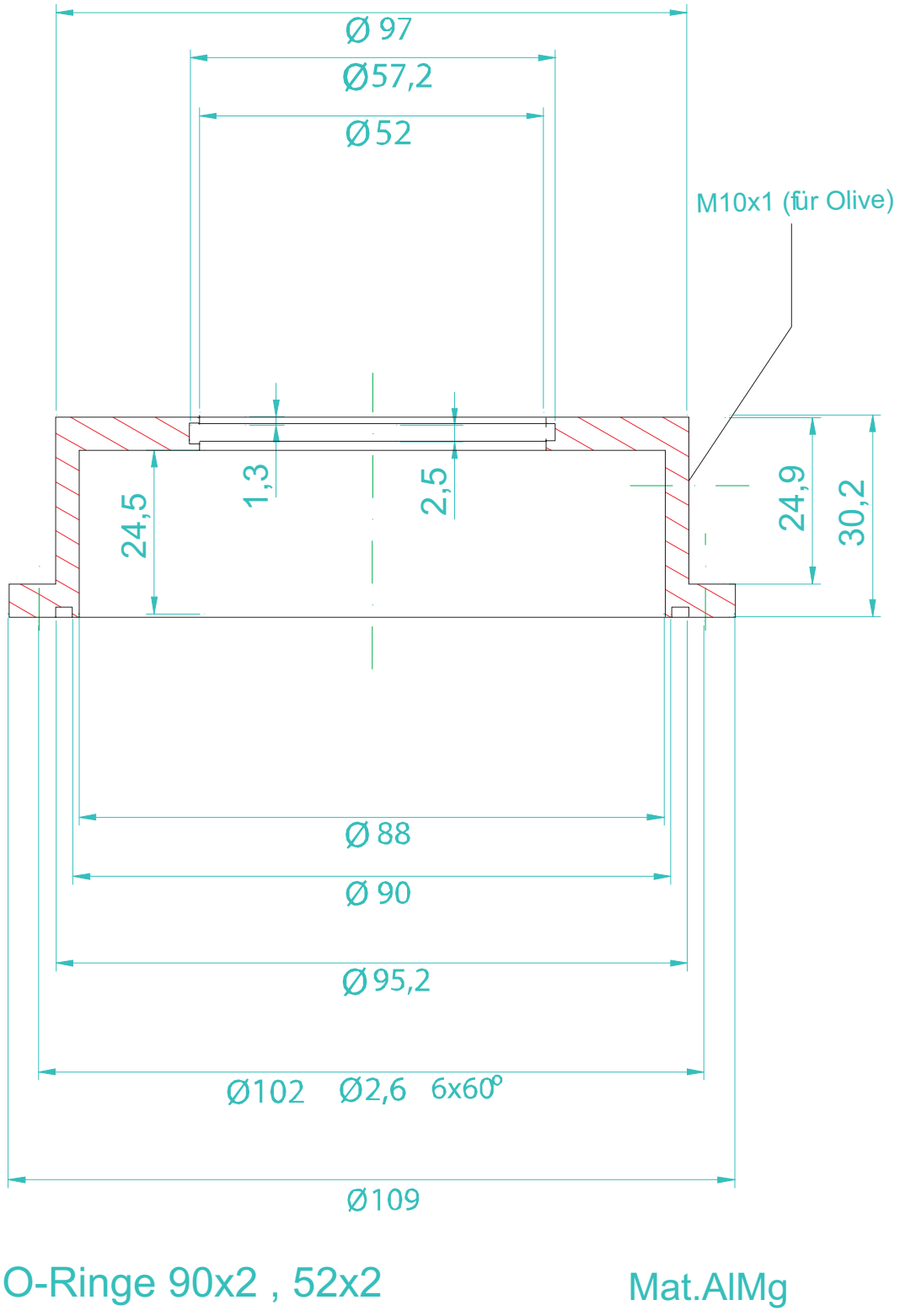

Figure 12.4: Cooling jacket anclosing the outer cup of the shear geometry.

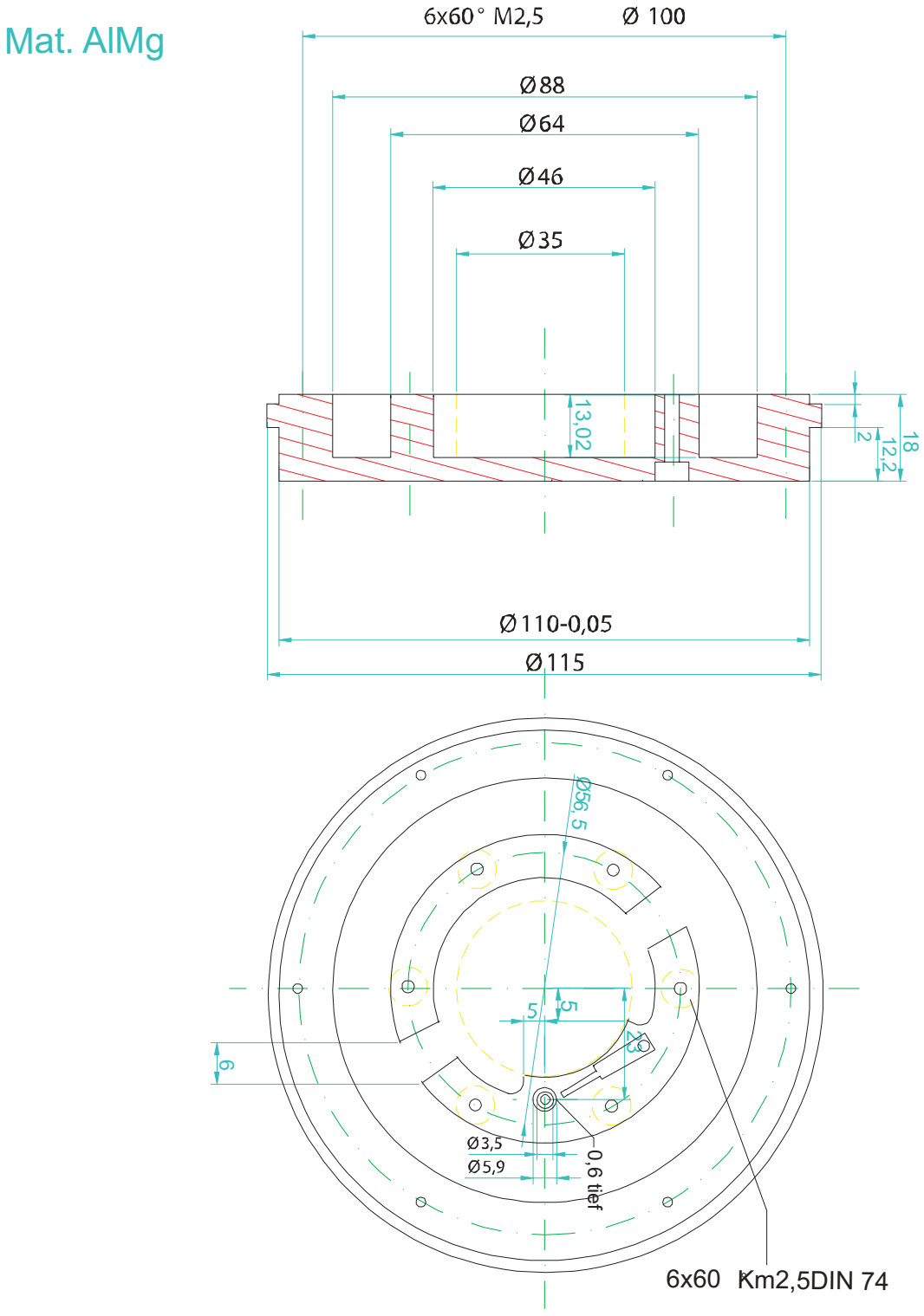

Figure 12.5: Base of the construction, holding the outer cup and the cooling jacket.

12.2 NSE-Experiments

NSE-experiments were performed at the NSE instrument at the FZ-Jülich with a 33wt% $C_{12}E_4$ sample in a H_2O/D_2O mixture (0.327w/w) without and with laponite (S/L=0.39%).

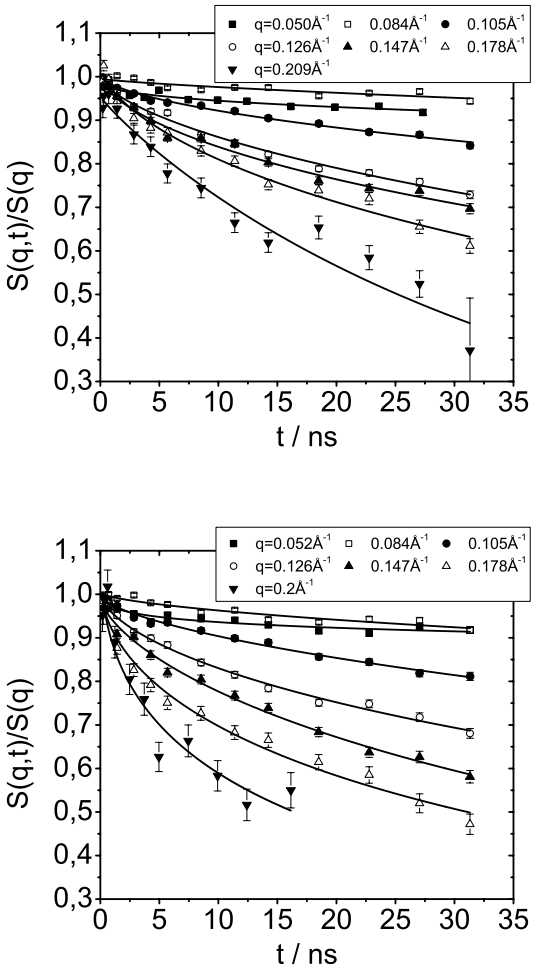

Figure 12.6: S(q,t)/S(q) as a function of scattering vector q for the sample without laponite (top) and with laponite (bottom). Lines are fits according to a streched exponentrial.

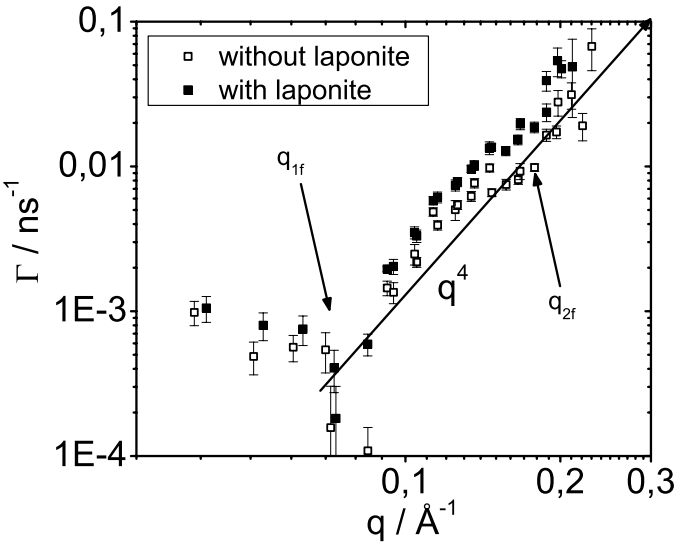

Figure 12.7: Relaxation rates of the samples with and without laponite determined by a stretched exponential analysis with the stretch-exponent β fixed to 2/3 as a function of scattering vector. The arrows point to the position of the first and second order Bragg-peaks. The solid line describes the asymtotic behavior.

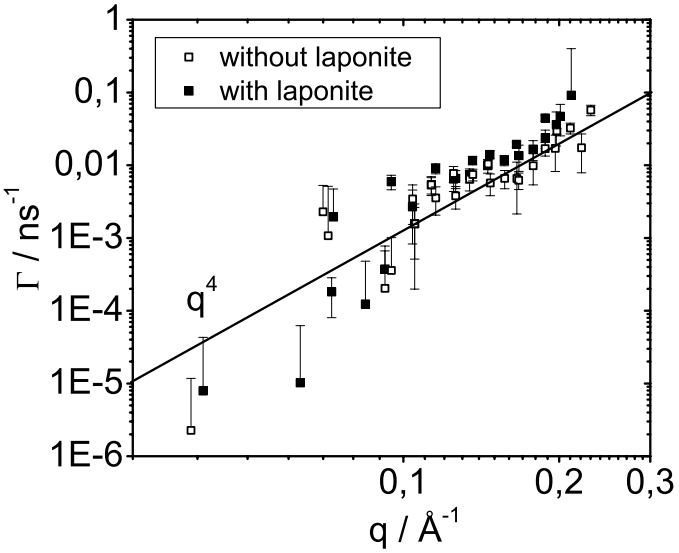

Figure 12.8: Same analysis with β as a free fit-parameter.

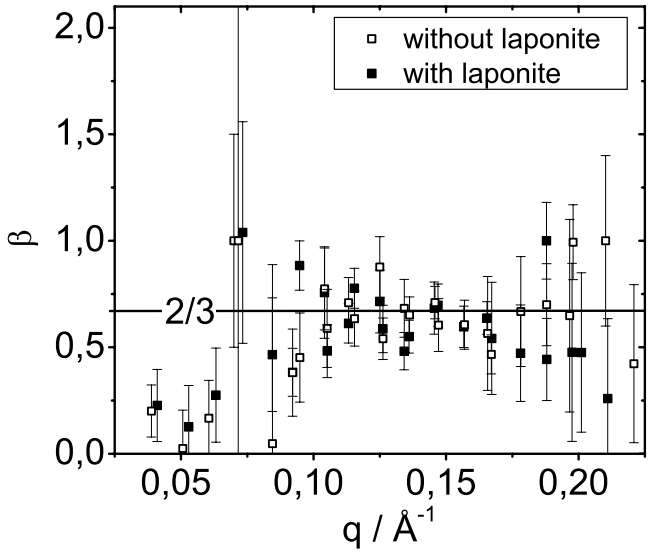

Figure 12.9: β as a function of $\vec{q}$ for both samples.

12.3 Oscillatory Rheo-SALS Experiments

Oscillatory experiments with a constant frequency of 1Hz were performed on parallel aligned lamellae of $C_{10}E_3$ 40wt%. In separate experiments the stress amplitude was varied from 1 to 5Pa. The example shown below shows the data of the experiment with 5Pa.

12.4 Hexagonal MLV-Packing

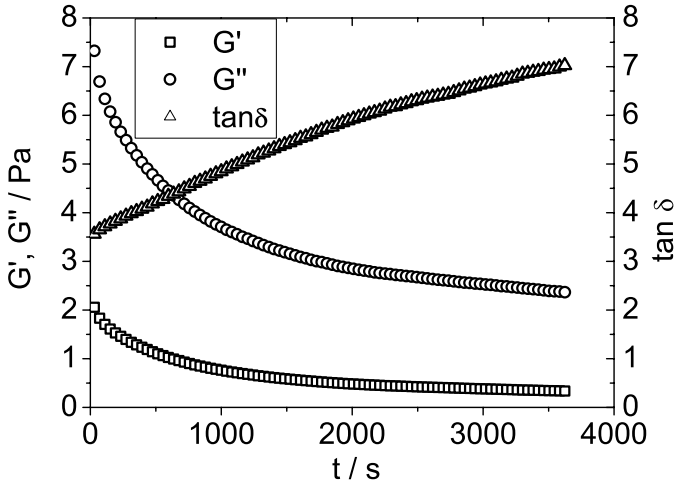

Figure 12.10: Evolution of storage, loss modulus and $\tan\delta$ with time in a stress controlled dynamic experiment with a stress amplitude of 5pa and a frequency of 1Hz.

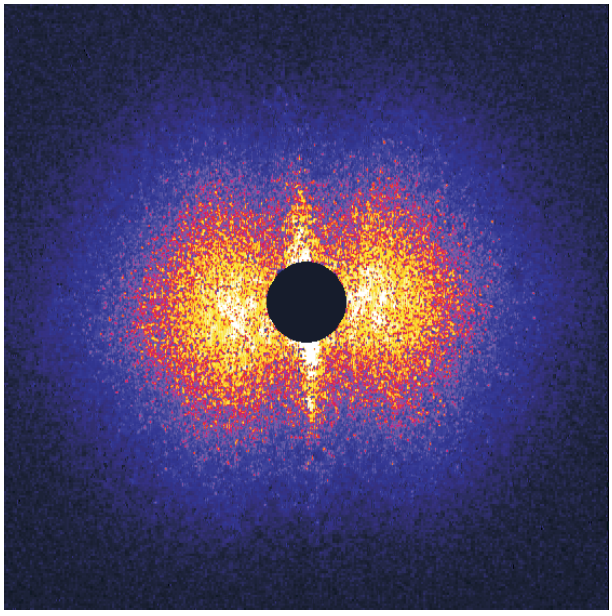

Figure 12.11: Depolaried SALS image of the same experiment toward the end ($\approx$ 3500s) of the experiment. The horizontal represents the flow, the vertical the neutral direction.

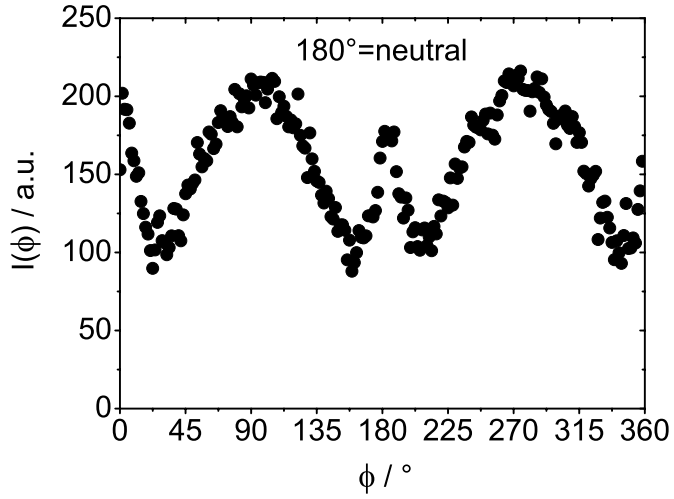

Figure 12.12: Azimuthal average of the SALS image at $0.7 \leq q \leq 1.2\mu m^{-1}$.

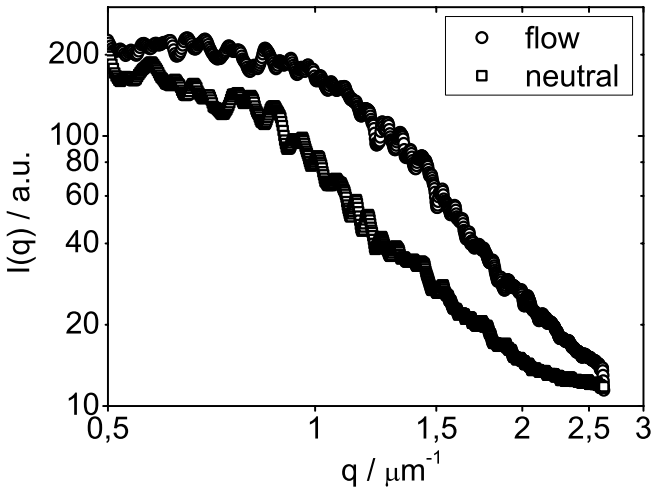

Figure 12.13: Radial sector averages in 10° sectors along the flow and the neutral directions.

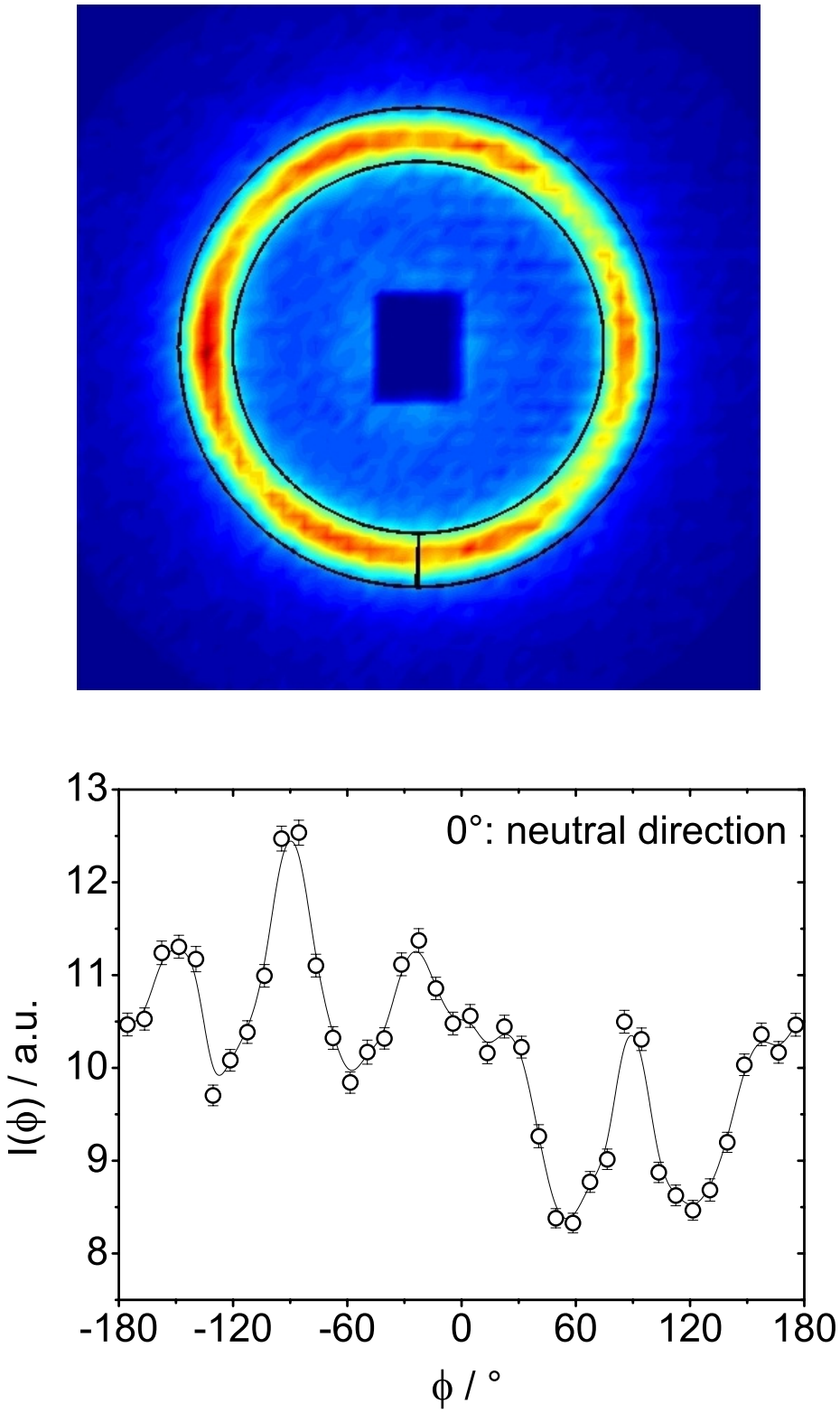

Figure 12.14: Top: SANS-image of a 40wt% $C_{10}E_3$ sheared with $50s^{-1}$ until steady state. The hexagonal symmetry is visible as a rather subtle modulation of the azimuthal intensity distribution. Bottom: Corresponding azimuthal intensity distribution evaluated in a sector at the Bragg-peak position (see image above).

List of Figures